Effects of the Non-ionic Surfactant Tween 80 on the Enzymatic Hydrolysis of Model Cellulose and Lignocellulosic Substrates

Feng Jiang

Dissertation submitted to the faculty of the
Virginia Polytechnic Institute and State University
in partial fulfillment of the requirements for the degree of

Doctor of Philosophy
in
Macromolecular Science and Engineering

Maren Roman, Chair
Kevin J. Edgar
Alan R. Esker
Charles E. Frazier
Scott H. Renneckar

August 25, 2011
Blacksburg, VA

Keywords: cellulose nanocrystals, lignin, cellulases, bioethanol, biomass, adsorption

Effects of the Non-ionic Surfactant Tween 80 on the Enzymatic Hydrolysis of Model Cellulose and Lignocellulosic Substrates

Feng Jiang

ABSTRACT

Non-ionic surfactants are known to enhance the biochemical conversion of lignocellulosic (LC) biomass to bioethanol. Their mechanisms of action, however, are incompletely understood. This research was conducted to elucidate the effects of the non-ionic surfactant Tween 80 on the enzymatic hydrolysis of cellulose and LC substrates. Model cellulose substrates were prepared from cellulose nanocrystals (CNCs) obtained by sulfuric acid hydrolysis of wood pulp. Two methods were developed for the removal of the sulfate groups on the CNCs, resulting from the use of sulfuric acid in their preparation. The effect of sulfate groups, which may be introduced into LC biomass during pretreatment with sulfuric acid, on the enzymatic hydrolysis of cellulose was studied with model cellulose substrates prepared from CNCs with different sulfate group densities. Adsorption of cellulases onto sulfated substrates increased with increasing sulfate group density but their rate of hydrolysis decreased. The decrease indicated an inhibitory effect of sulfate groups on the enzymatic hydrolysis of cellulose, possibly due to non-productive binding of the cellulases onto the substrates through electrostatic interactions instead of their cellulose binding domains. The effect of Tween 80 on the adsorption of cellulases onto lignin, often present as residual lignin in pretreated biomass, was studied with model lignin substrates, prepared from kraft lignin, organosolv lignin, and milled wood lignin. Cellulases appeared to adsorb onto the lignin substrates *via* both hydrophobic and polar interactions. Tween 80 molecules on the lignin substrates seemed to hinder cellulase adsorption *via* hydrophobic interactions and reduced the adsorption rate. Finally, the effects of lignin and Tween 80 on the enzymatic hydrolysis of cellulose and LC substrates were studied. Lignin hindered both the adsorption of cellulases onto the substrates and the enzymatic hydrolysis of the substrates. Tween 80 was found to form surfactant–protein complexes with cellulases in solution without compromising cellulase activity. Either substrate-adsorbed or in solution, Tween 80 had no effect on the hydrolysis of cellulose by cellulases. Substrate-adsorbed Tween 80 increased the apparent enzymatic hydrolysis rates of LC substrates but the ability of Tween 80 to increase their apparent hydrolysis rate depended strongly on their structural properties and the chemical properties of the lignin. Hence, Tween 80 may be able to mitigate the inhibitory effect of lignin on the enzymatic hydrolysis of pretreated biomass.

ACKNOWLEDGMENTS

First and foremost, I would like to express my deepest gratitude to my advisor, Prof. Maren Roman, for offering me the opportunity to study and work in her group and for her support and guidance during my research, without which I could never have accomplished this work. Her patience, encouragement, skillful guidance, and intelligence always motivated me to proceed along the right track in my research. I appreciate the tremendous time and effort that she invested in training me as a scientist. I am also very grateful to my committee members: Prof. Kevin J. Edgar, Prof. Alan R. Esker, Prof. Charles E. Frazier, and Prof. Scott H. Renneckar, for their input, advice, and comments on my work. Prof. Edgar always provided insightful and helpful comments and advice at every seminar I gave. Prof. Esker has put much time and effort in helping me to discuss and explain my results. Discussions with him always refreshed my mind and clarified some of my misunderstandings. Prof. Frazier has provided much useful advice and many helpful comments that enriched the lignin part of my work. Prof. Renneckar has provided much valuable advice and shared his expertise in several aspects of my work.

I want to thank Rick Caudill for helping me with the X-ray diffraction measurements, Dr. Jerry Hunter for helping me with the X-ray photoelectron spectroscopy measurements, and Dr. Hugo Azurmendi for helping me set up my NMR spectroscopy experiments.

I am truly grateful to the administrative faculty and staff of the MACR program and the Department of Wood Science and Forest Products, Prof. Judy S. Riffle, Mary Jane Smith, and Debbie Garnand, for their assistance during my study.

I would like to thank Dr. Zelin Liu, Dr. Abdulaziz Kaya, Dr. Ufuk Karabiyik, Joshua Kittle, and Xiaosong Du in Prof. Esker's lab, Adam Larkin in Profs. Davis's and Rajagopalan's lab, Raquel Mejia-Ariza in Prof. Davis's lab, and Lei Pan in Prof. Yoon's lab for their help in using their instruments. I want to thank Dr. Bin Li in Prof. Edgar's lab for his help with the lignin characterization. I also want to thank all my former and current group members: Dr. Hezhong Wang, Dr. Fernando Navarro, Shuping Dong, Jung Ki Hong, Chen Qian, and Xinyi Tan, and all

the fellow graduate students in the Department of Wood Science and Forest Products, for their help and support in both my research and life.

Last but not least, I would like to thank my parents, Picong Jiang and Shuqing Yan, and my elder sister, Dandan Jiang, for their continuous and unconditional love and support. I want to give special thanks to my wife, Ge Zhang, who has been accompanying, supporting, and encouraging me all the time. I could not have accomplished this without her support and sacrifice.

TABLE OF CONTENTS

Title Page i

Abstract ii

Acknowledgments iii

Table of Contents v

List of Figures xiii

List of Tables xxiii

CHAPTER 1

Introduction 1

1.1. Motivation 1

1.2. Goals and objectives 2

1.3. Dissertation outline 3

1.4. References 4

CHAPTER 2

Literature review 6

2.1. Cellulose 6

2.1.1. Molecular structure of cellulose 6

2.1.2. Crystal structure of cellulose 7

2.1.3. Cellulose nanocrystals 8

2.1.4. Model cellulose substrates 9

2.2. Lignin 10

2.2.1. Lignin structure and classification 10
2.2.2. Lignin isolation methods and resulting structural changes 12
2.2.3. Model lignin substrates 16
2.3. Enzymatic hydrolysis of cellulose 17
2.3.1. Enzymatic hydrolysis mechanism 17
2.3.2. 3-D structure of cellulases 18
2.4. Surfactants 20
2.4.1. Surfactant structure and classification 20
2.4.2. Solution properties of surfactants 21
2.4.3. Effects of surfactants on the enzymatic hydrolysis of cellulose 23
2.4.4. Interactions between surfactants and proteins 24
2.4.5. Interactions between surfactants and polymers 26
2.5. Substrate characterization techniques 27
2.5.1. Conductometric titration 28
2.5.2. X-ray photoelectron spectroscopy 30
2.5.3. X-ray diffraction 31
2.5.4. Atomic force microscopy 37
2.6. Surfactant characterization techniques 41
2.6.1. Tensiometry 41
2.6.2. Fluorescence spectroscopy 44
2.7. Measurement of surface adsorption and enzymatic hydrolysis 45
2.7.1. Quartz crystal microbalance with dissipation monitoring 45
2.7.2. Surface plasmon resonance spectroscopy 51
2.8. References 56

CHAPTER 3

Acid-catalyzed and solvolytic desulfation of H_2SO_4-hydrolyzed cellulose nanocrystals.....77

3.1. Abstract.....77

3.2. Introduction.....78

3.3. Experimental section.....80

3.3.1. Materials.....80

3.3.2. Preparation of H_2SO_4-hydrolyzed CNCs.....80

3.3.3. Preparation of HCl-hydrolyzed CNCs.....81

3.3.4. Acid-catalyzed desulfation.....81

3.3.5. Solvolytic desulfation.....82

3.3.6. Conductometric titration.....82

3.3.7. X-ray photoelectron spectroscopy (XPS).....83

3.3.8. X-ray diffraction (XRD).....84

3.3.9. Atomic force microscopy (AFM).....85

3.3.10. Dynamic light scattering (DLS).....85

3.4. Results and discussion.....86

3.4.1. Surface charge density.....86

3.4.2. Chemical composition.....89

3.4.3. Crystallite dimensions.....91

3.4.4. Extent of particle aggregation.....93

3.5. Conclusions.....96

3.6. Acknowledgments.....97

3.7. References.....97

CHAPTER 4

Effects of sulfate groups on the adsorption and activity of cellulases on cellulose substrates 103

4.1. Abstract 103

4.2. Introduction 104

4.3. Experimental section 106

4.3.1. Materials 106

4.3.2. CNC preparation 106

4.3.3. Cellulose substrate preparation 107

4.3.4. Determination of CNC surface density 108

4.3.5. Analysis of substrate accessibility 108

4.3.6. Preparation of enzyme solution 109

4.3.7. Isolation of CBDs 110

4.3.8. CBD adsorption onto the cellulose substrates 111

4.3.8.1. Viscoelastic modeling 111

4.3.9. Enzymatic hydrolysis of the cellulose substrates 112

4.3.10. Substrate imaging and surface roughness determination 113

4.3.11. Mapping of protein surface potential 113

4.4. Results and discussion 113

4.4.1. CNC surface density and substrate accessibility 113

4.4.2. CBD adsorption onto the cellulose substrates 116

4.4.3. Enzymatic hydrolysis of the cellulose substrates 119

4.4.4. Electrostatic potential maps for the catalytic domains of CBH I and EG I 124

4.4.5. AFM investigation of the cellulose substrates 126

4.5. Conclusions 129

4.6. Acknowledgments....130
4.7. References....130

CHAPTER 5

Effects of the non-ionic surfactant Tween 80 on the adsorption of cellulases onto lignin substrates....138

5.1. Abstract....138
5.2. Introduction....139
5.3. Experimental section....140
5.3.1. Materials....140
5.3.2. Lignin purification and fractionation....141
5.3.3. Quantitative ^{31}P NMR lignin analysis....141
5.3.4. Lignin substrate preparation....142
5.3.5. Surface energy measurements....143
5.3.6. QCM-D adsorption experiments....144
5.3.7. Substrate imaging and surface roughness determination....146
5.4. Results and discussion....146
5.4.1. Distribution of functional groups in the three lignins....146
5.4.2. Surface properties of the lignin substrates....148
5.4.3. Tween 80 adsorption experiments....151
5.4.4. Cellulase adsorption experiments....155
5.4.5. Quantification and visualization of cellulase on the lignin substrates....163
5.4.6. Cellulase adsorption kinetics....168
5.5. Conclusions....169
5.6. Acknowledgments....169

5.7. References 170

CHAPTER 6

Preparation and enzymatic hydrolysis of model lignocellulosic substrates: A QCM-D and AFM study 177

6.1. Abstract 177

6.2. Introduction 178

6.3. Experimental section 180

6.3.1. Materials 180

6.3.2. Cellulose nanocrystal (CNC) preparation 180

6.3.3. Lignin purification and fractionation 181

6.3.4. LC substrate preparation 181

6.3.5. Surface density measurements 182

6.3.6. X-ray photoelectron spectroscopy (XPS) 183

6.3.7. QCM-D hydrolysis experiments 183

6.3.8. Surface morphology and RMS surface roughness determination 184

6.4. Results and discussion 184

6.4.1. Surface properties of the LC substrates 184

6.4.2. Enzymatic hydrolysis of the LC substrates 190

6.4.3. Morphology change during enzymatic hydrolysis 197

6.5. Conclusions 200

6.6. Acknowledgments 200

6.7. References 201

CHAPTER 7

Effects of the non-ionic surfactant Tween 80 on the enzymatic hydrolysis of model cellulose and lignocellulosic substrates 206

7.1. Abstract 206

7.2. Introduction 207

7.3. Experimental section 209

7.3.1. Materials 209

7.3.2. Cellulose nanocrystal (CNC) preparation 209

7.3.3. Lignin purification and fractionation 210

7.3.4. Cellulose and LC substrate preparation 210

7.3.5. Surface tension measurements 211

7.3.6. Steady-state fluorescence spectroscopy 211

7.3.7. Tween 80 adsorption onto cellulase substrates 212

7.3.8. QCM-D hydrolysis experiments 214

7.3.9. Surface morphology and RMS surface roughness determination 215

7.3.10. Statistical analysis 216

7.4. Results and discussion 216

7.4.1. Interactions between Tween 80 and cellulase 216

7.4.2. Adsorption of Tween 80 onto cellulose substrates 219

7.4.3. Effects of Tween 80 on the enzymatic hydrolysis of cellulose substrates 220

7.4.4. Adsorption of Tween 80 onto LC substrates 223

7.4.5. Effects of Tween 80 on the enzymatic hydrolysis of LC substrates 228

7.5. Conclusions 236

7.6. Acknowledgments 236

7.7. References 237

CHAPTER 8

Conclusions and future work 242

8.1. Conclusions 242

8.2. Future work 244

8.2.1. Preparation of model wood substrates 244

8.2.2. Study of other non-ionic surfactants 244

APPENDIX

Appendix A 245

Appendix B 248

Appendix C 250

Appendix D 252

Appendix E 256

Appendix F: Additional experiments 260

F.1. Enzymatic hydrolysis of non-sulfated and sulfated cellulose substrates studied by surface plasmon resonance (SPR) 260

F.1.1. Experimental section 260

F.1.2. Results and discussion 261

F.2. Effects of Tween 80 on the enzymatic hydrolysis of cellulose substrates covered with a dehydrogenase polymer (DHP) lignin layer 263

F.2.1. Experimental section 263

F.2.2. Results and discussion 264

LIST OF FIGURES

Chapter 2

Figure 2.1. Molecular structure of cellulose.....6

Figure 2.2. Interconversions of cellulose crystal structures. (Reprinted from ref 5; fair use; Copyright 1984 Springer Verlag) 7

Figure 2.3. The lignin precursors (a) *p*-coumaryl alcohol, (b) coniferyl alcohol, and (c) sinapyl alcohol. 10

Figure 2.4. The three phenylpropanoid units of lignin: (a) *p*-hydroxyphenyl unit (H), (b) guaiacyl unit (G), and (c) syringyl unit (S).....11

Figure 2.5. Common linkages between the phenylpropanoid units in lignin. (Adapted from ref 47; fair use; Copyright 2004 Elsevier B.V.) 12

Figure 2.6. Alkaline cleavage of α-aryl ether bonds under formation of *para*-quinone methide intermediates (a), sulfidolytic cleavage of β-aryl ether bonds (b), and elimination of γ-hydroxymethyl group (c) during kraft pulping. (Adapted from ref 47; fair use; Copyright 2004 Elsevier B.V.) 14

Figure 2.7. Schematic illustration of the enzymatic hydrolysis of cellulose. (Reprinted from ref 76; fair use; Copyright 2002 American Society for Microbiology).....17

Figure 2.8. A Visual Molecular Dynamics rendering of the tunnel structure and catalytic site of *T. reesei* Cel7A (RCSB Protein Data Bank, ID 1cel). The tunnel is formed by a concave β-sandwich (yellow) and surface loops (green). The two loops (green) fold over the catalytic site (red: Glu 212, Asp 214, and Glu217) and close the tunnel through the interaction of two tyrosine residues (blue: Y247 and Y371).....18

Figure 2.9. A Visual Molecular Dynamics rendering of the tunnel structure and catalytic site of *T. reesei* Cel7B (RCSB Protein Data Bank, ID 1eg1). 19

Figure 2.10. A Visual Molecular Dynamics rendering of the CBD of *T. reesei* Cel7A. Binding sites are highlighted in yellow (Tyr 5, Tyr 31, and Tyr 32) (RCSB Protein Data Bank, ID 1cbh). 20

Figure 2.11. Chemical structures of common surfactants: a) the non-ionic surfactant polysorbate 80 (Tween 80); b) the anionic surfactant sodium dodecyl sulfate; and c) the cationic surfactant cetrimonium bromide. 21

Figure 2.12. Effect of surfactant concentration on various physical properties. (Adapted from ref 96; fair use; Copyright 1999 Wiley-VCH) 23

Figure 2.13. Schematic plot of number of bound SDS per protein molecule ($\overline{v}$) *versus* log[SDS]. (Reprinted from ref 105; fair use; Copyright 1995 American Chemical Society) 25

Figure 2.14. Surface tension versus ln[SDS] of aqueous SDS solutions (□, data from ref 126) and SDS solutions containing 0.025% (w/v) polyethylene oxide (○, data from ref 123). (Adapted from ref 123; fair use; Copyright 1967 Elsevier Inc., and ref 126; fair use; Copyright 1949 American Chemical Society) 27

Figure 2.15. Typical conductometric titration curves. 1. Strong acid; 2. Strong base; 3. Weak base. (Adapted from ref 127; fair use; Copyright 1978 Addison Wesley Longman Ltd.) 30

Figure 2.16. Atomic emission of a photoelectron from the core-level upon X-ray irradiation. (Reprinted from ref 129; fair use; Copyright 1997 John Wiley & Sons) 31

Figure 2.17. Schematic cross section of a filament X-ray tube. (Reprinted from ref 131; fair use; Copyright 2007 ISTE Ltd) 32

Figure 2.18. X-ray emission spectrum of a Cu target. 33

Figure 2.19. The crystallographic unit cell. (Reprinted from ref 135; fair use; Copyright 1998 Plenum Press) 33

Figure 2.20. Examples of lattice planes with their Miller indices. (Reprinted from ref 132; fair use; Copyright 1978 Addison-Wesley Publishing Company, Inc) 35

Figure 2.21. Diffraction of X-rays by a crystal. (Reprinted from ref 135; fair use; Copyright 1998 Plenum Press) 36

Figure 2.22. Configurations of an atomic force microscope: (a) sample-scanning configuration, (b) probe-scanning configuration. (Reprinted from ref 144; fair use; Copyright 2010 Oxford University Press) 38

Figure 2.23. Configuration of the Asylum Research MFP-3D atomic force microscope. (Reprinted from ref 145; fair use; Copyright 2008 Asylum Research) 39

Figure 2.24. AFM scanning modes: (a) contact mode, (b) non-contact mode, and (c) tapping or intermittent-contact mode. (Reprinted from ref 140; fair use; Copyright 2004 Elsevier) 40

Figure 2.25. Surface tension of a liquid as a function of the surfactant concentration. 42

Figure 2.26. Wilhelmy plate technique for measuring surface tension (γ) at the air/water interface.....43

Figure 2.27. (a) Pyrene molecule and (b) its fluorescence emission spectrum for excitation at 334 nm. (Reprinted from ref 152; fair use; Copyright 1977 American Chemical Society) 45

Figure 2.28. Schematic illustration of quartz crystal sensors covered with gold electrodes. 46

Figure 2.29. Schematic illustration of the QCM-D measurement setup. (Reprinted from ref 154; fair use; Copyright 1995 American Institute of Physics) 47

Figure 2.30. Schematic illustration of the viscoelastic film model, describing a viscoelastic film on an oscillating quartz crystal immersed in a Newtonian liquid. (Reprinted from ref 158; fair use; Copyright 1997 Royal Society of Chemistry).....49

Figure 2.31. Kretschmann prism configuration. (Adapted from ref 175; fair use; Copyright 1998 Humana Press) 52

Figure 2.32. Schematic illustration of Snell's law. (Adapted from ref 175; fair use; Copyright 1998 Humana Press) 53

Figure 2.33. Reflected light intensity R(θ) as a function of the angle of incidence and the SPR angles before ($\theta_{sp}(1)$ and after ($\theta_{sp}(2)$ binding of the analyte. (Reprinted from ref 175; fair use; Copyright 1998 Humana Press).....55

Chapter 3

Figure 3.1. Conductometric titration curves for the CNC samples SH (○), HH (△), HD7 (●), and SD (▲). 87

Figure 3.2. XPS survey spectrum of the CNC sample SH. 89

Figure 3.3. High-resolution S 2p photoelectron spectra of the CNC samples SH (a), HD7 (b), and SD (c). 90

Figure 3.4. X-ray diffractograms for the CNC samples SH (a), HH (b), HD7 (c), and SD (d). 92

Figure 3.5. Deconvolution of the X-ray diffractogram for the CNC sample SH with Voigt line profiles. 92

Figure 3.6. AFM height images of the CNC samples SH (a), HH (b), HD7 (c), and SD (d) (*z*-scale = 8 nm). 94

Figure 3.7. Hydrodynamic diameter for the CNC samples measured by DLS. 96

Chapter 4

Figure 4.1. ($\Delta f_n/n$) curves (5^{th} overtone) from H_2O/D_2O exchange experiments for a bare quartz crystal (○), the HH-0 substrate (□), and the SH-0 substrate (△). 115

Figure 4.2. (a) Langmuir and (b) Freundlich isotherms for CBD adsorption onto SH-0 (○) and HH-0 (□) cellulose substrates. The solid lines are the fitting curves. 117

Figure 4.3. (a) Langmuir and (b) Freundlich isotherms for CBD adsorption onto SH-55 (○) and SH-293 (□) cellulose substrates. The solid lines are the fitting curves. 118

Figure 4.4. (a) ($\Delta f_n/n$) and (b) ΔD curves (3^{rd} overtone) for the enzymatic hydrolysis of the substrates SH-0 (○) and HH-0 (□). 119

Figure 4.5. ΔD *versus* ($\Delta f_n/n$) (3^{rd} overtone) during enzymatic hydrolysis of the SH-0 substrate. 121

Figure 4.6. (a) ($\Delta f_n/n$) and (b) ΔD curves (3^{rd} overtone) for the enzymatic hydrolysis of the substrates SH-55 (△), SH-152 (□), and SH-293 (○). 122

Figure 4.7. Electrostatic potential maps for the catalytic domains of CBH I and EG I. Potential isocontours are shown at +1 $kT \cdot e^{-1}$ (blue) and –1 $kT \cdot e^{-1}$ (red) and obtained at 300 mM ionic strength (50 mM sodium citrate buffer) with a solute dielectric of 2 and a solvent dielectric of 78.54. 125

Figure 4.8. AFM height images of the cellulose substrates: (a) SH-293, (b) SH-152, (c) SH-55, (d) SH-0, and (e) HH-0. The scan size and z-scale are 5 μm × 5 μm and 8 nm, respectively, for all images. 127

Figure 4.9. AFM height images of the cellulose substrates after incubation for 2 h at 50 ℃ in enzyme solution: (a) SH-293, (b) SH-152, (c) SH-55, (d) SH-0. The scan size and z-scale are 5 μm × 5 μm and 8 nm, respectively, for all images. 129

Chapter 5

Figure 5.1. Phosphitylation of hydroxyl groups by CTMDP. 142

Figure 5.2. Quantitative ^{31}P NMR spectra of (a) MWL, (b) KL, and (c) OL after phosphitylation with CTMDP. The internal standard peak stems from phosphitylated e-HNDI. 147

Figure 5.3. AFM height images of untreated and Tween 80-treated lignin substrates. The scan size and z-scale for the images are 2 μm × 2 μm and 8 nm, respectively. 149

Figure 5.4. (a) ($\Delta f_n/n$) and (b) ΔD curves (5th overtone) from Tween 80 adsorption experiments on lignin substrates: OL substrate (red ○), KL substrate (blue △), and MWL substrate (purple □). Arrows indicate a switch in liquid feed to the QCM-D flow modules. 151

Figure 5.5. (a) ($\Delta f_n/n$) and (b) ΔD curves (5th overtone) from PEG adsorption experiments on lignin substrates: OL substrate (red ○), KL substrate (blue △), and MWL substrate (purple □). Arrows indicate a switch in liquid feed to the QCM-D flow modules. 154

Figure 5.6. ($\Delta f_n/n$) and ΔD curves (5th overtone) from cellulase adsorption experiments on (a) untreated, (b) PEG-treated, and (c) Tween 80-treated lignin substrates: OL substrate (○), KL substrate (△), and MWL substrate (□). Arrows indicate a switch in liquid feed to the QCM-D flow modules from cellulase solution to buffer. 156

Figure 5.7. (a) ($\Delta f_n/n$) and (b) ΔD curves (5th overtone) from cellulase adsorption experiments on untreated (open circle) and Tween 80-treated (filled circle) gold substrates. Arrows indicate a switch in liquid feed to the QCM-D flow modules.....158

Figure 5.8. (a) ($\Delta f_n/n$) and (b) ΔD curves (5th overtone) from cellulase adsorption experiments on untreated (open circle) and Tween 80-treated (filled circle silica substrates. Arrows indicate a switch in liquid feed to the QCM-D flow modules.....159

Figure 5.9. Plots of ΔD *versus* $(\Delta f_n/n)$ (5^{th} overtone) for the adsorption of cellulase onto untreated (black open symbols), PEG-treated (red filled symbols), and Tween 80-treated (black filled symbols) lignin substrates: (a) OL; (b) KL; (c) MWL. (Markers are spaced at 100 data points for clarity.) 161

Figure 5.10. AFM height images of untreated and Tween-80 treated lignin substrates after 10 min of cellulase adsorption. The scan size and z-scale are 5 μm × 5 μm and 8 nm, respectively, for all images......166

Figure 5.11. AFM height images of untreated and Tween-80 treated lignin substrates after 4 h of cellulase adsorption. The scan size and z-scale are 5 μm × 5 μm and 8 nm, respectively, for all images. 167

Chapter 6

Figure 6.1. Aqueous lignin/CNC suspensions with a solids concentration of 1 wt % and different lignin-to-CNC ratios: a) KL/CNC; b) OL/CNC; c) MWL/CNC. For each image, the lignin-to-CNC ratios are 1:9, 2:8, and 3:7 from left to right. 182

Figure 6.2. AFM height images of (a) a cellulose substrate and CLC substrates with a 30% nominal content of (b) KL, (c) OL, and (d) MWL. The scan size and z-scale are 2 μm × 2 μm and 15 nm, respectively, for all images.....186

Figure 6.3. AFM height images of LLC substrates prepared from 0.5 and 1 wt % aqueous lignin suspensions. The scan size and z-scale are 2 μm × 2 μm and 15 nm, respectively, for all images.....188

Figure 6.4. (a) $(\Delta f_n/n)$ and (b) ΔD curves (3^{rd} overtone) for the enzymatic hydrolysis of the cellulose substrate (○) and CLC substrates with a nominal KL content of 10% (□), 20% (△), and 30% (◇). 190

Figure 6.5. Values of (a) $(\Delta f_n/n)_{min}$ and (b) $(d(\Delta f_n/n)/dt)_{max}$, from 3^{rd} overtone $(\Delta f_n/n)$ curves, for the CLC substrates, as percentages of those for the cellulose substrate, $(\Delta f_n/n)_{min,CNC}$ (–489 Hz) and $(d(\Delta f_n/n)/dt)_{max,CNC}$ (2.64 s^{-2}).....192

Figure 6.6. (a) $(\Delta f_n/n)$ and (b) ΔD curves (3^{rd} overtone) for the enzymatic hydrolysis of the cellulose substrate (○) and LLC substrates prepared from 0.5 wt % (□) and 1 wt % (△) KL suspensions.....194

Figure 6.7. Values of (a) $(\Delta f_n/n)_{min}$ and (b) $(d(\Delta f_n/n)/dt)_{max}$, from 3^{rd} overtone $(\Delta f_n/n)$ curves, for the LLC substrates, as percentages of those for the cellulose substrate, $(\Delta f_n/n)_{min,CNC}$ (–489 Hz) and $(d(\Delta f_n/n)/dt)_{max,CNC}$ (2.64 s^{-2}), respectively. 195

Figure 6.8. AFM height images of CLC substrates with a 30% nominal content of (a) KL, (b) OL, and (c) MWL and (d) a cellulose substrate after enzymatic hydrolysis. The scan size and z-scale are 2 μm × 2 μm and 15 nm, respectively, for all images.. 198

Figure 6.9. AFM height images of LLC substrates prepared from 1 wt % aqueous suspensions of (a) KL, (b) OL, and (c) MWL after enzymatic hydrolysis. d) is an image of a bare silica quartz crystal, shown for comparison. The scan size and z-scale are 2 μm × 2 μm and 15 nm, respectively, for all images.....199

Chapter 7

Figure 7.1. Surface tension of 50 mM sodium citrate buffer (○) and cellulase solution (in buffer) (□) as a function of the Tween 80 concentration. (The dashed lines are guides to the eye.) 217

Figure 7.2. (a) Intensity ratio of the 1st and 3rd vibrational peaks (I_1/I_3) of the pyrene emission spectrum and (b) ratio of the pyrene excimer-to-monomer fluorescence emission (I_e/I_m) in 50 mM sodium citrate buffer (○) and cellulase solution (in buffer) (□) as functions of the Tween 80 concentration. (The dashed lines are guides to the eye.).....218

Figure 7.3. Langmuir adsorption isotherm for Tween 80 adsorption onto a model cellulose substrate measured by QCM-D (○) and SPR (□). The dash line is the fitting curve.. 220

Figure 7.4. Values of (a) $(\Delta f_n/n)_{min}$ and (b) $(d(\Delta f_n/n)/dt)_{max}$ from 3rd overtone ($\Delta f_n/n$) curves for the pre-adsorption experiments. The values are means of at least three measurements. An asterisk indicates a significant difference (Student's t-test, $p < 0.05$) from the 0-mM mean. 222

Figure 7.5. Values of (a) $(\Delta f_n/n)_{min}$ and (b) $(d(\Delta f_n/n)/dt)_{max}$ from 3rd overtone ($\Delta f_n/n$) curves for the mixed-solution experiments. The values are means of at least three measurements. An asterisk indicates a significant difference (Student's t-test, $p < 0.05$) from the 0-mM mean. 222

Figure 7.6. Representative (a) ($\Delta f_n/n$) and (b) ΔD curves (3rd overtone) for Tween 80 adsorption onto a cellulose substrate (◊) and CLC substrates with a 30% nominal content of KL (△), OL (○), and MWL (□). The arrows indicate the switch of the liquid feed to Tween 80 solution (1st) and buffer (2nd).....224

Figure 7.7. Representative (a) ($\Delta f_n/n$) and (b) ΔD curves (3rd overtone) for Tween 80 adsorption onto LLC substrates prepared from 1 wt % aqueous

suspensions of KL (△), OL (○), and MWL (□). The arrows indicate the switch of the liquid feed to Tween 80 solution (1st) and buffer (2nd).....224

Figure 7.8. AFM height images of untreated and Tween 80-treated LLC substrates prepared from 1 wt % aqueous lignin suspensions. The scan size and z-scale are 2 μm × 2 μm and 15 nm, respectively, for all images.....227

Figure 7.9. ($\Delta f_n/n$) and ΔD curves (3rd overtone) for the enzymatic hydrolysis of untreated (□) and Tween 80-treated (○) CLC substrates with a nominal lignin content of 30%.....229

Figure 7.10. $(d(\Delta f_n/n)/dt)_{max}$, from 3rd overtone ($\Delta f_n/n$) curves, for untreated and Tween 80-treated CLC substrates, prepared from a) KL, b) OL, and c) MWL, as a percentage of that for a cellulose substrate, $(d(\Delta f_n/n)/dt)_{max,CNC}$ (2.64 s^{-2}).....230

Figure 7.11. ($\Delta f_n/n$) and ΔD curves (3rd overtone) for the enzymatic hydrolysis of untreated (□) and Tween 80-treated (○) LLC substrates prepared from 1 wt % aqueous lignin suspensions.....232

Figure 7.12. $(d(\Delta f_n/n)/dt)_{max}$, from 3rd overtone ($\Delta f_n/n$) curves, for untreated and Tween 80-treated LLC substrates, prepared from a) 0.5 wt % and b) 1 wt % lignin suspensions, as a percentage of that for a cellulose substrate, $(d(\Delta f_n/n)/dt)_{max,CNC}$ (2.64 s^{-2}).....233

Appendix

Figure A.1. Mechanism for the solvolytic desulfation of CNC pyridinium salt. 245

Figure A.2. High-resolution C 1s photoelectron spectra of the CNC samples (a) SH, (b) HH, (c) HD7, and (d) SD 246

Figure B.1. Representative ($\Delta f_n/n$) curves (5th overtone) from H_2O/D_2O solvent exchange QCM-D experiments for (a) the SH-55 substrate, (b) the SH-151 substrate, and (c) the SH-293 substrate.....248

Figure B.2. Representative fitting curves for the adsorption of CBDs (100 $\mu g \cdot mL^{-1}$) onto the CNC substrates SH-292 (a), SH-55 (b), SH-0 (c), and HH-0 (d). Fitting was conducted with QTools 3 software using the 3rd and 5th overtones. The density and viscosity of water at 25 ℃ are 997 $kg \cdot m^{-3}$ and $0.89 \cdot 10^{-3}$ $kg \cdot m^{-1}s^{-1}$, and the density of the viscoelastic film was fixed at 1152 $kg \cdot m^{-3}$.....249

Figure C.1. (a) ($\Delta f_n/n$) and (b) ΔD curves (5th overtone) from Tween 80 adsorption experiments on gold substrates. The arrows indicate a switch in liquid feed to the QCM-D flow modules. 251

Figure C.2. (a) ($\Delta f_n/n$) and (b) ΔD curves (5th overtone) from Tween 80 adsorption experiments on silica substrates. The arrows indicate a switch in liquid feed to the QCM-D flow modules. 251

Figure D.1. AFM height images of CLC substrates with a 10 or 20% nominal lignin content. The scan size and z-scale are 2 μm × 2 μm and 15 nm, respectively, for all images. 252

Figure D.2. ($\Delta f_n/n$) and ΔD curves (3rd overtone) for the enzymatic hydrolysis of the cellulose substrate (○) and CLC substrates with a nominal OL or MWL content of 10% (□), 20% (△), and 30% (◇). 253

Figure D.3. ($\Delta f_n/n$) and ΔD curves (3rd overtone) for the enzymatic hydrolysis of the cellulose substrate (○) and LLC substrates prepared from 0.5 wt % (□) and 1 wt % (△) OL or MWL suspensions. 254

Figure D.4. AFM height images of CLC substrates with a 10 or 20% nominal lignin content after enzymatic hydrolysis. The scan size and z-scale are 2 μm × 2 μm and 15 nm, respectively, for all images. 255

Figure E.1. ($\Delta f_n/n$) and ΔD curves (3rd overtone) for the enzymatic hydrolysis of untreated (□) and Tween 80-treated (○) CLC substrates with a nominal lignin content of 10%. 256

Figure E.2. ($\Delta f_n/n$) and ΔD curves (3rd overtone) for the enzymatic hydrolysis of untreated (□) and Tween 80-treated (○) CLC substrates with a nominal lignin content of 20%. 257

Figure E.3. ($\Delta f_n/n$) and ΔD curves (3rd overtone) for the enzymatic hydrolysis of untreated (□) and Tween 80-treated (○) LLC substrates prepared from 0.5 wt % aqueous lignin suspensions. 259

Figure F.1. ($\Delta \theta_{SP}$) curves for the enzymatic hydrolysis of the substrates SH-0 (○) and HH-0 (□). The arrows indicate a switch of the liquid feed from enzyme solution to buffer. 261

Figure F.2. ($\Delta \theta_{SP}$) curves for the enzymatic hydrolysis of the substrates SH-55 (△), SH-152 (□), and SH-293 (○). The arrows indicate a switch of the liquid feed from enzyme solution to buffer. 262

Figure F.3. AFM height images of DHP lignin covered cellulose substrates (high-CAC). The scan sizes are (a) 5 μm × 5 μm and (b) 2 μm × 2 μm. The z-

scale is 15 nm. The RMS surface roughness was determined from the entire area of the image. 265

Figure F.4. (a) ($\Delta f_n/n$) and (b) ΔD curves (3rd overtone) for the adsorption of Tween 80 onto the high-CAC substrate (□) and low-CAC substrate (○). The arrows indicate the switch of the liquid feed from Tween 80 solution to buffer. 266

Figure F.5. (a) ($\Delta f_n/n$) and (b) ΔD curves (3rd overtone) for the enzymatic hydrolysis of untreated (□) and Tween 80-treated (○) high-CAC substrates. The arrows indicate a switch of the liquid feed from enzyme solution to buffer. 267

Figure F.6. (a) ($\Delta f_n/n$) and (b) ΔD curves (3rd overtone) for the enzymatic hydrolysis of untreated (□) and Tween 80-treated (○) low-CAC substrates. The arrows indicate a switch of the liquid feed from enzyme solution to buffer. 268

LIST OF TABLES

Chapter 2

Table 2.1. Molar conductivities of ions at 25 ℃ ($\Omega^{-1}\cdot cm^{-2}\cdot mol^{-1}$) (from ref 127) 29

Table 2.2. Crystallographic unit cell types and Bravais lattices 34

Chapter 3

Table 3.1. CNC samples and their designations 86

Table 3.2. Surface charge densities of the CNC samples 88

Table 3.3. Atomic concentrations of C, O, and S for different CNC samples 91

Table 3.4. Crystallite dimensions for different CNC samples determined by deconvolution of the x-ray diffractograms with Voigt line profiles 93

Chapter 4

Table 4.1. CNC samples and their designations 107

Table 4.2. CNC surface densities, $\rho_{S,CNC}$, and H_2O surface densities, $\rho_{S,\,H_2O}$, of the cellulose substrates[a] 114

Table 4.3. Langmuir and Freundlich isotherm parameters for the adsorption of CBDs onto the cellulose substrates[a,b] 118

Table 4.4. Values of the ($\Delta f_n/n$) minima, ΔD maxima, and the minima and maxima of $d(\Delta f_n/n)/dt$, taken as a measure for the rate of enzyme adsorption and substrate hydrolysis, respectively[a] 123

Table 4.5. Surface roughnesses (nm) for the different cellulose substrates from 5 μm × 5 μm AFM height images 128

Chapter 5

Table 5.1. Surface tensions, γ_l, of the test liquids and their polar and dispersive components, γ_l^p and γ_l^d , respectively.[41] 144

Table 5.2. Measured absolute and relative hydroxyl and carboxyl group contents of the three lignins determined by quantitative ^{31}P NMR spectroscopy 147

Table 5.3. Surface energies, γ_s, of untreated and Tween 80-treated lignin substrates and their polar and dispersive components, γ_s^p and γ_s^d , respectively[a].....150

Table 5.4. Values for $\Delta(\Delta f_n/n)_I$,[a] $\Delta(\Delta f_n/n)_{II}$,[b] and $\Delta(\Delta f_n/n)_{III}$.[c,d]. 153

Table 5.5. Surface excess concentrations of adsorbed cellulase on untreated and Tween 80-treated lignin substrates after 10 min and 4 h of adsorption[a,b].....163

Table 5.6. Values of the frequency change due primarily to cellulase adsorption *via* polar interactions, Δf_h, and the relaxation time, τ , obtained by fitting the gradually decreasing section of the ($\Delta f_n/n$) curves (5th overtone) with eq 5.2.....168

Chapter 6

Table 6.1. RMS surface roughnesses, surface densities, atomic concentrations of C, O, and S, and C/O ratios for the cellulose and CLC substrates[a] 187

Table 6.2. RMS surface roughnesses and surface densities of the lignin layer of the LLC substrates 189

Table 6.3. Times of the ($\Delta f_n/n$) minima, t_{min}, for the cellulose and LLC substrates[a] 197

Chapter 7

Table 7.2. Times of the ($\Delta f_n/n$) minima, t_{min}, for untreated and Tween 80-treated cellulose and LLC substrates[a] 235

Appendix

Table A.1. Relative amounts of C1, C2, and C3 carbon species and C2/C3 ratios for different CNC samples.....247

Table C.1. Average contact angles of the three test liquids on untreated and Tween 80-treated lignin substrates[a].....250

Table E.1. $(d(\Delta f_n/n)/dt)_{max}/(d(\Delta f_n/n)/dt)_{max,CNC} \times 100\%$, from 3rd overtone ($\Delta f_n/n$) curves, for untreated and Tween 80-treated CLC substrates[a].....258

Table E.2. $(d(\Delta f_n/n)/dt)_{max}/(d(\Delta f_n/n)/dt)_{max,CNC} \times 100\%$, from 3rd overtone ($\Delta f_n/n$) curves, for untreated and Tween 80-treated LLC substrates[a].....258

CHAPTER 1

Introduction

1.1. Motivation

Because of the steady increase in world population and industrialization, the demand for energy has increased dramatically in recent years.[1] According to the most recent World Energy Outlook, an annual publication of the International Energy Agency, by the year 2035 the world energy demand will have risen by 36% from its 2008 level, with crude oil still being the dominant fuel. The global demand for crude oil in 2035 is predicted to be 99 million barrels per day. However, depending on the vigor of government actions, global oil production is predicted to either peak at 88 million barrels per day before 2020, falling to 81 million barrels per day in 2035, or to reach 96 million barrels per day, approaching peak level, in 2035. In either scenario, by the year 2035 crude oil production will not meet global demand. The predicted future shortage of crude oil makes finding a sustainable alternative a top priority in many countries. Besides the consideration of a future shortage of fossil fuels, environmental concerns are another driving force for countries to explore clean and sustainable alternatives to petroleum. During the past 150 years, the CO_2 content of the air has increased from 280 ppm to 365 ppm.[2] This increase has caused serious worldwide concern about global warming.[2,3] Of the increase in the air's CO_2 content, 73% is attributed to the combustion of fossil fuel.[4] Because of the aforementioned challenges associated with crude oil as the primary source for liquid fuels, fuels from renewable resources, so-called biofuels, have been pursued extensively around the globe during the past decades. Currently, two classes of liquid biofuels are attracting considerable attention, namely bioethanol (or biobutanol) for the replacement of gasoline and biodiesel for the replacement of

diesel fuel.[5] In the United States, the gasoline at most gas stations already contains 10% ethanol and biodiesel can be used in diesel engines with little or no modification to the engine.[1-3]

"First-generation" bioethanol is produced by the fermentation of glucose that has been derived from the edible part of food crops, such as corn, wheat, sugar cane, or sugar beet. There are several problems related to using food as a source for biofuels. First, obviously, using food as a fuel source poses ethical issues, considering that people are starving in underdeveloped countries, and will likely cause an increase in food prices. Second, fuels derived from food crops are not carbon neutral because of the extensive use of fertilizer and pesticides in their production.[6,7] "Second-generation" bioethanol is produced from lignocellulosic biomass, *i.e.* non-edible plant matter consisting primarily of cellulose, hemicellulose, and lignin, which is a more sustainable alternative, compared to food crops, and could solve both the "fuel/food dilemma" and "carbon positive" problems.[5,6] The most widely investigated feedstocks for the production of second-generation bioethanol are fast growing trees, such as poplar or willow, perennial grasses, such as switchgrass or miscanthus, and lignocellulosic agricultural waste, including corn stalks, wheat straw, and bagasse. Economically the most promising process for the production of bioethanol from lignocellulosic biomass is enzymatic hydrolysis followed by microbial fermentation. However, there are still many technical challenges related to this process that need to be overcome to make bioethanol cost-competitive with gasoline. Several recent studies have shown that non-ionic surfactants may have beneficial effects on the enzymatic hydrolysis of lignocellulosic biomass.[8-13] However, the mechanisms for these effects are not well understood.

1.2. Goals and objectives

The goal of my research was to elucidate the mechanisms by which non-ionic surfactants enhance the enzymatic hydrolysis of lignocellulosic biomass. The approach that I took was based on the use of model cellulose, lignin, and lignocellulosic substrates in conjunction with surface analytical techniques to study cellulase adsorption onto and hydrolysis of these substrates in the absence and presence of the non-ionic surfactant Tween 80. The specific objectives for this research were:

1. To develop methods for the preparation of model cellulose substrates that have surface properties similar to those of native cellulose

2. To develop methods for the preparation of model lignin and lignocellulosic substrates

3. To determine the interactions of these model substrates with Tween 80 and cellulase molecules as well as between Tween 80 and cellulase molecules

4. To determine the effects of Tween 80 molecules on the interactions of the model substrates with cellulase molecules

1.3. Dissertation outline

The dissertation contains eight chapters and an appendix. Chapter 2 reviews some background information relating to this project. The review covers the primary materials of this research, namely cellulose, lignin, cellulases and their hydrolysis mechanisms, and surfactants. It also summarizes the postulated mechanisms for the enhancement of the enzymatic hydrolysis of lignocellulosic biomass by surfactants and the interactions between surfactants and polymers as well as proteins. Lastly, it discusses the main characterization techniques used in this research, including conductometric titration, X-ray photoelectron spectroscopy, X-ray diffraction, atomic force microscopy, tensiometry, fluorescence spectroscopy, quartz crystal microbalance with dissipation monitoring (QCM-D), and surface plasmon resonance spectroscopy.

Chapter 3 describes two new methods for the preparation of cellulose nanocrystals with a native (non-sulfated) cellulose surface by sulfuric acid hydrolysis and subsequent desulfation as well as their characterization in terms of surface charge density, chemical composition, crystallite size, particle size, aggregation behavior, and particle morphology. This chapter has been published in the ACS journal *Langmuir*.[14]

Chapter 4 describes the preparation and characterization of cellulose substrates with different sulfate group densities from fully and partially desulfated cellulose nanocrystals and the effects of the negatively charged sulfate groups on the enzymatic hydrolysis of the substrates.

Chapter 5 discusses the preparation and characterization of lignin substrates from three different lignins, namely kraft lignin, organosolv lignin, and milled wood lignin, and the interactions of these substrates with the non-ionic surfactant Tween 80 as well as cellulases.

Chapter 6 presents preparation methods for lignocellulosic substrates from desulfated cellulose nanocrystals and the three lignins as well as their characterization and reports an inhibitory effect of lignin on the enzymatic hydrolysis of these substrates.

Chapter 7 describes the interactions between Tween 80 and cellulases, determined by tensiometry and fluorescence spectroscopy, and discusses the beneficial effect of Tween 80 on the enzymatic hydrolysis of lignocellulosic substrates observed in QCM-D hydrolysis experiments.

Chapter 8 summarizes the conclusions of this research and the appendix provides supplementary information to Chapters 3–7 and describes some additional experiments.

1.4. References

1. Sun, Y.; Cheng, J. Y. Hydrolysis of Lignocellulosic Materials for Ethanol Production: A Review. *Bioresource Technology* **2002,** *83,* 1-11.

2. Galbe, M.; Zacchi, G. A Review of the Production of Ethanol from Softwood. *Applied Microbiology and Biotechnology* **2002,** *59,* 618-628.

3. Balat, M.; Balat, H.; Oz, C. Progress in Bioethanol Processing. *Progress in Energy and Combustion Science* **2008,** *34,* 551-573.

4. Lokhorst, A.; Wildenborg, I. Introduction on CO_2 Geological Storage. Classification of Storage Options. *Oil & Gas Science and Technology-Revue de l Institut Francais du Petrole* **2005,** *60,* 513-515.

5. Gupta, R. B.; Deirbas, A. In: Gasoline, Diesel, and Ethanol Biofuels from Grasses and Plants; Cambridge University Press: New York, 2010; pp 16-24.

6. Gomez, L. D.; Steele-King, C. G.; McQueen-Mason, S. J. Sustainable Liquid Biofuels from Biomass: The Writing's on the Walls. *New Phytologist* **2008,** *178,* 473-485.

7. Hill, J.; Nelson, E.; Tilman, D.; Polasky, S.; Tiffany, D. Environmental, Economic, and Energetic Costs and Benefits of Biodiesel and Ethanol Biofuels. *Proceedings of the National Academy of Sciences of the United States of America* **2006,** *103,* 11206-11210.

8. Castanon, M.; Wilke, C. R. Effects of the Surfactant Tween-80 on Enzymatic-Hydrolysis of Newspaper. *Biotechnology and Bioengineering* **1981,** *23,* 1365-1372.

9. Kaya, F.; Heitmann, J. A.; Joyce, T. W. Influence of Surfactants on the Enzymatic-Hydrolysis of Xylan and Cellulose. *TAPPI Journal* **1995,** *78,* 150-157.

10. Kaar, W. E.; Holtzapple, M. T. Benefits from Tween During Enzymic Hydrolysis of Corn Stover. *Biotechnology and Bioengineering* **1998,** *59,* 419-427.

11. Kristensen, J. B.; Borjesson, J.; Bruun, M. H.; Tjerneld, F.; Jorgensen, H. Use of Surface Active Additives in Enzymatic Hydrolysis of Wheat Straw Lignocellulose. *Enzyme and Microbial Technology* **2007,** *40,* 888-895.

12. Alkasrawi, M.; Eriksson, T.; Borjesson, J.; Wingren, A.; Galbe, M.; Tjerneld, F.; Zacchi, G. The Effect of Tween-20 on Simultaneous Saccharification and Fermentation of Softwood to Ethanol. *Enzyme and Microbial Technology* **2003,** *33,* 71-78.

13. Eriksson, T.; Borjesson, J.; Tjerneld, F. Mechanism of Surfactant Effect in Enzymatic Hydrolysis of Lignocellulose. *Enzyme and Microbial Technology* **2002,** *31,* 353-364.

14. Jiang, F.; Esker, A. R.; Roman, M. Acid-Catalyzed and Solvolytic Desulfation of H_2SO_4-Hydrolyzed Cellulose Nanocrystals. *Langmuir* **2010,** *26,* 17919-17925.

CHAPTER 2

Literature review

2.1. Cellulose

2.1.1. **Molecular structure of cellulose**

Cellulose-based materials have been used as energy sources, building materials, and clothing for thousands of years. However, it was not until 1838 that cellulose was discovered in plant tissue, by the French chemist Anselme Payen, as a chemical compound with the empirical formula $C_6H_{10}O_5$.[1,2]

Cellulose is the most abundant, natural polymer on earth, occurring abundantly in woody plants, cotton, bacteria, fungi, algae, and even some animals. The molecular structure of cellulose has been accepted to be a linear homopolysaccharide, composed of β-D-glucopyranose units linked by (1→4) glycosidic bonds,[3-5] as shown in Figure 2.1

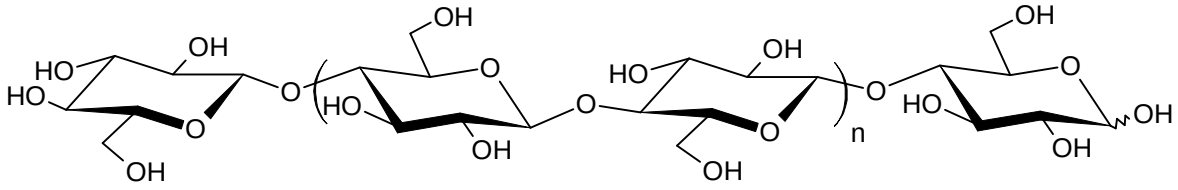

Figure 2.1. Molecular structure of cellulose.

In cellulose, the pyranose rings are in their $^4C_1$ chair conformation, with all hydroxyl groups in equatorial positions. The preferred bond angles of the acetal oxygen bridges are

preserved by in-plane rotation of every other anhydroglucose unit (AGU) so that the cellulose repeat unit is composed of two adjacent AGUs (cellobiose). The terminal D-glucose unit with the original hydroxyl group at C4 is the non-reducing chain end (left end in Figure 2.1) whereas the terminal D-glucose unit with the original hydroxyl group at C1, which exists in equilibrium with the open-ring aldehyde structure, is the reducing end (right end in Figure 2.1).[3]

2.1.2. **Crystal structure of cellulose**

Cellulose has a tendency to crystallize. To date, six different crystal structures have been identified, namely cellulose I, II, III_I, III_{II}, IV_I, and IV_{II}. The structural interconversions of these polymorphs are shown in Figure 2.2.[4-7]

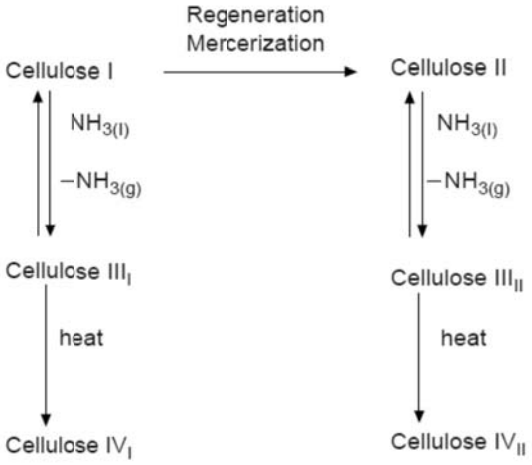

Figure 2.2. Interconversions of cellulose crystal structures. (Reprinted from ref 5; fair use; Copyright 1984 Springer Verlag)

Native cellulose has a cellulose I crystal structure, which has been shown to have two crystalline allomorphs, namely cellulose I_α and I_β. The ratio of the two allomorphs differs for different cellulose sources.[5,6,8,9] Cellulose I_α is the dominant crystal structure in algal and bacterial cellulose, whereas cellulose I_β is dominant in cellulose from higher plants, such as that found in cotton, wood, and ramie fibers.[5,8,10] The two cellulose I allomorphs have the same chain conformation but differ in their hydrogen bonding patterns. Cellulose I_α has a triclinic unit cell

with one cellulose chain, whereas cellulose I_β has a monoclinic unit cell with two cellulose chains of parallel orientation.[10,11]

Besides crystalline regions, native cellulose also contains amorphous regions. The degree of crystallinity, *i.e.*, the fraction of cellulose that is crystalline, depends on the cellulose origin and ranges from 0.43 to more than 0.80.[3,5]

2.1.3. **Cellulose nanocrystals**

In the amorphous regions, the cellulose chains are less tightly packed than in the crystalline regions, making them more susceptible to acid attack. In the presence of strong acids, such as HCl or H_2SO_4, hydronium ions will penetrate the cellulose chains in the amorphous region and cleave the glycosidic bonds between the AGUs. Cleavage of these bonds will eventually lead to a release of individual crystallites.[12,13]

Cellulose crystallites have been isolated in 1951 by hydrolysis of native cellulose (cellulose I) and mercerized cellulose (cellulose II) with sulfuric acid. The crystallites were found to have the same lattice structure as the original cellulose fibers.[14] In 1959, aqueous suspensions of cellulose crystallites were found to have interesting liquid crystal properties. Colloidal suspensions of cellulose crystallites exhibited birefringence when observed between crossed polarizers under a polarized-light microscope.[15]

During the isolation of cellulose crystallites, more commonly called cellulose nanocrystals (CNCs), by sulfuric acid hydrolysis, two processes occur simultaneously. The first one is hydrolytic breakdown of the cellulose chains, preferentially those in the amorphous regions. The second one is esterification of some of the hydroxyl groups on the pyranose rings, resulting in negatively charged sulfate groups. Electrostatic repulsive forces generated by these negative sulfate groups stabilize cellulose nanocrystal suspensions.[12,16]

Owing to their exceptional properties, including optical birefringence, ionic surface groups, high mechanical strength and stiffness, and high chemical functionalizability, CNCs are being studied for a wide range of potential applications including drug delivery,[17] polymer nanocomposites,[18] and for polyelectrolyte interactions.[12]

2.1.4. **Model cellulose substrates**

Because the number of cellulose applications has increased dramatically in recent years, a thorough understanding of the chemical structure and properties of cellulosic fibers is of great importance. However, cellulose fibers are small, porous, and have a rough surface. These properties make it difficult to study their surface interactions and properties.[19] Model cellulose substrates are able to mimic the outer surface of cellulose fibers to facilitate characterization by surface analytical techniques, such as quartz crystal microbalance with dissipation monitoring (QCM-D), surface plasmon resonance (SPR) spectroscopy, and ellipsometry, practical for studying cellulose surface properties.

In the past few years, thin cellulose films have been studied extensively as model cellulose substrates and very smooth films with a roughness on the order of a few nanometers have been prepared. As the preparation methods for cellulose films with controlled morphology, *e.g.*, completely amorphous[20,21] or with a cellulose I crystal structure,[22,23] matured, cellulose thin films have been used to investigate the interactions between two cellulose surfaces,[24-27] a cellulose surface and the cellulose binding domains (CBDs) of cellulolytic enzymes,[28] or cellulose surfaces and polyelectrolytes.[29] More recently, cellulose thin films have been used to investigate the enzymatic hydrolysis of cellulose with surface analytical techniques. The results of these studies demonstrate that model cellulose substrates provide a tool through which a better understanding of how enzymes function during cellulose hydrolysis can be obtained.[30-33]

On the basis of the film deposition methods and materials used for film deposition, several cellulose thin film preparation methods can be distinguished. The two most frequently used film deposition methods for the preparation of cellulose thin films are Langmuir-Blodgett (LB) deposition[34,35] and spin coating.[20-23] Regarding the materials used for deposition, there are mainly three different types: a) cellulose derivatives that are soluble in common organic solvents and can be converted back to cellulose after the film is formed, such as trimethylsilyl cellulose;[20,21,36] b) cellulose dissolved in various solvents that can be removed after film deposition, such as *N*-methylmorpholine-*N*-oxide (NMMO)[37] or dimethylacetamide (DMAC)/LiCl;[19] or c) aqueous colloidal suspensions of CNCs[22,23] or cellulose nanofibrils.[38] Cellulose thin films prepared by these methods have smooth surfaces, with a roughness on the order of several nanometers, and thus provide ideal model surfaces for the study of cellulose surface properties and interactions.

2.2. Lignin

2.2.1. **Lignin structure and classification**

Occurring generally in combination with cellulose, lignin is the most abundant aromatic (phenolic) natural polymer.[39,40] Lignin accounts for roughly 15–36% of the dry weight of lignocellulosic biomass,[41] including softwood (25–31% lignin), hardwood (16–24% lignin), and agricultural residues.[39] The main functions of lignin in woody plants include support of the plant against external forces, sealing of the water-conducting system, and protection of the plant from an attack by microorganisms.[42,43] In nature, lignin is formed through enzyme-initiated dehydrogenative polymerization of three hydroxycinnamyl alcohol monomers, differing in their degree of methoxylation: *p*-coumaryl, coniferyl, and sinapyl alcohol (Figure 2.3).[43,44]

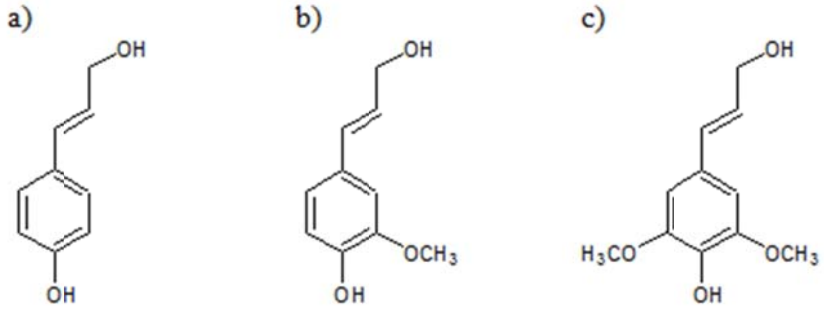

Figure 2.3. The lignin precursors (a) *p*-coumaryl alcohol, (b) coniferyl alcohol, and (c) sinapyl alcohol.

The lignin phenylpropanoid units that are derived from these precursors are the *p*-hydroxyphenyl unit (H), the guaiacyl unit (G), and the syringyl unit (S), respectively (Figure 2.4).[43,45]

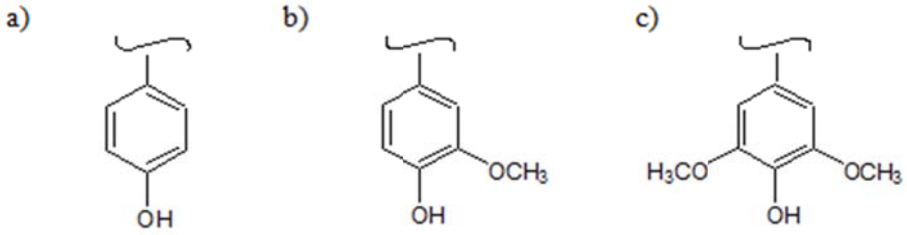

Figure 2.4. The three phenylpropanoid units of lignin: (a) *p*-hydroxyphenyl unit (H), (b) guaiacyl unit (G), and (c) syringyl unit (S).

On the basis of the relative amounts of the three phenylpropanoid units, lignins are classified as guaiacyl lignin (G-lignin), guaiacyl-syringyl lignin (GS-lignin), and guaiacyl-syringyl-*p*-hydroxyphenyl lignin (GSH-lignin).[42,45] Gymnosperm (softwood) lignins, derived primarily from coniferyl alcohol, are G-lignins, whereas dicotyledonous angiosperm (hardwood) lignins, derived from a combination of coniferyl and sinapyl alcohol, are GS-lignins. Grass lignins also contain p-hydroxyphenyl units, derived from *p*-coumaryl alcohol, and are therefore GSH-lignins.[42,43] The phenylpropanoid units are linked together by ether (C-O-C) and carbon-carbon (C-C) linkages.[46] The different types of linkages that occur in lignin are depicted in Figure 2.5. The most abundant linkages in softwood lignin are the β-O-4 linkages, which account for approximately 45–50% of the total linkages.[47] The β-O-4 linkages as well as the α-O-4 linkages (approx. 6–8%)[47] are susceptible to acid- and base-catalyzed hydrolysis, leading to the depolymerization and fragmentation of the lignin, frequently observed during lignin isolation.[48] Other linkage types between phenylpropanoid units in lignin are the β-5 (approx. 9–12%), 5-5 (approx. 18–25%), 4-O-5 (approx. 4–8%), β-1 (approx. 7–10%), and β-β (approx. 3%) linkage, as shown in Figure 2.5.[47]

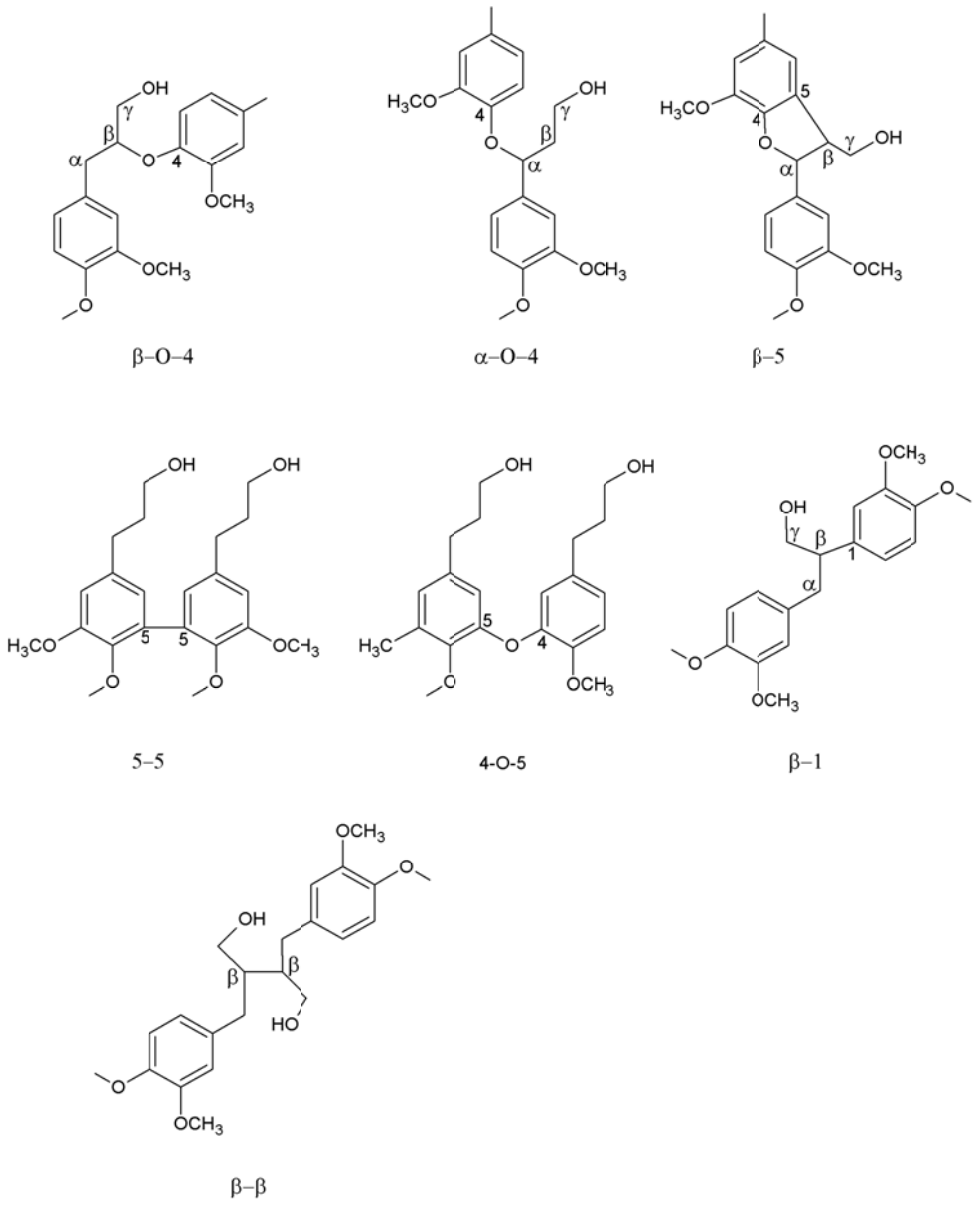

Figure 2.5. Common linkages between the phenylpropanoid units in lignin. (Adapted from ref 47; fair use; Copyright 2004 Elsevier B.V.)

2.2.2. **Lignin isolation methods and resulting structural changes**

In addition to origin-related structural differences, differences based on the isolation method exist. The isolation of lignin from plant matter without alteration of its structure still poses a problem because of its intimate association with plant polysaccharides. Lignins are

isolated either by chemical or solvent treatment of the plant matter.[49,50] During chemical treatment, such as the sulfite pulping process, using a combination of sulfur dioxide and water at high temperature and pressure, or the kraft pulping process, using sodium hydroxide and sodium sulfide, a series of chemical reactions, including sulfonation, hydrolysis, and condensation, occur, rendering structural changes in the lignin. A nearly sulfur-free lignin, more closely resembling native lignin, can be obtained by:[40,42]

i. Extraction in the solvent pulping process (organosolv lignin);
ii. Solvent extraction after extensive grinding (milled wood lignin); and
iii. Removal of associated polysaccharides with cellulolytic enzymes in the biomass conversion process (cellulolytic enzyme lignin).

The following section reviews the isolation methods and structural properties of the three types of lignin used in this research, namely kraft lignin, organosolv lignin, and milled wood lignin. Kraft lignin is lignin that has been recovered from black liquor during the kraft pulping process, also known as the sulfate process. Kraft pulping is conducted by reacting wood with an aqueous solution of sodium hydroxide and sodium sulfide at a temperature of about 170 °C for several hours. The active chemicals in kraft cooking liquor are the hydroxide ion (OH^-) and the hydrogen sulfide ion (HS^-), which can cause depolymerization and fragmentation of the lignin.[47,51] The most prevalent reactions in the kraft lignin isolation process are the cleavage of α- and β-aryl ether bonds, as depicted in Figure 2.6.[52] Under basic conditions, α-aryl ether bonds are readily cleaved under formation of *para*-quinone methide intermediates (**2** in Figure 2.6a). The reaction of **2** with hydrogen sulfide ions (Figure 2.6b) yields a benzyl mercaptide structure (**3**). Attack of the β-carbon by the mercaptide anion leads to a thiirane intermediate (**4**) and the cleavage of β-aryl ether bonds.[47] The cleavage of α- and β-aryl ether bonds results in an increase in phenolic hydroxyl groups. For example, the number of phenolic hydroxyl groups in the residual lignin of a softwood kraft pulp (*Pinus sylvestris,* kappa number of 31.4) was reported as 27 and that in the dissolved lignin as 55–70 per 100 C-9 units, as compared to 13 in the original wood lignin.[52,53]

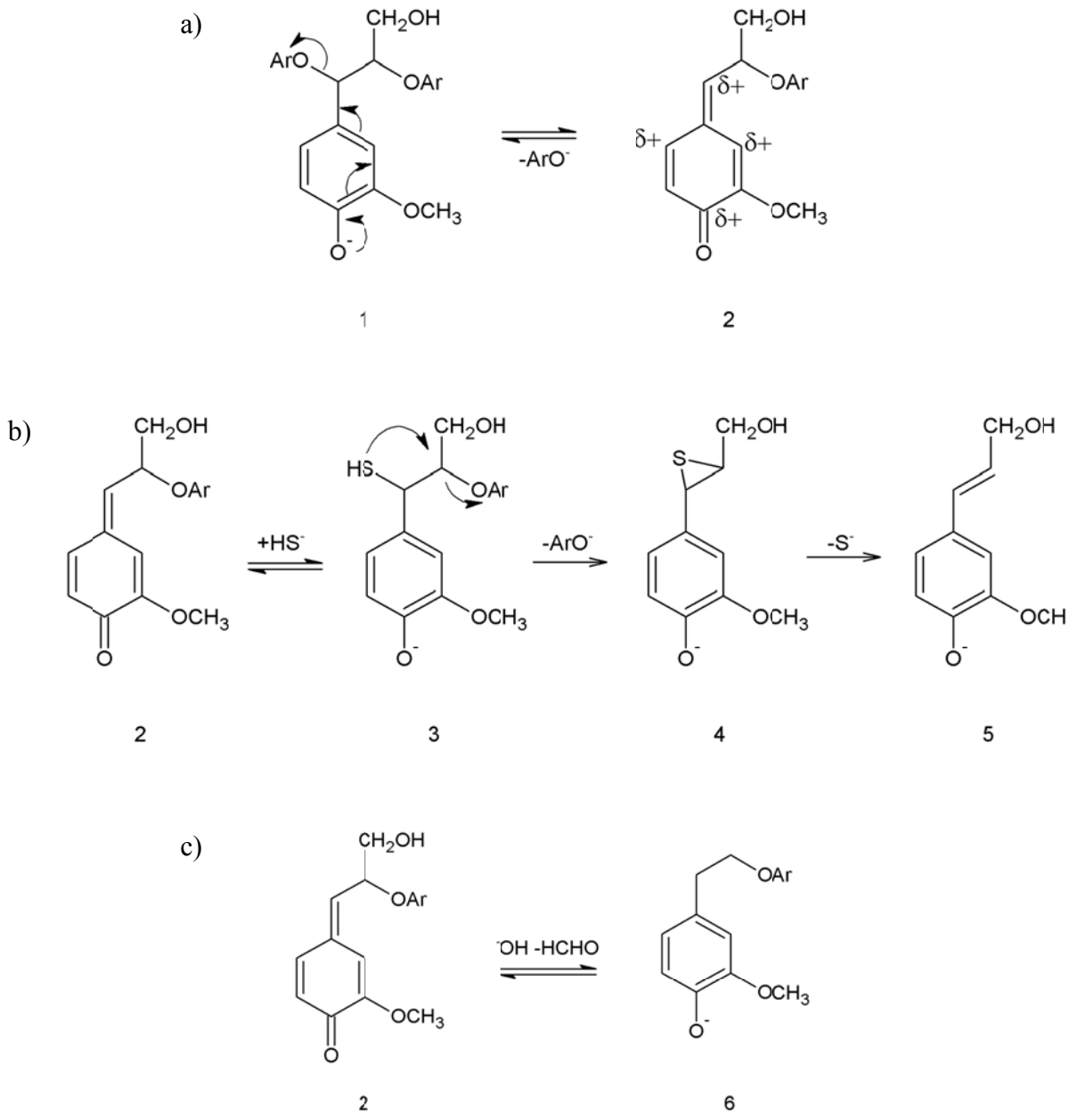

Figure 2.6. Alkaline cleavage of α-aryl ether bonds under formation of *para*-quinone methide intermediates (a), sulfidolytic cleavage of β-aryl ether bonds (b), and elimination of γ-hydroxymethyl group (c) during kraft pulping. (Adapted from ref 47; fair use; Copyright 2004 Elsevier B.V.)

Native wood lignin is rich in primary hydroxyl groups positioned at the γ-carbon of the phenylpropanoid units. Besides the increase in phenolic hydroxyl groups, kraft pulping causes a decrease in primary hydroxyl groups due to the elimination of the γ-hydroxymethyl group as formaldehyde (Figure 2.6c), resulting in an enol ether unit (**6**).[51,54]

Organosolv lignin is lignin that has been recovered during the organosolv pulping process, which is a wood delignification process based on non-aqueous media. In organosolv pulping, wood chips are treated at elevated temperature and pressure with an organic solvent generally containing either some water or an acid or base catalyst.[55] Commonly used solvents in organosolv pulping are methanol, ethanol, butanol, dioxane, phenol, and dimethyl sulfoxide.[56] As in kraft pulping, the cleavage of ether linkages is the primary reason for lignin fragmentation and causes an increase in phenolic hydroxyl groups. The solvolytic cleavage of an α-aryl ether linkage, facilitated by a free phenolic hydroxyl group in the *para* position, leads to the formation of a quinone methide intermediate, nucleophilic substitution at the benzylic position, or formation of a benzyl carbocation.[55] The cleavage of β-aryl ether linkages does also occur during organosolv pulping, especially under more acidic conditions, as has been shown for the acidolysis reaction of lignin in a 9:1 (v/v) dioxane–water mixture containing 0.2 M hydrogen chloride.[57] Organosolv lignin is generally free of carbohydrate contamination and has a very low molecular weight due to hydrolytic depolymerization.[58]

Milled wood lignin has traditionally been regarded as the best representative for native lignin because its isolation does not involve reactive chemicals or drastic reaction conditions.[59,60] The isolation of milled wood lignin starts with the suspension of finely ground wood meal in an inert and non-swelling medium, followed by vibratory or rotary ball milling. Finally, the lignin is extracted from the milled wood with a 9:1 (v/v) dioxane–water mixture.[48] Despite having a less altered chemical structure, compared to kraft and organosolv lignin, milled wood lignin has several shortcomings that limit its suitability as a native lignin model. First, milled wood lignin stems primarily from secondary cell walls and is therefore not representative of the entire lignin sample.[61] Second, milled wood lignin contains some carbohydrate contamination that cannot be removed even by enzymatic digestion.[48,62] Third, although to a lesser extent than kraft and organosolv lignin, milled wood lignin is chemically altered. As for kraft and organosolv lignin,

chemical modifications are primarily the cleavage of aryl ether linkages[60,63] and an increase in the number or phenolic hydroxyl groups.[60,64]

2.2.3. **Model lignin substrates**

The study of lignin interactions with cellulose and cellulolytic enzymes requires well-defined lignin films with low surface roughness, high uniformity, and high stability. Constantino *et al.* prepared lignin LB films with acetosolv lignin from sugar cane bagasse and *Pinus caribaea hondurensis* dissolved in tetrahydrofuran,[65-67]and calculated a root-mean-square (RMS) roughness of 1.8 Å[67] and a thickness of 300 Å[65] for lignin from sugar cane bagasse. Pasquini *et al.* prepared five-layer lignin LB and cast films by depositing ethanol and saccharification lignins onto mica and achieved RMS roughnesses of 3.8 nm for the ethanol lignin LB films and 0.24 nm for the saccharification lignin LB films.[68] The RMS roughnesses of LB films prepared with acetone–oxygen and soda lignins were 0.30 nm and 1.25 nm, respectively.[69] The low roughnesses obtained with the ethanol and acetone–oxygen lignins were ascribed to the higher content of COOH groups. Pillai and Renneckar prepared lignin substrates from kraft lignin and poly(diallyldimethylammonium chloride) (PDDA) using a layer-by-layer technique and found that the total film thickness was proportional to the number of layers and that a substrate with a thickness of 50 nm could be achieved with 15 layers.[70] More recently, spin-coating has been applied for the preparation of lignin thin films because of its simplicity and ability to obtain thin, uniform films on flat substrates.[71] Softwood kraft lignin was dissolved in various solvents and spin-coated onto silicon wafers. Excellent films for use as model lignin substrates were obtained from kraft lignin dissolved in 0.75 M NH_4OH. The thickness of the films varied from 20–140 nm and depended on the lignin concentration and spinning speed. The RMS roughness of the films was around 1 nm, independent of lignin concentration and spinning speed.[71] Such smooth, uniform lignin films provide valuable model substrates for the study of lignin-cellulose interactions in aqueous electrolyte solutions,[72] adsorption of polyelectrolyte or polyelectrolyte complexes onto lignin,[73,74] and the surface energy and wettability of lignin.[75]

2.3. Enzymatic hydrolysis of cellulose

2.3.1. **Enzymatic hydrolysis mechanism**

Our ability to enzymatically hydrolyze cellulose is critical for the large-scale production of biofuels and chemicals from plant matter.[76] The enzymatic hydrolysis of cellulose, depicted schematically in Figure 2.7,[77,78] involves three kinds of cellulases: (i) endoglucanases (EG, 1,4-β-D-glucanohydrolase, E.C. 3.2.1.4), which cut the cellulose chains in the more accessible, amorphous regions randomly to oligosaccharides of various lengths; (ii) exoglucanases, also called cellobiohydrolases (CBH, 1,4-β-D-glucan cellobiohydrolase, E.C. 3.2.1.91), which gradually cut off the ends of cellulose chains to release cellobiose; and (iii) β-glucosidases, which hydrolyze soluble cellodextrins and cellobiose to glucose. Exoglucanases can be further divided into two types, one acting on the reducing chain end (*e.g.* CBH I) and the other acting on the non-reducing chain end (*e.g.* CBH II).

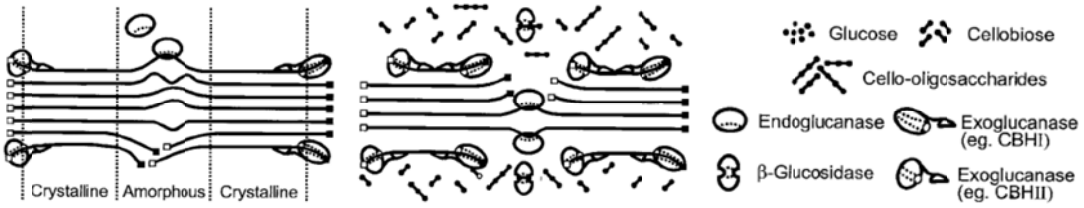

Figure 2.7. Schematic illustration of the enzymatic hydrolysis of cellulose. (Reprinted from ref 76; fair use; Copyright 2002 American Society for Microbiology)

The most widely and well studied fungal cellulase system is produced by the aerobic, mesophilic, filamentous fungus *Trichoderma reesei*.[79] In *T. reesei*, there exist two cellobiohydrolases, CBH I (or Cel7A) and CBH II (or Cel6A), which represent about 50% and 20% of the total cellulase content, respectively, and five endoglucanases, EG1 (or Cel7B), EG2 (or Cel5A), EG3 (or Cel12A), EG4 (or Cel61A), and EG5 (or Cel45A), which represent about 15%, 10%, 1%, <1% and <1% of the total cellulase content, respectively.[79-82]

2.3.2. **3-D structure of cellulases**

Our understanding of the hydrolytic mechanisms of the three major kinds of cellulase enzymes advanced rapidly after their crystal structures were solved. The 3-D structure of the catalytic core domain of *T. reesei* CBH I, shown in Figure 2.8 revealed a β-sandwich formed by two antiparallel β-sheets. The sandwich is highly concave and, together with four long loops extending from the catalytic core, forms a roughly 50 Å long cellulose-binding tunnel.[83,84] The active site of CBH I contains three carboxylate residues, Glu 212, Asp 214, and Glu217, which are located at one end of the tunnel. During hydrolysis, a single cellulose chain enters the tunnel, reducing end first, from the opposite end of the tunnel until it reaches the active site. At the active site, cellobiose or oligosaccharides are cleaved and released from the reducing end of the chain. The remaining chain remains bound in the tunnel for further breakdown.[79,84-86]

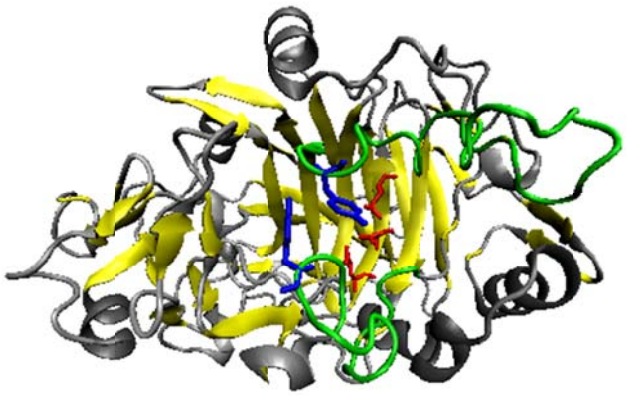

Figure 2.8. A Visual Molecular Dynamics rendering of the tunnel structure and catalytic site of *T. reesei* Cel7A (RCSB Protein Data Bank, ID 1cel). The tunnel is formed by a concave β-sandwich (yellow) and surface loops (green). The two loops (green) fold over the catalytic site (red: Glu 212, Asp 214, and Glu217) and close the tunnel through the interaction of two tyrosine residues (blue: Y247 and Y371).

The 3-D crystal structure of EG I, also known as Cel7B, has been resolved by Kleywegt *et al.*[87] and is shown in Figure 2.9. The crystal structure of EG I is very similar to that of CBH I, with a β-sandwich formed by two antiparallel β-sheets packing face-to-face. These β-sheets are

also connected by loops. However, the loops that form the tunnel in CBH I are absent in EG I. Therefore, instead of a tunnel, EG I has an open active-site cleft. Like that of CBH I, the active site of EG I contains three carboxylate residues, Glu 196, Asp 198, and Glu 201. Because of the open-cleft structure of their active sites, endoglucanases act preferentially on amorphous or disordered regions of cellulose and can breakdown cellulose randomly along the chains. This behavior can be explained by the fact that the open-cleft active site makes it possible for cellulose chains to diffuse freely in and out during hydrolysis.

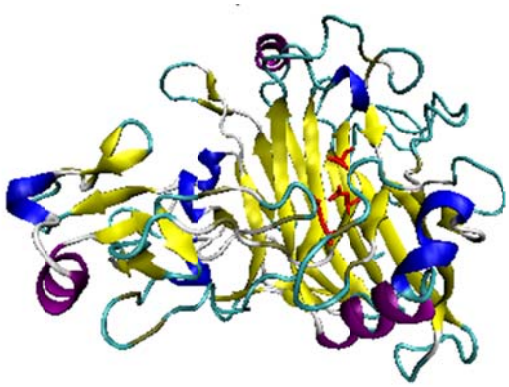

Figure 2.9. A Visual Molecular Dynamics rendering of the tunnel structure and catalytic site of *T. reesei* Cel7B (RCSB Protein Data Bank, ID 1eg1).

Of the seven *T. reesei* cellulases (2 cellobiohydrolases and 5 endoglucanases), all except EG3 have a multi-domain structure, consisting of a catalytic core domain (~400–500 residues), a CBD (~40 residues), and a highly glycosylated linker region (~30 residues) connecting the two.[81,82,88] Both the catalytic domain and the CBD bind to cellulose, but the affinity of the CBD is much higher than that of the catalytic domain.[89] The CBD of *T. reesei* CBH I has a wedge-like shape with overall dimensions of 30 × 18 × 10 Å, as shown in Figure 2.10.[88] As evident from Figure 2.10, the CBD has two distinct faces, one of which is flat and the other rough. The flat face contains three aromatic residues, Y5, Y31, and Y32, which are believed to be responsible for binding cellulose.[88,90-93] The spacing of the three aromatic residues equals the length of two glucose residues in cellulose. It is postulated that the aromatic amino acids of CBDs engage in van der Waals interactions and aromatic ring polarization interactions with the pyranose rings exposed on the 110 crystalline face of cellulose.[94]

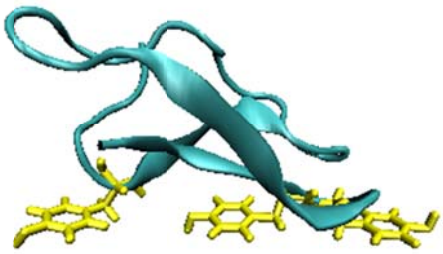

Figure 2.10. A Visual Molecular Dynamics rendering of the CBD of *T. reesei* Cel7A. Binding sites are highlighted in yellow (Tyr 5, Tyr 31, and Tyr 32) (RCSB Protein Data Bank, ID 1cbh).

2.4. Surfactants

2.4.1. **Surfactant structure and classification**

Surfactants, an abbreviation for surface-active agents, are compounds that lower the interfacial tension between two phases. On account of this property, surfactants find broad use in consumer products, including detergents, cosmetics, pharmaceuticals, and foods, and in industrial application, *e.g.* mining and oil drilling.

Surfactant molecules generally have two parts, a hydrophilic head and a hydrophobic tail. The hydrophilic head has an affinity for aqueous media and is usually composed of ionic or polar groups. The hydrophobic tail is insoluble in aqueous media and is usually composed of hydrocarbon, fluorocarbon, or siloxane chains.

Surfactants are most commonly divided on the basis of the nature of their hydrophilic groups into four classes[95]:

i. Anionic surfactants, containing a negatively charged headgroup, such as a carboxyl (COO^-), sulfonate (SO_3^-), sulfate (OSO_3^-), or phosphate (OPO_3^-) group;

ii. Cationic surfactants, containing a positively charged headgroup, such as a quaternary ammonium group;

iii. Non-ionic surfactants, containing a hydrophilic headgroup without charge, such as polyoxyethylene; and

iv. Zwitterionic surfactants, containing a headgroup with both positive and negative charge.

The chemical structures of three common surfactants, namely the non-ionic surfactant polysorbate 80 (polyoxyethylene (80) sorbitan monooleate), marketed under the brand name Tween 80, the anionic surfactant sodium dodecyl sulfate (SDS), and the cationic surfactant cetrimonium bromide, are depicted in Figure 2.11.

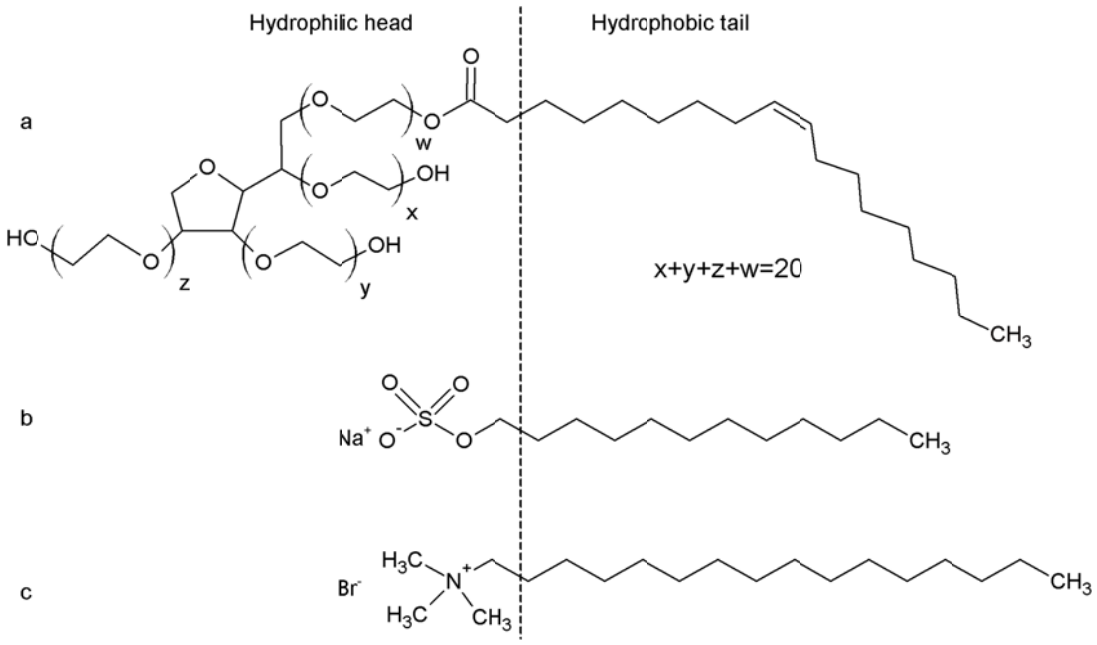

Figure 2.11. Chemical structures of common surfactants: a) the non-ionic surfactant polysorbate 80 (Tween 80); b) the anionic surfactant sodium dodecyl sulfate; and c) the cationic surfactant cetrimonium bromide.

2.4.2. **Solution properties of surfactants**

When placed in aqueous media, surfactants tend to partition to the air/water interface by pointing the hydrophobic tail into the air and the hydrophilic head into the aqueous phase in order to minimize the free energy of the system. Occupation of the air/water interface by the surfactant causes a decrease in the surface tension. However, when the surfactant concentration exceeds a critical value, the surface tension does not decrease further with increasing surfactant

concentration. At this concentration, called the critical micelle concentration (CMC), the surfactant molecules start to aggregate and form micelles, a thermodynamically stable molecular arrangement able to disperse in aqueous media, to minimize the free energy of the system.

Besides surfactant concentration, temperature governs the formation of micelles. Below a critical temperature, the solubility of the surfactant is below its CMC so that no micelles can form. This critical temperature is called the critical micelle temperature or Krafft temperature. Non-ionic surfactants do not have a Krafft temperature because their solubility decreases with increasing temperature. The temperature at which a suspension of surfactant aggregates becomes cloudy is called the cloud point.

The CMC can be determined by measuring the surface tension, electrical conductance, response of an ion-selective electrode, osmotic pressure, or turbidity of the surfactant solution as a function of surfactant concentration because these properties exhibit abrupt changes at the CMC, as shown in Figure 2.12.[96] CMC values measured *via* different techniques differ from one another because micellization occurs over a finite concentration range as opposed to a fixed surfactant concentration.

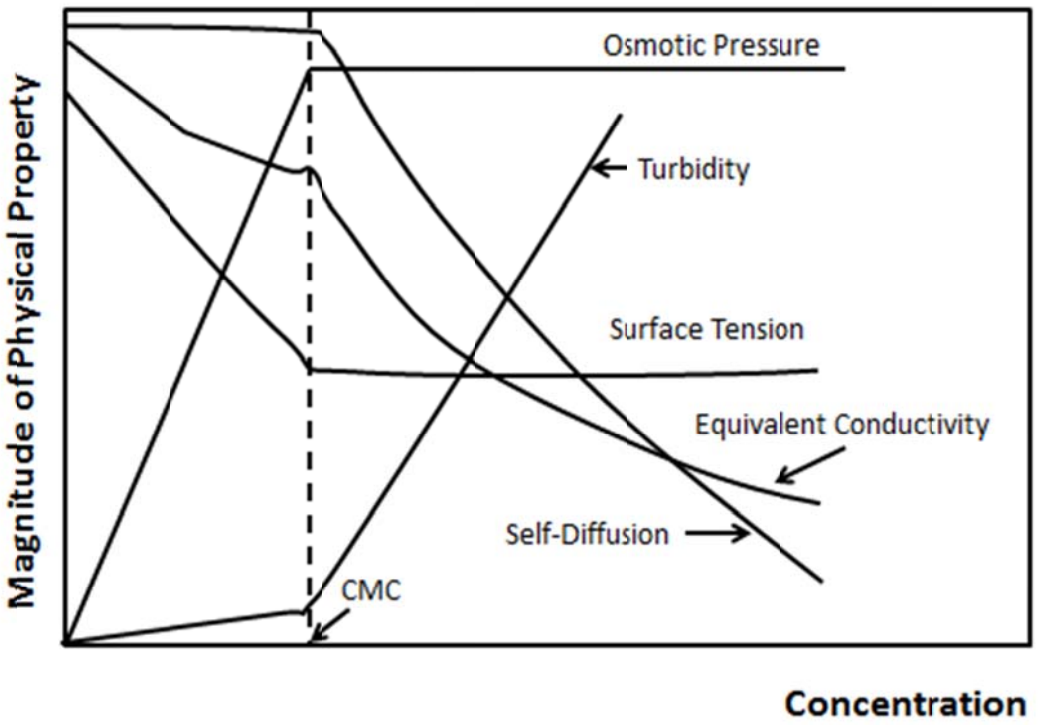

Figure 2.12. Effect of surfactant concentration on various physical properties. (Adapted from ref 96; fair use; Copyright 1999 Wiley-VCH)

2.4.3. **Effects of surfactants on the enzymatic hydrolysis of cellulose**

Surfactants have been reported to be effective in enhancing the efficiency of the enzymatic hydrolysis of lignocellulosic biomass, with the most effective and common being non-ionic surfactants.[97-99] According to previous studies, addition of non-ionic surfactants, biosurfactants, or other non-hydrolytic proteins, such as Tween 20,[97,99,100] Tween 80,[98,100] or BSA,[98,101] can improve the conversion of cellulose to glucose, while decreasing non-productive adsorption of cellulase onto the substrate, and thus can potentially reduce the processing costs for lignocellulosic biomass conversion.

The study of surfactant effects on the enzymatic conversion of lignocellulosic biomass dates back to the 1980s. Castanon and Wilke[102] reported that the addition of Tween 80 enhances the rate of enzymatic hydrolysis of newspaper cellulose by 33% while doubling the amount of recoverable enzyme. Kaya *et al.*[103] studied the effects of surfactants on the saccharification of

carboxymethyl cellulose and xylan, and found that the addition of Tween 80 increased their conversion by 50% and 9%, respectively. Kaar *et al.*[97] studied the effects of both Tween 20 and Tween 80 on the enzymatic hydrolysis of corn stover and found Tween 20 to be slightly more effective than Tween 80, with a maximum increase of cellulose, xylan, and total conversion by 42%, 40%, and 42%, respectively.

Researchers have offered three potential explanations for why surfactants improve the efficiency of the enzymatic hydrolysis of lignocellulosic biomass: (i) surfactants may increase enzyme stability and prevent denaturation of the enzymes during hydrolysis; (ii) surfactants may alter the structure of the substrate and make it more accessible for enzyme hydrolysis; and (iii) surfactants may positively affect enzyme-substrate interactions leading to more effective conversion of cellulose.[100]

2.4.4. **Interactions between surfactants and proteins**

Interactions between surfactants and proteins have been extensively studied for decades. Among the studied systems, the combination of bovine serum albumin (BSA), a globular protein, and SDS is the most extensively studied.[104-107] The interactions of other globular proteins, such as papain,[108,109] lysozyme,[110,111] and ovalbumin,[112] and of cationic[113-115] and non-ionic surfactants[116] have also attract attention because of the widespread application of protein–surfactant complexes in cosmetic, food, industrial, biological, and pharmaceutical sciences.

Depending on the type of surfactant, *i.e.*, cationic, anionic, or non-ionic, and the structure of the protein, two types of interactions between surfactants and proteins have been identified. They are specific binding by electrostatic attraction and cooperative association of the surfactant to the protein *via* hydrophobic affinity.[117] Through their interactions with proteins, surfactants usually function as denaturants and solubilizing agents for proteins. Protein denaturation by surfactants is considered to be due to surfactant-induced unfolding of the protein.[105,108,109]

Four characteristic binding regions have been observed in the binding isotherms of proteins and anionic surfactants, such as SDS,[105,118] as shown in Figure 2.13. In the first region, at very low surfactant concentrations, surfactant monomers bind to specific high-energy sites on the protein through electrostatic interactions. The second region is a plateau or only slightly

positively sloped section of the isotherm. The binding in this region is non-cooperative. The third region is defined by a rapid increase in binding due to cooperative interactions of the surfactant molecules in solution with already bound surfactant molecules. This is also the region where unfolding of the protein occurs. Beyond this region, the binding isotherm shows a plateau, indicating that excess surfactant molecules do not bind to the protein but form regular micelles instead.

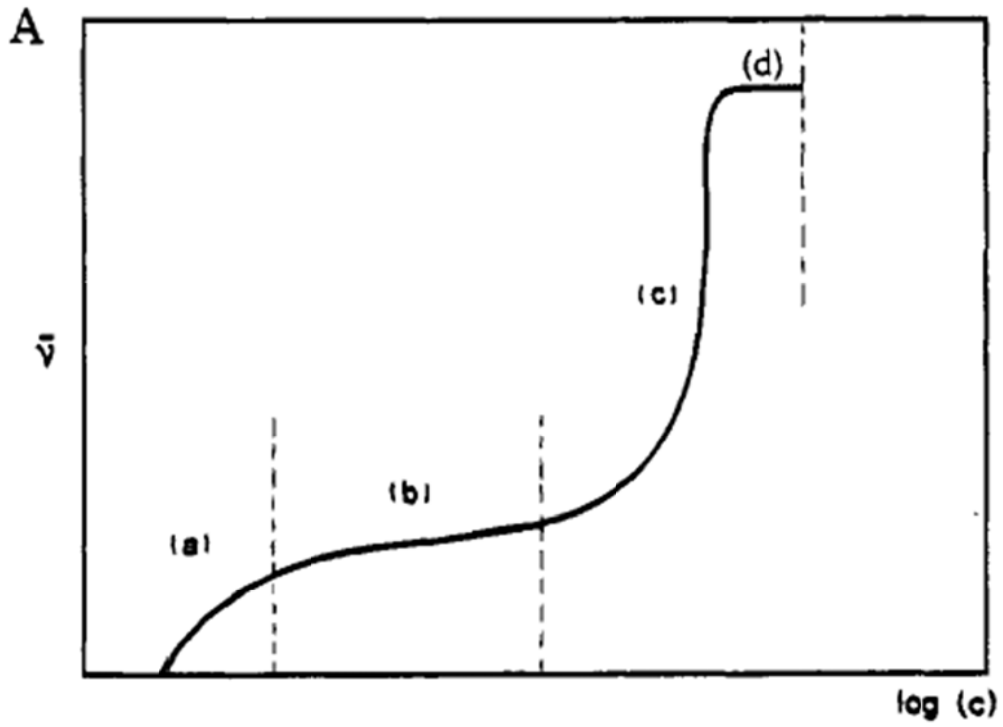

Figure 2.13. Schematic plot of number of bound SDS per protein molecule ($\bar{v}$) *versus* log[SDS]. (Reprinted from ref 105; fair use; Copyright 1995 American Chemical Society)

Because of the interactions between surfactants and proteins, sequential introduction of surfactants into systems containing surface-adsorbed protein may result in desorption of the protein from the surface. There are two possible mechanisms for this phenomenon. The first one is the formation of soluble surfactant–protein complexes through strong surfactant–protein

interactions. The second one is replacement of the surface-adsorbed protein by surfactant molecules due to stronger surfactant–surface interactions.[119]

2.4.5. **Interactions between surfactants and polymers**

Polymer–surfactant mixtures have been studied extensively because of their broad industrial application in areas such as cosmetics, detergents, and mining.[120,121] Interactions between polymers and surfactants can be classified as weak interactions between the polymer molecules and surfactant headgroups, strong electrostatic interactions between oppositely charged polymer molecules and surfactant headgroups, and hydrophobic interactions between the polymer molecules and hydrophobic tails of the surfactant.[122]

The interactions between neutral polymers and surfactants have been well studied by means of surface tension measurements.[123-125] As an example, Figure 2.14 shows the surface tension of pure SDS solution[126] and an SDS solution containing poly(ethylene oxide), as a function of SDS concentration.[123] Initially, the surface tension of the surfactant solution decreases as the surfactant adsorbs at the air/water interface, and there is no interaction between the surfactant and the polymer. At a certain surfactant concentration, which is usually below the CMC of the surfactant, the surfactant starts to form aggregates with the polymer molecules. This concentration is called the critical aggregation concentration and is indicated by a change in slope in Figure 2.14. When the polymer is saturated with surfactant molecules, excess surfactant molecules start to form regular micelles, indicated by the second change in slope in Figure 2.14.[122-124]

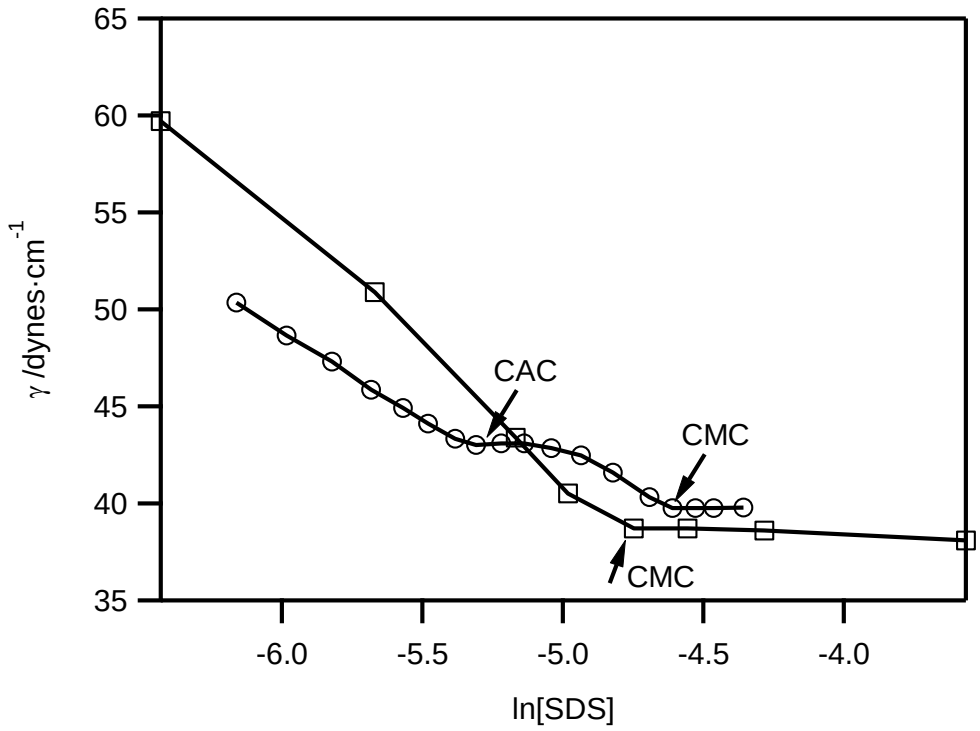

Figure 2.14. Surface tension versus ln[SDS] of aqueous SDS solutions (□, data from ref 126) and SDS solutions containing 0.025% (w/v) polyethylene oxide (○, data from ref 123). (Adapted from ref 123; fair use; Copyright 1967 Elsevier Inc., and ref 126; fair use; Copyright 1949 American Chemical Society)

Interactions between polymers and surfactants of opposite charge are much stronger than those in neutral polymer–surfactant system because of the strong electrostatic interactions between the charged groups of the polymer molecules and surfactant headgroups.

2.5. Substrate characterization techniques

The most important substrate properties that will affect enzyme adsorption onto and enzymatic hydrolysis of the substrate are surface charge, morphology, and surface roughness. The surface charge of model cellulose surfaces prepared from CNCs stems from the sulfate groups on the surface of the CNCs. The surface sulfate groups of CNCs are most commonly

quantified by conductometric titration.[127] The surface charge of planar substrates can be deduced from their chemical composition, commonly measured by x-ray photoelectron spectroscopy (XPS). Substrate morphology, *i.e.*, amorphous or crystalline, can be determined by x-ray diffraction (XRD). The surface roughness of planar substrates is commonly measured by atomic force microscopy (AFM).

2.5.1. **Conductometric titration**

Titration is a chemical analysis technique used to determine unknown properties of a particular *analyte* or *titrand* by gradually adding a standard solution of titrating reagent or *titrant*. Like metallic conductors, electrolytic solutions obey Ohm's Law, stating that the electrical current, I, is proportional to the applied electromotive force, E, and inversely proportional to the electrical resistance, R:

$$I = E/R \qquad [2.1]$$

The electrical resistance depends on the cross-sectional area, a, and length, l, of current flow. A material property that is independent of a and l can be obtained by

$$\rho = Ra/l \qquad [2.2]$$

The quantity ρ is the specific electrical resistance or electrical resistivity of a material subjected to an electromotive force. The reciprocal of electrical resistivity is the electrical conductivity, k. The electrical conductivity of an electrolytic solution depends on the concentrations and mobilities of the ions present. The molar conductivity, Λ, of an electrolyte is related to its electrical conductivity by

$$\Lambda = 1000k/c \qquad [2.3]$$

where c is the molar concentration of the electrolyte. The molar conductivities of some common ions are listed in Table 2.1.

Table 2.1. Molar conductivities of ions at 25°C ($\Omega^{-1}\cdot cm^{-2}\cdot mol^{-1}$) (from ref 127)

Cations				Anions					
M^+		M^{2+}		X^-		X^{2-}		X^{3-}	
H^+	349.8	Ca^{2+}	119.0	OH^-	198.3	CO_3^{2-}	138.6	PO_4^{3-}	240
Na^+	50.1	Mg^{2+}	106.2	Cl^-	76.3	SO_4^{2-}	160.0		
K^+	73.5	Cu^{2+}	107.2	NO^{3-}	71.5				

The principle of conductometric titration is the substitution of ions of one molar conductivity with ions of another molar conductivity through an ionic reaction. During the titration of strong acid with base, the conductivity decreases because of the replacement of hydrogen ions, which have the greatest molar conductivity, as shown in Table 2.1, with another cation of lower molar conductivity. The conductivity of the titrand is measured after each addition of a small amount of titrant and then plotted against the volume of titrant to give a graph with two straight lines intersecting at the equivalence point. In order to maintain the volume of titrant and avoid a decrease in conductivity due to dilution, the concentration of the titrant is usually 20 to 100 times higher than that of the titrand.

Some typical conductometric titration curves are shown in Figure 2.15. Figure 2.15a shows curves for the titration of strong acid with strong base (1, 2) and weak base (1, 3). The initial decrease (1) in conductivity is due to the replacement of hydrogen ions with cations of lower molar conductivity. After the equivalence point has been reached, addition of strong base causes a rapid increase in conductivity (2), due to the large molar conductivity of hydroxyl ions, whereas addition of weak base gives a horizontal line (3), due to the low ionization of weak base.

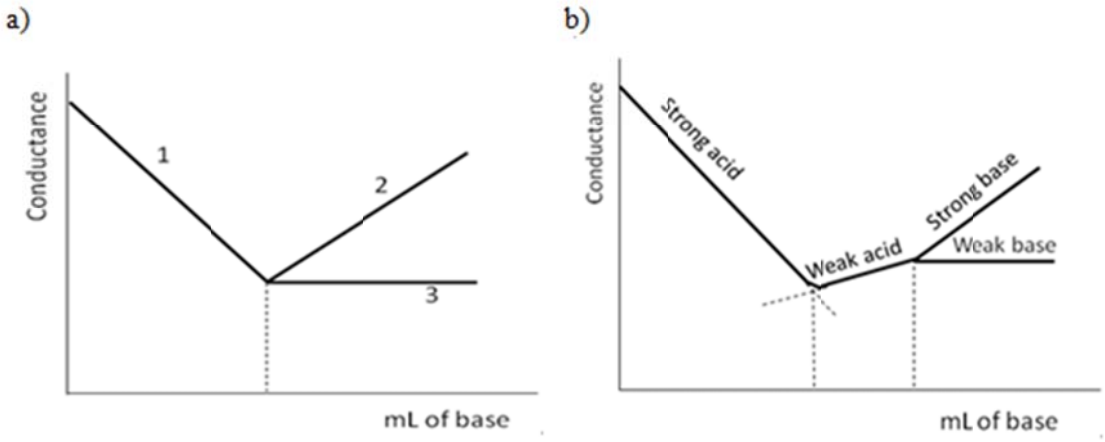

Figure 2.15. Typical conductometric titration curves. 1. Strong acid; 2. Strong base; 3. Weak base. (Adapted from ref 127; fair use; Copyright 1978 Addison Wesley Longman Ltd.)

Figure 2.15b shows curves for the titration of a mixture of strong and weak acids with strong and weak base. The curves show a steep initial decrease in conductivity, due to the neutralization of strong acid, followed by a less steep increase, caused by conversion of the weak acid into its salt. After the equivalence points for the strong and weak acid have been reached, the conductivity increases rapidly in the case of the strong base or stays almost constant in the case of the weak base.

2.5.2. **X-ray photoelectron spectroscopy**

X-ray photoelectron spectroscopy (XPS), also sometimes called electron spectroscopy for chemical analysis (ESCA), is a spectroscopic technique that is frequently used in surface science for the characterization and quantification of the elemental composition of surface layers and chemical states of surface atoms. The principles of XPS are rooted in the photoelectric effect, discovered by Hertz in 1887,[128] who observed that matter, when exposed to electromagnetic radiation of sufficient energy, emits electrons. In XPS, a material is irradiated with photons of X-ray energy. After the energy has been transferred to the atomic core-level electrons in the surface layer of the material, photoelectrons are emitted, separated according to energy, and counted.

The atomic emission of a photoelectron from the core-level upon X-ray irritation is shown schematically in Figure 2.16.[129]

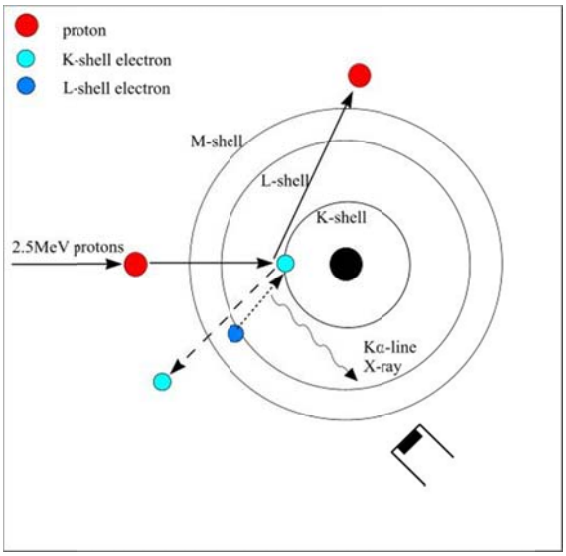

Figure 2.16. Atomic emission of a photoelectron from the core-level upon X-ray irradiation. (Reprinted from ref 129; fair use; Copyright 1997 John Wiley & Sons)

The ionization or binding energy for the emitted electron, E_{BE}, which contains information about the chemical state of the electron before its emission, is related to its kinetic energy, E_K, measured by the XPS instrument, and the energy of the incident photons, $h\nu$, where h is Planck's constant and ν is the frequency of the incident radiation, by the Einstein relation[130]

$$h\nu = E_{BE}+E_K \qquad [2.4]$$

2.5.3. **X-ray diffraction**

Diffraction is a phenomenon that occurs when a propagating wave passes an obstacle. Electromagnetic waves with a wavelength on the order of the interatomic distances in a crystal lattice, such as X-rays, electron beams, or neutron beams, are diffracted upon encountering a crystal, and the resulting diffraction patterns contain information about the atomic arrangement within the crystal lattice. X-rays for XRD experiments are generated in an X-ray tube by irradiation of a metal target, usually copper, with an electron beam, as shown in Figure 2.17.[131]

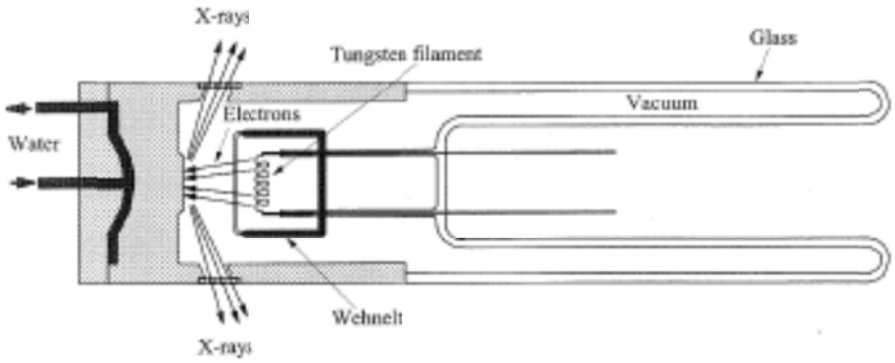

Figure 2.17. Schematic cross section of a filament X-ray tube. (Reprinted from ref 131; fair use; Copyright 2007 ISTE Ltd)

Upon hitting the target, some electrons, provided that they have sufficient kinetic energy, collide with and dislodge an inner-shell electron, thus leaving the target metal atom in an excited, high-energy state. The vacancy is immediately filled by one of the outer electrons under emission of X-rays of characteristic wavelength, which depends on the differences in binding energies for the initial and final state of the electron. The resulting emission peaks, referred to as *K, L, M,* etc. lines, comprise the characteristic emission spectrum of the target metal. A vacancy in the *K* shell, for example, will produce characteristic *K* radiation. *K* radiation may be further divided into K_α and K_β emissions, with K_α emissions arising from L–K electronic transitions and K_β emissions from M–K transitions. Superimposed on the characteristic X-ray emission spectrum is the continuous emission spectrum, caused by interactions of incident electrons with atomic nuclei in the target. Incident electrons that get close to a nucleus are slowed down and redirected by its attractive force. The kinetic energy lost by the electron is released in the form of X-rays, and the wavelength of these X-rays depends on the amount of kinetic energy lost.[132,133] A typical X-ray emission spectrum for a copper target is shown in Figure 2.18. As seen in Figure 2.18, copper has a characteristic K_α wavelength of 1.54 Å.[134]

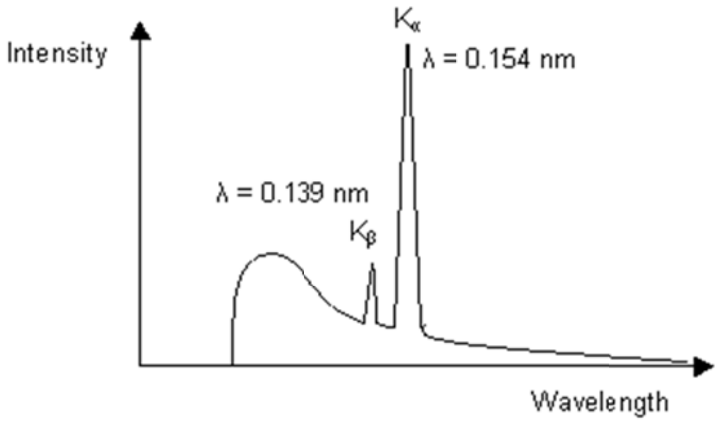

Figure 2.18. X-ray emission spectrum of a Cu target.

The interatomic distances in solid matter are on the order of 1 to 2 Å. Consequently, X-rays are diffracted when impinging on solid matter. In a crystalline solid, the atoms are arranged in a 3-D lattice. The smallest repeating unit, defining the lattice, is called the unit cell. The unit cell is described by the lengths (*a*, *b*, *c*) of its edges in three directions, called the crystallographic axes, and the angles (α, β, γ) between the crystallographic axes, as showed in Figure 2.19. The angle α, for example, is the angle between the crystallographic axes *b* and *c*. In a crystal lattice, the unit cell is repeated infinitely in all three directions.[135]

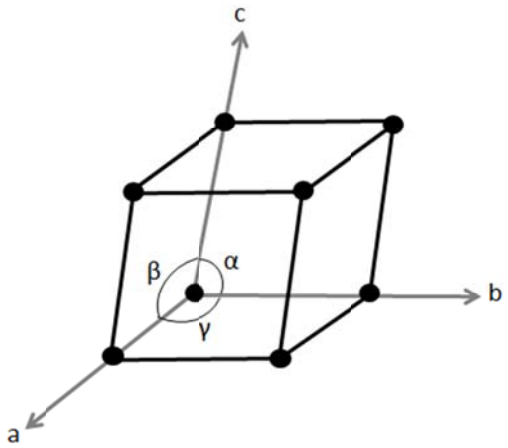

Figure 2.19. The crystallographic unit cell. (Reprinted from ref 135; fair use; Copyright 1998 Plenum Press)

On the basis of the relative lengths of the crystallographic axes and the angles between them, seven different unit cell types can be defined, as shown in Table 2.2. The French crystallographer Auguste Bravais further divided the unit cell types into primitive, body-centered, face-centered, and base-centered types, on the basis of the location of lattice points within the unit cell. He thus arrived at 14 different lattice types, listed in Table 2.2.[132]

Table 2.2. Crystallographic unit cell types and Bravais lattices

Unit cell type	Axial lengths and angles	14 Bravais lattices[1]
Cubic	$a = b = c$, $\alpha = \beta = \gamma = 90°$	Primitive Body-centered Face-centered
Tetragonal	$a = b \neq c$, $\alpha = \beta = \gamma = 90°$	Primitive Body-centered
Orthorhombic	$a \neq b \neq c$, $\alpha = \beta = \gamma = 90°$	Primitive Body-centered Base-centered Face-centered
Rhombohedral	$a = b = c$, $\alpha = \beta = \gamma \neq 90°$	Primitive
Hexagonal	$a = b \neq c$, $\alpha = \beta = 90°$, $\gamma = 120°$	Primitive
Monoclinic	$a \neq b \neq c$, $\alpha = \gamma = 90° \neq \beta$	Primitive Base-centered
Triclinic	$a \neq b \neq c$, $\alpha \neq \beta \neq \gamma \neq 90°$	Primitive

[1] Primitive: One lattice point located at each corner of the unit cell (total of one lattice point per unit cell); Body-centered: like the primitive lattice with an additional lattice point at the center of the unit cell (total of two lattice points per unit cell); Face-centered: like the primitive lattice, with additional lattice points at the center of each face of the unit cell (total of four lattice points per unit cell); Base-centered: like the primitive lattice, with an additional lattice point at the center of one of the faces of the unit cell (total of two lattice points per unit cell).

Because of its 3-D periodicity, a crystal lattice can be thought of as a family of parallel planes containing the lattice points. The orientation of a lattice plane, or family of lattice planes,

in the crystal lattice can be described with so called Miller indices (*h, k, l*), which are the reciprocals of the fractional intercepts of the plane with the crystallographic axes. In other words, a plane of the *hkl* family of lattice planes intercepts the crystallographic axes *a*, *b*, and *c* at 1/*h*, 1/*k*, and 1/*l*. Negative integers are written with an overbar, *i.e.* as $\bar{h}, \bar{k}, \bar{l}$.[132] Examples of lattice planes with their Miller indices are shown in Figure 2.20.

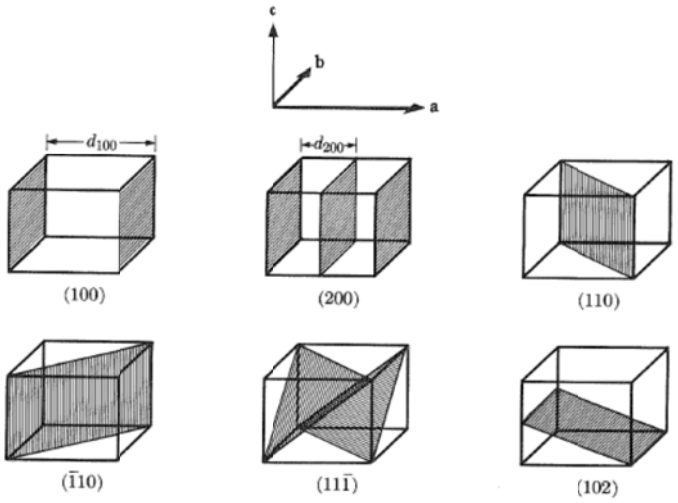

Figure 2.20. Examples of lattice planes with their Miller indices. (Reprinted from ref 132; fair use; Copyright 1978 Addison-Wesley Publishing Company, Inc)

By definition, the distance, *d*, between the planes in a family of lattice planes is constant. An incident X-ray beam impinging on a family of lattice planes is elastically scattered in all directions by the atoms in the crystal lattice. In most directions, the scattered waves are out of phase and annul each other through destructive interference. However, in certain directions, which depend on *d*, the waves are in phase with each other and interfere constructively. The conditions for constructive interference are depicted in Figure 2.21. The angle between the incident X-ray beam and the lattice planes at which constructive interference occurs is called the Bragg angle, θ.[135]

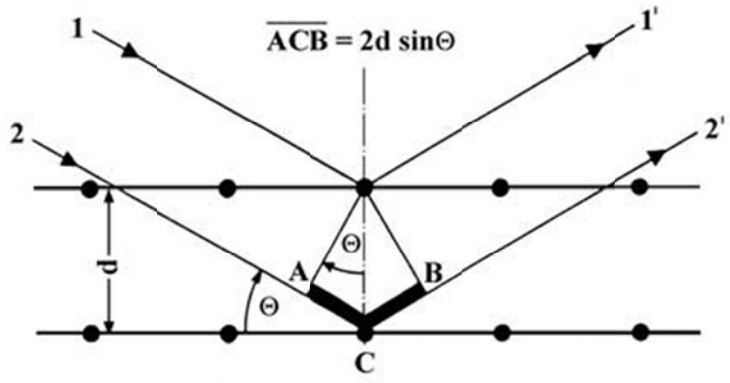

Figure 2.21. Diffraction of X-rays by a crystal. (Reprinted from ref 135; fair use; Copyright 1998 Plenum Press)

As seen in Figure 2.21, the phase difference between waves scattered by the top plane and waves scattered by the bottom plane is the sum of the distances between points A and C and points C and B, denoted as AC and CB, respectively. The mathematical relation between AC, d, and θ is

$$\mathrm{AC} = d \cdot \sin\theta, \qquad [2.5]$$

and because AC = CB

$$\mathrm{CB} = d \cdot \sin\theta, \qquad [2.6]$$

Thus, the phase difference between waves scattered by the top plane and waves scattered by the bottom plane is

$$\mathrm{AC} + \mathrm{CB} = 2d \cdot \sin\theta \qquad [2.7]$$

Constructive interference occurs only when waves are in phase with one another, which means that AC + CB must be an integral multiple of the wavelength, λ. Substituting AC + CB with $n\lambda$ gives Bragg's law

$$n\lambda = 2d \cdot \sin\theta \qquad [2.8]$$

Scherrer observed that the angular width of a diffraction peak, commonly called reflection, is related to the size of the crystal in the direction normal to the *hkl* family of lattice planes, D_{hkl}, by the equation[136]

$$D_{hkl} = \frac{K \cdot \lambda}{B_{hkl} \cdot \cos\theta} \qquad [2.9]$$

where K is the Scherrer constant (1.00 for equatorial reflections of needle-like crystallites)[137] and B_{hkl} is the full width at half maximum in radians of the reflection of that family of lattice planes.

2.5.4. **Atomic force microscopy**

AFM was invented in 1986 by Binnig *et al.*[138] and has evolved to become an important method for the characterization of nanoparticles and solid surfaces. AFM, along with scanning tunneling microscopy (STM), also invented by Binnig *et al.*,[139] are both scanning probe microscopies. Although STM was invented before AFM, AFM is more commonly used in various research fields including materials science, physics, chemistry, biology, and engineering because of the limitation that STM can only image electrically conductive samples.[140,141]

The heart of an atomic force microscopy is a sharp tip mounted on the end of a cantilever with a low spring constant, which scans systematically across the sample during a measurement. As the tip scans the sample, the cantilever bends because of interactions between the tip and the sample. As the tip approaches the sample from a distance, the force that the tip experiences increases from zero to weakly attractive. Eventually, as the tip gets closer to the sample, the interaction force becomes repulsive.[142] Nowadays, some of the most commonly used cantilevers are made of silicon or silicon nitride. The rectangular silicon cantilevers have spring constants between 0.1 and 40 $N \cdot m^{-1}$, whereas the triangular nitride cantilevers have spring constants between 0.01 and 0.58 $N \cdot m^{-1}$.[143]

Besides the cantilever and the tip, piezoelectric actuators are also important components of an atomic force microscope. Piezoelectric materials can convert electrical potential into mechanical motion. On the basis of the position of the piezoelectric actuator, atomic force microscopes can be divided into sample-scanning and probe-scanning instruments, as illustrated

in Figure 2.22. In the sample-scanning configuration, shown in Figure 2.22a, the cantilever is in a fixed position and the sample moves in the x-, y-, and z-direction underneath it for scanning. In the probe-scanning configuration, the sample is in a fixed position and the probe (tip) of the piezoelectric scanner moves in the x-, y-, and z-direction across the sample.[144]

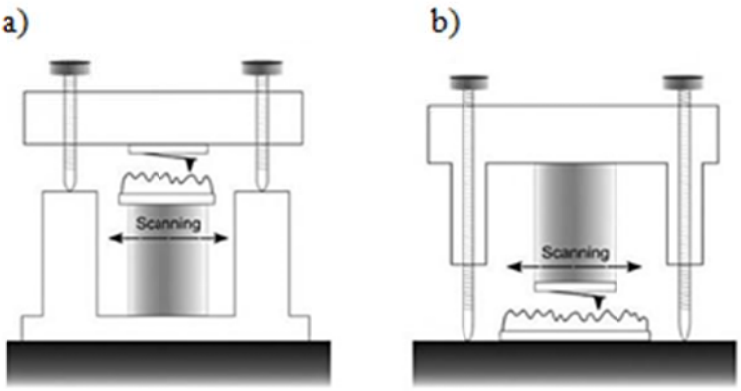

Figure 2.22. Configurations of an atomic force microscope: (a) sample-scanning configuration, (b) probe-scanning configuration. (Reprinted from ref 144; fair use; Copyright 2010 Oxford University Press)

The atomic force microscope of Asylum Research (MFP-3D) uses a different configuration, shown in Figure 2.23. In this configuration, the sample is mounted on a X-Y piezoelectric scanner and moves in the x- and y-direction while the probe is on a Z piezoelectric scanner and moves in the z-direction. The Z scanner maintains a constant force between tip and sample and oscillates the cantilever in AC mode.[145]

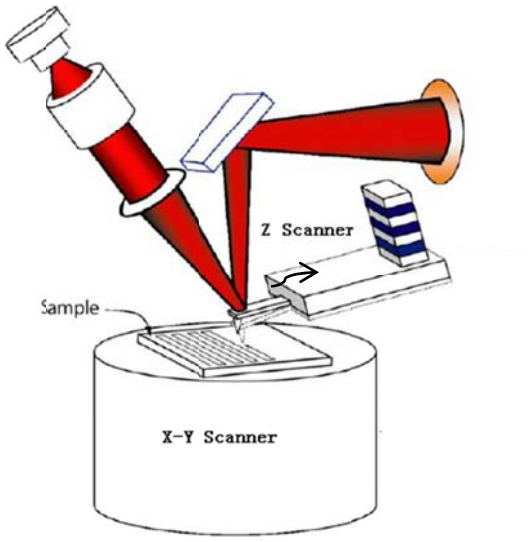

Figure 2.23. Configuration of the Asylum Research MFP-3D atomic force microscope. (Reprinted from ref 145; fair use; Copyright 2008 Asylum Research)

During an AFM experiment, the position of the probe above the sample is constantly monitored. The most common way to do this in modern atomic force microscopes is the laser reflection technique, also shown in Figure 2.23. As the sample moves back and forth underneath the probe, the cantilever bends in response to the surface topography. The bending of the cantilever cause a deflection of the laser beam reflected from its top surface into a four-quadrant photodetector. The vertical motion of the cantilever is proportional to the current difference between the top and bottom of the photodetector.[143]

AFM offers three basic scanning modes for measuring the topography of a surface: contact mode, non-contact mode, and tapping or intermittent-contact mode. The three modes and the surface topographies generated by them are depicted schematically in Figure 2.24.[140]

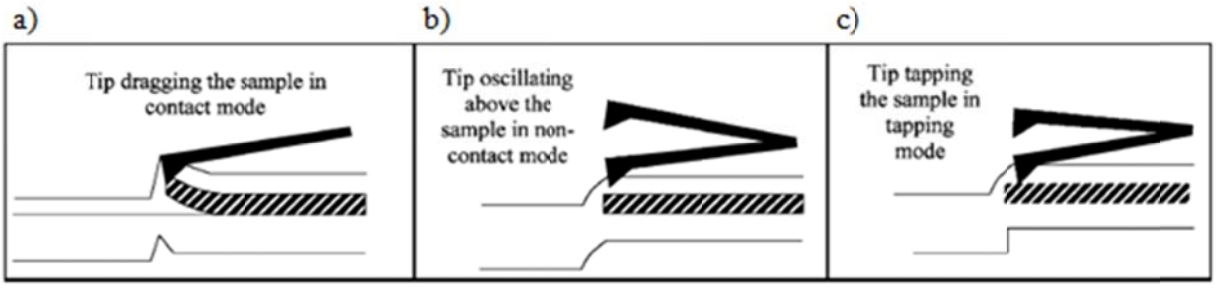

Figure 2.24. AFM scanning modes: (a) contact mode, (b) non-contact mode, and (c) tapping or intermittent-contact mode. (Reprinted from ref 140; fair use; Copyright 2004 Elsevier)

In contact mode (Figure 2.24a), the tip is in constant contact with the sample as it scans across the surface, and the interactions between the tip and the sample are dominated by strong, repulsive van der Waals forces. There are two contact mode methods for determination of the surface topography: the constant-height and constant-force methods. In the constant-height method, the tip does not move in the z-direction as it laterally scans the surface, whereas in the constant-force method, the tip is moved up and down by the Z-piezoelectric scanner to maintain a constant force between the tip and the sample. The lateral force exerted by the tip on the sample as it scans across the surface may be between 10 and 100 nN at ambient conditions and is strong enough to damage some surface.[146] Consequently, contact mode is primarily used to image hard and stable samples, resulting in high-resolution images. However, because of the potentially damaging effects of the lateral tip–sample forces, it is not suited for soft biological and polymeric surfaces.[140]

In non-contact mode (Figure 2.24b), the cantilever is oscillated at a fixed height, usually between 50 and 150 Å, above the sample so that the tip does not make contact with the surface. In this mode, the interactions between the tip and the sample are dominated by attractive van der Waals forces. The relatively weak forces are detected by a change in the amplitude, phase, or frequency of the cantilever's oscillation. Because the forces between the tip and the sample in this mode are weak, usually between 10 and 12 pN, and because the tip never touches the surface, this mode has minimal potential of damaging or contaminating the sample and therefore is frequently used to image soft or elastic samples.[140]

In tapping mode (Figure 2.24c), which combines both contact and non-contact mode, the cantilever oscillates at or near its resonant frequency at an amplitude between 20 and 100 nm when it is not in contact and maintains a fixed average height over the surface during scanning. During the scan, the tip touches the surface intermittently and lifts off at a frequency of 50–500 kHz. The amplitude of the oscillation decreases as a result of the energy loss during tip contact with the sample. The surface topography is obtained by comparing the oscillation amplitude to a reference value. This mode avoids damaging the sample by eliminating lateral forces between the tip and the sample, present in contact mode, and makes it possible to obtain high-resolution topographical images of soft samples.[140,147]

2.6. Surfactant characterization techniques

2.6.1. **Tensiometry**

Surface tension is a phenomenon caused by the cohesive forces among liquid molecules at the air/liquid interface. For molecules in the bulk liquid, cohesive forces are exerted from all directions and thus balance to a net force of zero. The liquid molecules at an air/liquid interface, however, are only surrounded by other liquid molecules in the liquid phase but not in the gas phase. As a consequence, there is a net force pulling surface molecules towards the liquid phase. Thermodynamically, the surface tension, γ, is defined as the Gibbs free energy per unit area at constant temperature, T, pressure, p, and number of moles of component, n

$$\gamma = \left(\frac{\partial G}{\partial a} \right)_{T,p,n} \qquad [2.10]$$

As discussed in section 2.4.2, the surface tension of a liquid is affected by surfactants. Figure 2.25 shows the surface tension of a liquid as a function of surfactant concentration. Above a minimum concentration, the surface tension decreases with increasing surfactant concentration. When the surfactant concentration exceeds the CMC, the surface tension stays constant. Pure

water has a surface tension of 72 $mN \cdot m^{-1}$. The minimum surface tension of water above the CMC is usually between 30 and 40 $mN \cdot m^{-1}$, depending on the type of surfactant.[96]

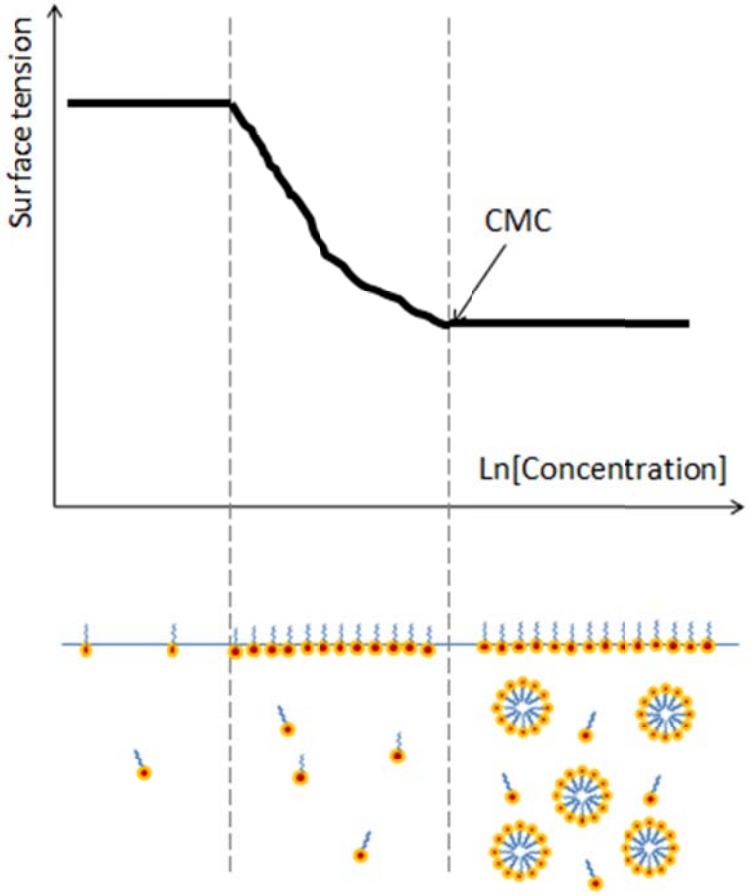

Figure 2.25. Surface tension of a liquid as a function of the surfactant concentration.

Surface tension can be measured with various methods, including the pendant drop method, the maximum-bubble-pressure method, the drop-weight method, the Du-Nouy ring method, and the Wilhelmy-plate method.[148] Because of space limitations, only the Wilhelmy-plate method will be described in detail. In the Wilhelmy plate method, a Wilhelmy plate, commonly made of platinum, glass, or filter paper, is lowered into the liquid, as shown in Figure 2.26.

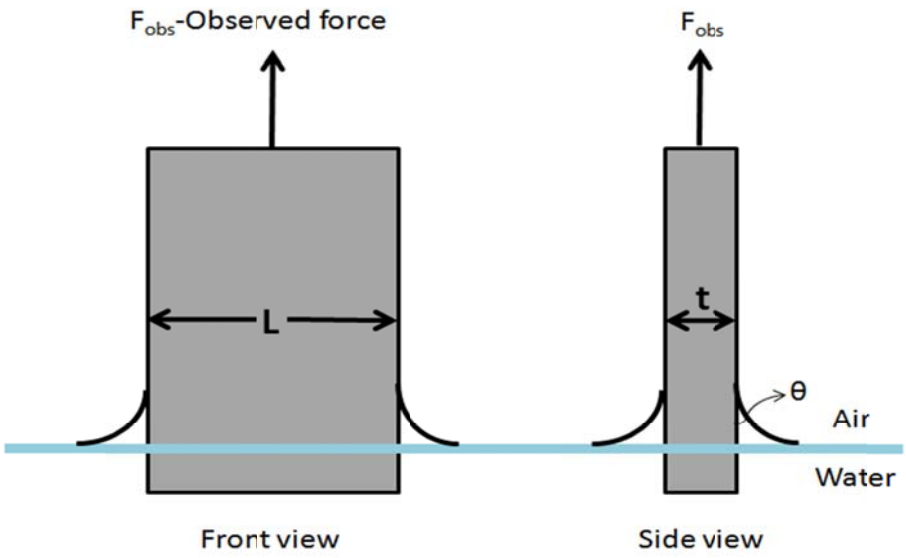

Figure 2.26. Wilhelmy plate technique for measuring surface tension (γ) at the air/water interface.

The net force acting on the plate in Figure 2.26 is measured with a sensitive electrobalance.[149] The net force is a result of downward forces, such as gravity and surface tension, and upward forces, specifically buoyancy, which results from the displacement of the liquid by the plate. Assuming the buoyant force is negligible, the surface tension is calculated as

$$\gamma = \frac{F_{obs} - W}{2(L + t)\cos\theta} \qquad [2.11]$$

where F_{obs} is the force measured by the electrobalance when the plate is in contact with the liquid, W is the gravitational force acting on the wet plate out of the liquid, L and t are the length and thickness of the plate, respectively, and θ is the contact angle between the liquid and the plate. As evident from eq 2.11, the measured surface tension depends on the contact angle between the liquid and the plate. To eliminate this factor, the plate is usually designed to ensure complete wetting by the liquid, *i.e.* $\theta = 0°$.

2.6.2. **Fluorescence spectroscopy**

Fluorescence is the emission of light associated with the transition of electronically excited molecules from a singlet state back to the ground state, with the molecules previously having been excited from the electronic ground state to the electronic excited state by absorption of light.[150,151] During a fluorescence measurement, a fluorescent probe is employed to emit light as it transitions from the excited state to the ground state, and the emission spectrum is obtained by plotting the intensity of emitted fluorescence as a function of wavelength. The fluorescent properties detected by the instrument are very sensitive to changes in the microenvironment of the probe, and can be used to characterize the microenvironment. Properties of the microenvironment that can be detected from a change in fluorescence include micropolarity, microviscosity, diffusion, partitioning between phases, concentration of quenchers, and distance between groups.[150]

Pyrene (Figure 2.27a) is a commonly used fluorescence probe because it exhibits solvent induced variation in the ratio of emission intensities. The fluorescence spectrum of pyrene is shown in Figure 2.27b. The five peaks in the spectrum correspond to the transitions of pi electrons from the excited state to the various vibrational modes of the ground state. The ratio of the intensity of the third vibronic band (386.0 nm, I_{m3}) to that of the first vibronic band (375.0 nm, I_{m1}) reflects the electronic polarity of the microenvironment that pyrene experiences. Higher I_{m3}/I_{m1} values indicate a more hydrophobic microenvironment.[151,152] Consequently, pyrene fluorescence measurements can be used to determine the CMC of a surfactant by measuring the changes in I_{m3}/I_{m1} with increasing surfactant concentration. I_{m3}/I_{m1} increases sharply at the onset of micelle formation because pyrene partitions to the hydrophobic core of the micelles and thus experiences a change to a more hydrophobic microenvironment.[153]

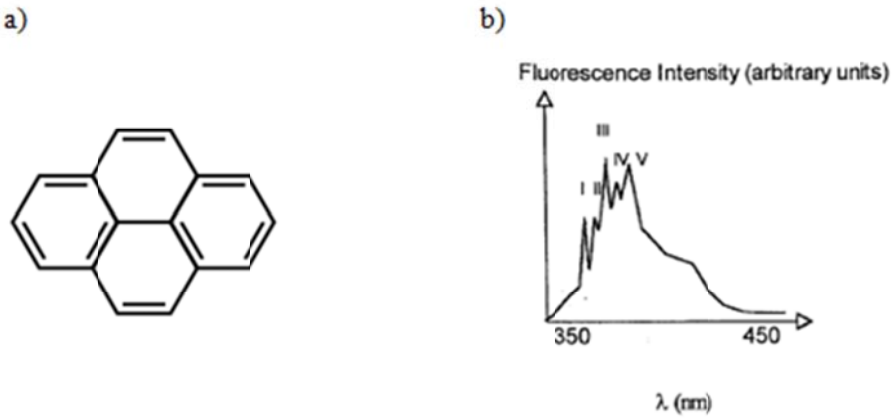

Figure 2.27. (a) Pyrene molecule and (b) its fluorescence emission spectrum for excitation at 334 nm. (Reprinted from ref 152; fair use; Copyright 1977 American Chemical Society)

2.7. Measurement of enzyme adsorption and enzymatic hydrolysis

2.7.1. **Quartz crystal microbalance with dissipation monitoring**

Quartz crystal microbalance with dissipation monitoring (QCM-D) enables precise, real-time determination of adsorbed masses on quartz crystal sensors, detecting weight changes of less than 1 ng·cm^{-2}, as well as the viscoelastic properties of the adsorbed film, by simultaneously measuring changes in the oscillation frequency of the quartz crystal (Δf) and the energy dissipation factor during oscillation (ΔD).[154,155] A QCM-D sensor consists of a thin, AT-cut single crystal quartz disc with a diameter of 14 mm and gold electrodes deposited on both sides, as illustrated in Figure 2.28.[156]

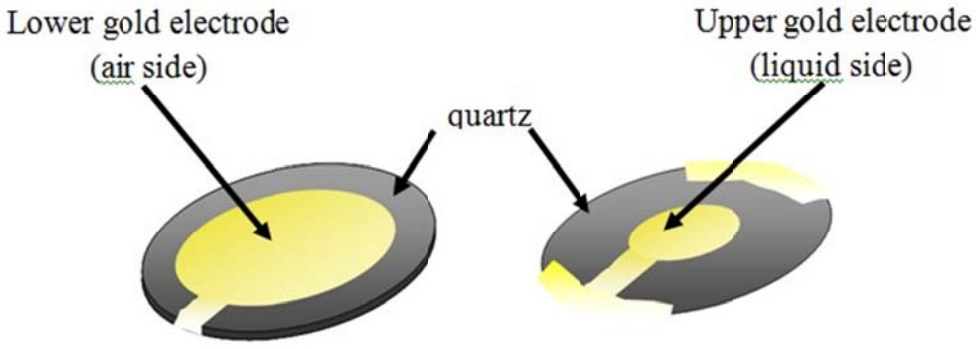

Figure 2.28. Schematic illustration of quartz crystal sensors covered with gold electrodes.

The piezoelectric properties of quartz crystals were discovered in 1880 by Pierre and Jacques Curie,[157] who found that they could generate electricity with crystals of Rochelle salt by applying pressure in certain crystallographic directions, and that the crystals were able to exert pressure when subjected to electrical current. During a QCM-D measurement, an alternating current electric field is applied to the AT-cut quartz crystal through the gold electrodes. Under the influence of the electric field, the quartz crystal oscillates in a thickness shear mode.

The principle of QCM-D can be explained by the aforementioned electrical potential–mechanical strain inter-induction within a quartz crystal. The oscillation frequency and dissipation are measured by periodically connecting and disconnecting the quartz crystal *via* a computer-controlled relay, as shown in the QCM-D measurement setup in Figure 2.29.[154,156,158]

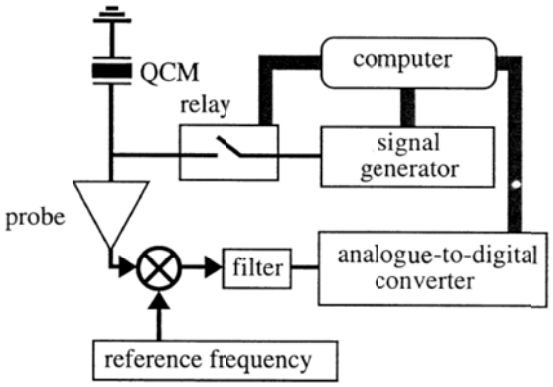

Figure 2.29. Schematic illustration of the QCM-D measurement setup. (Reprinted from ref 154; fair use; Copyright 1995 American Institute of Physics)

At the start of a measurement, the relay is closed and the quartz crystal is made to oscillate at its fundamental or an overtone resonant frequency by the oscillator. When the oscillation of the crystal remains stable over a set period of time, the computer triggers the relay to open, and the amplitude, A, of the crystal's sinusoidal oscillation will decay exponentially according to

$$A(t) = A_0 e^{-t/\tau} \sin(2\pi f t + \varphi) \qquad [2.12]$$

where τ is the decay time constant, φ is the phase, and f is the frequency at resonance. The amplitude decay curve is recorded by an oscilloscope and fit with a least-squares procedure to the theoretical decay equation, yielding a value for τ. With τ and f known, the dissipation factor, D, can be calculated as[154]

$$D = 1/\pi f \tau \qquad [2.13]$$

D is also defined as

$$D = \frac{E_{\text{dissipated}}}{2\pi E_{\text{stored}}} \qquad [2.14]$$

where $E_{dissipated}$ is the energy dissipated during one period of oscillation and E_{stored} is the energy stored in the oscillating system. $E_{dissipated}$ is the result of uncoupled oscillatory motion by energy dissipating subsystems of the composite oscillating system. Thus, D contains information about the rigidity of the adsorbed film. A change in mass, Δm, of the oscillating system through adsorption, will induce a change in the oscillation frequency, Δf.

Sauerbrey model

The Sauerbrey model is a frequently applied model for the conversion of frequency changes into mass changes. It is based on a linear relationship between Δm and Δf, derived by Sauerbrey in 1959 as[159]

$$\Delta m = -\frac{\rho_q t_q \Delta f}{f_0 n} = -\frac{\rho_q v_q \Delta f}{2 f_0^2 n} = -\frac{C \Delta f}{n} \qquad [2.15]$$

where ρ_q is the density of quartz, t_q is the thickness of the quartz disc, f_0 is the fundamental resonance frequency of the first overtone (n = 1), n is the overtone number (n = 1, 3, 5, 7…), and v_q is the shear wave velocity in quartz. With ρ_q = 2648 kg·m^{-3}, v_q = 3340 m·s^{-1}, and f_0 = 5 MHz, the mass sensitivity constant, C, becomes 17.7 ng·cm^{-2}·Hz^{-1}. The Sauerbrey model assumes that the adsorbed mass is: (i) evenly distributed over the entire crystal, (ii) small with respect to the mass of the crystal itself (< 1%), and (iii) rigidly attached to the crystal without slip or inelastic deformation caused by the oscillation. [154,155] Hence, eq 2.15 treats the adsorbed mass as part of the crystal itself, oscillating in phase with the crystal and causing minimal changes in energy dissipation. However, when ΔD exceeds $1 \cdot 10^{-6}$ per 10 Hz, the adsorbed film is not rigid enough to be regarded as part of the crystal and the upper layer of the film will be out of phase with the oscillating crystal. In a non-rigid film, such as an adsorbed protein layer, the frequency change does not result solely from the mass of the adsorbed film, but also is affected by energy dissipation caused by the oscillatory motion within the film. As a result, the Sauerbrey model underestimates the adsorbed mass of non-rigid adsorbed films. In order to obtain accurate mass changes for non-rigid films, one has to consider ΔD and Δf values for several overtones and use a viscoelastic model to describe the oscillating system.[160]

Voigt-based Viscoelastic model

The most frequently used viscoelastic film model for films immersed in a Newtonian liquid is the Voigt model, which applies to viscoelastic films that maintain their shape and do not flow. The key parameters of this model are illustrated in Figure 2.30, and have been explained in detail by Rodahl *et al.*[158,161,162] and Hook *et al.*[157, 158]

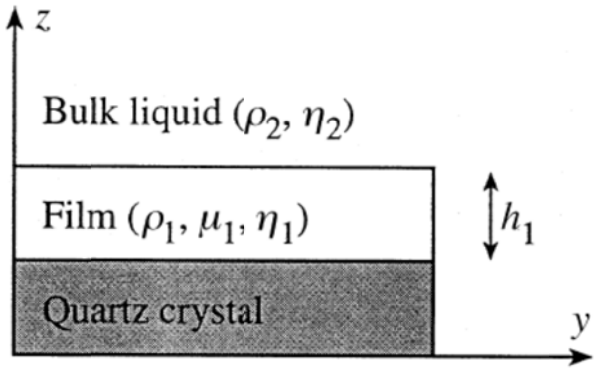

Figure 2.30. Schematic illustration of the viscoelastic film model, describing a viscoelastic film on an oscillating quartz crystal immersed in a Newtonian liquid. (Reprinted from ref 158; fair use; Copyright 1997 Royal Society of Chemistry)

In the Voigt-based viscoelastic film model, the adsorbed film is represented by a frequency-dependent complex shear modulus, G

$$G = G' + iG'' = \mu_1 + i2\pi f\eta_1 = \mu_1(1 + i2\pi f\tau_1) \qquad [2.16]$$

where μ_1 and η_1 are the elastic shear (storage) modulus and shear viscosity of the film, respectively, f is the oscillation frequency, and τ_1 is the characteristic relaxation time of the film. Other important parameters that represent the film are the film thickness, h_1, and the film density ρ_1. In the Voigt-based viscoelastic film model, Δf and ΔD are expressed as

$$\Delta f = \frac{\mathrm{Im}(\beta)}{2\pi t_q \rho_q} \qquad [2.17]$$

and

$$\Delta D = -\frac{\mathrm{Re}(\beta)}{\pi f t_q \rho_q} \qquad [2.18]$$

where

$$\beta = \xi_1 \frac{2\pi f \eta_1 - i\mu_1}{2\pi f} \frac{1 - \alpha \exp(2\xi_1 h_1)}{1 + \alpha \exp(2\xi_1 h_1)} \qquad [2.19]$$

with

$$\alpha = \frac{\frac{\xi_1}{\xi_2}\frac{2\pi f \eta_1 - i\mu_1}{2\pi f \eta_2} + 1}{\frac{\xi_1}{\xi_2}\frac{2\pi f \eta_1 - i\mu_1}{2\pi f \eta_2} - 1}, \qquad [2.20]$$

and

$$\xi_1 = \sqrt{\left[-\frac{(2\pi f)^2 \rho_1}{\mu_1 + i 2\pi f \eta_1} \right]}, \qquad [2.21]$$

and

$$\xi_2 = \sqrt{\left(i \frac{2\pi f \rho_2}{\eta_2} \right)} \qquad [2.22]$$

ρ_2 and η_2 in eq 2.22 are the density and viscosity of the bulk liquid, respectively. Application of the viscoelastic film model requires a series of measurements at several overtones (n = 1, 3, 5, 7…) and comparison of the obtained values with the theoretical ones.

In QCM-D measurements of the adsorption of enzymes onto model cellulose surfaces, which are rigid enough to be regarded as part of the crystal, and of their enzymatic hydrolysis, ΔD can be attributed to (i) the oscillatory motion within the enzyme film, which includes the

effect of trapped water molecules, (ii) the interfacial oscillatory motion (slip) between the adsorbed enzyme layer and the rigid cellulose film, and (iii) the change in surface roughness of the cellulose film resulting from the hydrolytic action of the enzymes.

Because QCM-D is widely used for the study of biological phenomena, such as protein adsorption,[158] cell adhesion,[158,163] and lipid vesicle adsorption,[158,164] methods for the calculation of masses of non-rigid adsorbed layers have become a top priority for its application. As mentioned above, the mass of non-rigid films is underestimated by the Sauerbrey equation.[156,165] Voinnova *et al.*[165] applied the Sauerbrey equation to the data of Keller and Kasemo[164] and obtained a reduction of Δf = 51 Hz, which was termed the "missing mass". Compared to the Sauerbrey equation, the Voigt viscoelastic model gave more accurate changes in the adsorbed mass because it used a combination of frequency and dissipation change in the calculation. Hook et al.[162] studied the adsorption of mussel adhesive protein (Mefp-1) on a methyl-terminated gold surface. The thickness values for the adsorbed Mefp-1 layer, calculated with the Sauerbrey equation, were 15.2, 11.3, and 9.9 nm for the overtones 1, 3, and 5, respectively. However, the viscoelastic model gave a thickness of 22.4 nm. The "missing mass" effect is obvious from this comparison. In addition to providing mass values for non-rigid adsorbed layers, the viscoelastic model can also be used to estimate the rheological properties of proteins[162,166,167] and polymers.[168,169]

2.7.2. **Surface plasmon resonance spectroscopy**

Surface plasmon resonance spectroscopy (SPR) relies on an optical biosensor that uses an evanescent wave to monitor small real time changes in refractive index near the surface of a sensor. In SPR, the binding of analyte in solution with a ligand immobilized on the sensor surface, causes an increase in the refractive index close to the sensor surface. The amount of bound analyte, the affinity between analyte and ligand, and the association and dissociation kinetics can be determined from the change in refractive index.[170,171] Besides measuring binding parameters with very high accuracy, SPR can be used for real-time measurement of biomolecular interactions. An advantage of SPR over other methods used for this purpose is that sample preparation is relatively easy and does not require labeling.[172]

A frequently used set-up for SPR refractometers is the Kretschmann prism configuration, shown in Figure 2.31, which consists of a monochromatic, p-polarized light source, a glass prism coated with a thin metal film, and a light detector.[173]

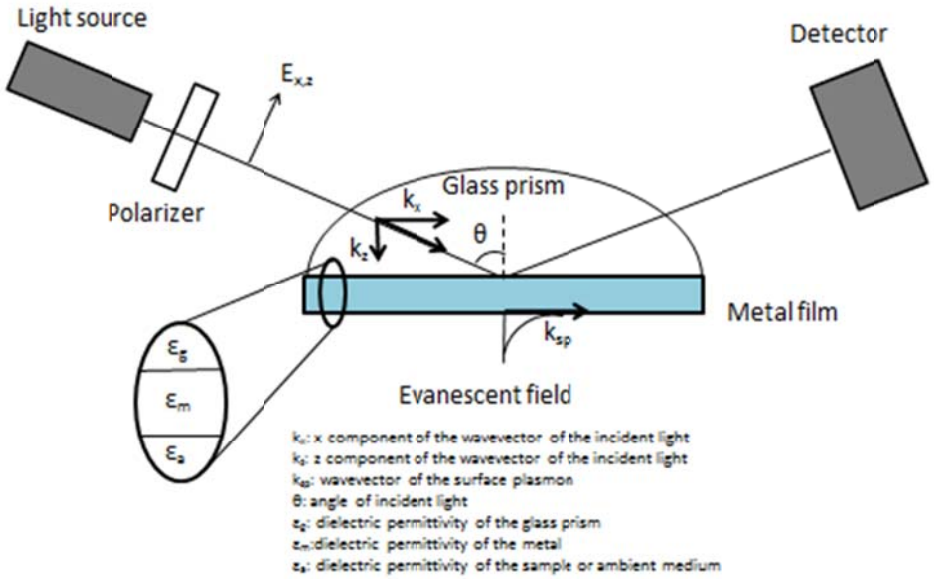

Figure 2.31. Kretschmann prism configuration. (Adapted from ref 175; fair use; Copyright 1998 Humana Press)

The Kretschmann prism configuration is based on the phenomenon of total internal reflection, which occurs when light travels from a medium with higher refractive index to a medium with lower refractive index, *e.g.* from glass to air, and the angle of incidence exceeds a critical value. Although the incident light is totally reflected at the glass–metal interface and not refracted into the ambient medium, a component of the incident light (evanescent wave or field) penetrates the metal film under these conditions, provided that it is sufficiently thin (≈ 50 nm). This evanescent wave excites surface plasmons, which propagate along the interface between the metal and the ambient medium.[174,175]

The critical angle of incidence, θ_c, above which total internal reflection occurs, can be derived from Snell's law[176]

$$n_1 \sin \theta_1 = n_2 \sin \theta_2 \qquad [2.23]$$

where n_1 is the refractive index of medium 1, n_2 is the refractive index of medium 2, θ_1 is the angle of incidence, and θ_2 is the angle of refraction. The relation between θ_1 and θ_2 is illustrated in Figure 2.32. θ_c is the angle of incidence at which the angle of refraction becomes 90°. For $n_2 > n_1$ and $\theta_2 = 90°$, Snell's law becomes[176]

$$\sin \theta_c = \frac{n_2}{n_1} \qquad [2.24]$$

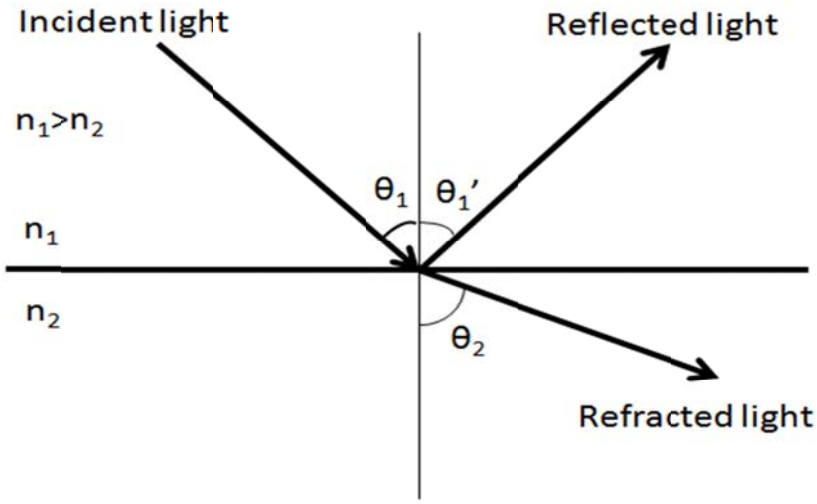

Figure 2.32. Schematic illustration of Snell's law. (Adapted from ref 175; fair use; Copyright 1998 Humana Press)

The propagation vector, k_{sp}, of the surface plasmon propagating along the interface between the metal and the ambient medium is given by

$$k_{sp} = \frac{2\pi}{\lambda}\sqrt{\frac{\varepsilon_m \varepsilon_a}{\varepsilon_m + \varepsilon_a}} \qquad [2.25]$$

where λ is the wavelength of the incident light, ε_m is the dielectric permittivity of the metal, and ε_a is the dielectric permittivity of the ambient medium.[175,177] The propagation vector of the incident light in the glass prism, k, is given by

$$k = \frac{2\pi}{\lambda}\sqrt{\varepsilon_g} \qquad [2.26]$$

where ε_g is the dielectric permittivity of the glass prism. The component of the propagation vector that is parallel to the interface, k_x, is

$$k_x = k \cdot \sin\theta = \frac{2\pi}{\lambda}\sqrt{\varepsilon_g} \cdot \sin\theta \qquad [2.27]$$

In an SPR-based measurement, the surface-parallel component k_x is tuned by varying the angle of incidence, θ, until $k_x = k_{sp}$. The angle of incidence at which the condition $k_x = k_{sp}$ is satisfied is called resonance angle or SPR angle, θ_{sp}. Combining eqs 2.25 and 2.27 gives

$$\sqrt{\varepsilon_g}\sin\theta_{sp} = \sqrt{\frac{\varepsilon_m \varepsilon_a}{\varepsilon_m + \varepsilon_a}} \qquad [2.28]$$

For non-polar insulators, $n = \sqrt{\varepsilon}$, such that eq 2.28 becomes[178]

$$n_g \sin\theta_{sp} = \sqrt{\frac{n_m^2 n_a^2}{n_m + n_a}} \qquad [2.29]$$

where n_g, n_m, and n_a are the refractive indices of glass, metal, and the ambient medium, respectively.

θ_{sp} can be determined by measuring the intensity of the reflected light as a function of the angle of incidence. When the angle of incidence is equal to θ_{sp}, the intensity of the reflected light is minimal because most of the incident light is dissipated in the metal film in the form of surface plasmons. Figure 2.33 shows the reflected light intensity as a function of the angle of incidence before and after binding of the analyte.

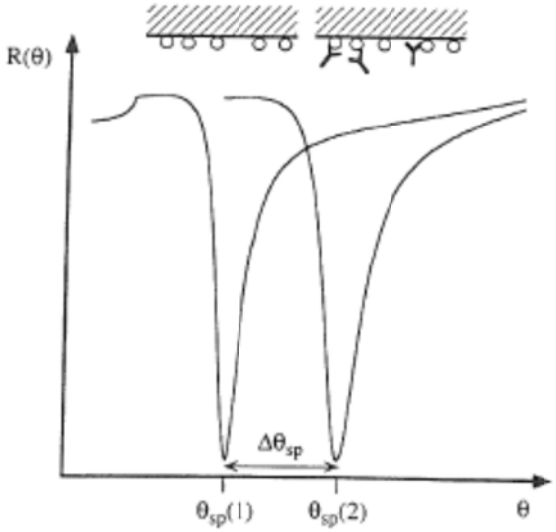

Figure 2.33. Reflected light intensity R(θ) as a function of the angle of incidence and the SPR angles before ($\theta_{sp}(1)$ and after ($\theta_{sp}(2)$ binding of the analyte. (Reprinted from ref 175; fair use; Copyright 1998 Humana Press)

According to eq 2.27, θ_{sp} depends on the refractive indices of the prism, the metal film, and the ambient medium. The refractive indices of the prism and the metal film remain unchanged during the experiment but the refractive index of the ambient medium changes upon accumulation of adsorbed mass at the interface between the metal and the ambient medium. Consequently, θ_{sp} can be used to monitor binding of the analyte, as illustrated in Figure 2.33.

The change in refractive index, determined from the change in θ_{sp}, can be used to calculate the surface concentration of bound analyte, Γ, with the equation of de Feijter *et al.*[179]

$$\Gamma = \frac{L \cdot \Delta n_a}{(dn/dc)} \qquad [2.30]$$

where L is the thickness of the adsorbed layer, Δn_a is the refractive index difference between the analyte and the solvent, n is the refractive index of the analyte solution, and c is the concentration of the analyte. (dn/dc), the refractive index increment of the analyte, can be measured with a differential refractometer and expressed as

$$\left(\frac{dn}{dc}\right)=\left(\frac{dn}{d\theta_{sp}}\right)\left(\frac{d\theta_{sp}}{dc}\right) \qquad [2.31]$$

where ($dn/d\theta_{sp}$) is an instrument constant, and ($d\theta_{sp}/dc$) is the change in resonant angle with bulk analyte concentration.

The thickness of the layer is given by

$$L=\Delta\theta_{a}\left(\frac{dL}{d\theta}\right) \qquad [2.32]$$

where ($dL/d\theta$) can be obtained from a Fresnel calculation with a value for SDS of 0.04°/nm,[180] and $\Delta\theta_a$ is the change in angle due to analyte binding. $\Delta\theta_a$ needs to be corrected for bulk contribution to the refractive index change.[181]

$$\Delta\theta_{a}=\Delta\theta_{sp}-c\left(\frac{d\theta_{sp}}{dc}\right) \qquad [2.33]$$

Combining eqs 2.31, 2.32, and 2.33 gives

$$\Gamma=\Delta\theta_{a}\left(\frac{dL}{d\theta}\right)\Delta n_{a}\left(\frac{dc}{d\theta_{sp}}\right)\left(\frac{d\theta_{sp}}{dn}\right) \qquad [2.34]$$

2.8. References

1. Payen, A. Mémoire sur la Composition du Tissu Propre des Plantes et du Ligneux. *Comtes Rendus Hebdomadaires des Seances de l'Académie des Sciences* **1838,** *7*, 1052-1056.

2. Payen, A. Sur un Moyen d'isoler le Tissu Élémentaire des Bois. *Comtes Rendus Hebdomadaires des Seances de l'Académie des Sciences* **1838,** *7*, 1125.

3. Klemm, D.; Heublein, B.; Fink, H. P.; Bohn, A. Cellulose: Fascinating Biopolymer and Sustainable Raw Material. *Angewandte Chemie-International Edition* **2005,** *44*, 3358-3393.

4. Kontturi, E.; Tammelin, T.; Osterberg, M. Cellulose - Model Films and the Fundamental Approach. *Chemical Society Reviews* **2006,** *35*, 1287-1304.

5. Osullivan, A. C. Cellulose: The Structure Slowly Unravels. *Cellulose* **1997,** *4*, 173-207.

6. Zugenmaier, P. Conformation and Packing of Various Crystalline Cellulose Fibers. *Progress in Polymer Science* **2001,** *26*, 1341-1417.

7. Simon, I.; Glasser, L.; Scheraga, H. A.; Manley, R. S. Structure of Cellulose. 2. Low-Energy Crystalline Arrangements. *Macromolecules* **1988,** *21*, 990-998.

8. Nishiyama, Y.; Sugiyama, J.; Chanzy, H.; Langan, P. Crystal Structure and Hydrogen Bonding System in Cellulose 1(Alpha), from Synchrotron X-Ray and Neutron Fiber Diffraction. *Journal of the American Chemical Society* **2003,** *125*, 14300-14306.

9. Jarvis, M. Chemistry - Cellulose Stacks Up. *Nature* **2003,** *426*, 611-612.

10. Atalla, R. H.; Vanderhart, D. L. Native Cellulose - A Composite of 2 Distinct Crystalline Forms. *Science* **1984,** *223*, 283-285.

11. Sugiyama, J.; Vuong, R.; Chanzy, H. Electron-Diffraction Study on the 2 Crystalline Phases Occurring in Native Cellulose from an Algal Cell-Wall. *Macromolecules* **1991,** *24*, 4168-4175.

12. Lima, M. M. D.; Borsali, R. Rodlike Cellulose Microcrystals: Structure, Properties, and Applications. *Macromolecular Rapid Communications* **2004,** *25*, 771-787.

13. Battista, B. G. Microcrystalline Polymer Science. MacGraw-Hill: New York, 1975.

14. Ranby, B. G. The Colloidal Properties of Cellulose Micelles. *Discussions of the Faraday Society* **1951,** *11*, 158-164.

15. Marchessault, R. H. Liquid Crystal Systems from Fibrillar Polysaccharides. *Nature* **1959,** *184*, 632-633.

16. Dong, X. M.; Revol, J.-F.; Gray, D. G. Effect of Microcrystallite Preparation Conditions on the Formation of Colloid Crystals of Cellulose. *Cellulose* **1998,** *5*, 19-32.

17. Dong, S. P.; Roman, M. Fluorescently Labeled Cellulose Nanocrystals for Bioimaging Applications. *Journal of the American Chemical Society* **2007,** *129*, 13810-13811.

18. Favier, V.; Chanzy, H.; Cavaille, J. Y. Polymer Nanocomposites Reinforced by Cellulose Whiskers. *Macromolecules* **1995,** *28*, 6365-6367.

19. Sczech, R.; Riegler, H. Molecularly Smooth Cellulose Surfaces for Adhesion Studies. *Journal of Colloid and Interface Science* **2006,** *301*, 376-385.

20. Kontturi, E.; Thune, P. C.; Niemantsverdriet, J. W. Cellulose Model Surfaces-Simplified Preparation by Spin Coating and Characterization by X-Ray Photoelectron Spectroscopy, Infrared Spectroscopy, and Atomic Force Microscopy. *Langmuir* **2003,** *19*, 5735-5741.

21. Kontturi, E.; Thune, P. C.; Niemantsverdriet, J. W. Novel Method for Preparing Cellulose Model Surfaces by Spin Coating. *Polymer* **2003,** *44*, 3621-3625.

22. Kontturi, E.; Johansson, L. S.; Kontturi, K. S.; Ahonen, P.; Thune, P. C.; Laine, J. Cellulose Nanocrystal Submonolayers by Spin Coating. *Langmuir* **2007,** *23*, 9674-9680.

23. Edgar, C. D.; Gray, D. G. Smooth Model Cellulose I Surfaces from Nanocrystal Suspensions. *Cellulose* **2003,** *10*, 299-306.

24. Notley, S. M.; Pettersson, B.; Wagberg, L. Direct Measurement of Attractive Van Der Waals' Forces between Regenerated Cellulose Surfaces in an Aqueous Environment. *Journal of the American Chemical Society* **2004,** *126*, 13930-13931.

25. Notley, S. M.; Eriksson, M.; Wagberg, L.; Beck, S.; Gray, D. G. Surface Forces Measurements of Spin-Coated Cellulose Thin Films with Different Crystallinity. *Langmuir* **2006,** *22*, 3154-3160.

26. Rutland, M. W.; Carambassis, A.; Willing, G. A.; Neuman, R. D. Surface Force Measurements between Cellulose Surfaces Using Scanning Probe Microscopy. *Colloids and Surfaces a-Physicochemical and Engineering Aspects* **1997,** *123*, 369-374.

27. Carambassis, A.; Rutland, M. W. Interactions of Cellulose Surfaces: Effect of Electrolyte. *Langmuir* **1999,** *15*, 5584-5590.

28. Nigmatullin, R.; Lovitt, R.; Wright, C.; Linder, M.; Nakari-Setala, T.; Gama, A. Atomic Force Microscopy Study of Cellulose Surface Interaction Controlled by Cellulose Binding Domains. *Colloids and Surfaces B-Biointerfaces* **2004,** *35*, 125-135.

29. Lefebvre, J.; Gray, D. G. AFM of Adsorbed Polyelectrolytes on Cellulose I Surfaces Spin-Coated on Silicon Wafers. *Cellulose* **2005,** *12*, 127-134.

30. Eriksson, J.; Malmsten, M.; Tiberg, F.; Callisen, T. H.; Damhus, T.; Johansen, K. S. Enzymatic Degradation of Model Cellulose Films. *Journal of Colloid and Interface Science* **2005,** *284*, 99-106.

31. Eriksson, J.; Malmsten, M.; Tiberg, F.; Callisen, T. H.; Damhus, T.; Johansen, K. S. Model Cellulose Films Exposed to H-Insolens Glucoside Hydrolase Family 45 Endo-Cellulase - the Effect of the Carbohydrate-Binding Module. *Journal of Colloid and Interface Science* **2005,** *285*, 94-99.

32. Turon, X.; Rojas, O. J.; Deinhammer, R. S. Enzymatic Kinetics of Cellulose Hydrolysis: A QCM-D Study. *Langmuir* **2008,** *24*, 3880-3887.

33. Ahola, S.; Turon, X.; Osterberg, M.; Laine, J.; Rojas, O. J. Enzymatic Hydrolysis of Native Cellulose Nanofibrils and Other Cellulose Model Films: Effect of Surface Structure. *Langmuir* **2008,** *24*, 11592-11599.

34. Habibi, Y.; Foulon, L.; Aguie-Beghin, V.; Molinari, M.; Douillard, R. Langmuir-Blodgett Films of Cellulose Nanocrystals: Preparation and Characterization. *Journal of Colloid and Interface Science* **2007,** *316*, 388-397.

35. Tammelin, T.; Saarinen, T.; Osterberg, M.; Laine, J. Preparation of Langmuir/Blodgett-Cellulose Surfaces by Using Horizontal Dipping Procedure. Application for Polyelectrolyte Adsorption Studies Performed with QCM-D. *Cellulose* **2006,** *13*, 519-535.

36. Kontturi, E.; Thune, P. C.; Alexeev, A.; Niemantsverdriet, J. W. Introducing Open Films of Nanosized Cellulose - Atomic Force Microscopy and Quantification of Morphology. *Polymer* **2005,** *46*, 3307-3317.

37. Falt, S.; Wagberg, L.; Vesterlind, E. L.; Larsson, P. T. Model Films of Cellulose II - Improved Preparation Method and Characterization of the Cellulose Film. *Cellulose* **2004,** *11*, 151-162.

38. Ahola, S.; Salmi, J.; Johansson, L. S.; Laine, J.; Osterberg, M. Model Films from Native Cellulose Nanofibrils. Preparation, Swelling, and Surface Interactions. *Biomacromolecules* **2008,** *9*, 1273-1282.

39. Suhas; Carrott, P. J. M.; Carrott, M. Lignin - From Natural Adsorbent to Activated Carbon: A Review. *Bioresource Technology* **2007,** *98*, 2301-2312.

40. Lora, J. H.; Glasser, W. G. Recent Industrial Applications of Lignin: A Sustainable Alternative to Nonrenewable Materials. *Journal of Polymers and the Environment* **2002,** *10*, 39-48.

41. Whetten, R.; Sederoff, R. Lignin Biosynthesis. *Plant Cell* **1995,** *7*, 1001-1013.

42. Reale, S.; Di Tullio, A.; Spreti, N.; De Angelis, F. Mass Spectrometry in the Biosynthetic and Structural Investigation of Lignins. *Mass Spectrometry Reviews* **2004,** *23*, 87-126.

43. Boerjan, W.; Ralph, J.; Baucher, M. Lignin Biosynthesis. *Annual Review of Plant Biology* **2003,** *54*, 519-546.

44. Sarkanen, K.; Ludwig, C. Deffinition and Nomenclature. In: Lignins: Occurrence, Formation, Structure and Reactions; Sarkanen, K., Ludwig, C., Eds.; John Willey & Sons,Inc.: 1971.

45. Lewis, N. G.; Yamamoto, E. Lignin - Occurrence, Biogenesis and Biodegradation. *Annual Review of Plant Physiology and Plant Molecular Biology* **1990,** *41*, 455-496.

46. Gratzl, J.; Chen, C. Chemistry of Pulping: Lignin Reactions. In: Lignin: Historical, Biological, and Materials Perspectives; Glasser, W., Northey, R., Schultz, T., Eds.; Acs Symposium Series; American Chemical Society: Washington, DC, 2000; pp 392-421.

47. Chakar, F. S.; Ragauskas, A. J. Review of Current and Future Softwood Kraft Lignin Process Chemistry. *Industrial Crops and Products* **2004,** *20*, 131-141.

48. Lai, Y. Z.; Sarkanen, K. V. Isolation and Structural Studies. In: Lignins: Occurrence, Formation, Structure and Reactions; Sarkanen, K. V., Ludwig, C. H., Eds.; John Wiley & Sons, Inc.: New York, 1971; pp 165-240.

49. Rydholm, S., Pulping Processes. In John Wiley & Sons, Inc.: New York, 1965; pp 172-176.

50. Glasser, W.; Kelley, S. In: Encyclopedia of Polymer Science and Engineering; John Wiley & Sons, Inc.: New York, 1987; Vol. *8*, pp 795-852.

51. Sixta, H.; Potthast, A.; Krotschek, A. W. Chemical Pulping Processes. In: Handbook of Pulp; Sixta, H., Ed.; Wiley-VCH Verlag GmbH & Co. KGaA: Austria, 2006; Vol. 1, Chapter 4, pp 109-185.

52. Gellerstedt, G.; Lindfors, E. Structural-Changes in Lignin During Kraft Cooking .4. Phenolic Hydroxyl-Groups in Wood and Kraft Pulps. *Svensk Papperstidning-Nordisk Cellulosa* **1984,** *87*, R115-R118.

53. Robert, D. R.; Bardet, M.; Gellerstedt, G.; Lindfors, E. L. Structural-Changes in Lignin During Kraft Cooking .3. On the Structure of Dissolved Lignins. *Journal of Wood Chemistry and Technology* **1984,** *4*, 239-263.

54. Froass, P. M.; Ragauskas, A. J.; Jiang, J. Chemical Structure of Residual Lignin from Kraft Pulp. *Journal of Wood Chemistry and Technology* **1996,** *16*, 347-365.

55. McDonough, T. J. The Chemistry of Organosolv Delignification. *Tappi Journal* **1993,** *76*, 186-193.

56. Pearl, I. A. The Isolation of Lignin. In: The Chemistry of Lignin; Marcel Dekker, INC.: New York, 1967; pp 13-18.

57. Lundquist, K. Low-Molecular Weight Lignin Hydrolysis Products. *Applied Polymer Symposia* **1976,** *28*, 1393-1407.

58. Sarkanen, S.; Teller, D. C.; Hall, J.; McCarthy, J. L. Lignin .18. Associative Effects among Organosolv Lignin Components. *Macromolecules* **1981,** *14*, 426-434.

59. Bjorkman, A. Isolation of Lignin from Finely Divided Wood with Neutral Solvents. *Nature* **1954,** *174*, 1057-1058.

60. Ikeda, T.; Holtman, K.; Kadla, J. F.; Chang, H. M.; Jameel, H. Studies on the Effect of Ball Milling on Lignin Structure Using a Modified DFRC Method. *Journal of Agricultural and Food Chemistry* **2002,** *50*, 129-135.

61. Whiting, P.; Goring, D. A. I. The Morphological Origin of Milled Wood Lignin. *Svensk Papperstidning-Nordisk Cellulosa* **1981,** *84*, R120-R122.

62. Pew, J. C. Properties of Powered Wood and Isolation of Lignin by Cellulytic Enzymes. *Tappi* **1957,** *40*, 553-558.

63. Gellerstedt, G.; Northey, R. A. Analysis of Birch Wood Lignin by Oxidative-Degradation. *Wood Science and Technology* **1989,** *23*, 75-83.

64. Yang, J. M.; Goring, D. A. I. The Phenolic Hydroxyl Content of Lignin in Spruce Wood. *Canadian Journal of Chemistry-Revue Canadienne De Chimie* **1980,** *58*, 2411-2414.

65. Constantino, C. J. L.; Juliani, L. P.; Botaro, V. R.; Balogh, D. T.; Pereira, M. R.; Ticianelli, E. A.; Curvelo, A. A. S.; Oliveira, O. N. Langmuir-Blodgett Films from Lignins. *Thin Solid Films* **1996,** *284*, 191-194.

66. Constantino, C. J. L.; Dhanabalan, A.; Curvelo, A.; Oliveira, O. N. Preparation and Characterization of Composite LB Films of Lignin and Cadmium Stearate. *Thin Solid Films* **1998,** *327*, 47-51.

67. Constantino, C. J. L.; Dhanabalan, A.; Cotta, M. A.; Pereira-da-Silva, M. A.; Curvelo, A. A. S.; Oliveira, O. N. Atomic Force Microscopy (AFM) Investigation of Langmuir-Blodgett (LB) Films of Sugar Cane Bagasse Lignin. *Holzforschung* **2000,** *54*, 55-60.

68. Pasquini, D.; Balogh, D. T.; Antunes, P. A.; Constantino, C. J. L.; Curvelo, A. A. S.; Aroca, R. F.; Oliveira, O. N. Surface Morphology and Molecular Organization of Lignins in Langmuir-Blodgett Films. *Langmuir* **2002,** *18*, 6593-6596.

69. Pasquini, D.; Balogh, D. T.; Oliveira, O. N.; Curvelo, A. A. S. Lignin Molecular Arrangements in Langmuir and Langmuir-Blodgett Films: The Influence of Extraction Processes. *Colloids and Surfaces a-Physicochemical and Engineering Aspects* **2005,** *252*, 193-200.

70. Pillai, K. V.; Renneckar, S. Cation-Pi Interactions as a Mechanism in Technical Lignin Adsorption to Cationic Surfaces. *Biomacromolecules* **2009,** *10*, 798-804.

71. Norgren, M.; Notley, S. M.; Majtnerova, A.; Gellerstedt, G. Smooth Model Surfaces from Lignin Derivatives. I. Preparation and Characterization. *Langmuir* **2006,** *22*, 1209-1214.

72. Notley, S. M.; Norgren, M. Measurement of Interaction Forces between Lignin and Cellulose as a Function of Aqueous Electrolyte Solution Conditions. *Langmuir* **2006,** *22*, 11199-11204.

73. Norgren, M.; Gardlund, L.; Notley, S. M.; Htun, M.; Wagberg, L. Smooth Model Surfaces from Lignin Derivatives. II. Adsorption of Polyelectrolytes and PECs Monitored by QCM-D. *Langmuir* **2007,** *23*, 3737-3743.

74. Notley, S. M.; Norgren, M. Adsorption of a Strong Polyelectrolyte to Model Lignin Surfaces. *Biomacromolecules* **2008,** *9*, 2081-2086.

75. Notley, S. M.; Norgren, M. Surface Energy and Wettability of Spin-Coated Thin Films of Lignin Isolated from Wood. *Langmuir* **2010,** *26*, 5484-5490.

76. Zhang, Y. H. P.; Lynd, L. R. A Functionally Based Model for Hydrolysis of Cellulose by Fungal Cellulase. *Biotechnology and Bioengineering* **2006,** *94*, 888-898.

77. Lynd, L. R.; Weimer, P. J.; van Zyl, W. H.; Pretorius, I. S. Microbial Cellulose Utilization: Fundamentals and Biotechnology. *Microbiology and Molecular Biology Reviews* **2002,** *66*, 506-577.

78. Zhang, Y. H. P.; Lynd, L. R. Toward an Aggregated Understanding of Enzymatic Hydrolysis of Cellulose: Noncomplexed Cellulase Systems. *Biotechnology and Bioengineering* **2004,** *88*, 797-824.

79. Voutilainen, S. P.; Puranen, T.; Siika-Aho, M.; Lappalainen, A.; Alapuranen, M.; Kallio, J.; Hooman, S.; Viikri, L.; Vehmaanpera, J.; Koivula, A. Cloning, Expression, and Characterization of Novel Thermostable Family 7 Cellobiohydrolases. *Biotechnology and Bioengineering* **2008,** *101*, 515-528.

80. Sandgren, M.; Shaw, A.; Ropp, T. H.; Bott, S. W. R.; Cameron, A. D.; Stahlberg, J.; Mitchinson, C.; Jones, T. A. The X-Ray Crystal Structure of the Trichoderma Reesei Family 12 Endoglucanase 3, Cel12A, at 1.9 Angstrom Resolution. *Journal of Molecular Biology* **2001,** *308*, 295-310.

81. Kotiranta, P.; Karlsson, J.; Siika-Aho, M.; Medve, J.; Viikari, L.; Tjerneld, F.; Tenkanen, M. Adsorption and Activity of Trichoderma Reesei Cellobiohydrolase I, Endoglucanase II,

and the Corresponding Core Proteins on Steam Pretreated Willow. *Applied Biochemistry and Biotechnology* **1999,** *81*, 81-90.

82. Karlsson, J.; Siika-aho, M.; Tenkanen, M.; Tjerneld, F. Enzymatic Properties of the Low Molecular Mass Endoglucanases Cel12A (EG III) and Cel45A (EG V) of Trichoderma Reesei. *Journal of Biotechnology* **2002,** *99*, 63-78.

83. Divne, C.; Stahlberg, J.; Reinikainen, T.; Ruohonen, L.; Pettersson, G.; Knowles, J. K. C.; Teeri, T. T.; Jones, T. A. The 3-Dimensional Crystal-Structure of the Catalytic Core of Cellobiohydrolase-I from Trichoderma-Reesei. *Science* **1994,** *265*, 524-528.

84. Divne, C.; Stahlberg, J.; Teeri, T. T.; Jones, T. A. High-Resolution Crystal Structures Reveal How a Cellulose Chain is Bound in the 50 Angstrom Long Tunnel of Cellobiohydrolase I from Trichoderma Reesei. *Journal of Molecular Biology* **1998,** *275*, 309-325.

85. Stahlberg, J.; Divne, C.; Koivula, A.; Piens, K.; Claeyssens, M.; Teeri, T. T.; Jones, T. A. Activity Studies and Crystal Structures of Catalytically Deficient Mutants of Cellobiohydrolase I from Trichoderma Reesei. *Journal of Molecular Biology* **1996,** *264*, 337-349.

86. von Ossowski, I.; Stahlberg, J.; Koivula, A.; Piens, K.; Becker, D.; Boer, H.; Harle, R.; Harris, M.; Divne, C.; Mahdi, S.; Zhao, Y. X.; Driguez, H.; Claeyssens, M.; Sinnott, M. L.; Teeri, T. T. Engineering the Exo-Loop of Trichoderma Reesei Cellobiohydrolase, Ce17A. A Comparison with Phanerochaete Chrysosporium Cel7d. *Journal of Molecular Biology* **2003,** *333*, 817-829.

87. Kleywegt, G. J.; Zou, J. Y.; Divne, C.; Davies, G. J.; Sinning, I.; Stahlberg, J.; Reinikainen, T.; Srisodsuk, M.; Teeri, T. T.; Jones, T. A. The Crystal Structure of the Catalytic Core Domain of Endoglucanase I from Trichoderma Reesei at 3.6 Angstrom Resolution, and a Comparison with Related Enzymes. *Journal of Molecular Biology* **1997,** *272*, 383-397.

88. Kraulis, P. J.; Clore, G. M.; Nilges, M.; Jones, T. A.; Pettersson, G.; Knowles, J.; Gronenborn, A. M. Determination of the 3-Dimensional Solution Structure of the C-Terminal Domain of Cellobiohydrolase-I from Trichoderma-Reesei - a Study Using Nuclear Magnetic-Resonance and Hybrid Distance Geometry Dynamical Simulated Annealing. *Biochemistry* **1989,** *28*, 7241-7257.

89. Stahlberg, J.; Johansson, G.; Pettersson, G. A New Model for Enzymatic-Hydrolysis of Cellulose Based on the 2-Domain Structure of Cellobiohydrolase-I. *Nature Biotechnology* **1991,** *9*, 286-290.

90. Linder, M.; Mattinen, M. L.; Kontteli, M.; Lindeberg, G.; Stahlberg, J.; Drakenberg, T.; Reinikainen, T.; Pettersson, G.; Annila, A. Identification of Functionally Important Amino-Acids in the Cellulose-Binding Domain of Trichoderma-Reesei Cellobiohydrolase-I. *Protein Science* **1995,** *4*, 1056-1064.

91. Linder, M.; Teeri, T. T. The Roles and Function of Cellulose-Binding Domains. *Journal of Biotechnology* **1997,** *57*, 15-28.

92. Linder, M.; Lindeberg, G.; Reinikainen, T.; Teeri, T. T.; Pettersson, G. The Difference in Affinity between 2 Fungal Cellulose-Binding Domains is Dominated by a Single Amino-Acid Substitution. *Febs Letters* **1995,** *372*, 96-98.

93. Mattinen, M. L.; Kontteli, M.; Kerovuo, J.; Linder, M.; Annila, A.; Lindeberg, G.; Reinikainen, T.; Drakenberg, T. Three-Dimensional Structures of Three Engineered Cellulose-Binding Domains of Cellobiohydrolase I from Trichoderma Reesei. *Protein Science* **1997,** *6*, 294-303.

94. Lehtio, J.; Sugiyama, J.; Gustavsson, M.; Fransson, L.; Linder, M.; Teeri, T. T. The Binding Specificity and Affinity Determinants of Family 1 and Family 3 Cellulose Binding Modules. *Proceedings of the National Academy of Sciences of the United States of America* **2003,** *100*, 484-489.

95. Myers, D. In: Surfactant Science and Technology; John Wiley & Sons, Inc: Hoboken, New Jersey, 2006.

96. Evans, D. F.; Wennerstrom, H. In: The Collodial Domain: Where Physics, Chemistry, Biology, and Technology Meet; 2nd ed.; Wiley-VCH: New York, 1999.

97. Kaar, W. E.; Holtzapple, M. T. Benefits from Tween During Enzymic Hydrolysis of Corn Stover. *Biotechnology and Bioengineering* **1998,** *59*, 419-427.

98. Kristensen, J. B.; Borjesson, J.; Bruun, M. H.; Tjerneld, F.; Jorgensen, H. Use of Surface Active Additives in Enzymatic Hydrolysis of Wheat Straw Lignocellulose. *Enzyme and Microbial Technology* **2007,** *40*, 888-895.

99. Alkasrawi, M.; Eriksson, T.; Borjesson, J.; Wingren, A.; Galbe, M.; Tjerneld, F.; Zacchi, G. The Effect of Tween-20 on Simultaneous Saccharification and Fermentation of Softwood to Ethanol. *Enzyme and Microbial Technology* **2003,** *33*, 71-78.

100. Eriksson, T.; Borjesson, J.; Tjerneld, F. Mechanism of Surfactant Effect in Enzymatic Hydrolysis of Lignocellulose. *Enzyme and Microbial Technology* **2002,** *31*, 353-364.

101. Yang, B.; Wyman, C. E. Bsa Treatment to Enhance Enzymatic Hydrolysis of Cellulose in Lignin Containing Substrates. *Biotechnology and Bioengineering* **2006,** *94*, 611-617.

102. Castanon, M.; Wilke, C. R. Effects of the Surfactant Tween-80 on Enzymatic-Hydrolysis of Newspaper. *Biotechnology and Bioengineering* **1981,** *23*, 1365-1372.

103. Kaya, F.; Heitmann, J. A.; Joyce, T. W. Influence of Surfactants on the Enzymatic-Hydrolysis of Xylan and Cellulose. *Tappi Journal* **1995,** *78*, 150-157.

104. Shinagawa, S.; Sato, M.; Kameyama, K.; Takagi, T. Effect of Salt Concentration on the Structure of Protein-Sodium Dodecyl-Sulfate Complexes Revealed by Small-Angle X-Ray-Scattering. *Langmuir* **1994,** *10*, 1690-1694.

105. Turro, N. J.; Lei, X. G.; Ananthapadmanabhan, K. P.; Aronson, M. Spectroscopic Probe Analysis of Protein-Surfactant Interactions - the BSA/SDS System. *Langmuir* **1995,** *11*, 2525-2533.

106. Chakraborty, T.; Chakraborty, I.; Moulik, S. P.; Ghosh, S. Physicochemical and Conformational Studies on BSA-Surfactant Interaction in Aqueous Medium. *Langmuir* **2009,** *25*, 3062-3074.

107. Gelamo, E. L.; Itri, R.; Alonso, A.; da Silva, J. V.; Tabak, M. Small-Angle X-Ray Scattering and Electron Paramagnetic Resonance Study of the Interaction of Bovine Serum Albumin with Ionic Surfactants. *Journal of Colloid and Interface Science* **2004,** *277*, 471-482.

108. Ghosh, S. Conformational Study of Papain in the Presence of Sodium Dodecyl Sulfate in Aqueous Medium. *Colloids and Surfaces B-Biointerfaces* **2005,** *41*, 209-216.

109. Ghosh, S. Physicochemical and Conformational Studies of Papain/Sodium Dodecyl Sulfate System in Aqueous Medium. *Colloids and Surfaces A-Physicochemical and Engineering Aspects* **2005,** *264*, 6-16.

110. Stenstam, A.; Topgaard, D.; Wennerstrom, H. Aggregation in a Protein-Surfactant System. The Interplay between Hydrophobic and Electrostatic Interactions. *Journal of Physical Chemistry B* **2003,** *107*, 7987-7992.

111. Ciurleo, A.; Cinelli, S.; Guidi, M.; Bonincontro, A.; Onori, G.; La Mesa, C. Some Properties of Lysozyme-Lithium Perfluorononanoate Complexes. *Biomacromolecules* **2007,** *8*, 399-405.

112. Gonzalez-Perez, A.; Ruso, J. M.; Prieto, G.; Sarmiento, F. Physicochemical Study of Ovalbumin in the Presence of Sodium Dodecyl Sulphate in Aqueous Media. *Colloid and Polymer Science* **2004,** *282*, 351-356.

113. Gharibi, H.; Javadian, S.; Hashemianzadeh, M. Investigation of Interaction of Cationic Surfactant with HSA in the Presence of Alcohols Using PFG-NMR and Potentiometric Technique. *Colloids and Surfaces A-Physicochemical and Engineering Aspects* **2004,** *232*, 77-86.

114. Chatterjee, A.; Moulik, S. P.; Majhi, R.; Sanyal, S. K. Studies on Surfactant-Biopolymer Interaction. I. Microcalorimetric Investigation on the Interaction of Cetyltrimethylammonium Bromide (CTAB) and Sodium Dodecylsulfate (SDA) with Gelatin (Gn), Lysozyme (Lz) and Deoxyribonucleic Acid (DNA). *Biophysical Chemistry* **2002,** *98*, 313-327.

115. Mehta, S. K.; Bhawna; Bhasin, K. K.; Kumar, A. An Insight into the Micellization of Dodecyldimethylethylammonium Bromide (DDAB) in the Presence of Bovine Serum Albumin (BSA). *Journal of Colloid and Interface Science* **2008,** *323*, 426-434.

116. Wang, W.; Wang, Y. J.; Wang, D. Q. Dual Effects of Tween 80 on Protein Stability. *International Journal of Pharmaceutics* **2008,** *347*, 31-38.

117. Lu, R. C.; Cao, A. N.; Lai, L. H.; Xiao, J. X. Effect of Anionic Surfactant Molecular Structure on Bovine Serum Albumin (BSA) Fluorescence. *Colloids and Surfaces A-Physicochemical and Engineering Aspects* **2006,** *278*, 67-73.

118. Li, Y. J.; Wang, X. Y.; Wang, Y. L. Comparative Studies on Interactions of Bovine Serum Albumin with Cationic Gemini and Single-Chain Surfactants. *Journal of Physical Chemistry B* **2006,** *110*, 8499-8505.

119. Joshi, O.; McGuire, J. Adsorption Behavior of Lysozyme and Tween 80 at Hydrophilic and Hydrophobic Silica-Water Interfaces. *Applied Biochemistry and Biotechnology* **2009,** *152*, 235-248.

120. Goddard, E. D.; Ananthapadmanabhan, K. Applications of Polymer-Surfactant Systems. In: Surfactant Science Series,; Marcel Dekker: 1998; Vol. 77.

121. Goddard, E.; Ananthapadmanabhan, K. Interactions of Surfactants with Polymers and Proteins. CRC Press: Boca Raton, FL, 1993.

122. Taylor, D. J. F.; Thomas, R. K.; Penfold, J. Polymer/Surfactant Interactions at the Air/Water Interface. *Advances in Colloid and Interface Science* **2007,** *132*, 69-110.

123. Jones, M. The Interaction of Sodium Dodecyl Sulfate with Polyethylene Oxide. *Journal of Colloid and Interface Science* **1967,** *23*, 36-42.

124. Goddard, E. D. Polymer Surfactant Interaction .1. Uncharged Water-Soluble Polymers and Charged Surfactants. *Colloids and Surfaces* **1986,** *19*, 255-300.

125. Cooke, D. J.; Dong, C. C.; Lu, J. R.; Thomas, R. K.; Simister, E. A.; Penfold, J. Interaction between Poly(Ethylene Oxide) and Sodium Dodecyl Sulfate Studied by Neutron Reflection. *Journal of Physical Chemistry B* **1998,** *102*, 4912-4917.

126. Brady, A. P. Surface Tensions of Aqueous Solutions of Two Foam-Fractionated Detergents. *Journal of Physical Chemistry* **1949,** *53*, 56-67.

127. Vogel, A. A Textbook of Quantitative Inorganic Analysis: Including Elementary Instrumental Analysis. Addison Wesley Longman Limited: London, 1978; pp. 519-528.

128. Hertz, H. R. Ueber Einen Einfluss Des Ultravioletten Lichtes Auf Die Electrische Entladung. *Annalen der Physik und Chemie* **1887,** *31*, 983-1000.

129. Ratner, B.; Castner, D. Electron Spectroscopy for Chemical Analysis. In: Surface Analysis-the Principal Techniques; Vickerman, J., Ed.; John Wiley & Sons: New York, 1997; Chapter 3, pp 43-98.

130. Einstein, A. *Ann. Phys* **1905,** *17*.

131. Guinebretiere, R. X-Ray Diffraction by Polycrystalline Materials. ISTE Ltd: Newport Beach, 2007; pp. 2.

132. Cullity, B. Elements of X-Ray Diffraction. 2nd ed.; Addison-Wesley Publishing Company, Inc.: 1978.

133. Nuffield, E. X-Ray Diffraction Methods. John Wiley & Sons, Inc.: New York, 1966.

134. Http://Xray0.Princeton.Edu/~Phil/Facility/Guides/Xraydatacollection.Html.

135. Suryanarayana, C.; M., G. N. X-Ray Diffraction: A Practical Approach. Plenum Press: New York, 1998.

136. Scherrer, P. Estimation of the Size and Internal Structure of Colloidal Particles by Means of Röntgen Rays. *Nachrichten von der Gesellschaft der Wissenschaften zu Göttingen* **1918**, 96-100.

137. Smilgies, D. M. Scherrer Grain-Size Analysis Adapted to Grazing-Incidence Scattering with Area Detectors. *Journal of Applied Crystallography* **2009,** *42*, 1030-1034.

138. Binnig, G.; Quate, C. F.; Gerber, C. Atomic Force Microscope. *Physical Review Letters* **1986,** *56*, 930-933.

139. Binning, G.; Rohrer, H.; Gerber, C.; Weibel, E. Surface Studies by Scanning Tunneling Microscopy. *Physical Review Letters* **1982,** *49*, 57-61.

140. Jalili, N.; Laxminarayana, K. A Review of Atomic Force Microscopy Imaging Systems: Application to Molecular Metrology and Biological Sciences. *Mechatronics* **2004,** *14*, 907-945.

141. Giessibl, F. J. Advances in Atomic Force Microscopy. *Reviews of Modern Physics* **2003,** *75*, 949-983.

142. Sebastian, A.; Gannepalli, A.; Salapaka, M. V. A Review of the Systems Approach to the Analysis of Dynamic-Mode Atomic Force Microscopy. *IEEE Transactions on Control Systems Technology* **2007,** *15*, 952-959.

143. Zavala, G. Atomic Force Microscopy, a Tool for Characterization, Synthesis and Chemical Processes. *Colloid and Polymer Science* **2008,** *286*, 85-95.

144. Eaton, P.; West, P. Atomic Force Microscope. Oxford University Press: Oxford, 2010; pp. 8-14.

145. MFP-3D Manual. In Version 04-08 ed.; Asylum Research: 2008; pp 61-68.

146. Magonov, S. N.; Reneker, D. H. Characterization of Polymer Surfaces with Atomic Force Microscopy. *Annual Review of Materials Science* **1997,** *27*, 175-222.

147. Jandt, K. D. Atomic Force Microscopy of Biomaterials Surfaces and Interfaces. *Surface Science* **2001,** *491*, 303-332.

148. Butt, H.-J.; Graf, K.; Kappl, M. Physics and Chemistry of Interfaces. Wiley-VCH GmbH & Co. KGaA: Darmstadt, Germany, 2003.

149. Dynarowicz-Latka, P.; Dhanabalan, A.; Oliveira, O. N. Modern Physicochemical Research on Langmuir Monolayers. *Advances in Colloid and Interface Science* **2001**.

150. Turro, N. J.; Gratzel, M.; Braun, A. M. Photophysical and Photochemical Processes in Micellar Systems. *Angewandte Chemie-International Edition in English* **1980,** *19*, 675-696.

151. Somasundaran, P.; Huang, L.; Fan, A. Fluorescence and Esr Spectroscopy. In: Modern Characterization Methods of Surfactant Systems; Binks, B. P., Ed.; Marcel Dekker, Inc: New York, 1999; pp 213-254.

152. Kalyanasundaram, K.; Thomas, J. K. Environmental Effects on Vibronic Band Intensities in Pyrene Monomer Fluorescence and Their Application in Studies of Micellar Systems. *Journal of the American Chemical Society* **1977,** *99*, 2039-2044.

153. Winnik, F. M.; Regismond, S. T. A. Fluorescence Methods in the Study of Polymer-Surfactant Systems. In: Polymer-Surfactant Systems; Marcel Dekker, Inc.: New York, 1998; pp 267-315.

154. Rodahl, M.; Hook, F.; Krozer, A.; Brzezinski, P.; Kasemo, B. Quartz-Crystal Microbalance Setup for Frequency and Q-Factor Measurements in Gaseous and Liquid Environments. *Review of Scientific Instruments* **1995,** *66*, 3924-3930.

155. Hook, F.; Rodahl, M.; Brzezinski, P.; Kasemo, B. Energy Dissipation Kinetics for Protein and Antibody-Antigen Adsorption under Shear Oscillation on a Quartz Crystal Microbalance. *Langmuir* **1998,** *14*, 729-734.

156. Rodahl, M.; Kasemo, B. On the Measurement of Thin Liquid Overlayers with the Quartz-Crystal Microbalance. *Sensors and Actuators A-Physical* **1996,** *54*, 448-456.

157. Curie, J.; Curie, P. An Oscillating Quartz Crystal Mass Detector. *Rendu* **1880**, 294-297.

158. Rodahl, M.; Hook, F.; Fredriksson, C.; Keller, C. A.; Krozer, A.; Brzezinski, P.; Voinova, M.; Kasemo, B. Simultaneous Frequency and Dissipation Factor QCM Measurements of Biomolecular Adsorption and Cell Adhesion. *Faraday Discussions* **1997,** *107*, 229-246.

159. Sauerbrey, G. Verwendung Von Schwingquarzen Zur Wägung Dünner Schichten Und Zur Mikrowägung. *Z. Phys.* **1959,** *155*, 206-222.

160. Wang, G.; Rodahl, M.; Edvardsson, M.; Svedhem, S.; Ohlsson, G.; Hook, F.; Kasemo, B. A Combined Reflectometry and Quartz Crystal Microbalance with Dissipation Setup for Surface Interaction Studies. *Review of Scientific Instruments* **2008,** *79*.

161. Hook, F.; Voros, J.; Rodahl, M.; Kurrat, R.; Boni, P.; Ramsden, J. J.; Textor, M.; Spencer, N. D.; Tengvall, P.; Gold, J.; Kasemo, B. A Comparative Study of Protein Adsorption on Titanium Oxide Surfaces Using in Situ Ellipsometry, Optical Waveguide Lightmode Spectroscopy, and Quartz Crystal Microbalance/Dissipation. *Colloids and Surfaces B-Biointerfaces* **2002,** *24*, 155-170.

162. Hook, F.; Kasemo, B.; Nylander, T.; Fant, C.; Sott, K.; Elwing, H. Variations in Coupled Water, Viscoelastic Properties, and Film Thickness of a Mefp-1 Protein Film During Adsorption and Cross-Linking: A Quartz Crystal Microbalance with Dissipation

Monitoring, Ellipsometry, and Surface Plasmon Resonance Study. *Analytical Chemistry* **2001,** *73*, 5796-5804.

163. Fredriksson, C.; Kihlman, S.; Rodahl, M.; Kasemo, B. The Piezoelectric Quartz Crystal Mass and Dissipation Sensor: A Means of Studying Cell Adhesion. *Langmuir* **1998,** *14*, 248-251.

164. Keller, C. A.; Kasemo, B. Surface Specific Kinetics of Lipid Vesicle Adsorption Measured with a Quartz Crystal Microbalance. *Biophysical Journal* **1998,** *75*, 1397-1402.

165. Voinova, M. V.; Jonson, M.; Kasemo, B. 'Missing Mass' Effect in Biosensor's QCM Applications. *Biosensors & Bioelectronics* **2002,** *17*, 835-841.

166. Dutta, A. K.; Nayak, A.; Belfort, G. Viscoelastic Properties of Adsorbed and Cross-Linked Polypeptide and Protein Layers at a Solid-Liquid Interface. *Journal of Colloid and Interface Science* **2008,** *324*, 55-60.

167. Gurdak, E.; Booth, J.; Roberts, C. J.; Rouxhet, P. G.; Dupont-Gillain, C. C. Influence of Collagen Denaturation on the Nanoscale Organization of Adsorbed Layers. *Journal of Colloid and Interface Science* **2006,** *302*, 475-484.

168. Hedin, J.; Lofroth, J. E.; Nyden, M. Adsorption Behavior and Cross-Linking of Ehec and Hm-Ehec at Hydrophilic and Hydrophobic Modified Surfaces Monitored by SPR and QCM-D. *Langmuir* **2007,** *23*, 6148-6155.

169. Irwin, E. F.; Ho, J. E.; Kane, S. R.; Healy, K. E. Analysis of Interpenetrating Polymer Networks via Quartz Crystal Microbalance with Dissipation Monitoring. *Langmuir* **2005,** *21*, 5529-5536.

170. McDonnell, J. M. Surface Plasmon Resonance: Towards an Understanding of the Mechanisms of Biological Molecular Recognition. *Current Opinion in Chemical Biology* **2001,** *5*, 572-577.

171. Cooper, M. A. Optical Biosensors in Drug Discovery. *Nature Reviews Drug Discovery* **2002,** *1*, 515-528.

172. Brockman, J. M.; Nelson, B. P.; Corn, R. M. Surface Plasmon Resonance Imaging Measurements of Ultrathin Organic Films. *Annual Review of Physical Chemistry* **2000,** *51*, 41-63.

173. Salamon, Z.; Macleod, H. A.; Tollin, G. Surface Plasmon Resonance Spectroscopy as a Tool for Investigating the Biochemical and Biophysical Properties of Membrane Protein Systems .2. Applications to Biological Systems. *Biochimica Et Biophysica Acta-Reviews on Biomembranes* **1997,** *1331*, 131-152.

174. Green, R. J.; Frazier, R. A.; Shakesheff, K. M.; Davies, M. C.; Roberts, C. J.; Tendler, S. J. B. Surface Plasmon Resonance Analysis of Dynamic Biological Interactions with Biomaterials. *Biomaterials* **2000,** *21*, 1823-1835.

175. Liedberg, B.; Johansen, K. Affinity Biosensing Based on Surface Plasmon Resonance Detection. In: Affinity Biosensors: Techniques and Protocols; Rogers, K. R., Mulchandani, A., Eds.; Humana Press: Totowa, New Jersey, 1998; Chapter 3, pp 31-53.

176. Sambles, J. R.; Bradbery, G. W.; Yang, F. Z. Optical-Excitation of Surface-Plasmons - an Introduction. *Contemporary Physics* **1991,** *32*, 173-183.

177. Earp, R. L.; Dessy, R. E. In: Commercial Biosensors: Applications To Clinical, Bioprocess, And Environmental Samples;; Ramsay, G., Ed.; John Wiley & Sons, Inc.: New York, 1998; Vol. *148*, pp 99-164.

178. van Krevelen, D. W., Properties of Polymers: Their Correlation with Chemical Structure; Their Numerical Estimation and Prediction from Additive Group Contributions. In Elsevier: Amsterdam, 1997.

179. Defeijter, J. A.; Benjamins, J.; Veer, F. A. Ellipsometry as a Tool to Study Adsorption Behavior of Synthetic and Biopolymers at Air-Water-Interface. *Biopolymers* **1978,** *17*, 1759-1772.

180. Tulpar, A.; Ducker, W. A. Surfactant Adsorption at Solid-Aqueous Interfaces Containing Fixed Charges: Experiments Revealing the Role of Surface Charge Density and Surface Charge Regulation. *Journal of Physical Chemistry B* **2004,** *108*, 1667-1676.

181. Sigal, G. B.; Mrksich, M.; Whitesides, G. M. Using Surface Plasmon Resonance Spectroscopy to Measure the Association of Detergents with Self-Assembled Monolayers of Hexadecanethiolate on Gold. *Langmuir* **1997,** *13*, 2749-2755.

CHAPTER 3

Acid-catalyzed and solvolytic desulfation of H_2SO_4-hydrolyzed cellulose nanocrystals

3.1. Abstract

Cellulose nanocrystals (CNCs) prepared by H_2SO_4 hydrolysis have sulfate groups on their surface, which have negative implications for some CNC applications. In this study, two desulfation methods were evaluated, and the properties of desulfated CNCs were compared to those of unsulfated CNCs, prepared by HCl hydrolysis. H_2SO_4-hydrolyzed CNCs from softwood sulfite pulp were subjected to either a mild acid hydrolytic desulfation or a solvolytic desulfation in dimethyl sulfoxide *via* the pyridinium salt. Removal of the sulfate groups was confirmed by conductometric titration and X-ray photoelectron spectroscopy. The effect of the desulfation procedure on the lateral crystallite dimensions was analyzed by X-ray diffraction. The extent of particle aggregation in the samples was assessed by atomic force microscopy and dynamic light scattering. The acid hydrolytic method achieved only partial desulfation and produced gradually decreasing sulfate contents upon successive repetition. The solvolytic method achieved nearly complete desulfation in a single step. The desulfated CNCs showed similar particle aggregation as the HCl-hydrolyzed CNCs, but the extent of aggregation was slightly less.

This chapter is reproduced with permission from *Langmuir* **2010,** *26(23),* 17919-17925.

3.2. Introduction

Plant cellulose has a heterogeneous morphology with a crystalline and a noncrystalline component. Additionally, a paracrystalline component has been postulated.[1] The crystalline component, comprising the bulk of the material, has a much lower hydrolytic susceptibility than the noncrystalline component. Consequently, cellulose crystallites can be isolated from plant cellulose by controlled hydrolytic degradation. Cellulose crystallites were first isolated by Nickerson and Habrle more than half a century ago by the treatment of cotton for 30 min with boiling 2.5 N sulfuric acid.[2] Soon after, Rånby discovered that crystallites obtained from sulfite pulp hydrolyzed for 16 h formed stable sols at pH values between 3 and 10.5 in the absence of electrolytes.[3,4] He attributed the stability of the sols to the presence of stabilizing low molecular weight substances, such as oxidized oligosaccharides. Rånby also observed that the crystallites had a negative charge (3–5 mequiv per 100 g cellulose), which he ascribed to a high content of carboxyl groups.[3] The hydrolysis conditions for the isolation of cellulose crystallites were later optimized by Mukherjee and Woods, who observed that an acid concentration of 950 $g \cdot L^{-1}$ (~19 N) and a hydrolysis temperature of 40 °C resulted in better separation of the individual crystallites.[5] The enhanced separation of crystallites prepared under these conditions was subsequently attributed by Marchessault *et al.* to repulsive forces between the crystallites due to ionized sulfate half-esters, formed by the reaction of sulfuric acid molecules with alcoholic hydroxyl groups.[6] The authors showed that crystallites prepared under the more aggressive conditions contained sulfur (1–2%) whereas crystallites prepared with boiling 2.5 N sulfuric acid did not (0.013%). Current methods for the isolation of cellulose crystallites, nowadays commonly termed cellulose nanocrystals (CNCs), are based on the method of Revol *et al.*,[7] which uses 65 wt % (~20 N) sulfuric acid, a temperature of 70 °C, and a hydrolysis time of 30 min.

Different methods have been used for the quantification of sulfate half-esters in H_2SO_4-hydrolyzed CNCs. Dong *et al.*[8] determined the surface charge density of their CNC sample by conductometric titration. Assuming a cylindrical morphology for the CNCs with a diameter of 7 nm and a length of 115 nm, the authors calculated a surface charge density of 0.155 $e \cdot nm^{-2}$. In a subsequent report, the authors compared the sulfur contents obtained by conductometric titration and elemental analysis.[9] Elemental analysis was found to give slightly higher sulfur contents than conductometric titration. Roman and Winter used potentiometric titration to measure the sulfate

content of H_2SO_4-hydrolyzed CNCs from bacterial cellulose.[10] The method involved mathematical conversion of the S-shaped titration curve into a V-shaped one for easier determination of the equivalence point. To date, conductometric titration is the most widely adopted method for the quantification of sulfate half-esters in H_2SO_4-hydrolyzed CNCs.[11-14]

H_2SO_4-hydrolyzed CNCs have been extensively studied for their tendency to form chiral-nematic liquid crystalline phases.[7-9,14-24] While the ionized sulfate half-esters are beneficial to the stability of aqueous CNC suspensions, they have negative implications for some CNC applications. Surface sulfate groups have been found to significantly lower the degradation temperature of CNCs, thus limiting the use of sulfated CNCs in thermoplastic nanocomposites.[10] Moreover, sulfate half-esters dominate the intermolecular interactions of sulfated CNCs, thus limiting their use in model cellulose surfaces for cellulose interaction studies.[25-28] Neutral (uncharged) CNCs can be obtained by hydrolysis of cellulose with hydrochloric acid.[11] However, their strong tendency to aggregate renders HCl-hydrolyzed CNCs unsuitable for applications requiring high degrees of dispersion or uniform particle dimensions. An alternate route to neutral CNCs is desulfation of H_2SO_4-hydrolyzed CNCs.

Desulfation methods are a valuable tool in polysaccharide structure analysis and have been applied to many sulfated polysaccharides, including chondroitin sulfates,[29-31] dermatan sulfate,[30] heparin,[30] heparan sulfate,[30] keratan polysulfate,[30] carrageenans,[31,32] sulfated fucans,[31,33] and sodium spirulan.[34] The prevalent methods are mild acid hydrolysis[29,33] and solvolytic desulfation, involving the heating of the pyridinium salt of the polysaccharide in dimethyl sulfoxide (DMSO) in the presence of methanol or water.[30-32,34] The former method has several limitations. First, the glycosidic linkages in sulfated polysaccharides are often susceptible to acid hydrolysis. Thus, the use of a strong acid in the desulfation procedure may cause depolymerization. Second, the desulfation of sulfated fucans has been shown to be stereoselective, leading to the removal of 2-sulfate esters in fucosyl units linked to or preceded by a 4-sulfated residue.[33] Thus, complete desulfation may not always be achievable by mild acid hydrolysis.

Recently, Hasani *et al.*[35] have reported a desulfation procedure for CNCs that is based on the treatment of CNCs with 2 M sodium hydroxide. Alkaline-catalyzed desulfation methods, however, have the drawback that they result in 3:6- and 2:3-anhydride structures.[36,37] We have studied two alternative methods for the desulfation of CNCs. Mild HCl hydrolysis was found to

be incomplete and therefore allow the preparation of CNCs with different sulfate contents by successive repetition. Solvolytic desulfation resulted in the complete removal of the sulfate half-esters. The properties of partially and completely desulfated H_2SO_4-hydrolyzed CNCs are compared to those of HCl-hydrolyzed CNCs.

3.3. Experimental section

3.3.1. Materials

Dissolving-grade softwood sulfite pulp (Temalfa 93A-A) was kindly provided by Tembec, Inc. Sulfuric acid (95.9 wt %, Certified ACS Plus), hydrochloric acid (37.4 wt %, Certified ACS Plus), sodium hydroxide (0.1 N, Certified), sodium chloride (Certified ACS), hydrogen peroxide (34–37%, Technical grade), ammonium hydroxide (28.9%, Certified ACS Plus), pyridine (99.5%, Chemservice), DMSO (Certified ACS), and methanol (99.8%, Acros Organics) were purchased from Fisher Scientific. Poly(vinylamine) (PVAm, Lupamin 9095) was kindly provided by BASF Chemical Co. All water used was deionized (DI) water with a resistivity of 18.2 MΩ·cm, obtained from a Millipore Direct-Q 5 Ultrapure Water Systems.

3.3.2. Preparation of H_2SO_4-hydrolyzed CNCs

H_2SO_4-hydrolyzed CNCs were prepared according to the method of Revol *et al.*,[7] with some minor modifications. Lapsheets of the sulfite pulp were cut into small pieces and milled in a Thomas Wiley Mini-Mill (Thomas Scientific) to pass a 60-mesh screen. Sulfuric acid (500 mL, 64 wt %), preheated to 45 ℃, was added to 50 g of milled pulp in a 1 L round-bottom flask. The reaction was carried out under mechanical stirring at 45 ℃ for 60 min and was terminated by dilution of the reaction mixture with 3 L cold DI water. The acid was removed from the CNC suspension by repeated centrifugation (Thermo IEC Centra-GP8R refrigerated centrifuge, Thermo Fisher Scientific Inc.) at 25 ℃ and 4900 rpm for 15 min. After the third centrifugation, the sediment was collected and transferred to Spectra/Por 4 dialysis tubing (Spectrum Lab, Inc.). The suspension was dialyzed against DI water for several days until the pH of the dialysate

stayed constant. The final suspension, having a light-blue color due to the Tyndall effect, was sonicated for 5 min at 40% amplitude (VC 505 500 W ultrasonic processor, Sonics & Materials, Inc.) for the disruption of potential CNC aggregates and filtered through a 0.45 μm poly(vinylidene fluoride) (PVDF) syringe filter (Whatman, Ltd.).

3.3.3. Preparation of HCl-hydrolyzed CNCs

HCl-hydrolyzed CNCs were prepared according to the method of Araki *et al.*,[38] with some minor modifications. Hydrochloric acid (300 mL, 4 N), preheated to 80 ℃, was added to 10 g of pulp, milled as described in the preceding section, in a 1 L round-bottom flask. The reaction was carried out under mechanical stirring at 80 ℃ for 225 min and was terminated by partial immersion of the flask in an ice bath. The acid was removed from the suspension by repeated centrifugation followed by dialysis. In contrast to the H_2SO_4-hydrolyzed CNCs, the HCl-hydrolyzed CNCs settled to the bottom of the dialysis tube. The suspension was sonicated for 20 min as described in the preceding section and then centrifuged (Optima LE-80K ultracentrifuge, Beckman Coulter, Inc.) at 25 ℃ for 15 min at 18000 rpm. The white supernatant, which in contrast to the suspension of H_2SO_4-hydrolyzed CNCs did not show the Tyndall effect, was collected and filtered through a 0.45 μm PVDF syringe filter.

3.3.4. Acid-catalyzed desulfation

The acid-catalyzed desulfation of H_2SO_4-hydrolyzed CNCs was carried out according to the method of Pomin *et al.*[33] for the mild acid hydrolysis of sulfated fucans, with several modifications. Hydrochloric acid (12.5 mL, 1 N) was added to 500 mL of a 1 wt % suspension of H_2SO_4-hydrolyzed CNCs, preheated to 80 ℃, in a 1 L round-bottom flask, so that the final acid concentration was ~0.025 N. The reaction was carried out under mechanical stirring at 80 ℃ for 2.5 h and was terminated by partial immersion of the flask in an ice bath. The acid was removed from the suspension by dialysis against DI water as described above. An aliquot was filtered through a 0.45 μm PVDF syringe filter and set aside for particle characterization. The remaining suspension was concentrated under vacuum to 1 wt % with a rotary evaporator at a water bath

temperature of 40 ℃ and subjected to a second desulfation step according to the above procedure. The process was repeated two more times with aliquot removal at each step. The suspension remaining after the fourth desulfation step was subjected to three more desulfations without aliquot removal. The final suspension, which had undergone seven desulfation steps, was filtered through a 0.45 μm PVDF syringe filter and analyzed together with the aliquots from desulfation steps 1–4.

3.3.5. Solvolytic desulfation

The solvolytic desulfation of H_2SO_4-hydrolyzed CNCs was carried out according to the method of Nagasawa *et al.*[30] with the reaction conditions used by Lee *et al.*[34] For conversion of the sulfate half-esters into pyridinium salts, 200 mL of an aqueous suspension of H_2SO_4-hydrolyzed CNCs (1.14 wt %) was neutralized with pyridine (0.12 mL) and lyophilized (Freezone 4.5L freeze-dry system, Labconco Corp.). A 1 g portion of the freeze-dried product was dispersed in 90 mL of DMSO and sonicated for 5 min at 40% amplitude. Then, 10 mL of methanol was added, and the suspension was heated for 2 h under mechanical stirring at 80 ℃ with a water bath. The reaction was terminated by partial immersion of the flask in an ice bath and dilution of the reaction mixture with 100 mL of DI water. The suspension was transferred to dialysis tubing and dialyzed against DI water for 2 weeks. The final suspension, having a concentration of less than 1 wt %, was filtered through a 0.45 μm PVDF syringe filter. The mechanism for the solvolytic desulfation of CNCs in pyridinium salt form is shown in Figure A.1 in Appendix A.

3.3.6. Conductometric titration

Titrations were done with 50 g portions of 0.5 wt % CNC suspensions, containing 1 mM sodium chloride. The solvolytically desulfated sample was titrated in the absence of electrolyte because the addition of electrolyte caused flocculation of the CNC suspension. For the titration, the CNC suspension was placed in a 100 mL three-neck round-bottom flask, and a pH electrode (Inlab 413, Mettler-Toledo International, Inc.) and conductivity electrode (Inlab 730, Mettler-

Toledo International, Inc.) were inserted through the two peripheral necks. The suspension was titrated under nitrogen with a 0.02 N sodium hydroxide solution. Both pH and conductivity values were recorded when the meter (S47 SevenMulti, Mettler-Toledo International, Inc.) showed a stable reading.

The surface charge density, σ, in mequiv·g^{-1} was calculated from the titration results as

$$\sigma = \frac{c_{\mathrm{NaOH}} \cdot V_{\mathrm{NaOH}}}{c_{\mathrm{CNC}} \cdot \alpha_{\mathrm{CNC}}} \qquad [3.1]$$

where c_{NaOH} is the concentration of the titrant, V_{NaOH} is the titrant volume at the equivalence point, c_{CNC} is the concentration of the CNC suspension, and α_{CNC} is the amount of CNC suspension titrated. The surface charge density in e·nm^{-2} was calculated as

$$\sigma = -e \cdot \frac{c_{\mathrm{NaOH}} \cdot V_{\mathrm{NaOH}} \cdot N_{\mathrm{A}}}{A_{\mathrm{total}}} \qquad [3.2]$$

where e is the elementary charge, N_{A} is Avogadro's constant, and A_{total} is the total surface area of the CNCs, calculated as

$$A_{\mathrm{total}} = \frac{c_{\mathrm{CNC}} \cdot \alpha_{\mathrm{CNC}}}{\rho \cdot V_{\mathrm{particle}}} \cdot A_{\mathrm{particle}} \qquad [3.3]$$

where ρ is the density of crystalline cellulose (1.6 g·cm^{-3}),[39] V_{particle} is the average particle volume, and A_{particle} is the average particle surface area. For simplicity, the CNCs were assumed to be cylindrical, and all calculations were based on the average height and length of the H_2SO_4-hydrolyzed CNC sample, which were 4.8 ± 1.4 and 154 ± 84 nm, respectively, determined as described below.

3.3.7. X-ray photoelectron spectroscopy (XPS)

Samples for analysis by XPS were prepared by deposition of thin CNC films onto 1 cm × 1 cm silicon wafers. Before use, the silicon wafers were immersed for 1 h at 70 ℃ in a mixture of

aqueous ammonia, hydrogen peroxide, and DI water at a volume ratio of 1:1:5 and then for 1 h at ambient temperature in a mixture of sulfuric acid and hydrogen peroxide at a volume ratio of 7:3 for cleaning. The cleaned wafers were dried in a stream of nitrogen. CNC suspensions of 1 wt % concentration were spin-coated (WS-400B-6NPP-Lite, Laurell Technologies Corp.) onto the cleaned wafers at 4000 rpm for 1 min. After their retrieval from the spin-coater, the samples were dried in a vacuum oven at 65 ℃ overnight. Spectra were recorded with a PHI Quantera SXM-03 scanning photoelectron spectrometer microprobe (Physical Electronics, Inc.) with monochromatic Al Kα radiation (98.3 W) at a takeoff angle of 45 ° and a spot size of 100 μm. Elements were identified from survey spectra collected with an analyzer electron pass energy of 280 eV. High-resolution spectra were collected with an analyzer electron pass energy of 26 eV. Atomic concentrations were determined with CasaXPS software (Casa Software, Ltd.). Charge correction was carried out according to the method of Dorris and Gray.[40,41]

3.3.8. X-ray diffraction (XRD)

Smooth CNC films were prepared by evaporation of 10 mL aliquots of 1 wt % CNC suspensions in aluminum weighing dishes in a convection oven at 50 ℃ for several hours. Films produced at higher temperatures and shorter drying times were too brittle for handling. XRD analysis of the films was performed with a Bruker D8 Discover diffractometer (Bruker AXS, Inc.). Diffractograms were recorded during 15 min over an angular range of 10 °–50 ° at a step size of 0.01° with Cu Kα radiation and an anode voltage and current of 40 kV and 30 mA, respectively.

The crystallite dimensions in the films were calculated with the Scherrer equation[42]

$$D_{hkl} = \frac{K \cdot \lambda}{B_{hkl} \cdot \cos\theta} \qquad [3.4]$$

where D_{hkl} is the crystallite dimension in the direction normal to the *hkl* family of lattice planes, K is the Scherrer constant (1.00 for equatorial reflections of needlelike crystallites),[43] λ is the radiation wavelength (1.54 Å), B_{hkl} is the full width at half-maximum in radians of the reflection

of that family of lattice planes, and θ is the corresponding Bragg angle. B_{hkl} was determined from Voigt profile fits of the diffraction peaks calculated with PeakFit (v4.12, Systat Software, Inc.).

3.3.9. Atomic force microscopy (AFM)

AFM imaging was done with an Asylum Research MFP-3D-BIO atomic force microscope. For AFM sample preparation, silicon wafers, cleaned as described in the XPS section, were immersed for 2 min in a 0.01 $g \cdot L^{-1}$ solution of PVAm in DI water. Coating of the silicon wafers with PVAm creates a positively charged surface, which results in better separation of the negatively charged CNCs on the substrate after deposition.[44] CNCs were deposited onto the PVAm-coated wafers by spin-coating of 0.005 wt % CNC suspensions at 3000 rpm for 1 min. After their retrieval from the spin-coater, the samples were dried in a vacuum oven at 65 ℃ overnight. Samples were scanned in air at ambient relative humidity and temperature in tapping mode with OMCL-AC160TS standard silicon probes (Olympus Corp.). Reported average particle heights and lengths were determined from AFM height images according to a previously published procedure.[45] Values are reported in the format mean ± standard deviation. The reported average lengths have not been corrected for tip sample broadening.

3.3.10. Dynamic light scattering (DLS)

DLS experiments were performed with a Zetasizer Nano-ZS (Malvern Instruments, Ltd.) at a detection angle of 173 °. Reported values are mean intensity diameters obtained with the General Purpose algorithm of the Zetasizer Nano software. Measurements were done at 25 ℃ with 0.025 wt % CNC suspensions in the absence of added electrolyte. Immediately before the measurements, the CNC suspensions were sonicated for 10 min at 70 W in a Cole-Parmer 8890 ultrasonic cleaner for the disruption of potential aggregates. Measurements were carried out in quintuplicate for error analysis.

3.4. Results and discussion

The eight CNC samples investigated and their designations are listed in Table 3.1. The samples were characterized in terms of surface charge density, chemical composition, crystallite dimensions, and extent of particle aggregation.

Table 3.1. CNC samples and their designations

Sample	Designation
H_2SO_4-hydrolyzed CNCs	SH
HCl-hydrolyzed CNCs	HH
HCl-desulfated CNCs	
first step	HD1
second step	HD2
third step	HD3
fourth step	HD4
seventh step	HD7
solvolytically desulfated CNCs	SD

3.4.1. Surface charge density

The surface charge density of the CNC samples was determined by conductometric titration with sodium hydroxide. The titration curves for the samples SH, HH, HD7, and SD are shown in Figure 3.1. The initial conductivity of the CNC samples is mainly due to the added electrolyte and the counterions of the sulfate groups, if present. The sulfate groups themselves, being attached to the CNC surface, likely have a low ion mobility and therefore contribute little to the conductivity of the CNC suspension. At the beginning of the titration, the counterions of the sulfate groups are protons. Upon titration with sodium hydroxide, the protons are exchanged with sodium ions, which have a lower molar conductivity. As a result, the conductivity of the suspension decreases. When all sulfate protons have been replaced with sodium ions, the conductivity increases upon further addition of sodium hydroxide because of the increase in the sodium and hydroxyl ion concentrations of the suspension. Thus, the equivalence point is

indicated by a minimum in the titration curve and is usually determined from the intersection of two separate linear fits of the branches of the titration curve.

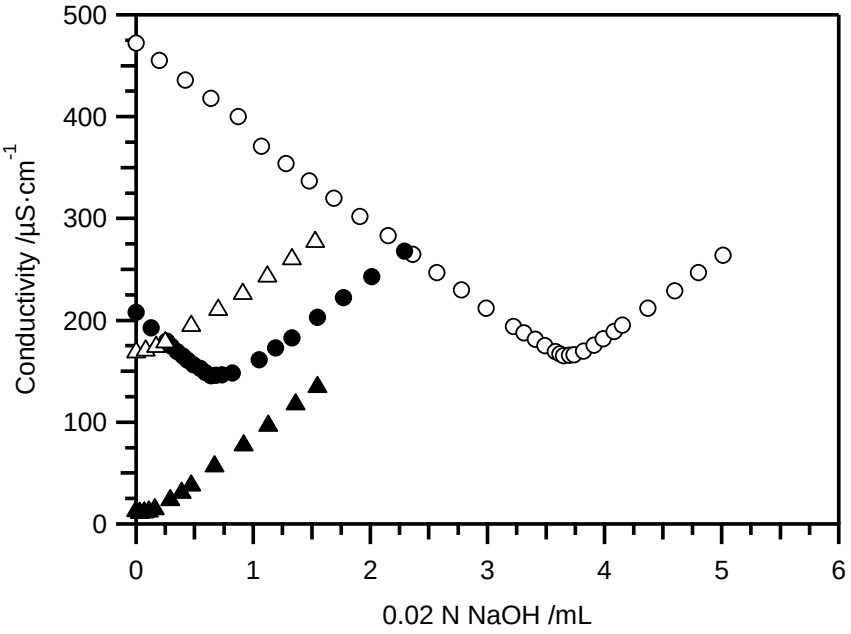

Figure 3.1. Conductometric titration curves for the CNC samples SH (○), HH (△), HD7 (●), and SD (▲).

An initial decrease in conductivity was observed in the titration curves for SH and HD7 (Figure 3.1), indicating the presence of CNC sulfate groups in these samples. The shift of the titration equivalence point for HD7 to a smaller titrant volume with respect to that for SH signified that HD7 had fewer sulfate groups than SH. The titration curve for HH showed no initial decrease in conductivity. Instead, an immediate increase in conductivity was observed upon addition of sodium hydroxide, indicating the complete absence of CNC sulfate groups in this sample. The titration curve for SD also showed no initial decrease in conductivity, but the increase in conductivity upon sodium hydroxide addition was slightly delayed compared to HH, which signified that the sample contained a small amount of CNC sulfate groups. The lower conductivity of SD with respect to HH was due to the absence of added electrolyte in this sample.

The surface charge densities obtained for the different CNC samples are listed in Table 3.2.

Table 3.2. Surface charge densities of the CNC samples

	Surface charge density (σ)	
Sample	mequiv·g^{-1}	e·nm^{-2}
SH	0.293	–0.333
HH	0.000	0.000
HD1	0.191	–0.217
HD2	0.153	–0.175
HD3	0.103	–0.117
HD4	0.058	–0.066
HD7	0.055	–0.062
SD	0.007	–0.008

The sample SH had a surface charge density of 0.293 mequiv·g^{-1}or –0.333 e·nm^{-2}. The surface charge density of HD1, *i.e.*, after one round of HCl-catalyzed desulfation, was lower by about 1/3 than that of SH but was not zero. Thus, the HCl-catalyzed desulfation procedure removed some but not all of the sulfate groups. The inability of the desulfation procedure to remove all of the sulfate groups is probably due to the reversibility of the acid-catalyzed desulfation reaction. We made several attempts to remove the generated SO_3 from the reaction medium, including bubbling nitrogen through the reaction medium, using *p*-toluenesulfonic acid (a nonvolatile acid) instead of hydrochloric acid to prevent removal of the acid by the carrier gas for the SO_3, and carrying out the reaction in the presence of barium chloride for precipitation of SO_3 as barium sulfate. However, none of these attempts were successful in driving the equilibrium of the reaction toward complete desulfation. Each repetition of the desulfation procedure, up to step 4, reduced the surface charge density by on average 1/3, thus yielding CNC samples with gradually decreasing surface charge densities. Almost no difference was observed in the surface charge densities of HD4 and HD7, indicating that the HCl-catalyzed desulfation procedure ultimately reached a limit and could not remove all of the sulfate groups. The reason could possibly be a stereoselectivity of the desulfation reaction. As mentioned in the Introduction, in the desulfation process of sulfated fucans by mild acid hydrolysis, 2-sulfate esters are only

removed from fucosyl units linked to, or preceded by, a 4-sulfated residue.[33] A similar stereoselectivity in the desulfation of sulfated cellulose could potentially prevent the removal of the remaining sulfate groups in HD4. The surface charge density of SD was 0.007 mequiv·g^{-1}. Thus, contrary to the HCl-catalyzed desulfation procedure, the solvolytic desulfation procedure, in one step, nearly completely removed the sulfate groups initially present on the CNC surface.

3.4.2. Chemical composition

The effects of the choice of acid during CNC preparation and the desulfation procedures on the chemical composition of the CNCs were analyzed by XPS. Figure 3.2 shows the XPS survey spectrum of the CNC sample SH.

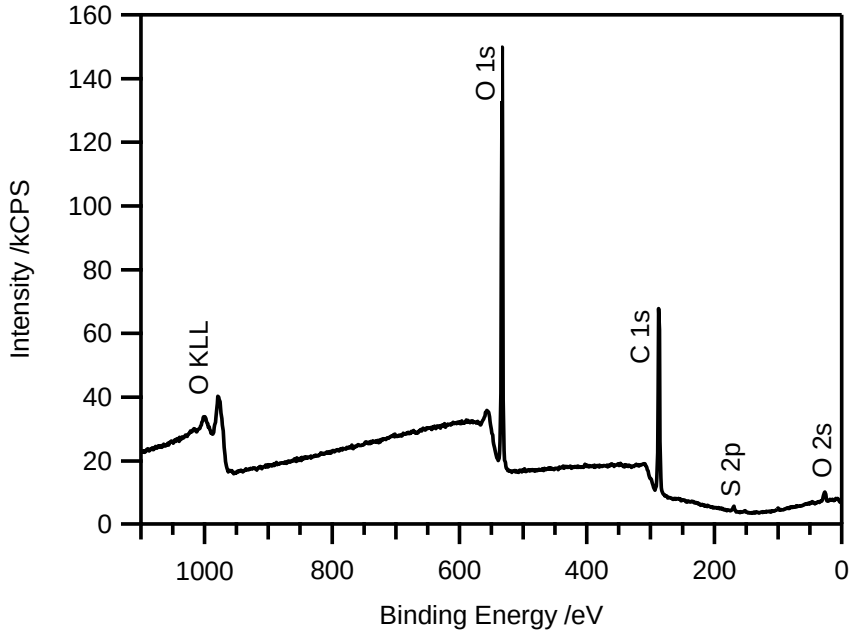

Figure 3.2. XPS survey spectrum of the CNC sample SH.

The peak at 287 eV is the C 1s peak[46] and that at 533 eV is the O 1s peak,[46] originating from the carbon and oxygen atoms of cellulose. Hydrogen atoms are not detected by XPS. The small peak at 169 eV is the S 2p peak,[46] originating from the sulfate groups in this sample. The S 2p peak region in the survey spectra of the samples SH, HD7, and SD was further analyzed in

high resolution (Figure 3.3). The S 2p peak was also present in the XPS spectrum of HD7 but was absent in the spectrum of SD.

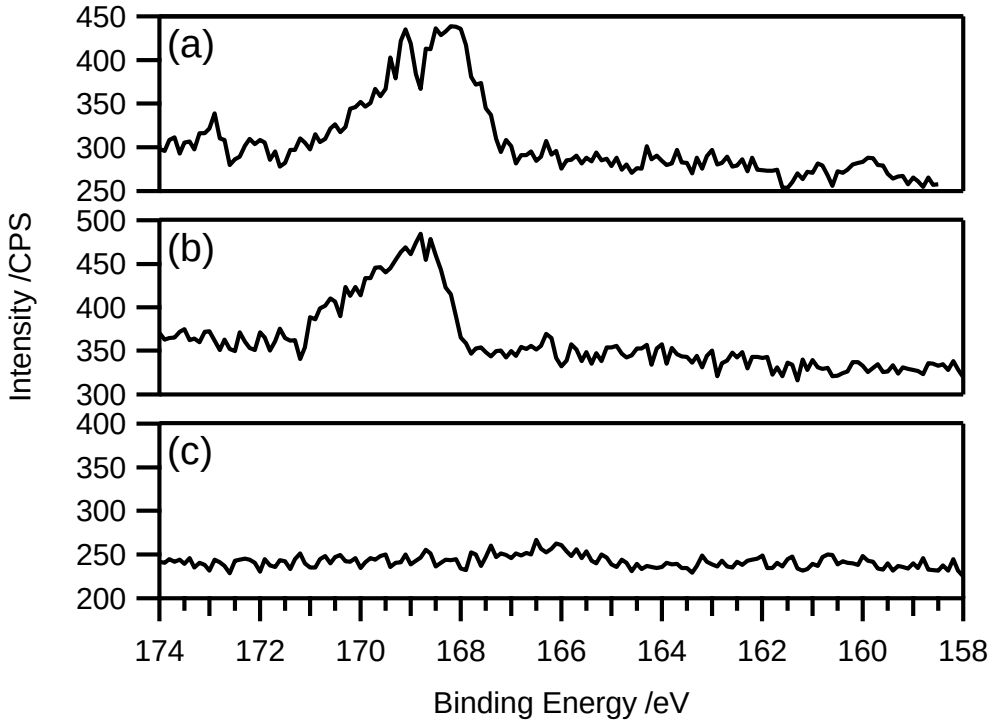

Figure 3.3. High-resolution S 2p photoelectron spectra of the CNC samples SH (a), HD7 (b), and SD (c).

The atomic concentrations in the samples SH, HH, HD7, and SD, calculated from the integrated areas under the peaks of the XPS survey spectra, are listed in Table 3.3. The C/O ratios of the samples SH (1.22) and HD7 (1.25) agreed well with the theoretical value for cellulose (1.20). The C/O ratios of the samples HH (1.32) and SD (1.38), however, were slightly higher than the theoretical value. The fact that neither nitrogen nor sulfur peaks were observed in the spectrum of SD indicated that the elevated C/O ratio of this sample was not due to residual pyridine or DMSO. The elevated C/O ratios in the samples HH and SD could indicate the presence of adventitious carbon possibly due to organic contaminants. However, the high-resolution C 1s spectra of these samples did not show elevated C1 (hydrocarbon) levels relative to that of SH (Figure A.2 and Table A.1 in Appendix A). The reason for the elevated C/O ratios

in the samples HH and SD is therefore unclear. The sulfur concentration in the HCl-desulfated CNC samples decreased from 0.57% in SH to 0.28% in HD7 in qualitative but not quantitative agreement with the conductometric titration results. Although the conductometric titration results revealed a small amount of sulfate groups in SD, sulfur was not detected in the XPS spectrum of this sample.

Table 3.3. Atomic concentrations of C, O, and S for different CNC samples

	Atomic concentration (at %)			
Sample	C	O	S	C/O ratio
SH	54.68	44.75	0.57	1.22
HH	56.82	43.18	N/A	1.32
HD7	55.42	44.30	0.28	1.25
SD	57.96	42.04	N/A	1.38
cellulose	54.50	45.50	N/A	1.20

3.4.3. Crystallite dimensions

Crystallite dimensions of the CNC samples were determined from X-ray diffractograms. The diffractograms for the samples SH, HH, HD7, and SD are shown in Figure 3.4. All samples showed three characteristic cellulose I reflections, corresponding to the $1\bar{1}0$, 110, and 200 crystallographic planes of the monoclinic cellulose I lattice, according to the indexing by Sugiyama *et al.*[47] To determine the full width at half-maximum of the reflection peaks, we deconvoluted the diffractograms using Voigt line profiles. Figure 3.5 illustrates the deconvolution procedure. In addition to the three obvious reflections, our deconvolution procedure allowed for a fourth peak, located between the 110 and 200 reflections, for a better overall fit of the diffraction profile. This peak could be attributed to the 102 and/or 012 reflections of the monoclinic cellulose I lattice, which occur at $2\theta \approx 20.4°$ and $20.6°$, respectively.[47]

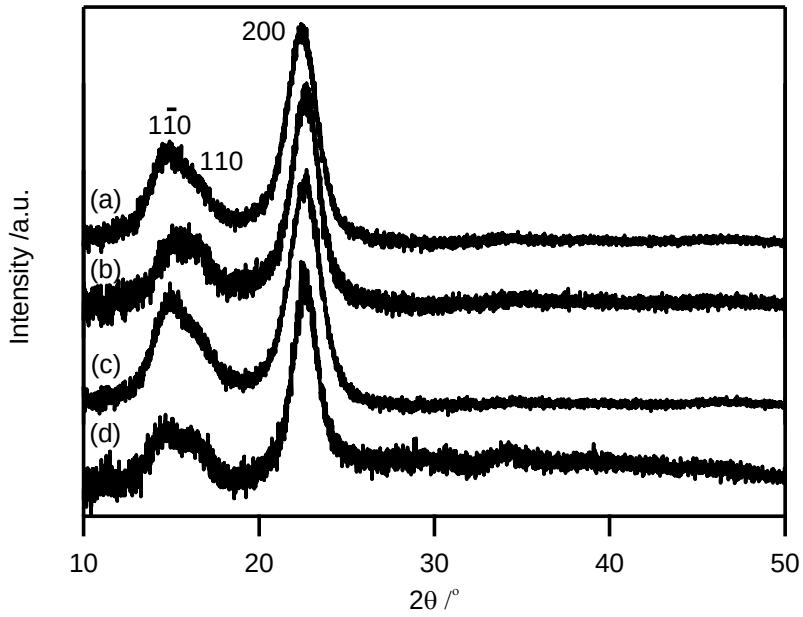

Figure 3.4. X-ray diffractograms for the CNC samples SH (a), HH (b), HD7 (c), and SD (d).

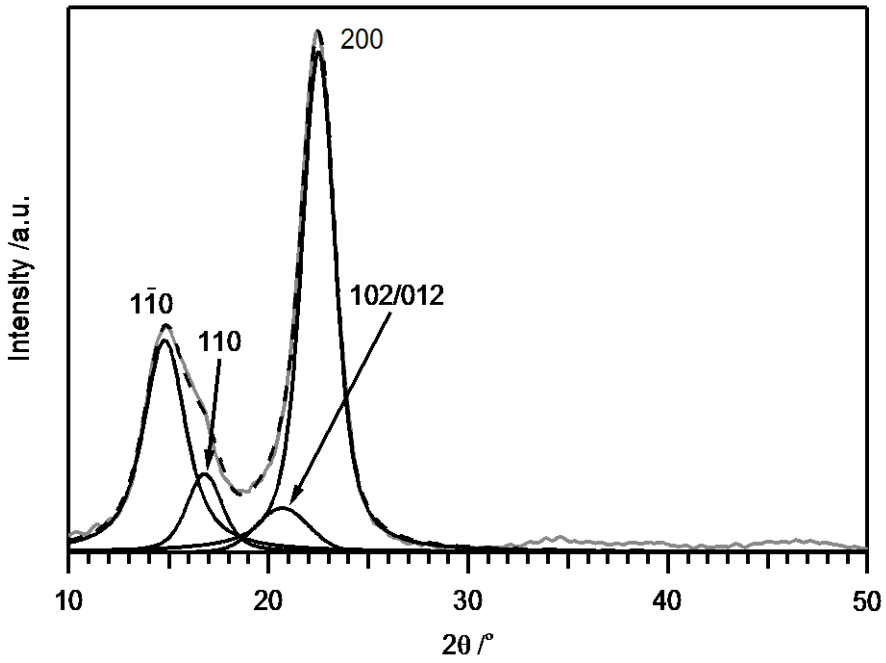

Figure 3.5. Deconvolution of the X-ray diffractogram for the CNC sample SH with Voigt line profiles.

The crystallite dimensions for the four samples, determined from the $1\bar{1}0$, 110, and 200 reflections, are listed in Table 3.4. The $1\bar{1}0$, 110, and 200 crystallographic planes are parallel to the cellulose chains and therefore to the long axis of the CNCs. Thus, the crystallite dimensions determined from the $1\bar{1}0$, 110, and 200 diffraction peaks are lateral dimensions. The fact that the samples SH and HD7 had similar crystallite dimensions suggested that the HCl-catalyzed desulfation procedure had no effect on the size of the crystallites. Hydrochloric acid produced CNCs with slightly larger crystallite dimensions than sulfuric acid, as evident from a comparison of the values for the samples SH and HH. The largest crystallite dimensions were observed for the solvolytically desulfated CNCs (sample SD). The solvolytic desulfation procedure involved sonication and heating of the CNCs in DMSO. DMSO is known to have a high swelling power with respect to cellulose.[48,49] The larger crystallite dimensions in this sample compared to SH might therefore be due to the swelling and subsequent crystallization of initially amorphous or paracrystalline cellulose regions during the solvolytic desulfation procedure.

Table 3.4. Crystallite dimensions for different CNC samples determined by deconvolution of the x-ray diffractograms with Voigt line profiles

	Crystallite dimensions (nm)		
Sample	1T0	110	200
SH	3.5	4.3	4.5
HH	4.1	4.2	5.0
HD7	3.8	3.9	4.4
SD	4.1	5.4	5.3

3.4.4. Extent of particle aggregation

The extent of particle aggregation in the samples was analyzed by AFM and DLS. Figure 3.6 shows AFM height images of the samples SH, HH, HD7, and SD.

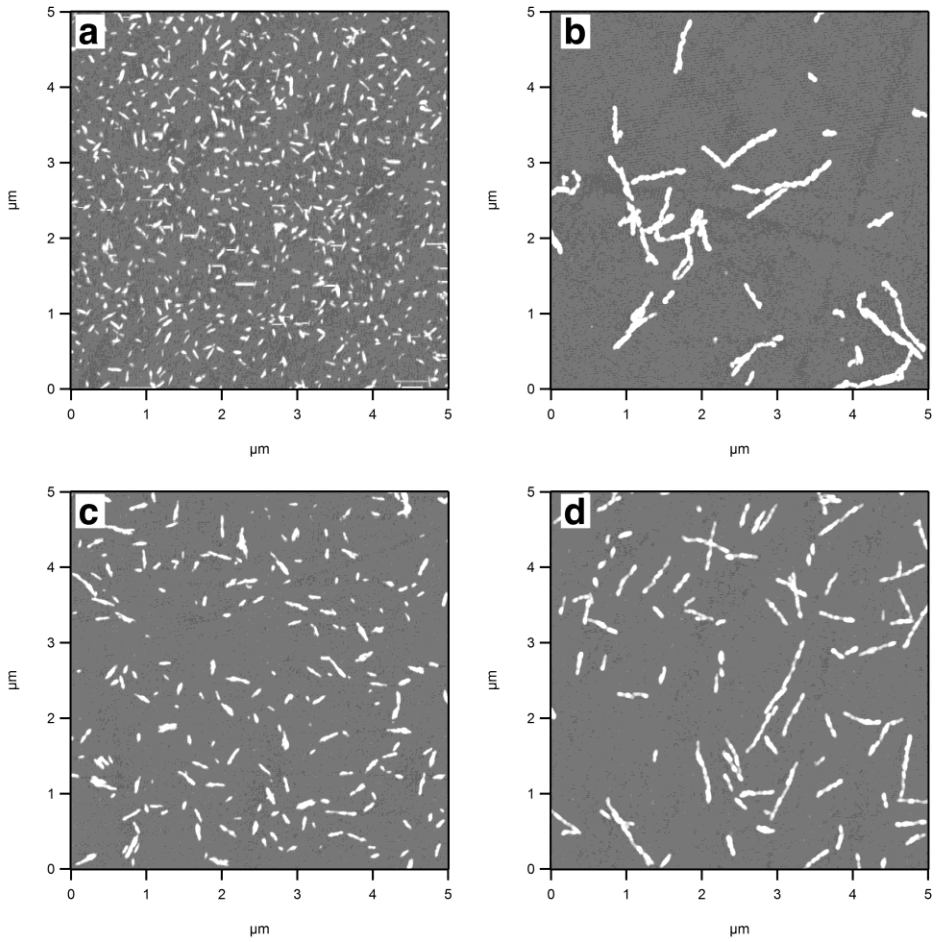

Figure 3.6. AFM height images of the CNC samples SH (a), HH (b), HD7 (c), and SD (d) (*z*-scale = 8 nm).

The highly sulfated CNCs of SH (Figure 3.6a) were well dispersed and uniformly distributed on the polycation-coated substrate. The AFM image of HD7 (Figure 3.6c) showed some degree of particle aggregation, but the aggregates were relatively small. Aggregation of the partially desulfated CNCs of HD7 was most likely a result of weaker repulsive forces between the particles and weaker attractive forces between the particles and the polycation-coated substrate compared to SH. The AFM image of SD (Figure 3.6d) showed a high degree of particle aggregation. As opposed to the partially desulfated CNCs of HD7, the fully desulfated CNCs of SD seemed to aggregate in an endwise manner. The observed aggregates were highly elongated. Lateral aggregation of the fully desulfated CNCs of SD, in addition to the curious endwise aggregation, was not evident from the AFM height data. With 4.3 ± 1.3 nm, the average height of

the particles in Figure 3.6d was smaller than that of the highly sulfated CNCs of SH (Figure 3.6a) of 4.8 ± 1.4 nm. The AFM image of HH (Figure 3.6b) showed similar elongated objects as that of SD. It is not clear from the image whether these objects were endwise aggregates of smaller particles or whether they were large fragments of the original cellulose microfibrils. The elongated objects appeared slightly wider than the aggregates of SD. The observed difference in width might, however, be due to a difference in the magnitude of tip broadening in the images.

To examine whether the observed aggregates existed in suspension or whether they formed during AFM sample preparation, we analyzed the CNC suspensions by DLS. We interpreted the DLS data in terms of equivalent spherical hydrodynamic diameters. The equivalent spherical hydrodynamic diameter of a particle is the diameter of a sphere with the same translational diffusion coefficient as the particle. For anisometric objects, such as CNCs or those seen in Figures 3.6b,d, the equivalent spherical hydrodynamic diameter does not represent the actual dimensions of the object. Nevertheless, a comparison of the equivalent spherical hydrodynamic diameters of the different samples should allow us to draw conclusions about the relative sizes or extents of aggregation of the particles in the suspensions. Alternatively, we could assume a certain mean particle diameter and calculated the mean particle length for each sample. However, because the mean particle diameter might not be the same for all samples, this approach could lead to misrepresentation of the mean particle length.

The hydrodynamic diameters obtained for the different samples are shown in Figure 3.7. A comparison of the values for SH, HD1, HD2, HD3, HD4, and HD7 revealed that the HCl-catalyzed desulfation procedure had nearly no effect on the extent of aggregation in suspension. The hydrodynamic diameter of HD7 (104 ± 2 nm) was only slightly larger than that of SH (83 ± 1 nm). Solvolytic desulfation resulted in aggregation of the CNCs in suspension, as evident from the more than 2-fold increased hydrodynamic diameter for SD (211 ± 6 nm) with respect to SH. The HCl-hydrolyzed sample (HH) showed the largest hydrodynamic diameter (329 ± 35 nm), indicating the largest particle or aggregate size in accordance with the AFM results.

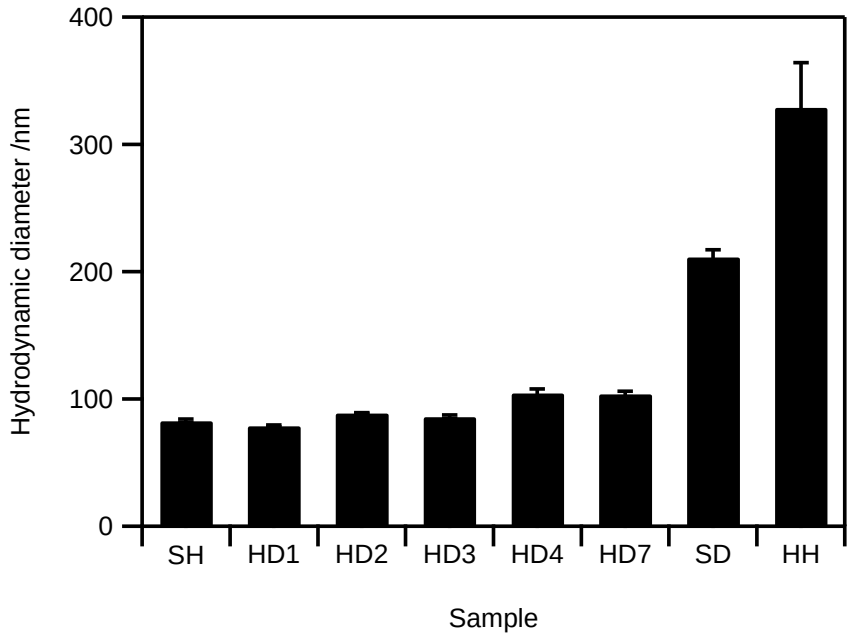

Figure 3.7. Hydrodynamic diameter for the CNC samples measured by DLS.

3.5. Conclusions

The objectives of this study were to develop a method for the desulfation of H_2SO_4-hydrolyzed CNCs and to compare the properties of the desulfated CNCs to CNCs prepared by HCl hydrolysis. In light of the above results, the following conclusions can be drawn. Complete desulfation of H_2SO_4-hydrolyzed CNCs cannot be achieved by HCl-catalyzed desulfation. The method may, however, be useful for the preparation of CNCs with different amounts of sulfate groups. Solvolytic desulfation of H_2SO_4-hydrolyzed CNCs in DMSO *via* a pyridinium salt yields CNCs with virtually no sulfate groups on the surface. HCl-catalyzed desulfation has no effect on the crystallite dimensions of the CNCs, whereas solvolytic desulfation increases the crystallite dimensions slightly. Removal of the sulfate groups of H_2SO_4-hydrolyzed CNCs leads to aggregation of the particles similar to that observed for HCl-hydrolyzed CNCs albeit slightly less extensive.

3.6. Acknowledgments

This project was supported by the National Research Initiative of the USDA Cooperative State Research, Education and Extension Service under Grant 2005-35504-16088, the National Science Foundation under Grant CHE-0724126 and DMR-0907567, the U.S. Department of Transportation through the Southeastern Sun Grant Center, and the Institute for Critical Technology and Applied Science. Parts of this work were carried out with instruments of the Nanoscale Characterization and Fabrication Laboratory, a Virginia Tech facility operated by the Institute for Critical Technology and Applied Science. The authors thank Dr. Jerry Hunter and Rick Caudill for assistance with the XPS and XRD experiments, respectively, Drs. Richey Davis and Audrey Zink-Sharp for access to the Zetasizer Nano-ZS and Bruker D8 Discover, respectively, Dr. Kevin Edgar for helpful discussions, and Dr. Fernando Navarro for help with analyzing the AFM data. Additional support from Omnova, Inc., and Tembec, Inc., is also acknowledged.

3.7. References

1. Nickerson, R. F.; Habrle, J. A. Hydrolysis and Catalytic Oxidation of Cellulosic Materials. *Industrial & Engineering Chemistry* **1945,** *37*, 1115-1118.

2. Nickerson, R. F.; Habrle, J. A. Cellulose Intercrystalline Structure. *Industrial & Engineering Chemistry* **1947,** *39*, 1507-1512.

3. Rånby, B. G. Aqueous Colloidal Solutions of Cellulose Micelles. *Acta Chemica Scandinavica* **1949,** *3*, 649-650.

4. Rånby, B. G. Fibrous Macromolecular Systems. Cellulose and Muscle. The Colloidal Properties of Cellulose Micelles. *Discussions of the Faraday Society* **1951,** *11*, 158-164.

5. Mukherjee, S. M.; Woods, H. J. X-Ray and Electron Microscope Studies of the Degradation of Cellulose by Sulphuric Acid. *Biochimica et biophysica acta* **1953,** *10*, 499-511.

6. Marchessault, R. H.; Morehead, F. F.; Koch, M. J. Hydrodynamic Properties of Neutral Suspensions of Cellulose Crystallites as Related to Size and Shape. *Journal of Colloid Science* **1961,** *16*, 327-344.

7. Revol, J. F.; Bradford, H.; Giasson, J.; Marchessault, R. H.; Gray, D. G. Helicoidal Self-Ordering of Cellulose Microfibrils in Aqueous Suspension. *International Journal of Biological Macromolecules* **1992,** *14*, 170-172.

8. Dong, X. M.; Kimura, T.; Revol, J. F.; Gray, D. G. Effects of Ionic Strength on the Isotropic-Chiral Nematic Phase Transition of Suspensions of Cellulose Crystallites. *Langmuir* **1996,** *12*, 2076-2082.

9. Dong, X. M.; Revol, J.-F.; Gray, D. G. Effect of Microcrystallite Preparation Conditions on the Formation of Colloid Crystals of Cellulose. *Cellulose* **1998,** *5*, 19-32.

10. Roman, M.; Winter, W. T. Effect of Sulfate Groups from Sulfuric Acid Hydrolysis on the Thermal Degradation Behavior of Bacterial Cellulose. *Biomacromolecules* **2004,** *5*, 1671-1677.

11. Araki, J.; Wada, M.; Kuga, S.; Okano, T. Flow Properties of Microcrystalline Cellulose Suspension Prepared by Acid Treatment of Native Cellulose. *Colloids and Surfaces, A: Physicochemical and Engineering Aspects* **1998,** *142*, 75-82.

12. Cranston, E. D.; Gray, D. G. Morphological and Optical Characterization of Polyelectrolyte Multilayers Incorporating Nanocrystalline Cellulose. *Biomacromolecules* **2006,** *7*, 2522-2530.

13. Bondeson, D.; Mathew, A.; Oksman, K. Optimization of the Isolation of Nanocrystals from Microcrystalline Cellulose by Acid Hydrolysis. *Cellulose* **2006,** *13*, 171-180.

14. Hirai, A.; Inui, O.; Horii, F.; Tsuji, M. Phase Separation Behavior in Aqueous Suspensions of Bacterial Cellulose Nanocrystals Prepared by Sulfuric Acid Treatment. *Langmuir* **2009,** *25*, 497-502.

15. Revol, J. F.; Godbout, L.; Dong, X. M.; Gray, D. G.; Chanzy, H.; Maret, G. Chiral Nematic Suspensions of Cellulose Crystallites - Phase-Separation and Magnetic-Field Orientation. *Liquid Crystals* **1994,** *16*, 127-134.

16. Dong, X. M.; Gray, D. G. Effect of Counterions on Ordered Phase Formation in Suspensions of Charged Rodlike Cellulose Crystallites. *Langmuir* **1997,** *13*, 2404-2409.

17. Dong, X. M.; Gray, D. G. Induced Circular Dichroism of Isotropic and Magnetically-Oriented Chiral Nematic Suspensions of Cellulose Crystallites. *Langmuir* **1997,** *13*, 3029-3034.

18. Revol, J. F.; Godbout, L.; Gray, D. G. Solid Self-Assembled Films of Cellulose with Chiral Nematic Order and Optically Variable Properties. *Journal of Pulp and Paper Science* **1998,** *24*, 146-149.

19. Araki, J.; Kuga, S. Effect of Trace Electrolyte on Liquid Crystal Type of Cellulose Microcrystals. *Langmuir* **2001,** *17*, 4493-4496.

20. Edgar, C. D.; Gray, D. G. Induced Circular Dichroism of Chiral Nematic Cellulose Films. *Cellulose* **2001,** *8*, 5-12.

21. Chen, W. L.; Gray, D. G. Interfacial Tension between Isotropic and Anisotropic Phases of a Suspension of Rodlike Particles. *Langmuir* **2002,** *18*, 633-637.

22. Beck-Candanedo, S.; Roman, M.; Gray, D. G. Effect of Reaction Conditions on the Properties and Behavior of Wood Cellulose Nanocrystal Suspensions. *Biomacromolecules* **2005,** *6*, 1048-1054.

23. Kimura, F.; Kimura, T.; Tamura, M.; Hirai, A.; Ikuno, M.; Horii, F. Magnetic Alignment of the Chiral Nematic Phase of a Cellulose Microfibril Suspension. *Langmuir* **2005,** *21*, 2034-2037.

24. Roman, M.; Gray, D. G. Parabolic Focal Conics in Self-Assembled Solid Films of Cellulose Nanocrystals. *Langmuir* **2005,** *21*, 5555-5561.

25. Roman, M. In: Model Cellulosic Surfaces; Roman, M., Ed.; ACS Symposium Series 1019; American Chemical Society: Washington, DC, 2009; pp 3-53.

26. Kontturi, E.; Österberg, M. In: Model Cellulosic Surfaces; Roman, M., Ed.; ACS Symposium Series 1019; American Chemical Society: Washington, DC, 2009; pp 57-74.

27. Cranston, E. D.; Gray, D. G. In: Model Cellulosic Surfaces; Roman, M., Ed.; ACS Symposium Series 1019; American Chemical Society: Washington, DC, 2009; pp 75-93.

28. Kontturi, E.; Tammelin, T.; Osterberg, M. Cellulose - Model Films and the Fundamental Approach. *Chemical Society Reviews* **2006,** *35*, 1287-1304.

29. Kantor, T. G.; Schubert, M. A Method for the Desulfation of Chondroitin Sulfate. *Journal of the American Chemical Society* **1957,** *79*, 152-3.

30. Nagasawa, K.; Inoue, Y.; Kamata, T. Solvolytic Desulfation of Glycosaminoglycuronan Sulfates with Dimethyl-Sulfoxide Containing Water and Methanol. *Carbohydrate Research* **1977,** *58*, 47-55.

31. Navarro, D. A.; Flores, M. L.; Stortz, C. A. Microwave-Assisted Desulfation of Sulfated Polysaccharides. *Carbohydrate Polymers* **2007,** *69*, 742-747.

32. Miller, I. J.; Blunt, J. W. Desulfation of Algal Galactans. *Carbohydrate Research* **1998,** *309*, 39-43.

33. Pomin, V. H.; Valente, A. P.; Pereira, M. S.; Mourao, P. A. S. Mild Acid Hydrolysis of Sulfated Fucans: A Selective 2-Desulfation Reaction and an Alternative Approach for Preparing Tailored Sulfated Oligosaccharides. *Glycobiology* **2005,** *15,* 1376-1385.

34. Lee, J. B.; Hou, X. L.; Hayashi, K.; Hayashi, T. Effect of Partial Desulfation and Oversulfation of Sodium Spirulan on the Potency of Anti-Herpetic Activities. *Carbohydrate Polymers* **2007,** *69,* 651-658.

35. Hasani, M.; Cranston, E. D.; Westman, G.; Gray, D. G. Cationic Surface Functionalization of Cellulose Nanocrystals. *Soft Matter* **2008,** *4,* 2238-2244.

36. Percival, E. G. V. Carbohydrate Sulfates. *Quarterly Review of the Chemical Society* **1949,** *3,* 369-384.

37. Viana, A. G.; Noseda, M. D.; Duarte, M. E. R.; Cerezo, A. S. Alkali Modification of Carrageenans. Part V. The Iota-Nu Hybrid Carrageenan from Eucheuma Denticulatum and Its Cyclization to Iota-Carrageenan. *Carbohydrate Polymers* **2004,** *58,* 455-460.

38. Araki, J.; Wada, M.; Kuga, S.; Okana, T. Influence of Surface Charge on Viscosity Behavior of Cellulose Microcrystal Suspension. *Journal of Wood Science* **1999,** *45,* 258-261.

39. Ganster, J.; Fink, H. P., *Polymer Handbook.* 4th ed.; Wiley & Sons: New York, 1999; pp V/135-V/157.

40. Dorris, G. M.; Gray, D. G. The Surface Analysis of Paper and Wood Fibres by ESCA (I). Application to Cellulose and Lignin. *Cellulose Chemistry and Technology* **1978,** *12,* 9-23.

41. Dorris, G. M.; Gray, D. G. The Surface Analysis of Paper and Wood Fibers by ESCA (II). Surface Composition of Mechanical Pulps. *Cellulose Chemistry and Technology* **1978,** *12,* 721-734.

42. Scherrer, P. Estimation of the Size and Internal Structure of Colloidal Particles by Means of Röntgen Rays. *Nachrichten von der Gesellschaft der Wissenschaften zu Göttingen* **1918**, 96-100.

43. Smilgies, D. M. Scherrer Grain-Size Analysis Adapted to Grazing-Incidence Scattering with Area Detectors. *Journal of Applied Crystallography* **2009,** *42*, 1030-1034.

44. Kontturi, E.; Johansson, L. S.; Kontturi, K. S.; Ahonen, P.; Thune, P. C.; Laine, J. Cellulose Nanocrystal Submonolayers by Spin Coating. *Langmuir* **2007,** *23*, 9674-9680.

45. Navarro, F. Cellulose Nanocrystals: Size Characterization and Controlled Deposition by Inkjet Printing. Virginia Polytechnic Institute and State University, Blacksburg, VA, 2010.

46. Watts, J. F.; Wolstenholme, J. An Introduction to Surface Analysis by XPS and AES. John Wiley and Sons: New York, 2003.

47. Sugiyama, J.; Vuong, R.; Chanzy, H. Electron Diffraction Study on the 2 Crystalline Phases Occurring in Native Cellulose from an Algal Cell Wall. *Macromolecules* **1991,** *24*, 4168-4175.

48. Philipp, B.; Schleicher, H.; Wagenknecht, W. The Influence of Cellulose Structure on the Swelling of Cellulose in Organic Liquids. *Journal of Polymer Science: Polymer Symposia* **1973,** *42*, 1531-1543.

49. Fidale, L. C.; Ruiz, N.; Heinze, T.; El Seoud, O. A. Cellulose Swelling by Aprotic and Protic Solvents: What are the Similarities and Differences? *Macromolecular Chemistry and Physics* **2008,** *209*, 1240-1254.

CHAPTER 4

Effects of sulfate groups on the adsorption and activity of cellulases on cellulose substrates

4.1. Abstract

Pretreatment of lignocellulosic biomass with sulfuric acid may leave sulfate groups on its surface that may hinder its biochemical conversion. This study investigates the effect of sulfate groups on cellulase adsorption onto and hydrolysis of cellulose substrates. Substrates with different sulfate group densities were prepared from H_2SO_4- and HCl-hydrolyzed and partially and fully desulfated cellulose nanocrystals. Adsorption onto and hydrolysis of the substrates was analyzed by quartz crystal microbalance with dissipation monitoring (QCM-D). The surface roughness of the substrates, measured by atomic force microscopy, increased with decreasing sulfate group density, but their surface accessibilities, measured by QCM-D H_2O/D_2O exchange experiments, were similar. Adsorption of cellulose binding domains onto sulfated substrates decreased with increasing sulfate group density, but adsorption of cellulases increased. The rate of hydrolysis of sulfated substrates decreased with increasing sulfate group density. The results indicated an inhibitory effect of sulfate groups on the enzymatic hydrolysis of cellulose, possibly due to non-productive binding of the cellulases onto the substrates through electrostatic interactions instead of their cellulose binding domains.

4.2. Introduction

During the past two decades, the conversion of lignocellulosic biomass, such as agricultural and forestry residues, municipal solid wastes, grasses, and wood, to bioethanol has drawn much attention for environmental and economic reasons, among others.[1,2] The most promising conversion technology for lignocellulosic biomass is based on the enzymatic hydrolysis of its cellulose fraction to glucose, followed by microbial fermentation of the glucose molecules to ethanol. The enzymatic hydrolysis of cellulose to glucose requires three kinds of cellulases working synergistically: endoglucanases randomly cut cellulose chains in amorphous regions, where they are easily accessible, into shorter fragments of various lengths; exoglucanases cleave off cellobiose units from the reducing or non-reducing end of cellulose chains in the less accessible crystalline regions; and β-glucosidases hydrolyze the released cellodextrin and cellobiose molecules to glucose.[3] The first step in the hydrolysis of cellulose by endo- and exoglucanases is the adsorption of the enzyme onto the cellulose substrate, which has been shown to involve a domain of the enzyme called a cellulose binding domain (CBD) that is separate from and linked to its catalytic domain. Adsorption of CBDs onto cellulose substrates has been postulated to occur *via* van der Waals interactions and aromatic ring polarization interactions between aromatic amino acids in the CBD and the glucopyranose rings exposed on the 110 face of crystalline cellulose.[4-6]

Due to the intricate structure of plant cell walls and the connectivity of their molecular components, lignocellulosic biomass is highly recalcitrant and resistant to hydrolysis.[7] To reduce the recalcitrance of lignocellulosic biomass and make it more accessible to hydrolytic enzymes, researchers have developed a number of different biomass pretreatment methods. Examples of such pretreatment methods, which employ either physical or chemical mechanisms or a combination thereof, are steam explosion, hot water, dilute sulfuric acid, flow-through acid, alkali, ammonia fiber/freeze explosion, and ammonia recycle percolation pretreatment.[8,9] Primarily for economic reasons, dilute sulfuric acid pretreatment at elevated temperature (160–220 ℃) is one of the most popular methods. However, the treatment of lignocellulosic biomass with sulfuric acid could potentially cause esterification of cellulose hydroxyl groups. Sulfate half-esters are known to impede or inhibit the enzymatic hydrolysis of cellulose.[10]

The objective of this study was to determine how sulfate groups in pretreated biomass might affect its biochemical conversion. For this purpose, we prepared cellulose substrates with different sulfate group densities and analyzed their enzymatic hydrolysis by quartz crystal microbalance with dissipation monitoring (QCM-D) and atomic force microscopy (AFM). QCM-D measures the frequency and dissipation factor of oscillating quartz crystals. Because of their ability to detect minute mass and viscoelasticity changes of adsorbed layers on the oscillating quartz crystal's surface, QCM-D instruments have become valuable tools for studying the enzymatic hydrolysis of cellulose. In the first literature report, Turon *et al.*[11] showed that QCM-D frequency and dissipation factor changes during the enzymatic hydrolysis of cellulose substrates could indicate different hydrolysis stages, including enzyme adsorption, cleavage of cellulose chains and film hydration, and the loss of film integrity. Other QCM-D studies of the hydrolysis of cellulose by enzymes investigated the effects of crystallinity and morphology of the cellulose substrate,[12] enzyme concentration,[13] and temperature.[13] QCM-D has also been used to measure the glucose concentration in cellulose hydrolyzates for enzyme activity determination.[14]

Different methods have been used for the preparation of cellulose substrates for QCM-D studies, including spin coating of cellulose solutions,[12,13] spin coating[15] or Langmuir–Schaefer deposition[12] of trimethylsilyl cellulose followed by cellulose regeneration, and spin coating of cellulose nanocrystal[12,15] (CNC) or nanofibril[12] suspensions. The latter method has the advantage of producing cellulose substrates with native cellulose morphology. CNCs are obtained by acid hydrolysis of a purified cellulose starting material.[16,17] Because hydrolysis occurs first in the more accessible amorphous regions, the crystalline regions can be isolated and collected. CNCs produced with sulfuric acid have sulfate groups on their surface, which stabilize CNC suspensions through repulsive Coulomb forces.[18] In the previous chapter, it has been shown that the sulfate groups on the surface of H_2SO_4-hydrolyzed CNCs can be partially or completely removed by HCl-catalyzed or solvolytic desulfation, respectively, while maintaining their native crystal structure.[19] The cellulose substrates for the present study were prepared from CNCs with different sulfate group densities.

In addition to the enzymatic hydrolysis of the cellulose substrates, we analyzed the adsorption of cellulases and isolated CBDs onto these substrates. CBD adsorption was modeled with the Langmuir and Freundlich adsorption isotherms. Cellulase adsorption and substrate

hydrolysis were quantified from QCM-D frequency curves. A higher sulfate group density was found to result in increased cellulase adsorption but a reduced hydrolysis rate. This seemingly contradictory result was explained on the basis of electrostatic potential maps for the catalytic domains of the cellulases CBH I and EG I.

4.3. Experimental section

4.3.1. Materials

Dissolving-grade softwood sulfite pulp (Temalfa 93A-A) was kindly provided by Tembec, Inc. Cellulases (Celluclast 1.5L, Novozyme), D_2O (99.9 atom % D), papain from papaya latex (16–40 units·mg^{-1} protein), and β-mercaptoethanol (>99.0%) were purchased from Sigma-Aldrich. Sulfuric acid (95.9 wt %, Certified ACS Plus), hydrochloric acid (37.4 wt %, Certified ACS Plus), citric acid monohydrate (Fisher Scientific, Certified ACS), sodium hydroxide (Acros Organics, 98.5%), hydrogen peroxide (34–37%, Technical Grade), aqueous ammonia (28.9%, Certified ACS Plus), pyridine (99.5%, Chemservice), dimethyl sulfoxide (DMSO, Certified ACS), and methanol (99.8%, Acros Organics) were purchased from Fisher Scientific. All water used was deionized (DI) water with a resistivity of 18.2 MΩ·cm, obtained from a Millipore Direct-Q 5 Ultrapure Water Systems.

4.3.2. CNC preparation

The procedures by which the CNCs for this study were prepared are described in detail in the previous chapter. In brief, CNCs with a high surface charge density (0.293 mequiv·g^{-1}) were prepared by hydrolysis of milled (60-mesh) softwood sulfite pulp with 64 wt % sulfuric acid (10 mL·g^{-1} cellulose) at 45 ℃ for 1 h. CNCs with lower surface charge densities (0.152 and 0.055 mequiv·g^{-1}) were prepared by HCl-catalyzed desulfation of the H_2SO_4-hydrolyzed CNCs. CNCs without surface charge were prepared by complete, solvolytic desulfation of the H_2SO_4-hydrolyzed CNCs in DMSO *via* the pyridinium salt.[19] For comparison, we also prepared HCl-hydrolyzed CNCs, carrying no surface sulfate groups, by hydrolysis of the milled pulp with 4 N

hydrochloric acid (30 mL·g^{-1} cellulose) at 80 ℃ for 225 min.[20] The various CNC samples used in this study are listed in Table 4.1.

Table 4.1. CNC samples and their designations

CNC preparation method	Desulfation method	Surface charge density (mequiv·g^{-1})	Sample designation
H_2SO_4 hydrolysis	-	0.293	SH-293
H_2SO_4 hydrolysis	HCl-catalyzed desulfation	0.152	SH-152
H_2SO_4 hydrolysis	HCl-catalyzed desulfation	0.055	SH-55
H_2SO_4 hydrolysis	Solvolytic desulfation	0.007	SH-0
HCl hydrolysis	-	0.000	HH-0

4.3.3. Cellulose substrate preparation

Cellulose substrates were prepared on silicon dioxide-coated AT-cut quartz crystals (Q-Sense). The quartz crystals were cleaned by immersion and shaking for 1 min in fresh piranha solution (7:3 (v/v) mixture of sulfuric acid and hydrogen peroxide), then rinsed with DI water, dried in a stream of nitrogen, and irradiated for 15 min with an ozone-producing mercury lamp (UV/Ozone cleaner, Bioforce Nanosciences). To minimize surface contamination, we cleaned the quartz crystals immediately prior to use

Cellulose substrates from H_2SO_4-hydrolyzed CNCs were prepared from 1 wt % aqueous suspensions by spin coating (WS-400B-6NPPLite, Laurell Technologies Corp.) the cleaned quartz crystals at 4000 rpm for 1 min with 140 µl of the suspension. Cellulose substrates from HCl-hydrolyzed CNCs were prepared from 0.6 wt % aqueous suspensions by spin coating at 2000 rpm for 2 min with 140 µl of the suspension. Use of a lower concentration and spinning speed was necessary because at 1 wt %, the suspension of HCl-hydrolyzed CNCs was too viscous and produced non-uniform substrates. As the final step in their preparation, the cellulose substrates were dried in a vacuum oven at 65 ℃ overnight for improved stability in aqueous media.

4.3.4. Determination of CNC surface density

The CNC surface density on the quartz crystals after spin coating, $\rho_{S,CNC}$, was determined by QCM-D (Q-sense E4) from the difference of the oscillation frequencies in air of the cleaned quartz crystals before and after spin coating. Because the CNC film is rigid and firmly attached to the quartz crystal's surface, it can be treated as an extension of the quartz crystal itself. Thus, $\rho_{S,CNC}$ can be calculated with the Sauerbrey equation,[21]

$$\rho_{S,CNC} = -\frac{2f_0^2}{\upsilon_q \rho_q}\frac{\Delta f_n}{n} = -\frac{2f_0^2}{\sqrt{\mu_q \rho_q}}\left(\left(\frac{f_n}{n}\right)_{CNC} - \left(\frac{f_n}{n}\right)_{bare}\right), \quad [4.1]$$

where f_0 is the resonant frequency of the quartz crystal (5 MHz), υ_q is the transverse sound wave velocity in AT-cut quartz, ρ_q is the density of quartz (2648 kg·m^{-3} at 25 ℃),[22] μ_q is the shear modulus of quartz ($2.947 \cdot 10^{10}$ kg·m^{-1}·s^{-2})[23], n is the frequency overtone number, $(f_n/n)_{bare}$ is the normalized oscillation frequency of the bare quartz crystal in air, and $(f_n/n)_{CNC}$ is the normalized oscillation frequency of the CNC-coated quartz crystal in air. The term $2f_0^2/\upsilon_q\rho_q$ has been called by Sauerbrey the sensitivity constant C and has the value 0.177 mg·m^{-2}·Hz^{-1} for the quartz crystals and experimental conditions used here.

4.3.5. Analysis of substrate accessibility

As a measure of the surface accessibility of the substrates, the surface density of water molecules, ρ_{S,H_2O}, in swollen cellulose substrates was measured with the H_2O/D_2O exchange method described by Kittle *et al.*[15] The CNC-coated quartz crystals were placed in QCM-D flow modules, and a 0.25 mL·min^{-1} feed of DI water was established with a peristaltic pump. The temperature inside the flow modules was controlled at 20.00 ± 0.02 ℃. Swelling of the cellulose substrates resulted in a decrease in oscillation frequency. When the normalized rate of change of the 3rd overtone frequency, $(\Delta f_3/3)$, became less than 2 Hz·h^{-1}, the substrates were considered saturated and equilibrated, and the DI water feed was replaced with a D_2O feed with the same flow rate. Exchange of the H_2O molecules in the films with D_2O molecules caused an increase in mass and a decrease in the quartz crystal's oscillation frequency. After 10 min, the DI water feed

was restored, and the oscillation frequency returned to its initial value. The changes in oscillation frequency, Δf, and dissipation factor, ΔD, were recorded in real time at the fundamental frequency (5 MHz) and 6 overtone frequencies (15, 25, 35, 45, 55, and 65 MHz) with QSoft 401 acquisition software (Q-Sense). ρ_{S,H_2O} values for the swollen cellulose substrates were calculated from the differences in normalized frequency changes measured upon H_2O/D_2O exchange on bare and CNC-coated quartz crystals with the equation

$$\rho_{S,H_2O} = C\left(\frac{\Delta f_n}{n}\right)_{H_2O} \quad [4.2]$$

where $(\Delta f_n/n)_{H_2O}$ is the normalized frequency change due to trapped water molecules in the swollen cellulose substrates, determined as

$$\left(\frac{\Delta f_n}{n}\right)_{H_2O} = \frac{\left(\frac{\Delta f_n}{n}\right)_{CNC} - \left(\frac{\Delta f_n}{n}\right)_{bare}}{\left(\frac{\rho_{D_2O}}{\rho_{H_2O}}\right) - 1} \quad [4.3]$$

where $(\Delta f_n/n)_{CNC}$ is the normalized frequency change upon H_2O/D_2O exchange on the cellulose substrates, $(\Delta f_n/n)_{bare}$ is the normalized frequency change upon H_2O/D_2O exchange on the bare quartz crystal, and ρ_{D_2O} and ρ_{H_2O} are the densities of D_2O and H_2O at 20 ℃, taken as 1.1050 $g \cdot cm^{-3}$ and 0.9982 $g \cdot cm^{-3}$, respectively.[24]

4.3.6. Preparation of enzyme solution

The cellulases used in this study were the commercial enzyme mixture Celluclast 1.5L, produced by the aerobic filamentous fungus *Trichoderma reesei*. *T. reesei* is known to generate a mixture of at least two exoglucanases (Cel7A (CBH I) and Cel6A (CBH II)), five endoglucanases (Cel7B (EG I), Cel5A (EG II), Cel12A (EG III), Cel61A (EG IV) and Cel45A (EG V)), and two β-glucosidases (BGL I and BGL II).[3,25-28] The synergism between its components renders Celluclast 1.5L highly efficient for the saccharification of lignocellulosic biomass.[29-31] The filter

paper activity of the original Celluclast 1.5L solution was measured according to the standard procedure[32] and determined to be 119 FPU·mL^{-1}. The protein concentration, determined with a BCA Protein Assay Kit (Pierce), was 143 mg·mL^{-1}. For the hydrolysis experiments, 0.5 g of Celluclast 1.5L solution was diluted to 100 mL with 50 mM sodium citrate buffer (pH 4.8). The buffer had been derived by 20-fold dilution with DI water from a 1 M sodium citrate buffer (pH 4.5), produced by dissolution of the appropriate amounts of citric acid monohydrate and sodium hydroxide in DI water.

4.3.7. Isolation of CBDs

Except for Cel12A, all components of the *T. reesei* cellulase mixture have a CBD linked to the catalytic domain by a flexible, highly glycosylated linker.[25,26] The CBDs from *T. reesei* belong to the carbohydrate binding module family I, containing 33–40 amino acids and having similar sequences with some conserved residues or residue characteristics.[5,6,33] The glycosylated linkers are rich in serine, threonine, and proline and are susceptible to proteolytic cleavage by papain.[34-37]

For CBD isolation, Celluclast 1.5L was diluted four times with 50 mM sodium citrate buffer and then concentrated by ultrafiltration (Amicon Stirred Ultrafiltration Cell) with a 30 kDa molecular weight cut-off polysulfone membrane (Amicon Bioseparations Ultrafiltration Membranes, Millipore) for the removal of low molecular weight compounds. For activation, papain was first dissolved in 50 mM sodium citrate buffer containing a small amount of β-mercaptoethanol (volume ratio 1:10^4). After 15 min of papain activation, the papain solution was added to the Celluclast 1.5L solution (23.7 mg·ml^{-1}), and the mixture, with a cellulase-to-papain ratio of 200:1, was stirred for 4 h at room temperature with a magnetic stir bar. After digestion of the Celluclast 1.5L cellulases by papain, the CBDs were isolated from the digestion mixture by ultrafiltration with a 10 kDa molecular weight cut-off polysulfone membrane (Amicon Bioseparations Ultrafiltration membranes, Millipore). The protein concentrations of the Celluclast 1.5L solution, after dilution and concentration by ultrafiltration, and the final CBD solution were measured with a BCA Protein Assay Kit (Pierce).

4.3.8. CBD adsorption onto the cellulose substrates

CBD solutions with different concentrations were prepared by dilution of the CBD stock solution with 50 mM sodium citrate buffer. Adsorption of CBDs onto cellulose substrates was monitored by QCM-D. Cellulose substrates were placed in QCM-D flow modules, and a 0.25 $mL \cdot min^{-1}$ buffer feed was established. The temperature inside the flow modules was controlled at 25 ± 0.02 ℃. When the substrates reached equilibrium, indicated by a ($\Delta f_3/3$) change rate of less than 2 $Hz \cdot h^{-1}$, 3 mL of CBD solution was injected into the flow module to fully replace the buffer in the chamber. Adsorption of CBDs onto the substrates was monitored for 3 h under static conditions. After 3 h, the buffer feed was restored and maintained for 20 min to rinse off any reversibly adsorbed CBDs. Δf and ΔD were recorded in real time at the fundamental frequency (5 MHz) and 6 overtone frequencies (15, 25, 35, 45, 55, and 65 MHz) with QSoft 401 acquisition software (Q-Sense).

4.3.8.1. Viscoelastic modeling

Viscoelastic films, such as those formed by adsorbed proteins, do not fully couple to the oscillating quartz crystal. As a result, the adsorbed mass is not linearly related to Δf, and the Sauerbrey equation is not applicable.[38] In this case, estimation of the adsorbed mass has to involve the dissipation factor, *D*. *D* is defined as the ratio of energy dissipated, $E_{\text{dissipated}}$, to energy stored, E_{stored}, during one oscillation period and is calculated from the decay rate, τ, of the crystal's oscillation amplitude after discontinuation of the drive voltage:[38,39]

$$D = \frac{1}{2\pi}\frac{E_{\text{dissipated}}}{E_{\text{stored}}} = \frac{1}{\pi f \tau} \qquad [4.4]$$

To quantify the amount of CBD adsorbed on the substrate, we modeled Δf and ΔD for the 3rd and 5th overtones with a single-layer Voigt element-based viscoelastic film model[40,41] using the QTools modeling center (v3.0, Q-Sense). The model treats the CNC layer on the quartz crystal's surface as an extension of the quartz crystal. The input parameters for the model are the density and viscosity of the bulk liquid above the viscoelastic layer and the density of the viscoelastic layer. The parameters to fit are the viscosity, shear modulus, and thickness of the

viscoelastic layer. For the density and viscosity of the bulk liquid, we used the density and viscosity of water at 25 ℃, which are 997 $kg \cdot m^{-3}$ and $0.89 \cdot 10^{-3}$ $kg \cdot m^{-1}s^{-1}$, respectively.[24] The density of the viscoelastic film was fixed at 1152 $kg \cdot m^{-3}$. This value was based on the molar mass of the CBD of CBH I (3746.14 $g \cdot mol^{-1}$), obtained from the Protein Data Bank, and its molar volume, calculated from its molecular dimensions (3 nm × 1.8 nm × 1 nm)[4] and Avogadro's constant. The fitting ranges for the viscosity, shear modulus, and thickness of the viscoelastic layer were $5 \cdot 10^{-4}$–10^{-2} $kg \cdot m^{-1}s^{-1}$, 10^{5}–10^{6} Pa, and 10^{-9}–10^{-7} m, respectively. The surface excess concentration of the CBDs was calculated from the thickness and density of the viscoelastic layer. Changing the density of the viscoelastic film from 1152 to 1500 $kg \cdot m^{-3}$ or 1000 $kg \cdot m^{-3}$ resulted in different thickness values but did not affect the calculated surface excess concentration. Thus, the assumed density did not affect the determined mass of the viscoelastic film. This observation has also been reported by others.[42,43] Non-linear least square analysis of the adsorption data was conducted with Igor Pro software (v6.22A, Wavemetrics).

4.3.9. Enzymatic hydrolysis of the cellulose substrates

The binding onto and subsequent hydrolysis of cellulose substrates by cellulases was monitored by QCM-D. Cellulose substrates were placed in QCM-D flow modules, and a 0.25 $mL \cdot min^{-1}$ feed of 50 mM sodium citrate buffer was established. The temperature inside the flow modules was controlled at 25 ± 0.02 ℃. When the substrates reached equilibrium, indicated by a ($\Delta f_3/3$) change rate of less than 2 $Hz \cdot h^{-1}$, the buffer feed was replaced with a feed of enzyme solution with the same flow rate. Δf and ΔD were recorded in real time at the fundamental frequency (5 MHz) and 6 overtone frequencies (15, 25, 35, 45, 55, and 65 MHz) with QSoft 401 acquisition software (Q-Sense). Experiments were terminated when Δf reached a plateau. In the case of sulfated cellulose substrates, because of the low hydrolysis rates, experiments were terminated after 8 h before Δf reached a plateau.

4.3.10. Substrate imaging and surface roughness determination

Cellulose substrates for AFM experiments were prepared by spin coating as described above but on 1 cm × 1 cm silicon wafer pieces. Before spin coating, the wafer pieces, cut from a 15 cm wafer (Wafer World, Inc. West Palm Beach, FL), had been cleaned by immersion for 1 h at 70 ℃ in a mixture of aqueous ammonia, hydrogen peroxide, and DI water at a volume ratio of 1:1:5 and then for 1 h at ambient temperature in fresh piranha solution, rinsed with DI water, and dried in a stream of nitrogen. The cellulose substrates were immersed in enzyme solution and incubated for 2 h at 50 ℃. After incubation, the substrates were thoroughly rinsed with DI water and dried in a stream of nitrogen. Enzyme-treated and untreated cellulose substrates were imaged with an Asylum Research MFP-3D-BIO atomic force microscope. Samples were scanned in air at ambient relative humidity and temperature in intermittent-contact mode with OMCL-AC160TS standard silicon probes (Olympus Corp.) with a scan frequency of 1 Hz, and 512 scans with 512 points/scan. RMS surface roughnesses were determined from 5 μm × 5 μm areas in AFM height images.

4.3.11. Mapping of protein surface potential

The electrostatic surface potentials of the catalytic domains of CBH I and EG I were calculated with the APBS (Adaptive Poisson-Boltzmann Solver) software package from the 1CEL and 1EG1 Protein Data Bank entry.[44,45] The electrostatic potential was mapped on the molecular surfaces of 1CEL and 1EG1 with the VMD (Visual Molecular Dynamics) molecular visualization program.[46]

4.4. Results and discussion

4.4.1. CNC surface density and substrate accessibility

The CNC surface densities, $\rho_{S,CNC}$, of the cellulose substrates prepared from the five CNC samples are listed in Table 4.2. The three sulfated substrates, SH-55, SH-152, and SH-293, and

the non-sulfated HH-0 substrate had similar $\rho_{S,CNC}$ values, averaging about 20 mg·m^{-2}, but the $\rho_{S,CNC}$ value for the non-sulfated SH-0 substrate was more than twice as high. The substrate coverage of spin-coated CNCs depends on the spinning speed of the substrate during spin coating and the concentration and viscosity of the CNC suspension.[47] For the substrates SH-0, SH-55, SH-152, and SH-293, the spinning speed was 4000 rpm and the concentration of the CNC suspension was 1 wt %. In the previous chapter, it has been shown that the absence of negatively charged surface groups and therefore repulsive forces between the CNCs in sample SH-0 leads to CNC aggregation.[19] The higher viscosity of the SH-0 CNC suspension, caused by the lack of repulsive forces between the particles, was likely the reason for the higher CNC surface density of the SH-0 substrate. The HH-0 substrate had a lower CNC surface density than the SH-0 substrate because the concentration of the HH-0 CNC suspension used for spin coating was only 0.6 wt % for reasons explained in the Experimental Section.

Table 4.2. CNC surface densities, $\rho_{S,CNC}$, and H_2O surface densities, ρ_{S,H_2O}, of the cellulose substrates[a]

Surface densities[b]	HH-0	SH-0	SH-55	SH-152	SH-293
$\rho_{S,CNC}$ (mg·m^{-2})	20.7 ± 2.6	42.3 ± 1.5	18.7 ± 2.4	19.9 ± 1.3	19.4 ± 0.4
ρ_{S,H_2O} (mg·m^{-2})	30.6 ± 2.0	84.4 ± 3.3	32.2 ± 1.6	27.2 ± 1.8	28.7 ± 2.0

[a] Data are means ± one standard deviation of three measurements.
[b] Surface densities represent the areal mass determined from the Sauerbrey equation.

Figure 4.1 shows ($\Delta f_n/n$) curves from H_2O/D_2O exchange experiments for a bare quartz crystal, the HH-0 substrate, and the SH-0 substrate. ($\Delta f_n/n$) curves for the SH-55, SH-152, and SH-293 substrate are shown in Figure B.1 in Appendix B. For the bare quartz crystal, the decrease in ($\Delta f_n/n$) after the solvent switch is solely due to the differences in viscosity and density between D_2O and H_2O. The measured value of –55.4 Hz is in good agreement with the calculated value of –55.9 Hz.[15] The decrease in ($\Delta f_n/n$) after the solvent switch was larger for the CNC-coated quartz crystals than for the bare crystal. The additional decrease, above and beyond that observed for the bare quartz crystal, was due to the exchange of trapped H_2O molecules in the swollen cellulose substrates for heavier D_2O molecules and was therefore a measure for the

accessibility of the substrates. The larger decrease in ($\Delta f_n/n$) for the SH-0 substrate, compared to that for the HH-0 substrate, indicated a larger amount of trapped H_2O molecules in the SH-0 substrate in accordance with the much higher CNC surface density of this substrate.

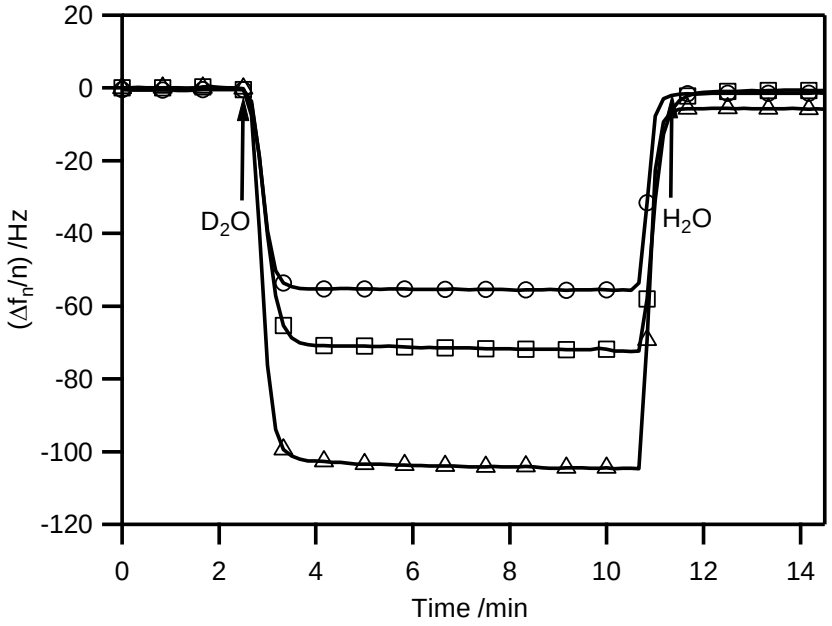

Figure 4.1. ($\Delta f_n/n$) curves (5^{th} overtone) from H_2O/D_2O exchange experiments for a bare quartz crystal (○), the HH-0 substrate (□), and the SH-0 substrate (△).

The H_2O surface densities, ρ_{S,H_2O}, for the five cellulose substrates are listed in Table 4.2. The ρ_{S,H_2O} values for the three sulfated substrates and the non-sulfated substrate HH-0 were similar and averaged about 30 mg·m^{-2}, yielding an H_2O-to-CNC weight ratio of about 3:2 in the swollen substrates. The similarity of the ρ_{S,H_2O} values for the three sulfated substrates, SH-55, SH-152, and SH-293, suggested that the amount of trapped H_2O molecules was unaffected by the surface charge of the CNCs in the substrate over this range of sulfate group densities. The swollen SH-0 substrate had a ρ_{S,H_2O} value of 84.4 mg·m^{-2} and an H_2O-to-CNC weight ratio of 2:1. The higher H_2O-to-CNC weight ratio in the SH-0 substrate indicated a 33% greater accessibility of the substrate compared to HH-0.

4.4.2. CBD adsorption onto the cellulose substrates

The adsorption of CBDs onto the cellulose substrates was measured at different CBD concentrations and modeled with the Langmuir and Freundlich adsorption isotherms. The Langmuir isotherm model assumes reversible adsorption of adsorbates without lateral interactions onto a homogenous surface with equivalent binding sites to the point of monolayer coverage. The model is described by the equation[48]

$$\Gamma_{eq} = \Gamma_{max} \frac{K_L C}{1 + K_L C} \qquad [4.5]$$

where Γ_{eq} and Γ_{max}, having the unit mg·m^{-2}, are the equilibrium surface excess concentration of adsorbate at concentration C and the saturation surface excess concentration as $C \rightarrow \infty$, respectively, and K_L is the Langmuir equilibrium constant. Eq 4.5 can be rewritten as

$$\frac{1}{\Gamma_{eq}} = \frac{1}{\Gamma_{max}} + \frac{1}{\Gamma_{max} K_L C}, \qquad [4.6]$$

allowing the determination of $1/(\Gamma_{max}K_L)$ and $1/\Gamma_{max}$ from the slope and intercept, respectively, of a plot of $1/\Gamma_{eq}$ *versus* $1/C$.

The Freundlich isotherm model is an empirical model for the adsorption of adsorbates onto a heterogenous surface with non-equivalent binding sites and is described by the equation[49]

$$\Gamma = K_F C^n \qquad [4.7]$$

where K_F is the Freundlich equilibrium constant and n is the heterogeneity factor. Eq 4.11 can be rewritten as

$$\ln \Gamma = \ln K_F + n \ln C, \qquad [4.8]$$

allowing the determination of n and $\ln K_F$ from the slope and intercept, respectively, of a plot of $\ln \Gamma$ *versus* $\ln C$.

The linear regression models described by eqs 4.6 and 4.8 are problematic, however, because they overemphasize the data in the low concentration region, especially in the case of the Langmuir model. We therefore used non-linear least squares analysis to fit eqs 4.5 and 4.7 to the data. The Langmuir and Freundlich adsorption isotherms for the SH-0 and HH-0 substrates are shown in Figure 4.2. Greater CBD surface excess concentrations were observed on the SH-0 than on the HH-0 substrate. As shown in the previous section, the SH-0 substrate had twice the CNC surface density and a 33% higher accessibility than the HH-0 substrate. The SH-0 substrate had therefore more accessible surface area for CBD adsorption than the HH-0 substrate. The χ^2 values for the fits, listed in Table 4.3, showed that the data for the HH-0 substrate were described well by either model, with the Freundlich model providing a slightly better fit. For the SH-0 substrate, however, only the Freundlich model gave a good fit. The high χ^2 value for the Langmuir model indicated a statistically significant ($p < 0.05$) deviation of the experimental data from the prediction.

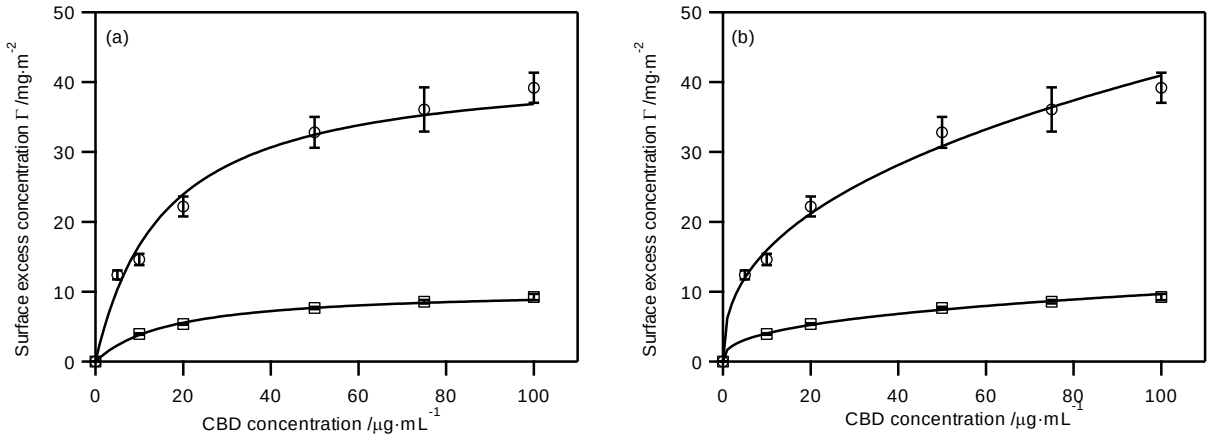

Figure 4.2. (a) Langmuir and (b) Freundlich isotherms for CBD adsorption onto SH-0 (○) and HH-0 (□) cellulose substrates. The solid lines are the fitting curves.

The Langmuir and Freundlich adsorption isotherms for the SH-55 and SH-293 substrates are shown in Figure 4.3.

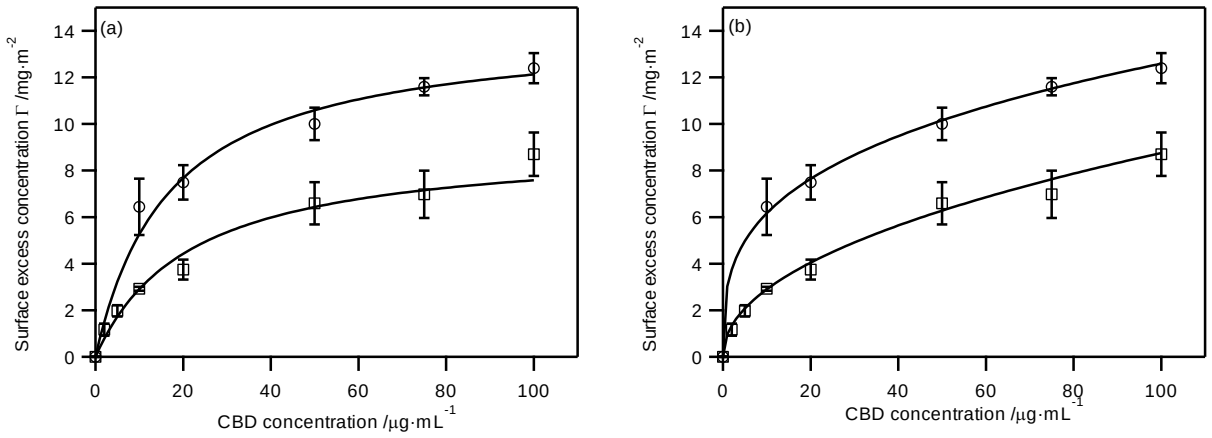

Figure 4.3. (a) Langmuir and (b) Freundlich isotherms for CBD adsorption onto SH-55 (○) and SH-293 (□) cellulose substrates. The solid lines are the fitting curves.

Table 4.3. Langmuir and Freundlich isotherm parameters for the adsorption of CBDs onto the cellulose substrates[a,b]

Parameters	HH-0	SH-0	SH-55	SH-293
Langmuir model				
Γ_{max} (mg·m^{-2})	10.3 ± 0.3	42.6 ± 2.3	14.2 ± 0.9	9.2 ± 1.0
K_L	0.058 ± 0.004	0.064 ± 0.007	0.059 ± 0.017	0.046 ± 0.008
χ^2 value	6.7	19.2	1.9	7.2
Freundlich model				
K	1.7 ± 0.1	6.2 ± 0.4	3.0 ± 0.7	1.0 ± 0.1
N	0.38 ± 0.01	0.41 ± 0.02	0.31 ± 0.05	0.48 ± 0.03
χ^2 value	4.5	5.0	0.3	1.6

[a] obtained by weighted non-linear least-squares fitting of eqs 4.9 and 4.11 to the experimental data
[b] Reported error ranges are ± one standard deviation.

The SH-55 substrate exhibited higher CBD surface excess concentrations than the SH-293 substrate. As shown in the previous section, the accessible surface areas for CBD adsorption of the two substrates, deduced from their CNC surface densities and H_2O-to-CNC weight ratios, were nearly equal. Adsorption of CBDs onto cellulose is believed to occur through hydrophobic

interactions between three precisely spaced tyrosine residues and the 110 crystal face of cellulose.[4,6,33] The lower CBD surface excess concentrations of the SH-293 substrate indicated that the negatively charged sulfate groups on the surface of the substrate hindered the hydrophobic interactions between the CBDs and the cellulose substrate. The χ^2 values for the fits (Table 4.3) showed that the data for both substrates were described well by either model, *i.e.* that the deviation of the experimental data from the predictions were statistically insignificant ($p \geq 0.05$). As in the case of the HH-0 substrate, the Freundlich model provided a better fit to the data than the Langmuir model.

4.4.3. Enzymatic hydrolysis of the cellulose substrates

Figure 4.4 shows ($\Delta f_n/n$) and ΔD curves for the enzymatic hydrolysis of the substrates HH-0 and SH-0. The initial rapid decrease in ($\Delta f_n/n$), due to enzyme adsorption onto the substrate,[11] was larger for the SH-0 substrate than for the HH-0 substrate. This finding was in accordance with the larger accessible surface area of the SH-0 substrate, compared to the HH-0 substrate, and the higher CBD surface excess concentrations, observed upon CBD adsorption (Figure 4.2).

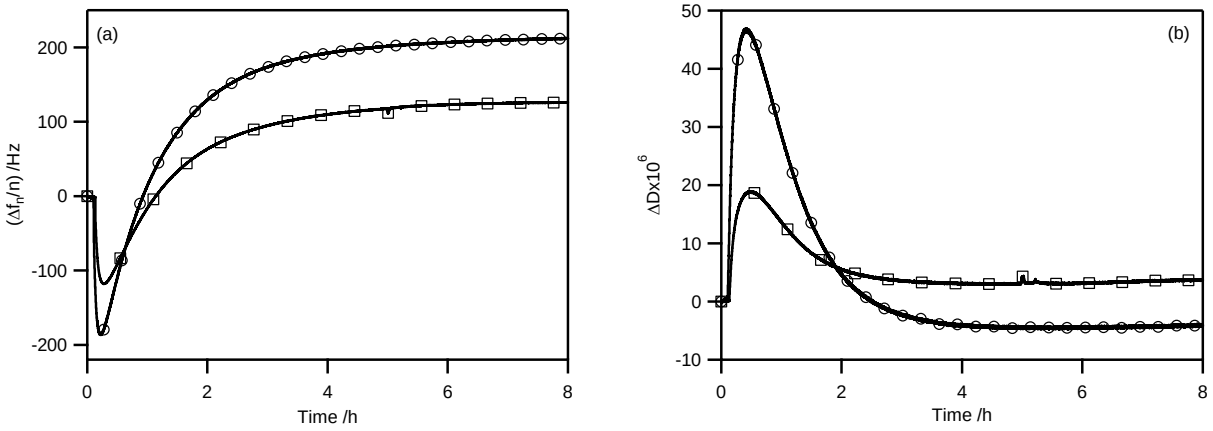

Figure 4.4. (a) ($\Delta f_n/n$) and (b) ΔD curves (3rd overtone) for the enzymatic hydrolysis of the substrates SH-0 (○) and HH-0 (□).

The increase in ($\Delta f_n/n$) after the minimum has previously been explained by the hydrolysis and gradual disintegration of the cellulose substrate.[11] After adsorption onto the substrate, the endo- and exoglucanases, present in the enzyme mixture, cleave the accessible cellulose chains into cellodextrins and cellobiose units, which are then further broken down by the β-glucosidases into individual glucose molecules. The conversion of cellodextrins and cellobiose to glucose cannot be measured by QCM-D, however, because it occurs primarily in solution. The ($\Delta f_n/n$) increase, signifying a decrease in mass on the quartz crystal's surface, results from the removal of soluble hydrolysis products and potentially adsorbed enzymes from the cellulose substrate. ($\Delta f_n/n$) reaches a plateau when all accessible areas of the substrate have been hydrolyzed, in which case the mass on the quartz crystal remains constant. For both substrates, ($\Delta f_n/n$) reached a plateau after about 4 h, at which point hydrolysis of the substrates was regarded as complete. The plateau value of ($\Delta f_n/n$), a measure for the amount of mass removed from the quartz crystal, depends on the initial CNC surface density of the substrate. Because the initial CNC surface density of the SH-0 substrate was much higher than that of the HH-0 substrate (Table 4.2), the plateau value of ($\Delta f_n/n$) for the SH-0 substrate was also higher.

The ΔD curves (Figure 4.4b) showed a rapid increase, followed by a decrease and leveling off. The shape of the ΔD curves is more easily explained in combination with the ($\Delta f_n/n$) data.[11] Figure 4.5 shows a plot of ΔD *versus* ($\Delta f_n/n$) for the SH-0 substrate.

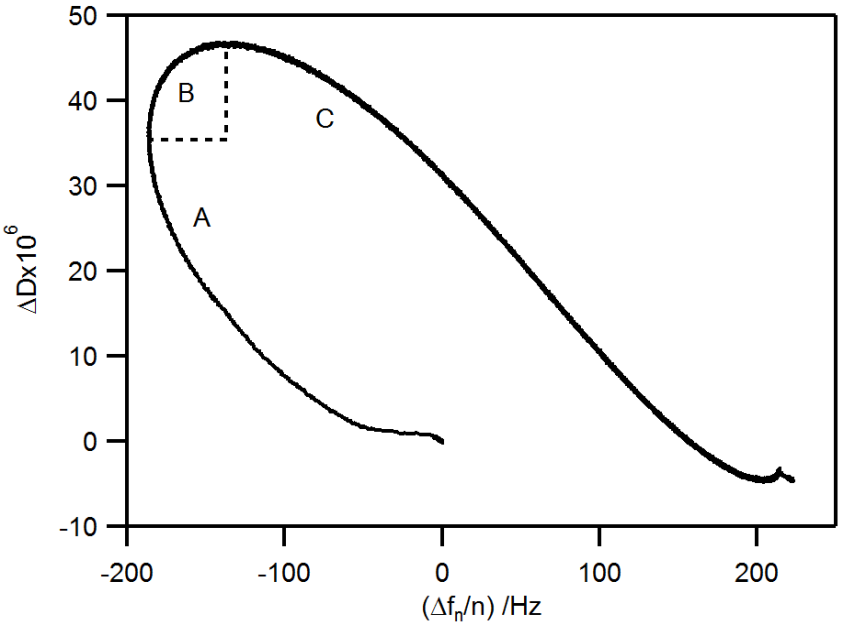

Figure 4.5. ΔD *versus* $(\Delta f_n/n)$ (3^{rd} overtone) during enzymatic hydrolysis of the SH-0 substrate.

The resulting curve can be divided into three sections. In section A, $(\Delta f_n/n)$ decreases while ΔD increases. This section indicates enzyme adsorption onto the substrate. The $(\Delta f_n/n)$ decrease is due to the mass increase on the quartz crystal and the ΔD increase is due to the dissipative nature of the soft, highly hydrated enzyme layer. In section B, both $(\Delta f_n/n)$ and ΔD increase. The $(\Delta f_n/n)$ increase is due to the decrease in substrate mass upon hydrolysis and the ΔD increase is due to the swelling and increased hydration of the substrate with increasing number of loose surface chains and dangling chain ends after cleavage of the cellulose chains by the endoglucanases. In section C, $(\Delta f_n/n)$ continues to increase while ΔD decreases. The increase in $(\Delta f_n/n)$ is again due to the decrease in substrate mass upon hydrolysis. The decrease in ΔD is due to the decrease in the dissipative nature of the hydrated cellulose substrate as it becomes thinner and is gradually removed from the quartz crystal by the enzymes. At the end of the hydrolysis, ΔD will be at or near zero, because the bare quartz crystal has a similar dissipation factor and rigidity as the cellulose substrate before hydrolysis.

The $(\Delta f_n/n)$ and ΔD curves for the enzymatic hydrolysis of the substrates SH-55, SH-152, and SH-293 are shown in Figure 4.6.

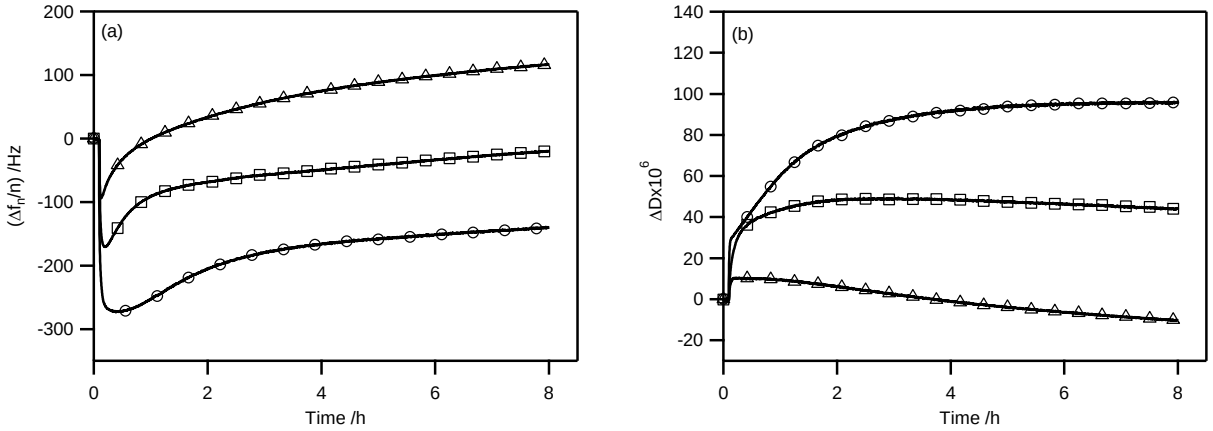

Figure 4.6. (a) $(\Delta f_n/n)$ and (b) ΔD curves (3^{rd} overtone) for the enzymatic hydrolysis of the substrates SH-55 (△), SH-152 (□), and SH-293 (○).

The initial $(\Delta f_n/n)$ decrease was largest for the SH-293 substrate and smallest for the SH-55 substrate. The values for the $(\Delta f_n/n)$ minima, $(\Delta f_n/n)_{min}$, are given in Table 4.4. The increase in magnitude of $(\Delta f_n/n)_{min}$ from SH-55 to SH-293 indicated greater enzyme adsorption on cellulose substrates with higher sulfate group density, which was further supported by an increase in the ΔD maximum, ΔD_{max}, from SH-55 to SH-293, as seen in Figure 4.6b and Table 4.4. The increase in ΔD_{max} with increasing sulfate group density indicated an increasingly thick and more dissipative enzyme layer on the substrate. This finding seemed to contradict the results of the CBD adsorption experiments, in which the SH-55 substrate exhibited greater CBD adsorption than the SH-293 substrate. The increase in enzyme adsorption with increasing sulfate group density of the substrates suggested that the adsorption process was governed by electrostatic interactions. Some enzymes in the Celluclast 1.5L enzyme mixture, including CBH II, EG II, and EG III, have isoelectric points above 4.8. These enzymes will have a net positive charge in the sodium citrate buffer that may result in adsorption onto the substrate through attractive Coulomb forces instead of the CBDs. The increase in $(\Delta f_n/n)$ after the minimum (Figure 4.6a) was much more gradual for the SH-293 substrate than for the SH-55 substrate, with the SH-152 substrate exhibiting intermediate behavior. The more gradual $(\Delta f_n/n)$ increase at higher sulfate group density indicated an inhibitory effect of the sulfate groups on the enzymatic hydrolysis of the substrates. Also, the ΔD decrease after the maximum, observed for the non-sulfated cellulose

substrates (Figure 4.5b), was either missing or much less pronounced for the sulfated substrates (Figure 4.6b). The fact that ΔD remained high until the end of the experiment indicated that an energy-dissipative layer was present and remained on the quartz crystal, *i.e.* that the hydrolysis of these substrates was incomplete. The conclusion was further supported by the smaller $(\Delta f_n/n)$ increases after the minima in the curves of the sulfated substrates as compared to those of the non-sulfated substrates, indicating a smaller mass loss during hydrolysis.

Table 4.4. Values of the $(\Delta f_n/n)$ minima, ΔD maxima, and the minima and maxima of $\mathrm{d}(\Delta f_n/n)/\mathrm{d}t$, taken as a measure for the rate of enzyme adsorption and substrate hydrolysis, respectively[a]

	HH-0	SH-0	SH-55	SH-152	SH-293
$(\Delta f_n/n)_{\min}$ (Hz)	–124 ± 6	–167 ± 19	–102 ± 11	–188 ± 25	–274 ± 2
$\Delta D_{\max}$ (10^{-6})	20 ± 2	38 ± 8	17 ± 8	49 ± 1	92 ± 5
$(\mathrm{d}(\Delta f_n/n)/\mathrm{d}t)_{\min}$ (s^{-2})	–0.58 ± 0.02	–0.82 ± 0.11	–0.79 ± 0.15	–1.25 ± 0.18	–1.62 ± 0.10
$(\mathrm{d}(\Delta f_n/n)/\mathrm{d}t)_{\max}$ (s^{-2})	0.049 ± 0.002	0.081 ± 0.012	0.057 ± 0.018	0.043 ± 0.009	0.025 ± 0.004

[a] Data are means ± one standard deviation of three measurements.

The rate of change of $(\Delta f_n/n)$ at the first and second inflection point of the $(\Delta f_n/n)$ curve, given by the minimum and maximum of its first derivative, $(\mathrm{d}(\Delta f_n/n)/\mathrm{d}t)_{\min}$ and $(\mathrm{d}(\Delta f_n/n)/\mathrm{d}t)_{\max}$, respectively, were taken as a measure for the rate of enzyme adsorption and substrate hydrolysis, respectively. The values are given in Table 4.4. The rate of enzyme adsorption was higher for the SH-0 substrate than for the HH-0 subtrate. The higher adsorption rate for the SH-0 substrate could be due to its larger accessible surface area. For the sulfated substrates, the rate of enzyme adsorption increased in the order SH-55<SH-152<SH-293. The fact that the substrate with the highest sulfate group density exhibited the highest rate of enzyme adsorption suggested that cellulase binding through electrostatic interactions is faster than binding through CBDs. The rate of substrate hydrolysis was also higher for the SH-0 substrate than for the HH-0 substrate in accordance with the larger amount of adsorbed enzymes (magnitude of $(\Delta f_n/n)_{\min}$) and the greater substrate surface area. For the sulfated substrates, the rate of substrate hydrolysis decreased from SH-55 to SH-293, despite the fact that the amount of adsorbed enzymes increased. In other words,

a higher surface charge density was associated with a larger amount of adsorbed enzymes but a lower hydrolysis rate. To explain this seemingly contradictory result, we analyzed electrostatic potential maps for the catalytic domains of CBH I and EG I, the two main components of the *T. reesei* enzyme mixture, accounting for up to 60%[50,51] and 6–10%[50] of the total amount of enzyme produced, respectively.

4.4.4. Electrostatic potential maps for the catalytic domains of CBH I and EG I

The electrostatic potential maps for the catalytic domains of CBH I and EG I are shown in Figure 4.7. CBH I is believed to play a key role in the hydrolysis of the crystalline regions of cellulose.[52,53] The catalytic domain of CBH I consists of a large, concave β-sandwich, formed by two antiparallel β-sheets stacked face-to-face, four short α-helices, and numerous short and long loops. The long loops, located between the two β-sheets and between the strands of the concave β-sheet, form a tunnel that runs the entire length of the concave sheet (~50 Å).[52-54] The active site, located at the far end of the tunnel, contains three acidic residues, Glu212, Asp214, and Glu217. During cellulose hydrolysis by CBH I, a single cellulose chain enters the front end of the tunnel with its reducing end. The chain remains in the tunnel while the active site at the far end of the tunnel cleaves off cellobiose units from the reducing end. The isoelectric point of CBH I is between 3.5 and 4.2.[50] Thus, CBH I has a net negative charge in pH 4.8 buffer. As seen in Figure 4.7 (left column), the electrostatic potential of the catalytic domain of CBH I is predominantly negative with a few spots exhibiting a positive electrostatic potential. The negative electrostatic potential in the tunnel and at the active site precludes negatively charged cellulose chains from entering the tunnel and the active site.

The catalytic domain of EG I is similar to that of CBH I in that it also consists of a β-sandwich, formed by two antiparallel β-sheets stacked face-to-face, four short α-helices, and several loops.[55] The main difference is that the tunnel-forming loops of CBH I are absent in EG I. As a result, instead of a tunnel, EG I has an open substrate-binding cleft, enabling EG I to cleave cellulose chains at random locations within the chain because the chains can diffuse freely in an out of the cleft. Like that of CBH I, the active site of EG I contains three acidic residues, Glu196,

Asp198, and Glu201.[55] The isoelectric point of EG I has been reported as 4.5[56] and 4.7.[57] The electrostatic potential map in Figure 4.7 (right column) shows both positive and negative spots. However, the inside of the cleft and active site have a negative electrostatic potential that again precludes negatively charged cellulose chains from entering the cleft and active site.

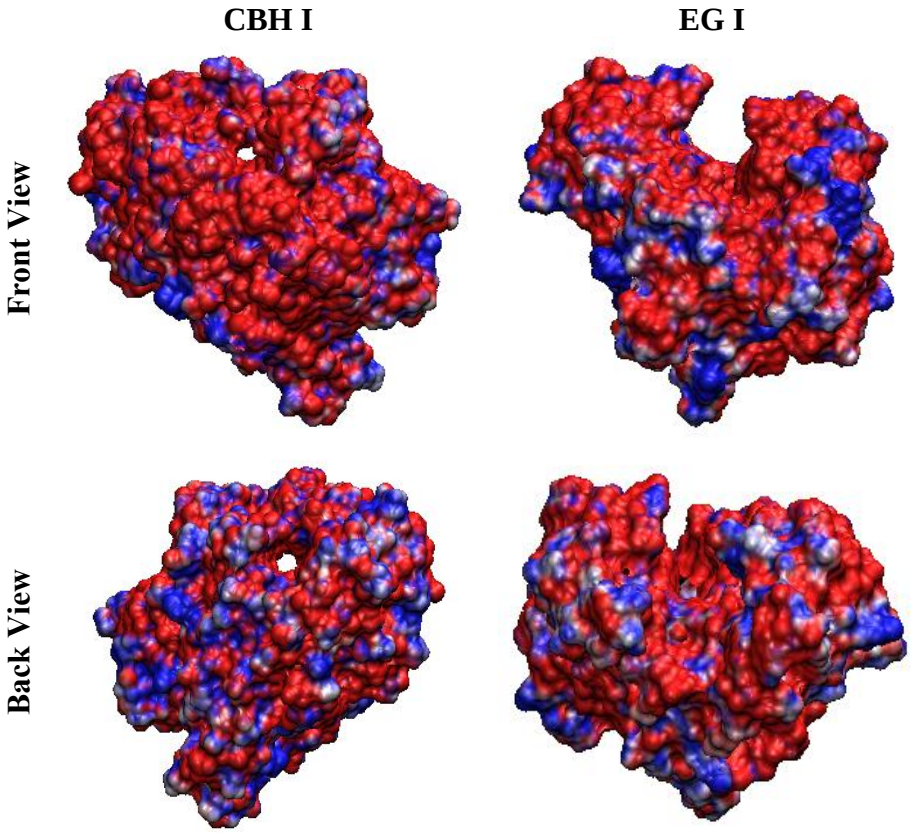

Figure 4.7. Electrostatic potential maps for the catalytic domains of CBH I and EG I. Potential isocontours are shown at +1 $kT \cdot e^{-1}$ (blue) and –1 $kT \cdot e^{-1}$ (red) and obtained at 300 mM ionic strength (50 mM sodium citrate buffer) with a solute dielectric of 2 and a solvent dielectric of 78.54.

4.4.5. AFM investigation of the cellulose substrates

Figure 4.8 shows AFM height images of the cellulose substrates before hydrolysis. The surface roughnesses for the substrates are listed in Table 4.5. The surface roughnesses of the substrates SH-0, SH-55, SH-152, and SH-293 increased with decreasing sulfate group density, probably because of increased aggregation in the CNC suspension used for spin coating with decreasing repulsive force between the CNCs in suspension. The surface roughness of the HH-0 substrate was much higher than that of the SH-0 substrate. In the previous chapter it has been shown that the HH-0 CNCs have the largest particle size of all the CNC samples.[19] The larger particle size of HH-0 CNCs was likely the reason for the higher surface roughness of the HH-0 substrate.

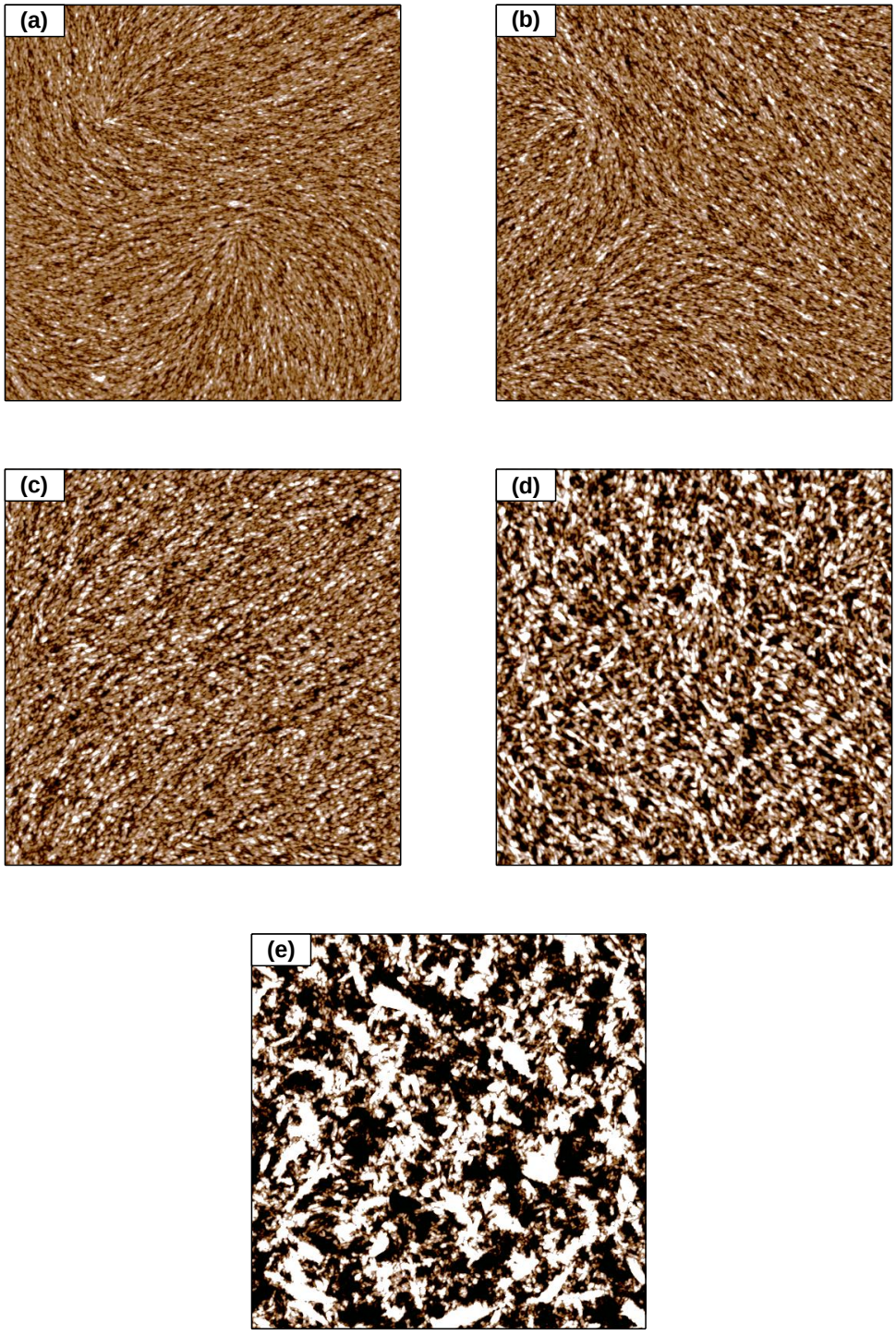

Figure 4.8. AFM height images of the cellulose substrates: (a) SH-293, (b) SH-152, (c) SH-55, (d) SH-0, and (e) HH-0. The scan size and z-scale are 5 μm × 5 μm and 8 nm, respectively, for all images.

Table 4.5. Surface roughnesses (nm) for the different cellulose substrates from 5 μm × 5 μm AFM height images

	RMS surface roughness (nm)				
	HH-0	SH-0	SH-55	SH-152	SH-293
Before hydrolysis	7.8	3.3	2.0	1.7	1.4
After hydrolysis	N/A	3.1	3.4	4.4	4.1

Figure 4.9 shows AFM height images of the cellulose substrates after incubation in enzyme solution at 50 ℃ for 2 h. All images showed large globular aggregates, which might be adsorbed enzymes. The fact that CNCs were still discernible under the enzymes in the case of the substrates SH-293, SH-152, and SH-55 (Figure 4.9a–c) indicated that hydrolysis of these substrates was incomplete after 2 h. The surface roughnesses of the substrates (Table 4.5) were higher after hydrolysis than before. The increase in surface roughness could either be due to the partial erosion of the substrate during hydrolysis or to the enzymes still adsorbed on the substrate. The image of the SH-0 substrate (Figure 4.9d) did not show any CNCs. The absence of CNCs indicated that hydrolysis of the SH-0 substrate was complete after 2 h and that it had proceeded much faster than those of the sulfated substrates. This finding is consistent with the results of the substrate hydrolysis study by QCM-D, which showed a much higher hydrolysis rate for the SH-0 substrate than the other substrates.

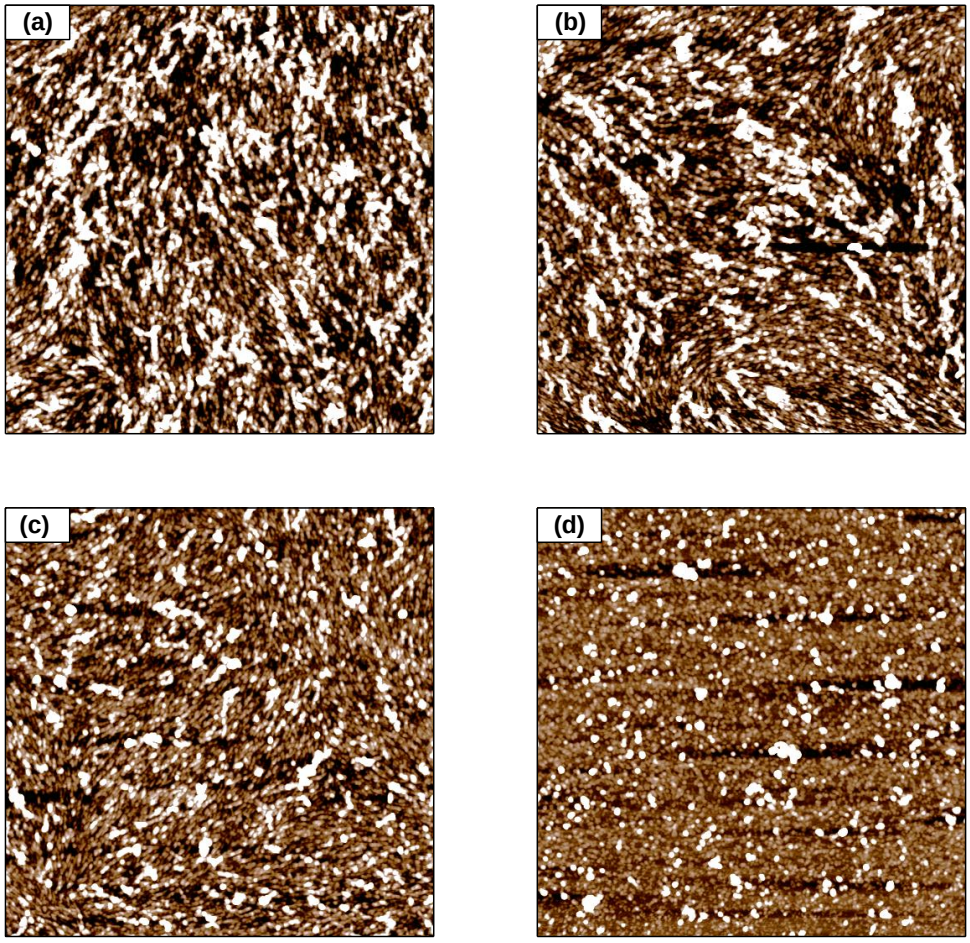

Figure 4.9. AFM height images of the cellulose substrates after incubation for 2 h at 50 ℃ in enzyme solution: (a) SH-293, (b) SH-152, (c) SH-55, (d) SH-0. The scan size and z-scale are 5 μm × 5 μm and 8 nm, respectively, for all images.

4.5. Conclusions

The objective of this study was to determine how sulfate groups in pretreated biomass might affect its biochemical conversion. The study has shown that sulfate groups on cellulose substrates hinder cellulase adsorption through the CBDs but promote cellulase adsorption through other, possibly electrostatic, interactions. The study has further shown that sulfate groups slow down or inhibit the enzymatic hydrolysis of cellulose substrates. The inhibitory effect of the

sulfate groups may be due to non-productive binding of the enzymes onto the substrate. In addition, negatively charged cellulose chains are unlikely to enter the active sites of the enzymes because of repulsive electrostatic forces between the cellulose chain and the acidic residues of the active site.

4.6. Acknowledgments

This project was supported by the National Research Initiative of the USDA Cooperative State Research, Education and Extension Service under Grant 2005-35504-16088, the National Science Foundation under Grant CHE-0724126 and DMR-0907567, the U.S. Department of Transportation through the Southeastern Sun Grant Center, and the Institute for Critical Technology and Applied Science. The authors thank Joshua Kittle in Dr. Esker's group for the help with the determination of the cellulose substrate accessibility, Dr. David R. Bevan in Biochemistry Department for his guidance in surface electrostatic potential mapping and visualization, Dr. Richey Davis for access to the QCM-D.

4.7. References

1. Lynd, L. R.; Cushman, J. H.; Nichols, R. J.; Wyman, C. E. Fuel Ethanol from Cellulosic Biomass. *Science* **1991,** *251*, 1318-1323.

2. Wyman, C. E. Biomass Ethanol: Technical Progress, Opportunities, and Commercial Challenges. *Annual Review of Energy and the Environment* **1999,** *24*, 189-226.

3. Lynd, L. R.; Weimer, P. J.; van Zyl, W. H.; Pretorius, I. S. Microbial Cellulose Utilization: Fundamentals and Biotechnology. *Microbiology and Molecular Biology Reviews* **2002,** *66*, 506-577.

4. Kraulis, P. J.; Clore, G. M.; Nilges, M.; Jones, T. A.; Pettersson, G.; Knowles, J.; Gronenborn, A. M. Determination of the 3-Dimensional Solution Structure of the C-

Terminal Domain of Cellobiohydrolase-I from Trichoderma-Reesei - a Study Using Nuclear Magnetic-Resonance and Hybrid Distance Geometry Dynamical Simulated Annealing. *Biochemistry* **1989,** *28*, 7241-7257.

5. Linder, M.; Lindeberg, G.; Reinikainen, T.; Teeri, T. T.; Pettersson, G. The Difference in Affinity between 2 Fungal Cellulose-Binding Domains is Dominated by a Single Amino-Acid Substitution. *Febs Letters* **1995,** *372*, 96-98.

6. Linder, M.; Teeri, T. T. The Roles and Function of Cellulose-Binding Domains. *Journal of Biotechnology* **1997,** *57*, 15-28.

7. Himmel, M. E.; Ding, S. Y.; Johnson, D. K.; Adney, W. S.; Nimlos, M. R.; Brady, J. W.; Foust, T. D. Biomass Recalcitrance: Engineering Plants and Enzymes for Biofuels Production. *Science* **2007,** *315*, 804-807.

8. Mosier, N.; Wyman, C.; Dale, B.; Elander, R.; Lee, Y. Y.; Holtzapple, M.; Ladisch, M. Features of Promising Technologies for Pretreatment of Lignocellulosic Biomass. *Bioresource Technology* **2005,** *96*, 673-686.

9. Wyman, C. E.; Dale, B. E.; Elander, R. T.; Holtzapple, M.; Ladisch, M. R.; Lee, Y. Y. Coordinated Development of Leading Biomass Pretreatment Technologies. *Bioresource Technology* **2005,** *96*, 1959-1966.

10. Gohdes, M.; Mischnick, P. Determination of the Substitution Pattern in the Polymer Chain of Cellulose Sulfates. *Carbohydrate Research* **1998,** *309*, 109–115.

11. Turon, X.; Rojas, O. J.; Deinhammer, R. S. Enzymatic Kinetics of Cellulose Hydrolysis: A Qcm-D Study. *Langmuir* **2008,** *24*, 3880-3887.

12. Ahola, S.; Turon, X.; Österberg, M.; Laine, J.; Rojas, O. J. Enzymatic Hydrolysis of Native Cellulose Nanofibrils and Other Cellulose Model Films: Effect of Surface Structure. *Langmuir* **2008,** *24*, 11592–11599.

13. Hu, G.; Heitmann, J. A.; Rojas, O. J. In Situ Monitoring of Cellulase Activity by Microgravimetry with a Quartz Crystal Microbalance. *Journal of Physical Chemistry B* **2009,** *113*, 14761-14768.

14. Hu, G.; Heitmann, J. A.; Rojas, O. J. Quantification of Cellulase Activity Using the Quartz Crystal Microbalance Technique. *Analytical Chemistry* **2009,** *81*, 1872-1880.

15. Kittle, J. D.; Du, X.; Jiang, F.; Qian, C.; Heinze, T.; Roman, M.; Esker, A. Equilibrium Water Content of Model Cellulose Substrates Determined *via* Solvent Exchange Andquartz Crystal Microbalance with Dissipation Monitoring. *Biomacromolecules* **2011,** *12*, 2881-2887.

16. Rånby, B. G. Aqueous Colloidal Solutions of Cellulose Micelles. *Acta Chemica Scandinavica* **1949,** *3*, 649–650.

17. Rånby, B. G. Fibrous Macromolecular Systems. Cellulose and Muscle. The Colloidal Properties of Cellulose Micelles. *Discussions of the Faraday Society* **1951,** *11*, 158–164.

18. Marchessault, R. H.; Morehead, F. F.; Koch, M. J. Hydrodynamic Properties of Neutral Suspensions of Cellulose Crystallites as Related to Size and Shape. *Journal of Colloid Science* **1961,** *16*, 327–344.

19. Jiang, F.; Esker, A. R.; Roman, M. Acid-Catalyzed and Solvolytic Desulfation of H_2SO_4-Hydrolyzed Cellulose Nanocrystals. *Languir* **2010,** *26*, 17919-17925.

20. Araki, J.; Wada, M.; Kuga, S.; Okano, T. Flow Properties of Microcrystalline Cellulose Suspension Prepared by Acid Treatment of Native Cellulose. *Colloids and Surfaces, A: Physicochemical and Engineering Aspects* **1998,** *142*, 75–82.

21. Sauerbrey, G. Verwendung Von Schwingquarzen Zur Wägung Dünner Schichten Und Zur Mikrowägung. *Z. Phys.* **1959,** *155*, 206-222.

22. Chapter 10, Q. In: Physical Properties and Data of Optical Materials; Optical Science and Engineering; CRC Press: 2007; pp 355-378.

23. Kanazawa, K. K.; Gordon, J. G. Frequency of a Quartz Microbalance in Contact with Liquid. *Analytical Chemistry* **1985,** *57*, 1770-1771.

24. Lide, D. R., *CRC Handbook of Chemistry and Physics (Internet Version)*. 91st ed.; CRC Press: Boca Raton, FL, 2011.

25. Kotiranta, P.; Karlsson, J.; Siika-Aho, M.; Medve, J.; Viikari, L.; Tjerneld, F.; Tenkanen, M. Adsorption and Activity of Trichoderma Reesei Cellobiohydrolase I, Endoglucanase II, and the Corresponding Core Proteins on Steam Pretreated Willow. *Applied Biochemistry and Biotechnology* **1999,** *81*, 81-90.

26. Eriksson, T.; Karlsson, J.; Tjerneld, F. A Model Explaining Declining Rate in Hydrolysis of Lignocellulose Substrates with Cellobiohydrolase I (Cel7A) and Endoglucanase I (Cel7B) of Trichoderma Reesei. *Applied Biochemistry and Biotechnology* **2002,** *101*, 41-60.

27. Rabinovich, M. L.; Melnik, M. S.; Boloboba, A. V. Microbial Cellulases (Review). *Applied Biochemistry and Microbiology* **2002,** *38*, 305-321.

28. Bezerra, R. M. F.; Dias, A. A. Enzymatic Kinetic of Cellulose Hydrolysis - Inhibition by Ethanol and Cellobiose. *Applied Biochemistry and Biotechnology* **2005,** *126*, 49-59.

29. Yang, B.; Wyman, C. E. Bsa Treatment to Enhance Enzymatic Hydrolysis of Cellulose in Lignin Containing Substrates. *Biotechnology and Bioengineering* **2006,** *94*, 611-617.

30. Borjesson, J.; Peterson, R.; Tjerneld, F. Enhanced Enzymatic Conversion of Softwood Lignocellulose by Poly(Ethylene Glycol) Addition. *Enzyme and Microbial Technology* **2007,** *40*, 754-762.

31. Medve, J.; Karlsson, J.; Lee, D.; Tjerneld, F. Hydrolysis of Microcrystalline Cellulose by Cellobiohydrolase I and Endoglucanase II from Trichoderma Reesei: Adsorption, Sugar

Production Pattern, and Synergism of the Enzymes. *Biotechnology and Bioengineering* **1998,** *59*, 621-634.

32. Ghose, T. K. Measurement of Cellulase Activities. *Pure and Applied Chemistry* **1987,** *59*, 257-268.

33. Linder, M.; Mattinen, M. L.; Kontteli, M.; Lindeberg, G.; Stahlberg, J.; Drakenberg, T.; Reinikainen, T.; Pettersson, G.; Annila, A. Identification of Functionally Important Amino-Acids in the Cellulose-Binding Domain of Trichoderma-Reesei Cellobiohydrolase-I. *Protein Science* **1995,** *4*, 1056-1064.

34. Johansson, G.; Stahlberg, J.; Lindeberg, G.; Engstrom, A.; Pettersson, G. Isolated Fungal Cellulase Terminal Domains and a Synthetic Minimum Analog Bind to Cellulose. *Febs Letters* **1989,** *243*, 389-393.

35. Lemos, M. A.; Teixeira, J. A.; Mota, M.; Gama, F. M. A Simple Method to Separate Cellulose-Binding Domains of Fungal Cellulases after Digestion by a Protease. *Biotechnology Letters* **2000,** *22*, 703-707.

36. Tomme, P.; Vantilbeurgh, H.; Pettersson, G.; Vandamme, J.; Vandekerckhove, J.; Knowles, J.; Teeri, T.; Claeyssens, M. Studies of the Cellulolytic System of Trichoderma-Reesei Qm-9414 - Analysis of Domain Function in 2 Cellobiohydrolases by Limited Proteolysis. *European Journal of Biochemistry* **1988,** *170*, 575-581.

37. Vantilbeurgh, H.; Tomme, P.; Claeyssens, M.; Bhikhabhai, R.; Pettersson, G. Limited Proteolysis of the Cellobiohydrolase I from Trichoderma-Reesei - Separation of Functional Domains. *Febs Letters* **1986,** *204*, 223-227.

38. Rodahl, M.; Hook, F.; Krozer, A.; Brzezinski, P.; Kasemo, B. Quartz-Crystal Microbalance Setup for Frequency and Q-Factor Measurements in Gaseous and Liquid Environments. *Review of Scientific Instruments* **1995,** *66*, 3924-3930.

39. Rodahl, M.; Kasemo, B. On the Measurement of Thin Liquid Overlayers with the Quartz-Crystal Microbalance. *Sensors and Actuators a-Physical* **1996,** *54*, 448-456.

40. Voinova, M. V.; Rodahl, M.; Jonson, M.; Kasemo, B. Viscoelastic Acoustic Response of Layered Polymer Films at Fluid-Solid Interfaces: Continuum Mechanics Approach. *Physica Scripta* **1999,** *59*, 391-396.

41. Hook, F.; Kasemo, B.; Nylander, T.; Fant, C.; Sott, K.; Elwing, H. Variations in Coupled Water, Viscoelastic Properties, and Film Thickness of a Mefp-1 Protein Film During Adsorption and Cross-Linking: A Quartz Crystal Microbalance with Dissipation Monitoring, Ellipsometry, and Surface Plasmon Resonance Study. *Analytical Chemistry* **2001,** *73*, 5796-5804.

42. Dutta, A. K.; Nayak, A.; Belfort, G. Viscoelastic Properties of Adsorbed and Cross-Linked Polypeptide and Protein Layers at a Solid-Liquid Interface. *Journal of Colloid and Interface Science* **2008,** *324*, 55-60.

43. Larsson, C.; Rodahl, M.; Hook, F. Characterization of DNA Immobilization and Subsequent Hybridization on a 2D Arrangement of Streptavidin on a Biotin-Modified Lipid Bilayer Supported on SiO_2. *Analytical Chemistry* **2003,** *75*, 5080-5087.

44. Holst, M.; Baker, N.; Wang, F. Adaptive Multilevel Finite Element Solution of the Poisson-Boltzmann Equation I. Algorithms and Examples. *Journal of Computational Chemistry* **2000,** *21*, 1319-1342.

45. Baker, N. A.; Sept, D.; Joseph, S.; Holst, M. J.; McCammon, J. A. Electrostatics of Nanosystems: Application to Microtubules and the Ribosome. *Proceedings of the National Academy of Sciences of the United States of America* **2001,** *98*, 10037-10041.

46. Humphrey, W.; Dalke, A.; Schulten, K. VMD: Visual Molecular Dynamics. *Journal of Molecular Graphics* **1996,** *14*, 33-38.

47. Kontturi, E.; Johansson, L. S.; Kontturi, K. S.; Ahonen, P.; Thune, P. C.; Laine, J. Cellulose Nanocrystal Submonolayers by Spin Coating. *Langmuir* **2007,** *23*, 9674-9680.

48. Langmuir, I. The Adsorption of Gases on Plane Surfaces of Glass, Mica and Platinum. *J. Am. Chem. Soc.* **1918,** *40*, 1361-1403.

49. Freundlich, H. *Z.* Ueber die Adsorption in Loesungen. *Phyzik. Chem.* **1907,** *57*, 385-470.

50. Goyal, A.; Ghosh, B.; Eveleigh, D. Characteristics of Fungal Cellulases. *Bioresource Technology* **1991,** *36*, 37-50.

51. Zhang, Y. H. P.; Lynd, L. R. Toward an Aggregated Understanding of Enzymatic Hydrolysis of Cellulose: Noncomplexed Cellulase Systems. *Biotechnology and Bioengineering* **2004,** *88*, 797–824.

52. Divne, C.; Stahlberg, J.; Reinikainen, T.; Ruohonen, L.; Pettersson, G.; Knowles, J. K. C.; Teeri, T. T.; Jones, T. A. The 3-Dimensional Crystal-Structure of the Catalytic Core of Cellobiohydrolase-I from Trichoderma-Reesei. *Science* **1994,** *265*, 524-528.

53. Divne, C.; Stahlberg, J.; Teeri, T. T.; Jones, T. A. High-Resolution Crystal Structures Reveal How a Cellulose Chain Is Bound in the 50 Angstrom Long Tunnel of Cellobiohydrolase I from Trichoderma Reesei. *Journal of Molecular Biology* **1998,** *275*, 309-325.

54. Stahlberg, J.; Divne, C.; Koivula, A.; Piens, K.; Claeyssens, M.; Teeri, T. T.; Jones, T. A. Activity Studies and Crystal Structures of Catalytically Deficient Mutants of Cellobiohydrolase I from Trichoderma Reesei. *Journal of Molecular Biology* **1996,** *264*, 337-349.

55. Kleywegt, G. J.; Zou, J. Y.; Divne, C.; Davies, G. J.; Sinning, I.; Stahlberg, J.; Reinikainen, T.; Srisodsuk, M.; Teeri, T. T.; Jones, T. A. The Crystal Structure of the Catalytic Core Domain of Endoglucanase I from Trichoderma Reesei at 3.6 Angstrom Resolution, and a Comparison with Related Enzymes. *Journal of Molecular Biology* **1997,** *272*, 383-397.

56. Bhikhabhai, R.; Johansson, G.; Pettersson, G. Isolation of Cellulolytic Enzymes from Trichoderma Reesei QM 9414. *J Appl Biochem* **1984,** *6*, 336-45.

57. Shoemaker, S.; Watt, K.; Tsitovsky, G.; Cox, R. Characterization and Properties of Cellulases Purified from Trichoderma-Reesei Strain-L27. *Nature Biotechnology* **1983,** *1*, 687-690.

CHAPTER 5

Effects of the non-ionic surfactant Tween 80 on the adsorption of cellulases onto lignin substrates

5.1. Abstract

Residual lignin in pretreated biomass impedes its enzymatic hydrolysis. Non-ionic surfactants are known to enhance the enzymatic hydrolysis of lignocellulosic biomass but their mechanisms of action are incompletely understood. This study investigates the effect of the non-ionic surfactant Tween 80 on the adsorption of cellulases onto model lignin substrates. Lignin substrates were prepared by spin coating from three different types of lignin: organosolv lignin, kraft lignin, and milled wood lignin. The functional group distributions in the lignins were analyzed by quantitative ^{31}P NMR spectroscopy. The surface energies and surface roughnesses of the substrates were determined by contact angle measurements and atomic force microscopy, respectively. Tween 80 and cellulase adsorption onto the lignin substrates were analyzed by quartz crystal microbalance with dissipation monitoring. Tween 80 adsorbed onto all lignin substrates and effected partial removal of lignin molecules. The ability of Tween 80 to remove lignin molecules from the substrate increased with lignin hydrophobicity. Cellulase appeared to adsorb onto the lignin substrates *via* both hydrophobic and polar interactions. Tween 80 molecules on the substrate's surface seemed to hinder cellulase adsorption *via* hydrophobic interactions and reduced the rate of cellulase adsorption.

5.2. Introduction

As the most abundant natural organic material, lignocellulose has been subject to extensive research because of its potential value in the production of biofuels. Lignocellulosic biomass is composed of a lignin and hemicellulose matrix encapsulating a cellulose scaffold. Functioning as support and protection for the cellulose scaffold against microbial degradation in living plants, lignin causes steric hindrance in the enzymatic hydrolysis of lignocellulosic biomass, limiting the enzyme accessibility of the cellulose scaffold. Researchers have shown that the presence of lignin in the substrate significantly reduces enzymatic hydrolysis yields.[1-5] Besides limiting access to the cellulose scaffold, lignin also causes non-specific adsorption of cellulase onto itself, thus preventing cellulase adsorption onto the cellulose scaffold, a necessary step in the hydrolysis of the scaffold.[6-12] To reduce the recalcitrance of lignocellulosic biomass to chemical and biochemical degradation, pretreatment methods have been developed that break down the lignin–hemicellulose–cellulose matrix and increase the enzyme accessibility of the cellulose scaffold. Chemical pretreatment methods include processes under acidic conditions,[13,14] basic conditions,[13,15,16] and organosolv pulping.[17,18] The caustic conditions during biomass pretreatment inevitably cause changes in the lignin structure, such as the cleavage of β-O-4 ether bonds, similar to those observed during traditional pulping processes.

Non-ionic surfactants have been studied widely for their potential use in the biochemical conversion of lignocellulosic biomass and have been shown to be able to increase enzymatic hydrolysis yields.[19-21] The most widely accepted mechanism for non-ionic surfactants to increase enzymatic hydrolysis yields is the prevention of unproductive enzyme adsorption onto the lignin fraction of the substrate. Reduced unproductive adsorption of cellulase onto lignocellulosic substrates has been observed for the non-ionic surfactants Agrimul,[20] Triton X-100,[20] Triton X-114,[20] Tween 20, [20,22] and Tween 80, [20,23] as well as BSA[8] and polyethylene glycol (PEG).[24,25]

This study was conducted to enhance our understanding of the mechanisms by which non-ionic surfactants prevent non-productive binding of cellulolytic enzymes onto lignin substrates. Tween 80 (polyoxyethylene (20) sorbitan monooleate), consisting of PEGylated sorbitan as the hydrophilic headgroup linked to a monounsaturated, 18-carbon hydrophobic tail, was chosen as the surfactant. The adsorption of cellulase onto untreated and Tween 80-treated model lignin substrates was studied by quartz crystal microbalance with dissipation monitoring (QCM-D).

QCM-D is able to detect minute mass and viscoelasticity changes of adsorbed layers on oscillating quartz crystals by measuring changes in the crystal's oscillation frequencies, Δf, and dissipation factors, ΔD, upon adsorption. Lignin films with thicknesses of ~300 Å and surface roughnesses of ~1.8 Å, suitable for use as model substrates, have previously been prepared by Langmuir–Blodgett deposition.[26-28] Only slightly higher surface roughnesses (0.6–1.5 nm) have been reported for lignin films prepared by spin coating.[29-33] Thus prepared lignin films have been used as model lignin surfaces to study lignin–cellulose interactions in aqueous electrolyte solutions,[31] adsorption of polyelectrolyte or polyelectrolyte complexes onto lignin,[30,32] and the surface energy and wettability of lignin.[33] The lignin substrates for this study were prepared by spin coating from three different types of lignin. Kraft lignin (KL) was chosen as a model for lignin from alkaline pretreatment methods, organosolv lignin (OL) was chosen as a model for lignin from acidic pretreatment methods, and milled wood lignin (MWL) was chosen as a model for native lignin.

5.3. Experimental section

5.3.1. Materials

KL (M_n $5 \cdot 10^3$ g·mol^{-1} M_w $28 \cdot 10^3$ g·mol^{-1}), Tween 80 (SigmaUltra), Celluclast 1.5L (Novozyme), and 2-chloro-4,4,5,5-tetramethyl-1,3,2-dioxaphospholane (CTMDP, 95%) were purchased from Sigma-Aldrich. Sulfuric acid (95.9 wt %, Certified ACS Plus), pyridine (Certified ACS), molecular sieves (4 Å), deuterated chloroform (Cambridge Isotope Laboratories, Inc. 99.8%), endo-N-hydroxy-5-norbornene-2,3-dicarboximide (e-HNDI, Acros Organics, 99+%), chromium (III) acetylacetonate ($Cr(acac)_3$, Acros Organics, 97%), diiodomethane (Acros Organics, 99+%, stabilized), formamide (Acros Organics, 99.5+%, extra pure), citric acid monohydrate (Certified ACS), sodium hydroxide (Acros Organics, 98.5%), hydrogen peroxide (34–37%, Technical Grade), aqueous ammonia (28.9%, Certified ACS Plus), and PEG ("PEG 4000", M_w 4,000 g·mol^{-1}, Bioworld, Biotechnology Grade) were purchased from Fisher Scientific. MWL from hemlock (*Tsuga* sp., M_n $2.6 \cdot 10^3$ g·mol^{-1}, M_w $15.2 \cdot 10^3$ g·mol^{-1})[34] and OL from cottonwood (*Populus trichocharpa*, $M_n < 10^3$ g·mol^{-1}, $M_w < 3 \cdot 10^3$ g·mol^{-1})[34] were kindly

provided by Prof. Em. Wolfgang Glasser. All water used was deionized (DI) water with a resistivity of 18.2 MΩ·cm, obtained from a Millipore Direct-Q 5 Ultrapure Water Systems.

5.3.2. Lignin purification and fractionation

KL and MWL, at a concentration of 1 wt %, were dissolved in 0.75 M aqueous ammonia. OL, also at 1 wt %, was dissolved in 1.5 M aqueous ammonia because it did not dissolve completely in 0.75 M or 1 M aqueous ammonia. The lignin solutions were transferred to Spectra/Por 4 dialysis tubing (MWCO: 12–14 kDa, Spectrum Lab, Inc.) and dialyzed against DI water for removal of the low molecular weight fraction and any water-soluble impurities. After two weeks of dialysis, the lignin suspensions were centrifuged at 25 °C and 4900 rpm for 15 min for removal of any sedimenting larger particles. The aqueous lignin suspensions obtained upon centrifugation were stable, *i.e.* the dispersed lignin particles did not settle to the bottom of the dialysis tubing. This observation has been previously reported for KL by T. Lindström.[35] Finally, the lignin suspensions were concentrated to 1.5 wt % with a rotary evaporator under vacuum at 45 °C and stored in the refrigerator until use.

5.3.3. Quantitative ^{31}P NMR lignin analysis

The functional group distributions in the lignins were analyzed by quantitative ^{31}P NMR spectroscopy according to the method of Granata and Argyropoulos[36] but with e-HNDI instead of cyclohexanol as the internal standard. The method is based on the phosphitylation of lignin hydroxyl and carboxyl groups by CTMDP as shown in Figure 5.1. e-HNDI has previously been shown to be superior to cyclohexanol as an internal standard because it circumvents the interference of the cyclohexanol phosphite peak during integration of the lignin phosphite peaks.[37]

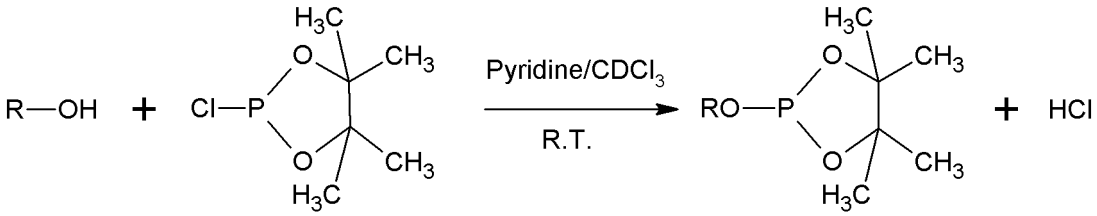

Figure 5.1. Phosphitylation of hydroxyl groups by CTMDP.

In brief, a mixture of pyridine and deuterated chloroform at a volume ratio of 1.6:1 was prepared and dried in the refrigerator over molecular sieves (4 Å) for several hours. The solvent mixture was then used to prepare separate solutions of $Cr(acac)_3$ (5 mg·mL^{-1}), serving as a relaxation agent, and e-HNDI (10.85 mg·mL^{-1}), which were subsequently stored in sealed containers in the refrigerator until use. For NMR sample preparation, an aliquot of the 1.5 wt % aqueous lignin suspension was freeze-dried, and 30 mg of the freeze-dried lignin, in an amber sample vial, was suspended in 500 µL of the solvent mixture by vortexing for 1 min. Then, 150 µL of CTMDP was added, and the reaction mixture was vortexed for 1 min. Upon vortexing, a clear solution was obtained. As the final step in the NMR sample preparation, 200 µL of the e-HNDI and 100 µL of the $Cr(acac)_3$ solution were added to the phosphitylated-lignin solution, after which it was again vortexed for 1 min and transferred to a 5 mm o.d. NMR tube.

Quantitative ^{31}P NMR spectra were acquired immediately after sample preparation with a Varian Unity 400 NMR spectrometer, an observation sweep width of 6600 Hz, and a relaxation time of 25 s between successive pulses. For chemical shift calibration, the peak of the reaction product of water and CTMDP at 132.2 ppm was used as a reference signal.

5.3.4. Lignin substrate preparation

Lignin substrates were prepared on silicon dioxide-coated AT-cut quartz crystals (Q-Sense). The quartz crystals were cleaned by immersion and shaking for 1 min in fresh piranha solution (7:3 (v/v) mixture of sulfuric acid and hydrogen peroxide), then rinsed with DI water, dried in a stream of nitrogen, and irradiated for 15 min with an ozone-producing mercury lamp (UV/Ozone cleaner, Bioforce Nanosciences). To minimize surface contamination, we cleaned the quartz crystals immediately prior to use.

The 1.5 wt % aqueous lignin suspensions, prepared as described above, were diluted by addition of aqueous ammonia and DI water so that clear solutions with a lignin concentration of 1 wt % and an ammonia concentration of 0.75 M for KL and MWL and 1.5 M for OL were obtained. A volume of 140 μL of the 1 wt % lignin solutions was spin-coated (WS-400B-6NPPLite, Laurell Technologies Corp.) for 1 min at 4000 rpm onto the cleaned quartz crystals. As the final step in their preparation, the lignin substrates were dried in a vacuum oven at 65 ℃ for several hours for improved stability in aqueous media.

5.3.5. Surface energy measurements

Lignin substrates for surface energy measurements were prepared by spin coating as described above but on 1 in. × 1 in. silicon wafer pieces. Before spin coating, the wafer pieces, cut from a 15 cm wafer (Wafer World, Inc. West Palm Beach, FL), had been cleaned by immersion for 1 h at 70 ℃ in a mixture of aqueous ammonia, hydrogen peroxide, and DI water at a volume ratio of 1:1:5 and then for 1 h at ambient temperature in fresh piranha solution, rinsed with DI water, and dried in a stream of nitrogen.

The surface energies of untreated and Tween 80-treated lignin substrates were determined from sessile drop contact angles, θ, measured with a video-based contact angle goniometer (FTA200, First Ten Angstroms, Inc.). For Tween 80 treatment, lignin substrates were placed in polystyrene Petri dishes and covered with 1 mM Tween 80 solution in 50 mM sodium citrate buffer (pH 4.8). The solution had been prepared by mixing 2 mL of a 50 mM Tween 80 solution in DI water with 5 mL of a 1 M sodium citrate buffer (pH 4.5) followed by dilution with DI water to a volume of 100 mL. The 1 M sodium citrate buffer had been prepared by dissolution of the appropriate amounts of citric acid monohydrate and sodium hydroxide in DI water. The Petri dishes were then shaken in a shaker for 140 min. After Tween 80 treatment, the substrates were rinsed with DI water, dried in a stream of nitrogen, and placed in a vacuum oven at 65 ℃ for several hours. For surface energy measurement, sessile drops of 20 μL of DI water, diiodomethane, and formamide were placed onto untreated and Tween 80-treated lignin substrates, and the contact angles of at least three different drops were measured for each liquid.

As explained by Notley and Norgren,[33] the three test liquids have Hansen solubility parameters that indicate that the liquids will not dissolve lignin.

The surface energies of the lignin substrates were derived from the measured contact angles with the Owens–Wendt–Rabel–Kaelble method. [38-40] The method is based on the equation

$$\frac{\gamma_l(1+\cos\theta)}{2\sqrt{\gamma_l^d}} = \sqrt{\gamma_s^p\left(\frac{\gamma_l^p}{\gamma_l^d}\right)} + \sqrt{\gamma_s^d} \qquad [5.1]$$

where γ_l is the surface tension of the test liquid, γ_l^d and γ_l^p are the dispersive and polar components of γ_l, respectively, γ_s is the surface energy of the substrate, and γ_s^d and γ_s^p are the dispersive and polar components of, γ_s, respectively. The values for γ_l, γ_l^d, and γ_l^p for the three test liquids are given in Table 5.1. γ_s^d and γ_s^p were obtained from the intercept and slope, respectively, of the line obtained by plotting $\gamma_l(1+\cos\theta)/2\sqrt{\gamma_l^d}$ *versus* $\sqrt{\gamma_l^p/\gamma_l^d}$, where θ was the average of the measured contact angles. γ_s was obtained by summation of γ_s^d and γ_s^p.

Table 5.1. Surface tensions, γ_l, of the test liquids and their polar and dispersive components, γ_l^p and γ_l^d, respectively.[41]

Test liquid	γ_l^p (mN·m^{-1})	γ_l^d (mN·m^{-1})	γ_l (mN·m^{-1})
Water	51	21.8	72.8
Diiodomethane	0	50.8	50.8
Formamide	19	39	58

5.3.6. QCM-D adsorption experiments

Adsorption of Tween 80 and cellulase onto the lignin substrates was analyzed by QCM-D (Q-sense E4). Lignin substrates were placed in QCM-D flow modules, and a 0.25 mL·min^{-1} feed of 50 mM sodium citrate buffer was established with a peristaltic pump. The temperature inside the flow modules was controlled at 22.00 ± 0.02 ℃. When the normalized rate of change of the

3^{rd} overtone frequency, ($\Delta f_3/3$), became less than 2 $Hz \cdot h^{-1}$, the substrates were considered saturated and equilibrated.

In Tween 80 adsorption experiments, the buffer feed was then replaced with a feed of 1 mM Tween 80 solution in buffer with the same flow rate. After 140 min, the sodium citrate buffer feed was restored so that any loosely bound Tween 80 molecules would be rinsed from the substrate. Tween 80 adsorption experiments were terminated after 60 min of buffer rinse.

In cellulase adsorption experiments on untreated lignin substrates, the initial buffer feed was replaced with a feed of cellulase solution in buffer, prepared by dilution of 0.5 g Celluclast 1.5L, a commercial cellulase solution derived from *Trichoderma reesei*, with 50 mM sodium citrate buffer to a volume of 100 mL. After 4 h, the sodium citrate buffer feed was restored so that any reversibly bound cellulase molecules would be rinsed from the substrate. In cellulase adsorption experiments on Tween 80-treated substrates, the initial buffer feed was first replaced with a feed of 1 mM Tween 80 solution in buffer for 140 min and then with a feed to buffer solution for 60min, and finally with a feed of cellulase solution in buffer for 4 h before it was restored. Cellulase adsorption experiments were terminated after 30 min of buffer rinse.

PEG adsorption experiments and cellulase adsorption experiments on PEG-treated lignin substrates were carried out as described above but with a 1 mM PEG solution in buffer instead of the 1 mM Tween 80 solution. The duration for the PEG solution feed was 20 min, as opposed to 140 min for the Tween 80 solution feed, because Δf and ΔD remained constant after only a few minutes of adsorption.

Tween 80 and cellulase adsorption experiments on gold and silica substrates were carried out as described above but with gold-coated or silicon dioxide-coated AT-cut quartz crystals in place of the lignin substrates. The gold-coated quartz crystals were cleaned like the silicon wafer pieces used for the surface energy measurements. The duration for the Tween 80 solution feed was 23 min for the gold substrate and 15 min for the silica substrate, instead of 140 min, and the duration for the cellulase solution feed was 40 min for the gold substrate and 75 min for the silica substrate, instead of 4 h.

Δf and ΔD were recorded in real time at the fundamental frequency (5 MHz) and 6 overtone frequencies (15, 25, 35, 45, 55, and 65 MHz) with QSoft 401 acquisition software (Q-Sense). The surface excess concentrations of adsorbed cellulase on the lignin substrates were estimated

with the QTools modeling center (v3.0, Q-Sense) by modeling Δf and ΔD for the 3rd and 5th overtones with a single-layer Voigt element-based viscoelastic film model[42,43] as described in Chapter 4. For the density and viscosity of the bulk liquid, we used the density and viscosity of water at 22 ℃, which are 998 $kg \cdot m^{-3}$[44] and $0.955 \cdot 10^{-3}$ $kg \cdot m^{-1}s^{-1}$.[45] The density of the viscoelastic film was fixed at 1100 $kg \cdot m^{-3}$.[46]

5.3.7. Substrate imaging and surface roughness determination

Upon completion of the QCM-D adsorption experiments, the lignin substrates were taken out of the flow modules, thoroughly rinsed with DI water, dried in a stream of nitrogen, and placed in a vacuum oven at 65 ℃ for several hours. The Tween 80- and cellulase-treated substrates as well as unused substrates on quartz crystals were imaged with an Asylum Research MFP-3D-BIO atomic force microscope. The substrates were scanned in air at ambient relative humidity and temperature in intermittent-contact mode with OMCL-AC160TS standard silicon probes (Olympus Corp.) with a scan frequency of 1 Hz, and 512 scans with 512 points/scan. RMS surface roughnesses were determined from the entire area of the AFM height image (2 μm × 2 μm or 5 μm × 5 μm, as specified).

5.4. Results and discussion

5.4.1. Distribution of functional groups in the three lignins

The distribution of functional groups in the three lignins was determined by quantitative ^{31}P NMR spectroscopy. The ^{31}P NMR spectra of the lignin samples are shown in Figure 5.2. The signal assignments are based on those established by Granata and Argyropoulos.[36] The measured absolute and relative hydroxyl and carboxyl group contents of the lignin samples, based on peak integrals relative to that of the internal standard, are listed in Table 5.2.

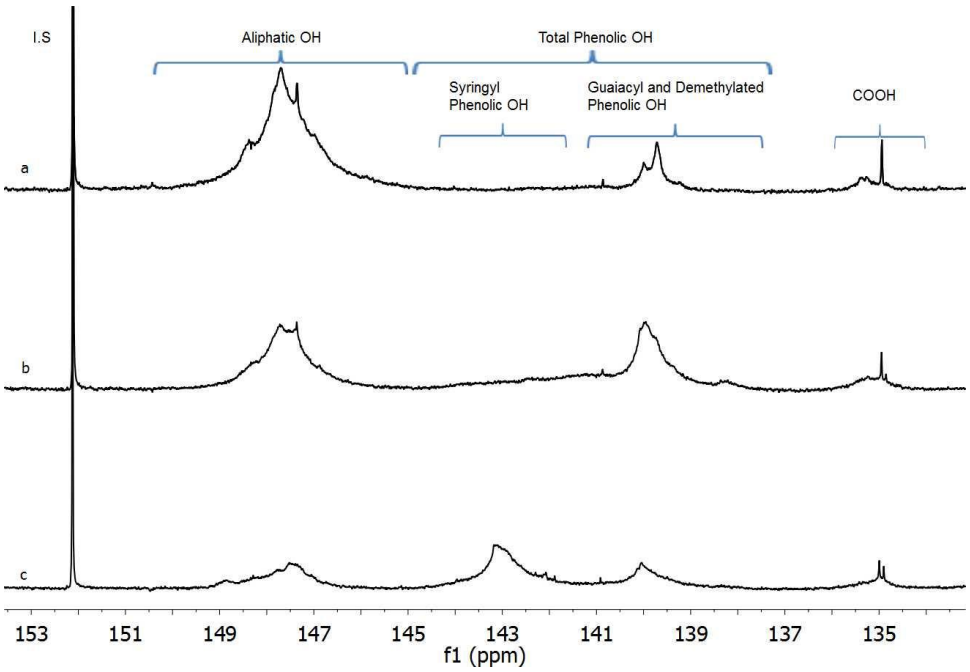

Figure 5.2. Quantitative ^{31}P NMR spectra of (a) MWL, (b) KL, and (c) OL after phosphitylation with CTMDP. The internal standard peak stems from phosphitylated e-HNDI.

Table 5.2. Measured absolute and relative hydroxyl and carboxyl group contents of the three lignins determined by quantitative ^{31}P NMR spectroscopy

	OL		KL		MWL	
Functional group	mmol·g^{-1}	%	mmol·g^{-1}	%	mmol·g^{-1}	%
Aliphatic OH	0.9	28	2.3	46	4.2	87
Guaiacyl and d.m.[a] OH	0.7	21	1.7	33	0.5	10
Syringyl OH	1.5	45	0.8	17	n/a	n/a
COOH	0.2	7	0.3	5	0.1	3
Total phenolic OH	2.2	66	2.5	49	0.5	10
Total OH	3.3	100	5.1	100	4.8	100

[a] demethylated

As seen in Table 5.2, the total measured hydroxyl group content was highest for KL and lowest for OL. The lower total measured hydroxyl group content of OL indicated a higher

hydrophobicity. Two thirds (66%) of the total measured hydroxyl groups of OL were phenolic hydroxyl groups and two thirds of those phenolic hydroxyl groups were syringyl hydroxyl groups. Aliphatic hydroxyl groups made up less than one third (28%) of the total measured hydroxyl groups of OL. In contrast, MWL had mostly aliphatic hydroxyl groups (87%) and only a small number of phenolic hydroxyl groups (10%), which were exclusively guaiacyl and demethylated hydroxyl groups. A low syringyl hydroxyl group content was to be expected for a softwood MWL. The high absolute value for the measured aliphatic hydroxyl group content of 4.22 $mmol \cdot g^{-1}$ was in good agreement with previously published values for softwood MWL, ranging from 4.00 to 4.27 $mmol \cdot g^{-1}$.[33,36,47] KL had nearly equal amounts of aliphatic (46%) and phenolic (49%) hydroxyl groups with syringyl hydroxyl groups making up one third of the measured phenolic hydroxyl group content, as opposed to two thirds in OL. The higher measured phenolic hydroxyl group contents of OL and KL, compared to MWL, were mainly due to the scission of β-O-4 linkages, catalyzed by acids (OL) and bases (KL), during the isolation process. The carboxyl group content was below 7% for all lignins with OL having the highest (6.6%) and MWL the lowest (3%).

5.4.2. Surface properties of the lignin substrates

The lignin substrates were characterized in terms of surface morphology, roughness, and energy. Figure 5.3 shows AFM height images of untreated and Tween 80-treated lignin substrates. The untreated substrates (left column) consisted of spherical lignin particles with diameters of 10–20 nm. Similar morphologies for lignin substrates prepared by spin coating have been reported previously.[29,30,33] It is noteworthy that the particle sizes of the three lignin substrates were similar. Notley and Norgren reported larger particle sizes for lignin substrates from MWL solutions in an acetone–water mixture than for substrates from KL solutions in aqueous ammonia.[33] The particle size of lignin substrates prepared by spin coating of lignin solutions probably depends on the degree of dissolution of the lignin in the solvent. The uniform small particle size of the lignin substrates observed in Figure 5.3 indicated that the three lignins were well dissolved in the aqueous ammonia solvent during substrate preparation.

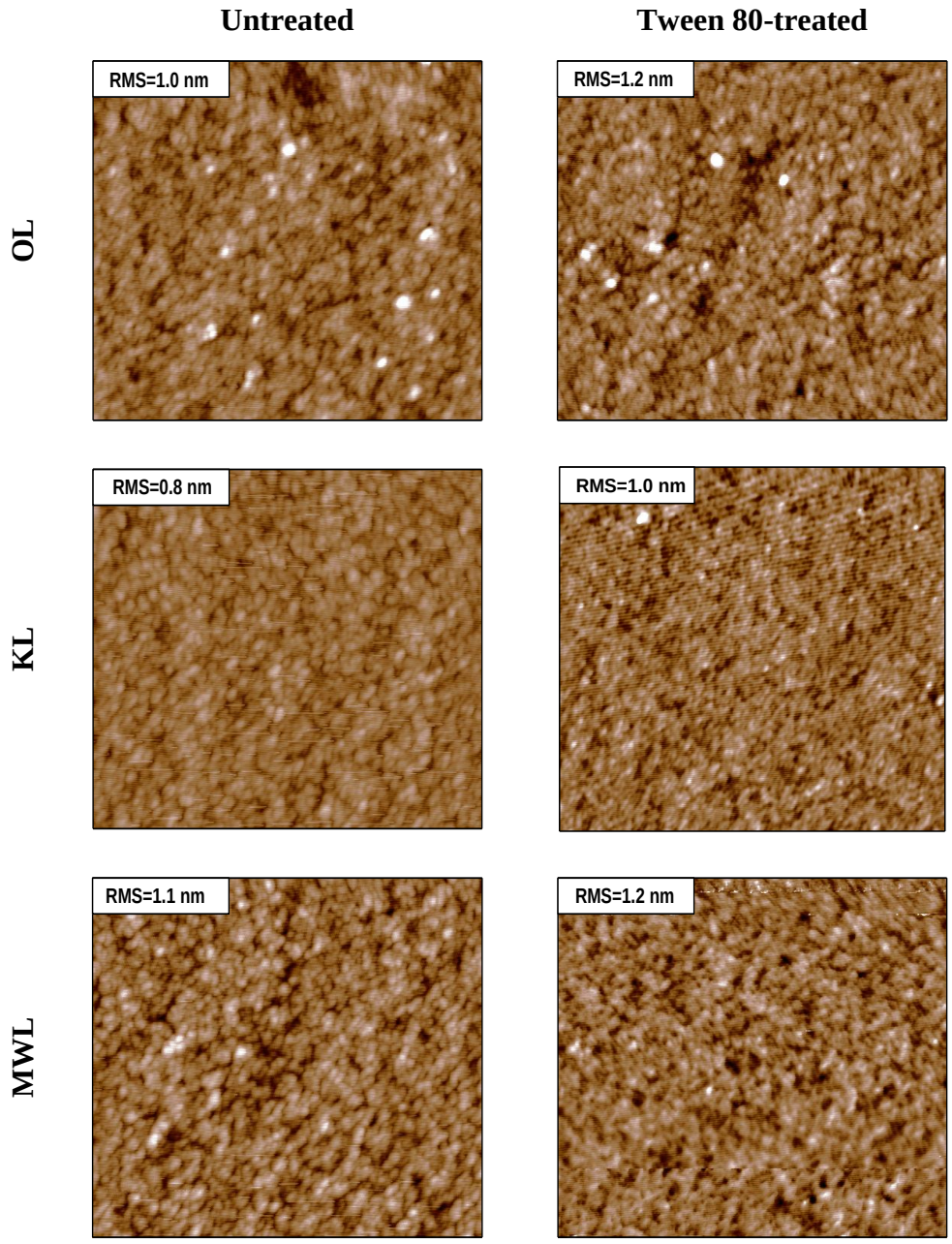

Figure 5.3. AFM height images of untreated and Tween 80-treated lignin substrates. The scan size and z-scale for the images are 2 μm × 2 μm and 8 nm, respectively.

Figure 5.3 also shows that the substrates were smooth and homogeneous without cracks or holes. The measured surface roughnesses of 1.0 nm for the OL substrate, 0.8 nm for the KL

substrate, and 1.1 nm for the MWL substrate were in good agreement with previously published values, ranging from 0.6 to 1.6 nm.[29,30,32,33,48]

The Tween 80-treated lignin substrates (right column) had similar morphologies as the untreated substrates but consistently higher surface roughnesses. A possible reason for the increase in surface roughness upon Tween 80 treatment will be given in the next section. With total surface roughnesses of 1.0–1.2 nm, however, the Tween 80-treated lignin substrates were still smooth enough for contact angle and QCM-D adsorption measurements.

The average contact angles of the three test liquids on untreated and Tween 80-treated lignin substrates are listed in Table C.1 in Appendix C. The surface energies and their polar and dispersive components, determined from those contact angles, are listed in Table 5.3.

Table 5.3. Surface energies, γ_s, of untreated and Tween 80-treated lignin substrates and their polar and dispersive components, γ_s^p and γ_s^d, respectively[a]

	OL		KL		MWL	
Γ	untreated	treated	untreated	treated	untreated	Treated
γ_s (mN·m^{-1})	54.2 ± 1.7	53.9 ± 1.2	55.5 ± 0.5	54.8 ± 1.7	58.1 ± 2.9	58.3 ± 4.3
γ_s^p (mN·m^{-1})	8.1 ± 0.7	11.1 ± 0.6	9.3 ± 0.2	12.5 ± 0.9	13.4 ± 1.4	15.2 ± 2.2
γ_s^d (mN·m^{-1})	46.1 ± 1.6	42.8 ± 1.1	46.2 ± 0.5	42.3 ± 1.5	44.7 ± 2.5	43.1 ± 3.6
γ_s^p (% of γ_s)	14.9 ± 1.4	20.5 ± 1.2	16.8 ± 0.4	22.8 ± 1.9	23.1 ± 2.9	26.0 ± 4.6
γ_s^d (% of γ_s)	85.1 ± 4.6	79.5 ± 3.2	83.2 ± 1.3	77.2 ± 4.3	76.9 ± 6.7	74.0 ± 9.7

[a] Data are means ± one standard deviation from the linear regression analysis.

As seen in Table 5.3, the OL substrate had the smallest polar component and largest dispersive component of the three substrates. This result was consistent with the results from the NMR lignin analysis, which showed that OL had the lowest total hydroxyl group content. The MWL substrate had a larger polar component than the KL substrate despite the fact that KL had a slightly higher total hydroxyl group content (Table 5.2). The larger polar component of the MWL substrate could be due to the higher aliphatic hydroxyl group content of MWL (Table 5.2). The aliphatic hydroxyl groups might protrude more from the substrate's surface than phenolic hydroxyl groups and, thus, dominate its surface chemistry. Treatment of the lignin substrates

with Tween 80 increased the polar component of the surface energy (Table 5.3), *i.e.* rendered the surfaces more hydrophilic. A possible explanation for the increase in hydrophilicity could be that the Tween 80 molecules interacted with the lignin substrates through their hydrocarbon tails, leaving the hydrophilic headgroups exposed on the substrate's surface. The presence of Tween 80 headgroups on the surface of the lignin substrates could have caused the observed increase in the polar component of their surface energies.

5.4.3. Tween 80 adsorption experiments

The adsorption of Tween 80 onto the lignin substrates was analyzed by QCM-D. Figure 5.4 shows curves of the normalized frequency change, ($\Delta f_n/n$), where n is the frequency's overtone number, and ΔD from Tween 80 adsorption experiments on the three lignin substrates.

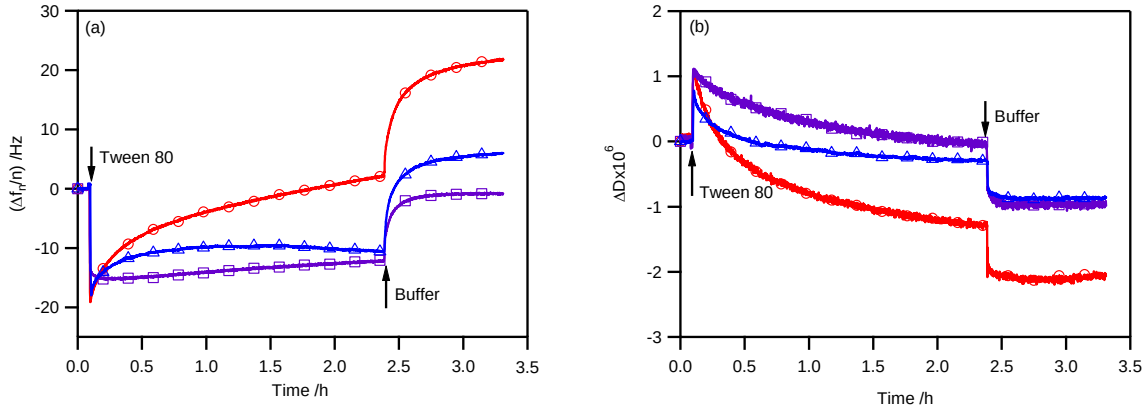

Figure 5.4. (a) ($\Delta f_n/n$) and (b) ΔD curves (5th overtone) from Tween 80 adsorption experiments on lignin substrates: OL substrate (red ○), KL substrate (blue △), and MWL substrate (purple □). Arrows indicate a switch in liquid feed to the QCM-D flow modules.

The initial rapid decrease in ($\Delta f_n/n$) (Figure 5.4a), upon switch of the liquid feed to the flow modules from buffer to Tween 80 solution, was due to the adsorption of Tween 80 molecules onto the lignin substrate. The decrease in ($\Delta f_n/n$) was associated with an increase in ΔD (Figure 5.4b) due to the soft, energy dissipative nature of the adsorbed surfactant layer. After reaching a

minimum, having different magnitudes for the different substrates, ($\Delta f_n/n$) gradually increased. The increase in ($\Delta f_n/n$) after the minimum was most pronounced for the OL substrate and least pronounced for the MWL substrate. An increase in ($\Delta f_n/n$) signifies a decrease in mass on the quartz crystal. The observed mass decrease was most likely due to Tween 80-mediated removal of lignin from the substrate. Amphiphilic micelle-forming molecules, like Tween 80, are able to solubilize hydrophobic molecules in aqueous media within their hydrophobic tails. Thus, Tween 80 may have solubilized lignin molecules on the surface of the lignin substrates, which would have subsequently been carried away in the liquid stream. The gradual increase in ($\Delta f_n/n$) was associated with a gradual decrease in ΔD, indicating that the surface layer became more rigid and dissipated less energy during oscillation of the quartz crystal. An increase in rigidity would be consistent with the postulated removal of lignin molecules from the substrate and the related decrease in the lignin substrate's thickness. Erosion of the lignin substrates by Tween 80 could have been the reason for the observed increase in surface roughness of the substrates upon Tween 80 treatment (Figure 5.3).

After 140 min, the liquid feed to the flow modules was switched from the Tween 80 solution back to buffer. Upon the switch, indicated by an arrow in Figure 5.4a, a rapid increase in ($\Delta f_n/n$) was observed. The increase was most likely due to the desorption of Tween 80 molecules and possibly removal of some loose, partially solubilized lignin molecules from the substrate's surface. The ($\Delta f_n/n$) increase was associated with a sharp decrease in ΔD, indicating a rapid increase in the substrate's rigidity, which would be consistent with the disappearance of the soft surfactant layer on the lignin substrate's surface.

The values for the ($\Delta f_n/n$) decrease upon switch of the liquid feed from buffer to Tween 80 solution, $\Delta(\Delta f_n/n)_{\mathrm{I}}$, the ($\Delta f_n/n$) increase from the minimum after 140 min of Tween 80 solution feed, $\Delta(\Delta f_n/n)_{\mathrm{II}}$, and the ($\Delta f_n/n$) increase upon switch from Tween 80 solution back to buffer, $\Delta(\Delta f_n/n)_{\mathrm{III}}$, are listed in Table 5.4.

Table 5.4. Values for $\Delta(\Delta f_n/n)_I$,[a] $\Delta(\Delta f_n/n)_{II}$,[b] and $\Delta(\Delta f_n/n)_{III}$.[c,d]

Substrate	$\Delta(\Delta f_n/n)_I$ (Hz)	$\Delta(\Delta f_n/n)_{II}$ (Hz)	$\Delta(\Delta f_n/n)_{III}$ (Hz)
OL	–20.5 ± 0.9	20.7 ± 2.0	19.4 ± 1.3
KL	–19.5 ± 0.9	8.1 ± 0.7	15.9 ± 1.0
MWL	–15.2 ± 0.8	5.0 ± 0.5	10.7 ± 1.4

[a] $(\Delta f_n/n)$ decrease upon switch of the liquid feed from buffer to Tween 80 solution
[b] $(\Delta f_n/n)$ increase from the minimum after 140 min of Tween 80 solution feed
[c] $(\Delta f_n/n)$ increase upon switch from Tween 80 solution back to buffer
[d] Data are means ± one standard deviation of three measurements.

The magnitude of $\Delta(\Delta f_n/n)_I$ was largest for the OL substrate and smallest for the MWL substrate. The magnitude of $\Delta(\Delta f_n/n)_I$ is a measure for the amount of Tween 80 adsorbed on the substrate. In the previous section, it was shown that the MWL substrate had the largest polar surface energy component and the OL substrate had the largest dispersive surface energy component. The fact that more Tween 80 adsorbed onto the OL substrate than onto the KL and MWL substrates suggested that hydrophobic interactions played a role in the adsorption of Tween 80 onto the lignin substrates. $\Delta(\Delta f_n/n)_{II}$ was also largest for the OL substrate and smallest for the MWL substrate. $\Delta(\Delta f_n/n)_{II}$ is a measure for the amount of lignin removed by Tween 80 from the lignin substrate. The fact that $\Delta(\Delta f_n/n)_{II}$ was largest for the OL substrate suggested that Tween 80 removed more lignin from the OL substrate than from the KL and MWL substrates during the 140 min of Tween 80 solution feed. For all substrates, the magnitude of $\Delta(\Delta f_n/n)_{III}$ was smaller than the magnitude of $\Delta(\Delta f_n/n)_I$. The difference in magnitudes suggested that some Tween 80 molecules stayed adsorbed on the lignin substrate after the switch of the liquid feed back to buffer. This interpretation is consistent with the results from the surface energy measurements, which showed changes in the surface energy of the substrates upon Tween 80 treatment after rinsing of the substrates with DI water, suggesting that some Tween 80 molecules were irreversibly adsorbed on the substrates.

To further analyze the role of hydrophobic interactions in the adsorption of Tween 80 on lignin substrates, we studied the adsorption of PEG, which is a component of the hydrophilic head group of Tween 80 molecules, on the lignin substrates. Figure 5.5 shows $(\Delta f_n/n)$ and ΔD curves for the three lignin substrates from PEG adsorption experiments.

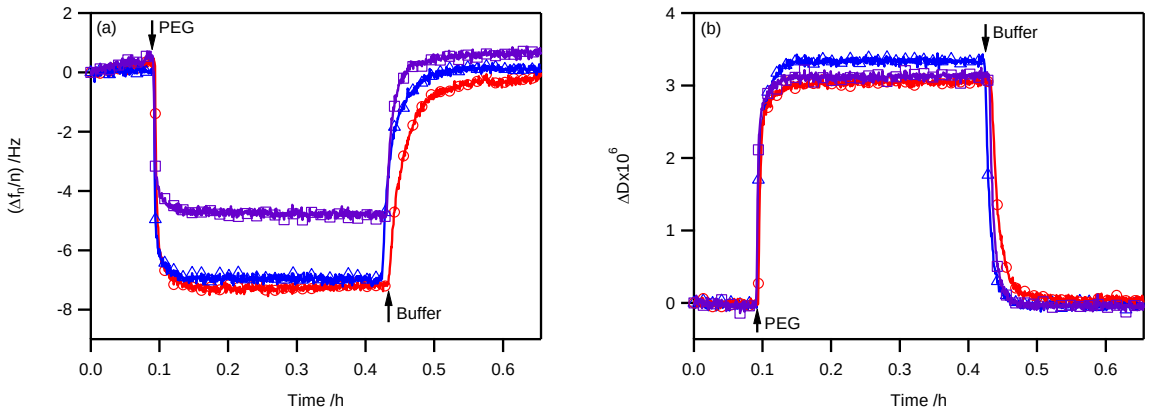

Figure 5.5. (a) ($\Delta f_n/n$) and (b) ΔD curves (5^{th} overtone) from PEG adsorption experiments on lignin substrates: OL substrate (red ○), KL substrate (blue △), and MWL substrate (purple □). Arrows indicate a switch in liquid feed to the QCM-D flow modules.

A switch of the liquid feed to the flow modules from buffer to a 1 mM PEG solution in buffer resulted in a rapid decrease in ($\Delta f_n/n$) and increase in ΔD. The changes in ($\Delta f_n/n$) and ΔD upon the switch could either be due to the change in density and viscosity of the liquid feed or the adsorption of PEG molecules on the lignin substrates or a combination of both. The magnitude of the ($\Delta f_n/n$) decrease, however, was much smaller than that observed for Tween 80. The smaller magnitude of the ($\Delta f_n/n$) decrease indicated that less PEG adsorbed onto the lignin substrates than Tween 80. ($\Delta f_n/n$) stayed nearly constant during the period of PEG solution feed (20 min). The absence of a ($\Delta f_n/n$) increase, observed for Tween 80, indicated that PEG did not remove any lignin molecules. Upon switch of the liquid feed back to buffer, ($\Delta f_n/n$) rapidly increased and ΔD rapidly decreased back to their initial values. Return of ($\Delta f_n/n$) and ΔD to their initial values indicated that PEG had completely desorbed and no lignin had been removed from the substrate. The experiments confirmed that the hydrophobic tail of Tween 80 was critical in the adsorption of Tween 80 onto lignin substrates and in the removal of lignin molecules by Tween 80.

5.4.4. Cellulase adsorption experiments

Figure 5.6 shows ($\Delta f_n/n$) and ΔD curves from cellulase QCM-D adsorption experiments on untreated and Tween 80-treated lignin substrates. PEG-treated substrates were included in the study for comparison. As seen in Figure 5.6, adsorption of cellulase onto the lignin substrates caused a large decrease in ($\Delta f_n/n$) (> 50 Hz) and increase in ΔD (> $5 \cdot 10^{6}$), indicating the build-up of thick, soft cellulase layers on the lignin substrates. Switch of the liquid feed to the flow modules from cellulase solution to buffer, marked by an arrow in Figure 5.6, only caused a small ($\Delta f_n/n$) increase (< 5 Hz) and ΔD decrease (< $1 \cdot 10^{-6}$). The fact that the ($\Delta f_n/n$) increase and ΔD decrease upon switch of the feed were small suggested that binding of the cellulase to the substrates was largely irreversible and the extent of cellulase desorption from the substrates was low.

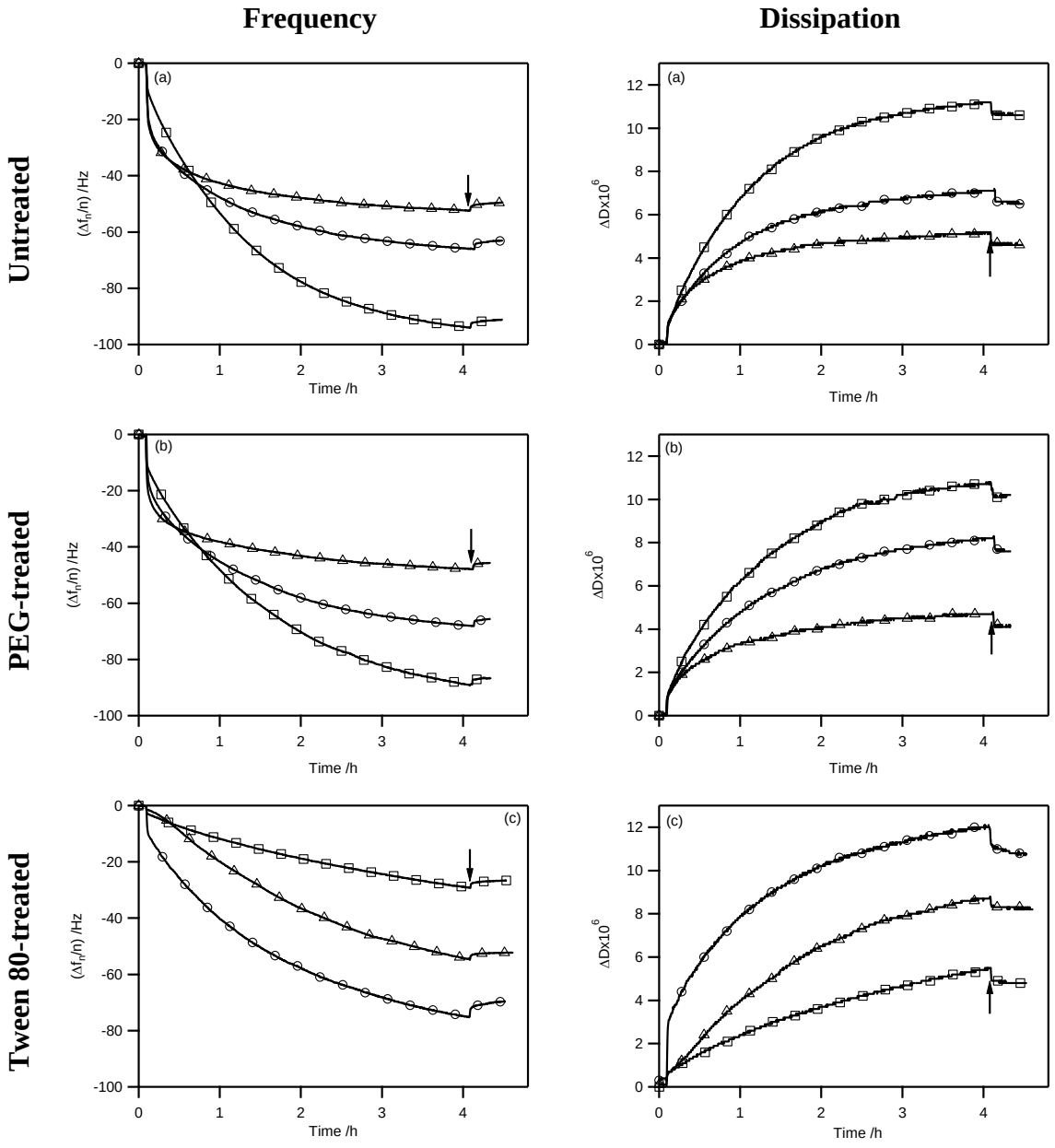

Figure 5.6. ($\Delta f_n/n$) and ΔD curves (5^{th} overtone) from cellulase adsorption experiments on (a) untreated, (b) PEG-treated, and (c) Tween 80-treated lignin substrates: OL substrate (○), KL substrate (△), and MWL substrate (□). Arrows indicate a switch in liquid feed to the QCM-D flow modules from cellulase solution to buffer.

In the case of untreated substrates (Figure 5.6a), the ($\Delta f_n/n$) decrease after 4 h of cellulase adsorption was largest for the MWL substrate and smallest for the KL substrate. However, the initial decrease in ($\Delta f_n/n$) was much faster for the OL and KL substrate than for the MWL substrate. The surface excess concentrations of cellulase on the lignin substrates after 10 min and 4 h of adsorption were estimated by viscoelastic modeling of the ($\Delta f_n/n$) and ΔD curves. The results from data modeling will be discussed in the next section.

The ($\Delta f_n/n$) and ΔD curves for PEG-treated lignin substrates (Figure 5.6b) were similar to those for the untreated substrates (Figure 5.6a). A similar behavior of the PEG-treated substrates to that of the untreated substrates was expected because, as shown in the previous section, PEG adsorption onto lignin substrates was nearly quantitatively reversible by buffer rinse. Thus, when the feed to the flow modules in the cellulase adsorption experiments was switched from PEG solution to cellulase solution, most of the PEG molecules probably desorbed from the lignin substrates and were rinsed off of the surface by the cellulase solution before they could have an effect on cellulase adsorption.

Treatment of the lignin substrates with Tween 80 changed cellulase adsorption dramatically (Figure 5.6c). The ($\Delta f_n/n$) decrease after 4 h of cellulase adsorption was larger for the Tween 80-treated OL and KL substrate than for the untreated substrates but was significantly reduced for the Tween 80-treated MWL substrate, compared to the untreated substrate, to the extent that the MWL substrate now had the smallest ($\Delta f_n/n$) decrease of the three substrates, as opposed to the largest, as in Figure 5.6a. In addition, the initial rapid decrease in ($\Delta f_n/n$) was no longer observed for the Tween 80-treated KL substrate and was significantly reduced for the OL substrate. As mentioned above, the adsorption data will be discussed in quantitative terms in the next section.

To determine the reason for the initial rapid decrease in the ($\Delta f_n/n$) curves of the untreated OL and KL substrates, which was missing from the curve of the MWL substrate, as well as the effect of Tween 80 on this decrease, we studied the adsorption of cellulase onto untreated and Tween 80-treated gold-coated and silica-coated quartz crystals. The ($\Delta f_n/n$) and ΔD curves from cellulase adsorption experiments on untreated and Tween 80-treated gold substrates are shown in Figure 5.7. Adsorption of Tween 80 molecules during the Tween 80 treatment prior to the cellulase adsorption experiment had caused an overall ($\Delta f_n/n$) change of –7 Hz (after the buffer rinse) indicating that the Tween 80-treated gold substrate had Tween 80 molecules attached to its

surface. (The ($\Delta f_n/n$) and ΔD curves from the Tween 80 adsorption experiments on the gold substrate are shown in Figure C.1 in Appendix C.)

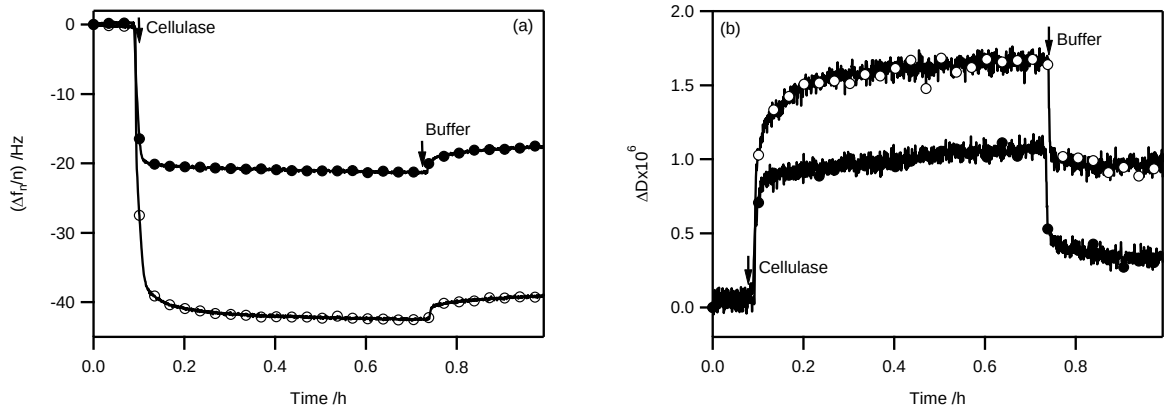

Figure 5.7. (a) ($\Delta f_n/n$) and (b) ΔD curves (5th overtone) from cellulase adsorption experiments on untreated (open circle) and Tween 80-treated (filled circle) gold substrates. Arrows indicate a switch in liquid feed to the QCM-D flow modules.

As seen in Figure 5.7a, cellulase adsorption onto both the untreated and Tween 80-treated gold substrate was rapid, reached a limit, and was nearly completely irreversible. More cellulose adsorbed onto the untreated gold substrate than onto the Tween 80-treated substrate. Gold surfaces are generally hydrophobic because of rapid contamination with carbonaceous materials, which has been shown to increase the contact angle of water to 30–40 ° after 10 min of exposure of the gold surface to atmospheric air.[49] Adsorption of both Tween 80 and cellulase molecules onto the untreated gold substrate could therefore have been driven by hydrophobic interactions. The fact that cellulase adsorption onto the untreated gold substrate was rapid might have indicated that the initial rapid decrease in the ($\Delta f_n/n$) curves of the untreated OL and KL substrates was due to cellulase adsorption *via* hydrophobic interactions (onto hydrophobic adsorption sites). Cellulases are known to use hydrophobic interactions, originating from three tyrosine residues in their cellulose binding domain, for adsorption onto cellulose.[50-52] Consequently, hydrophobic interactions between the tyrosine residues and the aromatic rings of lignin could be the reason for the initial rapid cellulase adsorption onto the OL and KL substrates. Figure 5.7a also shows that adsorbed Tween 80 molecules hinder the adsorption of cellulase. If

Tween 80 adsorption to gold is through the hydrophobic tails, cellulase adsorption is likely sterically inhibited by the swollen PEG portion of the Tween 80 molecules. The fact that some cellulase adsorption was still observed on the Tween 80-treated gold substrate indicated that not all adsorption sites were occupied by Tween 80 molecules or that the cellulase molecules interacted with the Tween 80 layer.

The ($\Delta f_n/n$) and ΔD curves from cellulase adsorption experiments on untreated and Tween 80-treated silica substrates are shown in Figure 5.8. The large overall ($\Delta f_n/n$) decrease during the Tween 80 treatment of the substrate (Figure C.2, Appendix C) of 25 Hz indicating that the Tween 80-treated silica substrate had a large number of Tween 80 molecules attached to its surface.

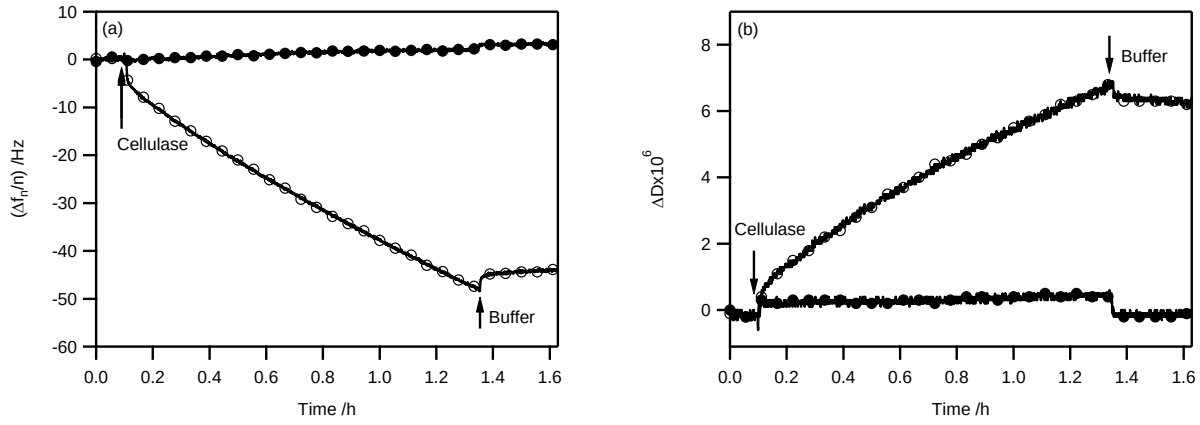

Figure 5.8. (a) ($\Delta f_n/n$) and (b) ΔD curves (5^{th} overtone) from cellulase adsorption experiments on untreated (open circle) and Tween 80-treated (filled circle) silica substrates. Arrows indicate a switch in liquid feed to the QCM-D flow modules.

As seen in Figure 5.8a, cellulase adsorption onto the untreated silica substrate was gradual, and did not saturate the surface during the experiment, and was nearly completely irreversible. Cellulase adsorption onto the Tween 80-treated silica substrate was minimal. Silica surfaces cleaned with piranha solution contain a large number of silanol groups enabling hydrogen bonding-driven adsorption processes. In addition, the Si–O bonds in silica are polar and can interact with adsorbates through Keesom and Debye forces. Thus, adsorption of both Tween 80 and cellulase molecules onto the untreated silica substrate was likely driven by polar interactions.

The fact that cellulase adsorption onto the untreated silica substrate was gradual allowed the conclusion that the gradual decrease in the ($\Delta f_n/n$) curves of the MWL and Tween 80-treated lignin substrates was in large part due to cellulase adsorption *via* polar interactions (onto hydrophilic adsorption sites). Figure 5.8a also shows that Tween 80 molecules that are adsorbed *via* polar interactions completely suppress the adsorption of cellulase possibly by blocking the substrate's hydrophilic adsorption sites.

In Figure 5.9, the QCM-D data is replotted as ΔD *versus* ($\Delta f_n/n$). *D–f* plots eliminate time as an explicit parameter and instead present the energy dissipation as a function of unit mass coupled to the quartz crystal.[53-55] The slope of a *D–f* curve provides information about the structural properties of the forming adsorption layer. A small slope indicates a mass increase with small dissipation increase, characteristic for a non-hydrated, rigid (elastic) layer. A large slope indicates a mass increase with large dissipation increase, characteristic for a hydrated, soft (viscoelastic) layer.[54,56] As seen in Figures 5.9a and b, the cellulase adsorption process on the untreated OL and KL substrates had two stages, represented by two slopes. The slope during the initial stage was low and therefore indicated that the adsorbed layer was rigid and contained little water. This stage corresponded to the initial rapid decrease in ($\Delta f_n/n$) observed for the OL and KL substrates in Figure 5.6a. As discussed above, this decrease was possibly due to cellulase adsorption *via* hydrophobic interactions. The hydrophobic interactions likely caused the expulsion of water molecules from the interface between the adsorbed cellulase layer and the substrate, allowing the adsorbed layer to couple strongly to the substrate and dissipate little energy during crystal oscillation. An alternative explanation could be that the cellulase molecules adsorbed onto these substrates in a flat conformation. The final adsorption stage had a larger slope, which indicated the build-up of a hydrated layer. This stage corresponded to the gradual ($\Delta f_n/n$) decrease following the initial rapid decrease. As discussed above, this decrease might have been in large part due to cellulase adsorption *via* polar interactions. A cellulase layer held together by polar interactions will contain more water molecules than a cellulase layer formed *via* hydrophobic interactions and will therefore be softer and more energy dissipative.

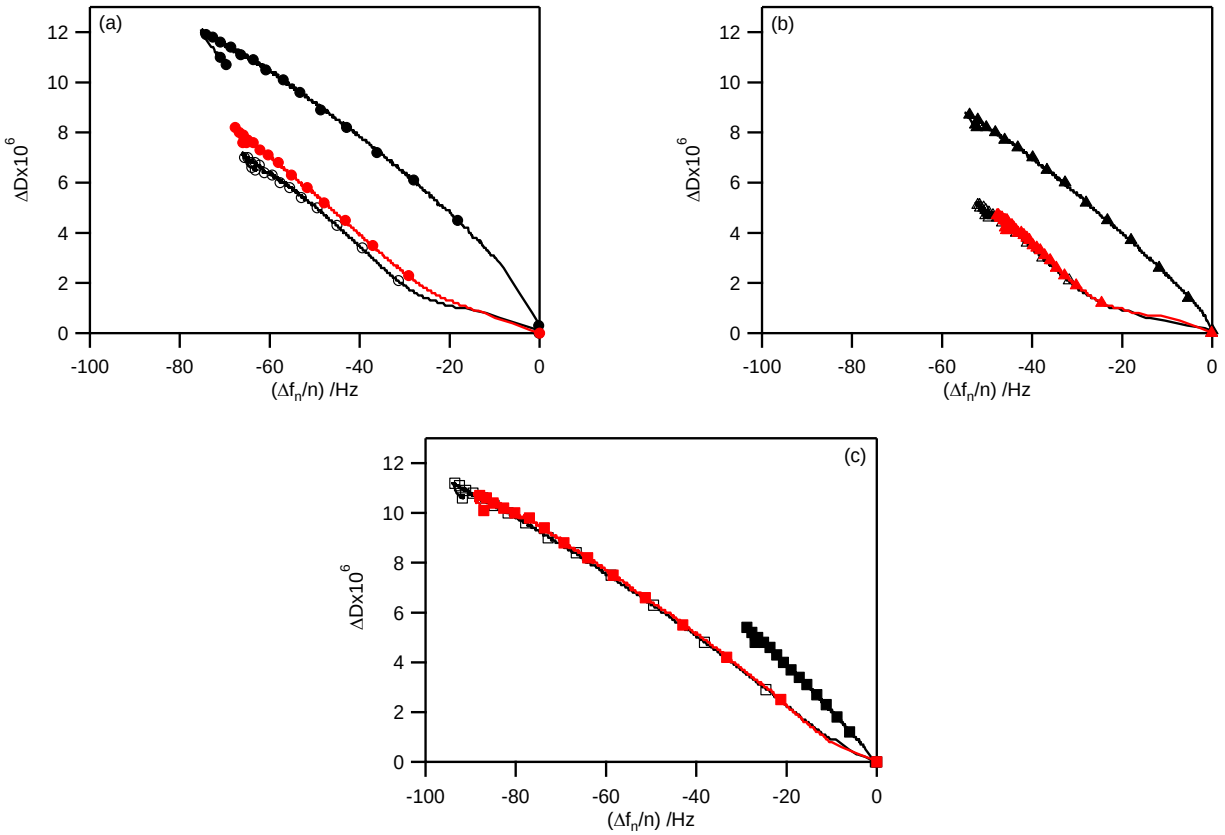

Figure 5.9. Plots of ΔD *versus* $(\Delta f_n/n)$ (5^{th} overtone) for the adsorption of cellulase onto untreated (black open symbols), PEG-treated (red filled symbols), and Tween 80-treated (black filled symbols) lignin substrates: (a) OL; (b) KL; (c) MWL. (Markers are spaced at 100 data points for clarity.)

The *D–f* curve of the untreated MWL substrate (Figure 5.9c) did not exhibit a low slope section. The absence of the low slope section arose from the differences in $(\Delta f_n/n)$ observed at the start of the adsorption process in Figure 5.6a. As shown above, MWL had more aliphatic hydroxyl groups than OL and KL, and the MWL substrate had a larger polar surface energy component than the OL and KL substrates. The aliphatic hydroxyl groups on the surface of the MWL substrate might have shielded the hydrophobic adsorption sites and promoted adsorption through hydrogen bonding. The high slope of the *D–f* curve indicated a hydrated, soft adsorption layer for the MWL substrate consistent with hydrogen bonding as the driving force for adsorption.

The *D–f* curves for the PEG-treated lignin substrates closely coincided with those for the untreated substrates and thus confirmed that PEG-treatment of the lignin substrates had no effect on cellulase adsorption. The *D–f* curves for the Tween 80-treated substrates were clearly different from those for the untreated substrates. The curves for the Tween 80-treated OL and KL substrates were missing the low slope section observed in the curves for the untreated substrates and had slopes similar to those of the high slope sections of the curves for the untreated substrates. As shown above, Tween 80 treatment increased the polar surface energy component of the substrates possibly by filling the hydrophobic adsorption sites of the substrates with Tween 80 molecules exposing their polar headgroups. The absence of the low slope section in the *D–f* curves for the Tween 80-treated OL and KL substrates indicated that rapid adsorption of cellulase, assumed to occur *via* hydrophobic interactions, was suppressed possibly by hydrophobically-adsorbed Tween 80 molecules blocking the hydrophobic adsorption sites. The high slopes of the *D–f* curves for the Tween 80-treated OL and KL substrates suggested that the adsorbed layer was soft and hydrated and therefore might have been based in large part on hydrogen bonding or other polar interactions. The *D–f* curve for the Tween 80-treated MWL substrates had a higher slope than the curve for the untreated substrate, indicating that the adsorbed cellulase layer was more hydrated on the Tween 80-treated MWL substrate, having a larger polar surface energy component, than on the untreated substrate, having a smaller polar surface energy component.

The values for the D/f ratio ($\Delta D/(\Delta f_n/n)$) at the end of the experiment, which is a measure for the extent of hydration of the adsorbed cellulase layer, were $10.4 \cdot 10^{-8}$ Hz^{-1}, $9.5 \cdot 10^{-8}$ Hz^{-1}, and $11.6 \cdot 10^{-8}$ Hz^{-1} for the untreated OL, KL, and MWL substrate, respectively, $11.7 \cdot 10^{-8}$ Hz^{-1}, $9.4 \cdot 10^{-8}$ Hz^{-1}, and $11.8 \cdot 10^{-8}$ Hz^{-1} for the PEG-treated OL, KL, and MWL substrate, respectively, and $15.4 \cdot 10^{-8}$ Hz^{-1}, $15.7 \cdot 10^{-8}$ Hz^{-1}, and $18.0 \cdot 10^{-8}$ Hz^{-1} for the Tween 80-treated OL, KL, and MWL substrate, respectively. The higher D/f ratios for the Tween 80-treated substrates, compared to those for the untreated substrates, indicated that the adsorbed cellulase layers on the Tween 80-treated substrates were more hydrated. The greater extent of hydration of the adsorbed cellulase layers on the Tween 80-treated substrates was consistent with the higher polarity and hydrophilicity of the Tween 80-treated lignin substrates compared to the untreated ones.

5.4.5. Quantification and visualization of cellulase on the lignin substrates

The surface excess concentrations of cellulase on the untreated and Tween 80-treated lignin substrates after 10 min and 4 h of adsorption, determined by viscoelastic modeling of the ($\Delta f_n/n$) and ΔD curves, are listed in Table 5.5. The surface excess concentration of an adsorbate on a substrate depends on the surface area accessible to the adsorbate. This parameter was not quantified for the lignin substrates. However, because the lignin solutions used for spin coating had the same lignin concentration and the surface roughnesses for the substrates were similar, the accessible surface area should be similar, at least for the untreated substrates. The accessible surface area of the Tween 80-treated substrates might differ between the substrates because of the different extents of substrate erosion during the Tween 80 treatment. As shown above, the amount of lignin removed during the Tween 80 treatment was largest for the OL substrate and smallest for the MWL substrate ($\Delta(\Delta f_n/n)_{II}$ values in Table 5.4). Therefore, the Tween 80-treated OL substrate might have had a larger and the Tween 80-treated MWL substrate a smaller surface area for adsorption than the Tween 80-treated KL substrate. In any case, the surface excess concentrations of cellulase on the lignin substrates should be compared with caution.

Table 5.5. Surface excess concentrations of adsorbed cellulase on untreated and Tween 80-treated lignin substrates after 10 min and 4 h of adsorption[a,b]

	Cellulase surface excess concentration ($mg \cdot m^{-2}$)			
	untreated		Tween 80-treated	
Substrate	10 min	4 h	10 min	4 h
OL	6.0 ± 0.3	13.9 ± 0.5	5.4 ± 0.3	16.5 ± 1.2
KL	5.5 ± 0.5	9.5 ± 0.4	1.3 ± 0.1	11.9 ± 0.6
MWL	3.7 ± 0.3	17.5 ± 0.9	1.4 ± 0.2	6.8 ± 0.1

[a] determined by viscoelastic modeling of Δf and ΔD for the 3rd and 5th overtones. The density of the adsorbed cellulase film was fixed at 1100 $kg \cdot m^{-3}$.
[a] Data are means ± one standard deviation of three measurements.

For the untreated lignin substrates, the surface excess concentrations of cellulase after 10 min of adsorption were highest on the OL substrate and lowest on the MWL substrate. For the

OL substrate, it was 43% and for the KL substrate 58% of the surface excess concentration after 4 h of adsorption. In other words, about half of the cellulase layer present on these substrates after 4 h formed during the first 10 min. In the previous section, it was shown that the rapid build-up of the initial cellulase layer on the untreated OL and KL substrates, which was not observed on the MWL substrate, might have been driven by hydrophobic interactions. The fact that the OL substrate, having the smallest polar surface energy component of the substrates, had the highest surface excess concentration after 10 min of adsorption, and the MWL substrate, having the largest polar surface energy component, had the lowest, was consistent with hydrophobic interactions as the driving force for the initial stage of cellulase adsorption on the OL and KL substrates.

Despite having the lowest surface excess concentration of cellulase after 10 min of adsorption, the untreated MWL substrate had the highest surface excess concentration after 4 h. It was in fact more than 84% higher than that of the KL substrate, which had the lowest surface excess concentration after 4 h. In the previous section, it was shown that cellulase adsorption onto the MWL substrate and during the final stage of adsorption onto the OL and KL substrates was in large part driven by polar interactions and resulted in hydrated adsorption layers. The fact that the MWL substrate, being the most polar of the substrates, had the highest surface excess concentration after 4 h of adsorption was consistent with polar interactions as the primary driving force for cellulase adsorption onto the MWL substrate. The fact that the OL substrate had a higher surface excess concentration after 4 h of adsorption than the KL substrate, despite it being less polar, could possibly be due to a larger accessible surface area, indicated by the higher surface roughness of the substrate (1.0 nm for the OL *versus* 0.8 nm for the KL substrate).

Treatment of the substrates with Tween 80 caused a decrease in the surface excess concentrations after 10 min of adsorption. As discussed in the previous section, the rapid build-up of the initial cellulase layer, possibly driven by hydrophobic interactions, might have been impeded by hydrophobically-adsorbed Tween 80 molecules blocking the hydrophobic adsorption sites. Interestingly, the surface excess concentration of cellulase after 4 h of adsorption was increased by 19% on the OL substrate and by 25% on the KL substrate after Tween 80 treatment of the substrates but was decreased by 61% on the MWL substrate. The increase in surface excess concentration on the OL and KL substrates could have two reasons. First, the

hydrophobically-adsorbed Tween 80 molecules that blocked the hydrophobic adsorption sites on the OL and KL substrates might have provided hydrophilic adsorption sites for the cellulase molecules by exposing their polar headgroups. Second, the partial erosion of the substrates during Tween 80 treatment could have increased the accessible surface area of the substrates. A possible reason for the strong decrease in the surface excess concentration of cellulase on the MWL substrate upon Tween 80 treatment could be the blocking of hydrophilic adsorption sites by Tween 80 molecules adsorbed *via* polar interactions. Such blocking has resulted in the complete suppression of cellulase adsorption on the Tween 80-treated silica substrate (Figure 5.8a). Adsorption of Tween 80 molecules onto the MWL substrate *via* polar interactions would also explain the low extent of substrate erosion and lignin removal observed for the MWL substrate during the Tween 80 treatment (Figure 5.4) because if the polar headgroup of the surfactant were adsorbed onto the lignin molecule it would not be available to interact with the aqueous liquid medium.

The cellulase adsorbed on the untreated and Tween 80-treated lignin substrates after 10 min and 4 h of adsorption was visualized by AFM. Figures 5.10 and 5.11 show AFM height images of untreated and Tween-80 treated lignin substrates after 10 min and 4 h of cellulase adsorption, respectively. The spherical objects protruding from the substrates, as indicated by their lighter shade, were assumed to be cellulase molecules or aggregates. As seen in Figure 5.10, after 10 min of adsorption more cellulase was observed on the untreated lignin substrates than on the Tween 80-treated substrates. The observed decrease in the amount of cellulose on the lignin substrates upon Tween 80 treatment was consistent with the decrease in surface excess concentration after 10 min of adsorption (Table 5.5). The images of the substrates after 4 h of adsorption (Figure 5.11) were also agreement with the surface excess concentrations (Table 5.5). For the OL and KL substrates, more cellulase was observed on the Tween 80-treated substrates than on the untreated substrates, whereas for the MWL substrate more cellulase was observed on the untreated substrate.

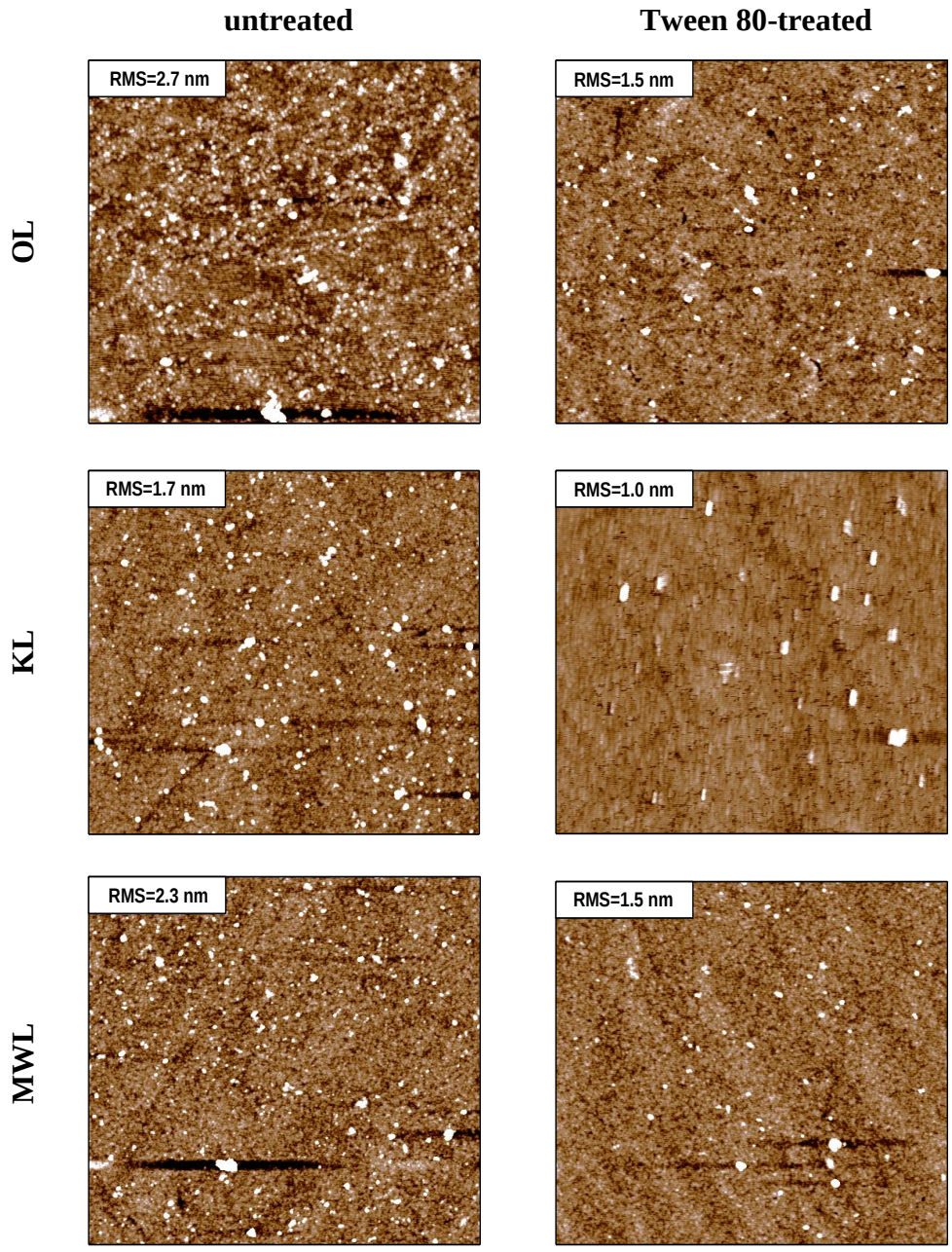

Figure 5.10. AFM height images of untreated and Tween-80 treated lignin substrates after 10 min of cellulase adsorption. The scan size and z-scale are 5 μm × 5 μm and 8 nm, respectively, for all images.

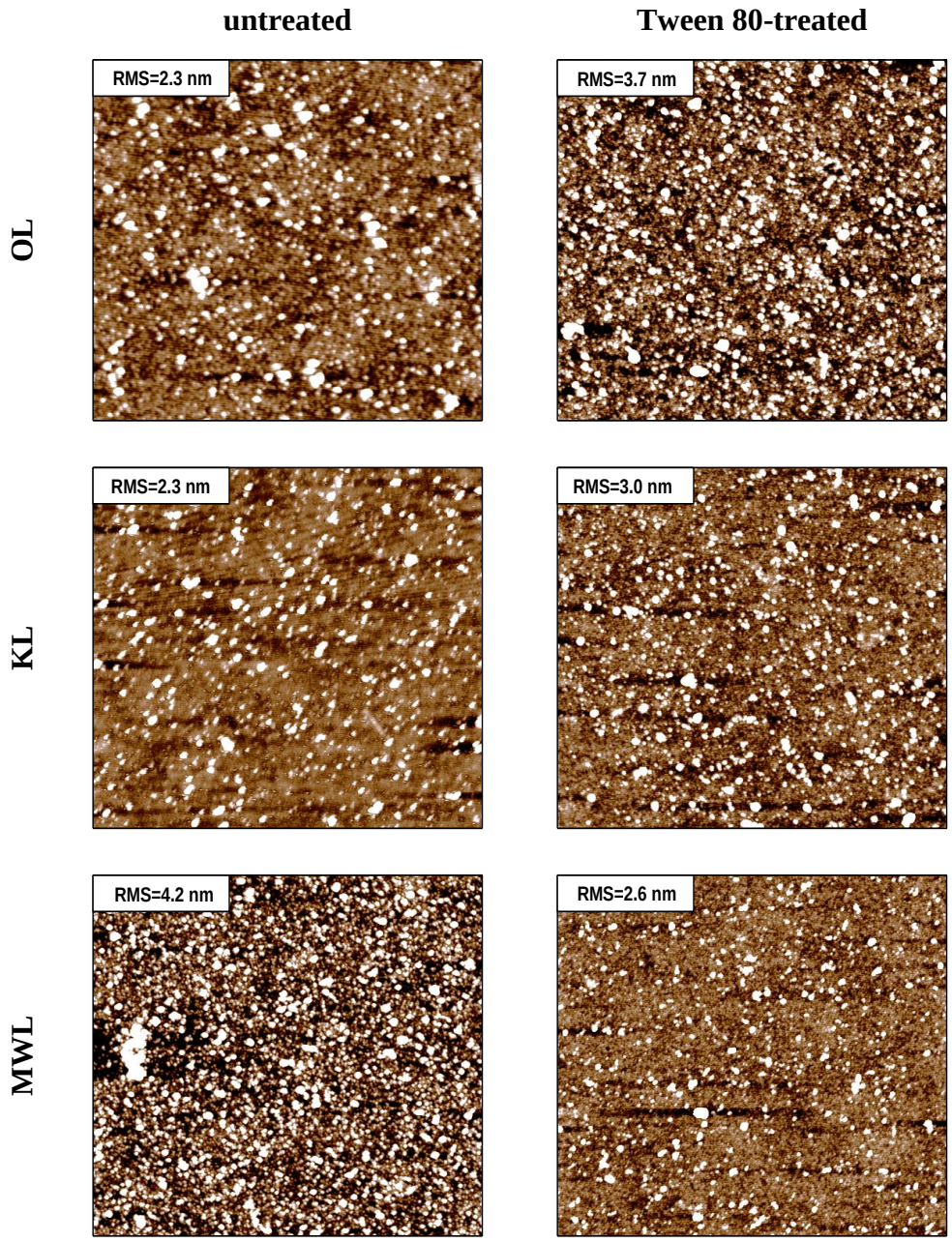

Figure 5.11. AFM height images of untreated and Tween-80 treated lignin substrates after 4 h of cellulase adsorption. The scan size and z-scale are 5 μm × 5 μm and 8 nm, respectively, for all images.

5.4.6. Cellulase adsorption kinetics

As shown in the previous sections, adsorption of cellulase onto lignin substrates might occur *via* both polar and hydrophobic interactions. Adsorption *via* hydrophobic interactions appears to be rapid whereas adsorption *via* polar interactions appears to be gradual. Following examples in the literature,[53,57,58] we fitted the gradually decreasing section of the ($\Delta f_n/n$) curves for cellulase adsorption onto the lignin substrates with an exponential decay equation

$$\Delta f = \Delta f_{\mathrm{p}}\left(1 - e^{-t/\tau}\right) + \Delta f_{\mathrm{h}} \qquad [5.2]$$

where Δf is the total frequency change due to cellulase adsorption onto the substrate, Δf_{p} is the frequency change assumed to be due primarily to adsorption *via* polar interactions, Δf_{h} is the frequency change assumed to be due to adsorption *via* hydrophobic interactions, and τ is the relaxation time or reciprocal of the adsorption rate.[57] The values for Δf_{h} and τ, obtained by fitting of the experimental data with eq 5.2, are listed in Table 5.6.

Table 5.6. Values of the frequency change due primarily to cellulase adsorption *via* polar interactions, Δf_{h}, and the relaxation time, τ, obtained by fitting the gradually decreasing section of the ($\Delta f_n/n$) curves (5^{th} overtone) with eq 5.2.

	untreated		Tween 80-treated	
Substrate	Δf_{h} (Hz)	τ (h)	Δf_{h} (Hz)	τ (h)
OL	–25.9	1.16	–11.2	1.72
KL	–29.8	1.03	–7.3	2.58
MWL	–10.1	1.32	–3.2	3.67

As seen in Table 5.6, Δf_{h} was lower for the Tween 80-treated lignin substrates than for the untreated substrates. The decrease in Δf_{h} upon Tween 80 treatment confirmed the findings of the previous sections that Tween 80 molecules on the surface of the lignin substrates prevented the initial rapid cellulase adsorption, assumed to occur *via* hydrophobic interactions, possibly by blocking the hydrophobic adsorption sites of the substrates. The relaxation time, τ, was higher for

the Tween 80-treated substrates than for the untreated substrates. The increase in τ upon Tween 80 treatment signified a decrease in the adsorption rate. Thus, Tween 80 molecules on the surface of the lignin substrates reduced the rate of cellulose adsorption onto the substrates.

5.5. Conclusions

The objective of this study was to enhance our understanding of the mechanisms by which non-ionic surfactants prevent non-productive binding of cellulolytic enzymes onto lignin substrates. The study has shown that the non-ionic surfactant Tween 80 adsorbs onto lignin substrates and, depending on the chemical properties of the lignin, may remove lignin molecules from their surface. Lignin removal by Tween 80 molecules is facilitated by a high lignin hydrophobicity. Adsorption of Tween 80 molecules onto lignin substrates increases the polar surface energy component (hydrophilicity) of the substrates. Cellulase appears to adsorb onto lignin substrates *via* both hydrophobic and polar interactions, depending on the chemical properties of the lignin. Tween 80 molecules on the substrate's surface seem to hinder cellulase adsorption *via* hydrophobic interactions and reduce the rate of cellulase adsorption.

5.6. Acknowledgments

This project was supported by the National Research Initiative of the USDA Cooperative State Research, Education and Extension Service under Grant 2005-35504-16088, the National Science Foundation under Grant CHE-0724126 and DMR-0907567, the U.S. Department of Transportation through the Southeastern Sun Grant Center, and the Institute for Critical Technology and Applied Science. The authors thank Dr. Bin Li for his help in preparing the samples and analyzing the spectra for the ^{31}P NMR experiments, Dr. Hugo Azurmendi for his help in setting up the NMR spectrometer, Dr. Charles E. Frazier for access to the contact angle goniometer, and Prof. Em. Wolfgang Glasser for providing the OL and MWL samples.

5.7. References

1. Mooney, C. A.; Mansfield, S. D.; Touhy, M. G.; Saddler, J. N. The Effect of Initial Pore Volume and Lignin Content on the Enzymatic Hydrolysis of Softwoods. *Bioresource Technology* **1998,** *64*, 113-119.

2. Chandra, R. P.; Bura, R.; Mabee, W. E.; Berlin, A.; Pan, X.; Saddler, J. N. Substrate Pretreatment: The Key to Effective Enzymatic Hydrolysis of Lignocellulosics? In: Biofuels; Advances in Biochemical Engineering / Biotechnology; 2007; Vol. *108*, pp 67-93.

3. Nakagame, S.; Chandra, R. P.; Saddler, J. N. The Effect of Isolated Lignins, Obtained from a Range of Pretreated Lignocellulosic Substrates, on Enzymatic Hydrolysis. *Biotechnology and Bioengineering* **2010,** *105*, 871-879.

4. Sewalt, V. J. H.; Ni, W. T.; Jung, H. G.; Dixon, R. A. Lignin Impact on Fiber Degradation: Increased Enzymatic Digestibility of Genetically Engineered Tobacco (Nicotiana Tabacum) Stems Reduced in Lignin Content. *Journal of Agricultural and Food Chemistry* **1997,** *45*, 1977-1983.

5. Sewalt, V. J. H.; Glasser, W. G.; Beauchemin, K. A. Lignin Impact on Fiber Degradation .3. Reversal of Inhibition of Enzymatic Hydrolysis by Chemical Modification of Lignin and by Additives. *Journal of Agricultural and Food Chemistry* **1997,** *45*, 1823-1828.

6. Berlin, A.; Balakshin, M.; Gilkes, N.; Kadla, J.; Maximenko, V.; Kubo, S.; Saddler, J. Inhibition of Cellulase, Xylanase and Beta-Glucosidase Activities by Softwood Lignin Preparations. *Journal of Biotechnology* **2006,** *125*, 198-209.

7. Chernoglazov, V. M.; Ermolova, O. V.; Klyosov, A. A. Adsorption of High-Purity Endo-1,4-Beta-Glucanases from Trichoderma-Reesei on Components of Lignocellulosic Materials - Cellulose, Lignin, and Xylan. *Enzyme and Microbial Technology* **1988,** *10*, 503-507.

8. Yang, B.; Wyman, C. E. Bsa Treatment to Enhance Enzymatic Hydrolysis of Cellulose in Lignin Containing Substrates. *Biotechnology and Bioengineering* **2006,** *94*, 611-617.

9. Converse, A. O.; Ooshima, H.; Burns, D. S. Kinetics of Enzymatic-Hydrolysis of Lignocellulosic Materials Based on Surface-Area of Cellulose Accessible to Enzyme and Enzyme Adsorption on Lignin and Cellulose. *Applied Biochemistry and Biotechnology* **1990,** *24-5*, 67-73.

10. Ooshima, H.; Burns, D. S.; Converse, A. O. Adsorption of Cellulase from Trichoderma-Reesei on Cellulose and Lignacious Residue in Wood Pretreated by Dilute Sulfuric-Acid with Explosive Decompression. *Biotechnology and Bioengineering* **1990,** *36*, 446-452.

11. Sutcliffe, R.; Saddler, J. N. The Role of Lignin in the Adsorption of Cellulases During Enzymatic Treatment of Lignocellulosic Material. *Biotechnology & Bioengineering Symposium* **1986,** 17.

12. Tu, M. B.; Pan, X. J.; Saddler, J. N. Adsorption of Cellulase on Cellulolytic Enzyme Lignin from Lodgepole Pine. *Journal of Agricultural and Food Chemistry* **2009,** *57*, 7771-7778.

13. Mosier, N.; Wyman, C.; Dale, B.; Elander, R.; Lee, Y. Y.; Holtzapple, M.; Ladisch, M. Features of Promising Technologies for Pretreatment of Lignocellulosic Biomass. *Bioresource Technology* **2005,** *96*, 673-686.

14. Saha, B. C.; Iten, L. B.; Cotta, M. A.; Wu, Y. V. Dilute Acid Pretreatment, Enzymatic Saccharification and Fermentation of Wheat Straw to Ethanol. *Process Biochemistry* **2005,** *40*, 3693-3700.

15. Yang, B.; Boussaid, A.; Mansfield, S. D.; Gregg, D. J.; Saddler, J. N. Fast and Efficient Alkaline Peroxide Treatment to Enhance the Enzymatic Digestibility of Steam-Exploded Softwood Substrates. *Biotechnology and Bioengineering* **2002,** *77*, 678-684.

16. Saha, B. C.; Cotta, M. A. Lime Pretreatment, Enzymatic Saccharification and Fermentation of Rice Hulls to Ethanol. *Biomass & Bioenergy* **2008,** *32*, 971-977.

17. Pan, X. J.; Arato, C.; Gilkes, N.; Gregg, D.; Mabee, W.; Pye, K.; Xiao, Z. Z.; Zhang, X.; Saddler, J. Biorefining of Softwoods Using Ethanol Organosolv Pulping: Preliminary Evaluation of Process Streams for Manufacture of Fuel-Grade Ethanol and Co-Products. *Biotechnology and Bioengineering* **2005,** *90*, 473-481.

18. Holtzapple, M. T.; Humphrey, A. E. The Effect of Organosolv Pretreatment on the Enzymatic-Hydrolysis of Poplar. *Biotechnology and Bioengineering* **1984,** *26*, 670-676.

19. Kristensen, J. B.; Borjesson, J.; Bruun, M. H.; Tjerneld, F.; Jorgensen, H. Use of Surface Active Additives in Enzymatic Hydrolysis of Wheat Straw Lignocellulose. *Enzyme and Microbial Technology* **2007,** *40*, 888-895.

20. Eriksson, T.; Borjesson, J.; Tjerneld, F. Mechanism of Surfactant Effect in Enzymatic Hydrolysis of Lignocellulose. *Enzyme and Microbial Technology* **2002,** *31*, 353-364.

21. Kaar, W. E.; Holtzapple, M. T. Benefits from Tween During Enzymic Hydrolysis of Corn Stover. *Biotechnology and Bioengineering* **1998,** *59*, 419-427.

22. Zheng, Y.; Pan, Z. L.; Zhang, R. H.; Wang, D. H.; Jenkins, B. Non-Ionic Surfactants and Non-Catalytic Protein Treatment on Enzymatic Hydrolysis of Pretreated Creeping Wild Ryegrass. *Applied Biochemistry and Biotechnology* **2008,** *146*, 231-248.

23. Qing, Q.; Yang, B.; Wyman, C. E. Impact of Surfactants on Pretreatment of Corn Stover. *Bioresource Technology* **2010,** *101*, 5941-5951.

24. Borjesson, J.; Peterson, R.; Tjerneld, F. Enhanced Enzymatic Conversion of Softwood Lignocellulose by Poly(Ethylene Glycol) Addition. *Enzyme and Microbial Technology* **2007,** *40*, 754-762.

25. Sipos, B.; Dienes, D.; Schleicher, A.; Perazzini, R.; Crestini, C.; Siika-Aho, M.; Reczey, K. Hydrolysis Efficiency and Enzyme Adsorption on Steam-Pretreated Spruce in the Presence of Poly(Ethylene Glycol). *Enzyme and Microbial Technology* **2010,** *47*, 84-90.

26. Constantino, C. J. L.; Juliani, L. P.; Botaro, V. R.; Balogh, D. T.; Pereira, M. R.; Ticianelli, E. A.; Curvelo, A. A. S.; Oliveira, O. N. Langmuir-Blodgett Films from Lignins. *Thin Solid Films* **1996,** *284*, 191-194.

27. Constantino, C. J. L.; Dhanabalan, A.; Curvelo, A.; Oliveira, O. N. Preparation and Characterization of Composite Lb Films of Lignin and Cadmium Stearate. *Thin Solid Films* **1998,** *327*, 47-51.

28. Constantino, C. J. L.; Dhanabalan, A.; Cotta, M. A.; Pereira-da-Silva, M. A.; Curvelo, A. A. S.; Oliveira, O. N. Atomic Force Microscopy (AFM) Investigation of Langmuir-Blodgett (LB) Films of Sugar Cane Bagasse Lignin. *Holzforschung* **2000,** *54*, 55-60.

29. Norgren, M.; Notley, S. M.; Majtnerova, A.; Gellerstedt, G. Smooth Model Surfaces from Lignin Derivatives. I. Preparation and Characterization. *Langmuir* **2006,** *22*, 1209-1214.

30. Norgren, M.; Gardlund, L.; Notley, S. M.; Htun, M.; Wagberg, L. Smooth Model Surfaces from Lignin Derivatives. II. Adsorption of Polyelectrolytes and PECs Monitored by QCM-D. *Langmuir* **2007,** *23*, 3737-3743.

31. Notley, S. M.; Norgren, M. Measurement of Interaction Forces between Lignin and Cellulose as a Function of Aqueous Electrolyte Solution Conditions. *Langmuir* **2006,** *22*, 11199-11204.

32. Notley, S. M.; Norgren, M. Adsorption of a Strong Polyelectrolyte to Model Lignin Surfaces. *Biomacromolecules* **2008,** *9*, 2081-2086.

33. Notley, S. M.; Norgren, M. Surface Energy and Wettability of Spin-Coated Thin Films of Lignin Isolated from Wood. *Langmuir* **2010,** *26*, 5484-5490.

34. Glasser, W. G.; Barnett, C. A.; Sano, Y., Classification of lignins with different genetic and industrial origins. *Journal of Applied Polymer Science: Applied Polymer Symposium* **1983,** *37*, 441-460.

35. Lindstrom, T. The Colloidal Behaviour of Kraft Lignin Part I.: Association and Gelation of Kraft Lignin in Aqueous Solutions. *Colloid and polymer science* **1979,** *257*, 277-285.

36. Granata, A.; Argyropoulos, D. S. 2-Chloro-4,4,5,5-Tetramethyl-1,3,2-Dioxaphospholane, a Reagent for the Accurate Determination of the Uncondensed and Condensed Phenolic Moieties in Lignins. *Journal of Agricultural and Food Chemistry* **1995,** *43*, 1538-1544.

37. Zawadzki, M.; Ragauskas, A. N-Hydroxy Compounds as New Internal Standards for the P-31-NMR Determination of Lignin Hydroxy Functional Groups. *Holzforschung* **2001,** *55*, 283-285.

38. Owens, D. K.; Wendt, R. C. Estimation of the Surface Free Energy of Polymers. *Journal of applied polymer science* **1969,** *13*, 1741-1747.

39. Rabel, W. Einige Aspekte Der Benetzungstheorie Und Ihre Anwendung Auf Die Untersuchung Und Veränderung Der Oberflächeneigenschaften Von Polymeren. *Farbe und Lack* **1971,** *77*, 997–1006.

40. Kaelble, D. H. Dispersion-Polar Surface Tension Properties of Organic Solids. *Journal of Adhesion* **1970,** *2*, 66–81.

41. Good, R. J.; Chaudhury, M. K.; van Oss, C. J. Theory of Adhesive Forces across Interfaces 2. Interfacial Hydrogen Bonds as Acid-Base Phenomena and as Factors Enhancing Adhesion. In: Fundamentals of Adhesion; Lee, L.-H., Ed.; Plenum Press: New York, 1991; pp 153-179.

42. Voinova, M. V.; Rodahl, M.; Jonson, M.; Kasemo, B. Viscoelastic Acoustic Response of Layered Polymer Films at Fluid-Solid Interfaces: Continuum Mechanics Approach. *Physica Scripta* **1999,** *59*, 391-396.

43. Hook, F.; Kasemo, B.; Nylander, T.; Fant, C.; Sott, K.; Elwing, H. Variations in Coupled Water, Viscoelastic Properties, and Film Thickness of a Mefp-1 Protein Film During Adsorption and Cross-Linking: A Quartz Crystal Microbalance with Dissipation

Monitoring, Ellipsometry, and Surface Plasmon Resonance Study. *Analytical Chemistry* **2001,** *73*, 5796-5804.

44. Lide, D. R. CRC Handbook of Chemistry and Physics (Internet Version). 91st ed.; CRC Press: Boca Raton, FL, 2011.

45. Weast, R. C.; Lide, D. R.; Astle, M. J.; Beyer, W. H. Crc Hand Book of Chemistry and Physics. 70 ed.; CRC Press: Boca Raton, FL, 1989; pp. F40.

46. Dutta, A. K.; Nayak, A.; Belfort, G. Viscoelastic Properties of Adsorbed and Cross-Linked Polypeptide and Protein Layers at a Solid-Liquid Interface. *Journal of Colloid and Interface Science* **2008,** *324*, 55-60.

47. Wu, S.; Argyropoulos, D. S. An Improved Method for Isolating Lignin in High Yield and Purity. *Journal of Pulp and Paper Science* **2003,** *29*, 235-240.

48. Notley, S. M.; Eriksson, M.; Wagberg, L.; Beck, S.; Gray, D. G. Surface Forces Measurements of Spin-Coated Cellulose Thin Films with Different Crystallinity. *Langmuir* **2006,** *22*, 3154-3160.

49. Smith, T. The Hydrophilic Nature of a Clean Gold Surface. *Journal of Colloid and Interface Science* **1980,** *75*, 51-55.

50. Kraulis, P. J.; Clore, G. M.; Nilges, M.; Jones, T. A.; Pettersson, G.; Knowles, J.; Gronenborn, A. M. Determination of the 3-Dimensional Solution Structure of the C-Terminal Domain of Cellobiohydrolase-I from Trichoderma-Reesei - a Study Using Nuclear Magnetic-Resonance and Hybrid Distance Geometry Dynamical Simulated Annealing. *Biochemistry* **1989,** *28*, 7241-7257.

51. Linder, M.; Teeri, T. T. The Roles and Function of Cellulose-Binding Domains. *Journal of Biotechnology* **1997,** *57*, 15-28.

52. Linder, M.; Mattinen, M. L.; Kontteli, M.; Lindeberg, G.; Stahlberg, J.; Drakenberg, T.; Reinikainen, T.; Pettersson, G.; Annila, A. Identification of Functionally Important Amino-Acids in the Cellulose-Binding Domain of Trichoderma-Reesei Cellobiohydrolase-I. *Protein Science* **1995,** *4*, 1056-1064.

53. Otzen, D. E.; Oliveberg, M.; Hook, F. Adsorption of a Small Protein to a Methyl-Terminated Hydrophobic Surfaces: Effect of Protein-Folding Thermodynamics and Kinetics. *Colloids and Surfaces B-Biointerfaces* **2003,** *29*, 67-73.

54. Rodahl, M.; Hook, F.; Fredriksson, C.; Keller, C. A.; Krozer, A.; Brzezinski, P.; Voinova, M.; Kasemo, B. Simultaneous Frequency and Dissipation Factor QCM Measurements of Biomolecular Adsorption and Cell Adhesion. *Faraday Discussions* **1997,** 107, 229-246.

55. Hook, F.; Rodahl, M.; Kasemo, B.; Brzezinski, P. Structural Changes in Hemoglobin During Adsorption to Solid Surfaces: Effects of Ph, Ionic Strength, and Ligand Binding. *Proceedings of the National Academy of Sciences of the United States of America* **1998,** 95, 12271-12276.

56. Feiler, A. A.; Sahlholm, A.; Sandberg, T.; Caldwell, K. D. Adsorption and Viscoelastic Properties of Fractionated Mucin (BSM) and Bovine Serum Albumin (BSA) Studied with Quartz Crystal Microbalance (QCM-D). *Journal of Colloid and Interface Science* **2007,** 315, 475-481.

57. Turon, X.; Rojas, O. J.; Deinhammer, R. S. Enzymatic Kinetics of Cellulose Hydrolysis: A QCM-D Study. *Langmuir* **2008,** 24, 3880-3887.

58. Takahashi, S.; Matsuno, H.; Furusawa, H.; Okahata, Y. Kinetic Analyses of Divalent Cation-Dependent Ecorv Digestions on a DNA-Immobilized Quartz Crystal Microbalance. *Analytical Biochemistry* **2007,** 361, 210-217.

CHAPTER 6

Preparation and enzymatic hydrolysis of model lignocellulosic substrates: A QCM-D and AFM study

6.1. Abstract

This study was conducted to elucidate the effects of lignin on the enzymatic hydrolysis of cellulose by means of quartz crystal microbalance with dissipation monitoring (QCM-D). Model lignocellulosic (LC) substrates containing both cellulose and lignin were prepared from kraft lignin, organosolv lignin, and milled wood lignin by spin coating of mixed aqueous lignin/cellulose nanocrystal (CNC) suspensions, to yield substrates that model the plant cell wall, and of aqueous lignin suspensions onto cellulose substrates, to yield substrates that model the cellulose fraction of pretreated biomass, containing redeposited lignin. The LC substrates were characterized in terms of surface morphology, surface roughness, surface density, and atomic composition. The hydrolysis of the substrates by *Trichoderma reesei* cellulases was monitored by QCM-D. Lignin was found to hinder both the adsorption of cellulases onto the substrates and the enzymatic hydrolysis of the substrates. The inhibitory effect of lignin increased with its content or layer thickness in the LC substrate and lignin surface layers had less of an inhibitory effect on cellulose hydrolysis than an embedding lignin matrix.

6.2. Introduction

The production of renewable fuels from lignocellulosic (LC) biomass for the reduction of our dependence on fossil fuels has drawn the attention of many researchers. One of the most promising methods for the production of bioethanol is the enzymatic hydrolysis of LC biomass followed by microbial fermentation.[1-3] A heterogeneous reaction, the enzymatic hydrolysis of LC biomass requires adsorption of cellulase onto the substrate.[4,5] However, the substrate, namely cellulose, is naturally protected against microbial degradation by being embedded in a lignin matrix. The protective lignin matrix inevitably limits enzyme access to cellulose and thus hinders its enzymatic saccharification and reduces process efficiency. The recalcitrance of LC biomass due to the presence of lignin and cellulose crystallinity are the primary factors that affect the enzymatic saccharification during biomass processing.[6] The inhibitory effect of lignin on the enzymatic hydrolysis of LC biomass has been widely investigated in the past few decades, and an inverse correlation between lignin content and hydrolysis rate has been established.[7-12]

In order to lose its recalcitrance and become accessible to hydrolytic enzymes, LC biomass has to undergo pretreatment before enzymatic hydrolysis, leading to increased hydrolysis efficiency.[13,14] Pretreatment processes effectively reduce cellulose crystallinity and break up the associations between cellulose, hemicellulose, and lignin. However, complete removal of lignin is not feasible and extensive pretreatment procedures increase bioethanol production costs.[13] Pretreatment processes often employ acids or bases to break down the protective lignin matrix and reduce cellulose crystallinity. As a result, lignin in pretreated LC biomass is chemically altered.

Because of its ability to measure small mass and viscoelasticity changes on the surface of model cellulose substrates, quartz crystal microbalance with dissipation monitoring (QCM-D) has found increasing use in recent years in the study of enzymatic cellulose hydrolysis. Based on changes in the oscillation frequency, f, and dissipation factor, D, of the quartz crystal. Turon *et al.*[15] reported different hydrolysis stages, namely cellulase adsorption, cellulose chain cleavage and film hydration, and loss of film integrity. In other studies, QCM-D was used to determine the effects of cellulose surface morphology on enzymatic hydrolysis[16] and cellulase activities.[17,18]

In situ monitoring of enzymatic hydrolysis processes by QCM-D requires smooth, uniform substrates. Model substrates from cellulose and lignin have been prepared through various thin

film deposition techniques, including Langmuir-Blodgett (LB) deposition[19-23] and spin coating,[24-33] as well as from many different materials, such as regenerated cellulose,[24,25,34] cellulose nanocrystals (CNCs),[27,28] cellulose nanofibrils,[35] acetosolv lignin,[21-23] kraft lignin (KL),[29,30,33] and milled wood lignin (MWL).[33] However, no studies have reported the preparation of model LC substrates, containing both cellulose and lignin, mimicking native or pretreated LC biomass. The difficulty in preparing model LC substrates lies in the lack of common solvents suitable for spin coating for both cellulose and lignin. The dissolution of wood in an ionic liquid (1-*n*-butyl-3-methylimidazolium chloride) has been reported.[36] However, because of their high viscosity at room temperature and their difficult removal from the substrate, ionic liquids are not suitable for LC substrate preparation by spin coating. CNCs prepared by sulfuric acid hydrolysis, followed by desulfation, as described in Chapter 3, can be readily suspended in aqueous media. Although not soluble in aqueous media, KL has been shown to form stable aqueous colloidal suspensions after being dissolved in basic media and subjected to extensive dialysis.[37] The ability to prepare stable colloidal suspensions from both cellulose and lignin makes the preparation of model LC substrates possible.

This study was conducted to elucidate the effects of lignin on the enzymatic hydrolysis of cellulose by means of QCM-D. Model LC substrates containing both cellulose and lignin were prepared from aqueous suspensions of CNCs, KL, MWL, and organosolv lignin (OL). KL and OL were selected as models for residual lignin in LC biomass after pretreatment under basic and acidic conditions, respectively. MWL was selected as a model for native lignin. The model LC substrates were characterized in terms of surface morphology, surface roughness, surface density, and atomic composition. The LC substrates were subjected to a mixture of different cellulases from the fungus *Trichoderma reesei*, and enzyme adsorption and substrate hydrolysis were monitored by QCM-D.

6.3. Experimental section

6.3.1. Materials

Dissolving-grade softwood sulfite pulp (Temalfa 93A-A) was kindly provided by Tembec, Inc. KL (M_n = $5{\cdot}10^3$ g·mol^{-1}, M_w = $28{\cdot}10^3$ g·mol^{-1}) and Celluclast 1.5L (Novozyme) were purchased from Sigma-Aldrich. Sulfuric acid (95.9 wt %, Certified ACS Plus), pyridine (99.5%, Chemservice), citric acid monohydrate (Fisher Scientific, Certified ACS), sodium hydroxide (Acros Organics, 98.5%), hydrogen peroxide (34–37%, Technical Grade), ammonium hydroxide (28.9%, Certified ACS Plus), dimethyl sulfoxide (DMSO, Certified ACS), and methanol (99.8%, Acros Organics) were purchased from Fisher Scientific. MWL from hemlock (*Tsuga* sp., M_n = $2.6{\cdot}10^3$ g·mol^{-1}, M_w = $15.2{\cdot}10^3$ g·mol^{-1})[38] and OL from cottonwood (*Populus trichocharpa*, M_n < 10^3 g·mol^{-1}, M_w < $3{\cdot}10^3$ g·mol^{-1})[38] were kindly provided by Prof. Em. Wolfgang Glasser. All water used was deionized (DI) water with a resistivity of 18.2 MΩ·cm, obtained from a Millipore Direct-Q 5 Ultrapure Water Systems.

6.3.2. Cellulose nanocrystal (CNC) preparation

CNCs were prepared from wood pulp by sulfuric acid hydrolysis followed by solvolytic desulfation, as described in detail in Chapter 3. In brief, milled (60-mesh) softwood sulfite pulp was hydrolyzed with 64 wt % sulfuric acid (10 mL·g^{-1} cellulose) at 45 ℃ for 1 h. The acid was removed from the CNC suspension by centrifugation and dialysis against DI water. The final suspension was sonicated and filtered through a 0.45 μm poly(vinylidene fluoride) (PVDF) syringe filter (Whatman, Ltd.). For desulfation of the CNCs, the suspension was neutralized with pyridine and lyophilized (Freezone 4.5L freeze-dry system, Labconco Corp.). The freeze-dried CNCs (pyridinium salt) were heated for 2 h at 80 ℃ at a concentration of ~1% (w/v) in a 9:1 (v/v) mixture of DMSO and methanol. After cooling and dilution of the reaction mixture with DI water, the suspension was dialyzed against DI water for several weeks and then sonicated and filtered through a 0.45 μm (PVDF) syringe filter.

6.3.3. Lignin purification and fractionation

The lignins were purified and fractionated as described in detail in Chapter 5. In brief, KL and MWL were dissolved in 0.75 M and OL in 1.5 M aqueous ammonia at a concentration of 1 wt %. The lignin solutions were dialyzed against DI water using Spectra/Por 4 dialysis tubing (MWCO: 12–14 kDa, Spectrum Lab, Inc.) for two weeks for removal of the low molecular weight fraction and water-soluble impurities and then centrifuged at 25 ℃ and 4900 rpm for 15 min for removal of any sedimenting larger particles. Finally, the lignin suspensions were concentrated to 1.5 wt % with a rotary evaporator under vacuum at 45 ℃ and stored in the refrigerator until use. Prior to use, the suspensions were diluted to 1 wt % with DI water.

6.3.4. LC substrate preparation

LC substrates were prepared on silicon dioxide-coated AT-cut quartz crystals (Q-Sense). The quartz crystals were cleaned by immersion and shaking for 1 min in fresh piranha solution (7:3 (v/v) mixture of sulfuric acid and hydrogen peroxide), then rinsed with DI water, dried in a stream of nitrogen, and irradiated for 15 min with an ozone-producing mercury lamp (UV/Ozone cleaner, Bioforce Nanosciences). To minimize surface contamination, we cleaned the quartz crystals immediately prior to use.

Two types of LC substrates were prepared, referred to as composite substrates and layered substrates. Composite LC (CLC) substrates were prepared *via* direct spin coating of lignin- and CNC-containing aqueous suspensions. Suspensions with a lignin-to-CNC ratio of 1:9, 2:8, and 3:7 (w/w) and a solids concentration of 1 wt % were prepared by mixing the appropriate volumes of a 1 wt % lignin suspension and a 1 wt % CNC suspension. The resulting suspensions, shown in Figure 6.1, were homogeneous and tan to brown in color, depending on the amount and color of the original lignin suspension. The composite substrates were prepared by spin coating (WS-400B-6NPPLite, Laurell Technologies Corp.) the cleaned quartz crystals for 1 min at 4000 rpm with 140 µl of the lignin/CNC suspension. Layered LC (LLC) substrates were prepared by spin coating of cellulose substrates with aqueous lignin suspensions. A cleaned quartz crystal was first spin-coated for 1 min at 4000 rpm with 140 µl of a 1 wt % CNC suspension. The obtained cellulose substrate was then spin-coated for 1 min at 4000 rpm with 140 µl of a 0.5 or 1 wt %

lignin suspension. Different lignin concentrations were used for different thicknesses of the lignin layer. Both the CLC and LLC substrates were dried in a vacuum oven at 65 ℃ for several hours for improved stability in aqueous media.

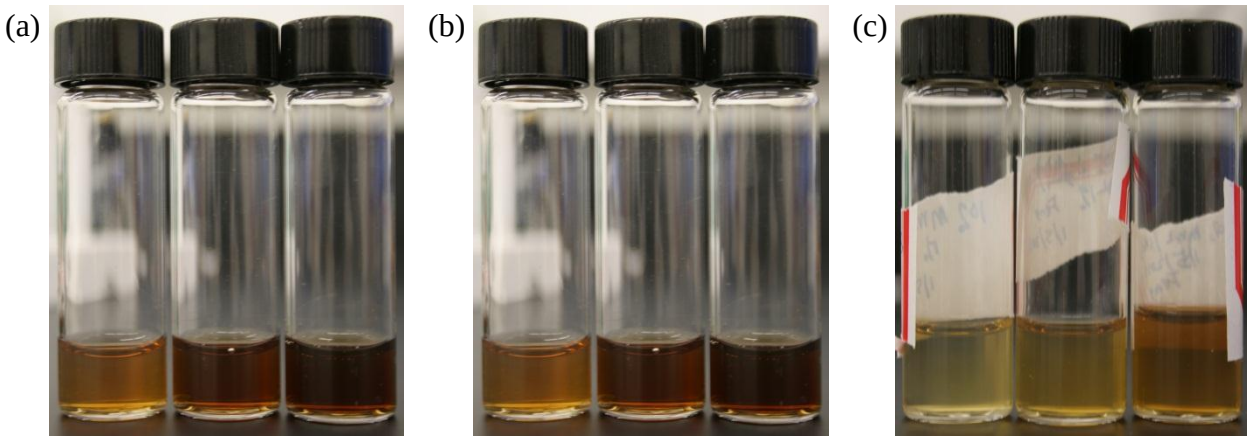

Figure 6.1. Aqueous lignin/CNC suspensions with a solids concentration of 1 wt % and different lignin-to-CNC ratios: a) KL/CNC; b) OL/CNC; c) MWL/CNC. For each image, the lignin-to-CNC ratios are 1:9, 2:8, and 3:7 from left to right.

6.3.5. Surface density measurements

The surface density of the CLC substrates, ρ_S, was measured by QCM-D (Q-sense E4) from the difference of the oscillation frequencies in air of the cleaned quartz crystals before and after spin coating. Because the LC film is rigid and firmly attached to the quartz crystal's surface, it can be treated as an extension of the quartz crystal itself. Thus, ρ_S can be calculated with the Sauerbrey equation,[39]

$$\rho_S = -\frac{2f_0^2}{\upsilon_q \rho_q}\frac{\Delta f_n}{n} = -\frac{2f_0^2}{\sqrt{\mu_q \rho_q}}\left(\left(\frac{f_n}{n}\right)_{LC} - \left(\frac{f_n}{n}\right)_{bare}\right) \quad [6.1]$$

where f_0 is the resonant frequency of the quartz crystal (5 MHz), υ_q is the transverse sound wave velocity in AT-cut quartz, ρ_q is the density of quartz (2648 kg·m^{-3} at 25 ℃),[40] μ_q is the shear

modulus of quartz ($2.947 \cdot 10^{10}$ kg·m^{-1}·s^{-2})[41], n is the frequency overtone number, $(f_n/n)_{bare}$ is the normalized oscillation frequency of the bare quartz crystal in air, and $(f_n/n)_{LC}$ is the normalized oscillation frequency of the LC-coated quartz crystal in air. The term $2f_0^2/\upsilon_q\rho_q$ has been called by Sauerbrey the sensitivity constant C and has the value 0.177 mg·m^{-2}·Hz^{-1} for the quartz crystals and experimental conditions used here.

The surface density of the lignin layer of layered LC substrates was determined by the same method from the difference of the oscillation frequencies in air of the CNC-coated quartz crystals before and after deposition of the lignin layer.

6.3.6. X-ray photoelectron spectroscopy (XPS)

The chemical composition of the CLC substrates was analyzed by XPS. CLC substrates for XPS analysis were prepared by spin coating as described above but on 1 cm × 1 cm silicon wafer pieces. Before spin coating, the wafer pieces, cut from a 15 cm wafer (Wafer World, Inc. West Palm Beach, FL), had been cleaned by immersion for 1 h at 70 ℃ in a mixture of aqueous ammonia, hydrogen peroxide, and DI water at a volume ratio of 1:1:5 and then for 1 h at ambient temperature in fresh piranha solution, rinsed with DI water, dried in a stream of nitrogen. Spectra of the LC substrates were recorded with a PHI Quantera SXM-03 scanning photoelectron spectrometer microprobe (ULVAC-PHI, Inc.) with monochromatic Al Kα radiation (98.3 W) at a take-off angle of 45° and a spot size of 100 μm. Elements were identified from survey spectra collected with an analyzer electron pass energy of 280 eV.

6.3.7. QCM-D hydrolysis experiments

The binding onto and subsequent hydrolysis of LC substrates by cellulases was monitored by QCM-D (Q-sense E4). LC substrates were placed in QCM-D flow modules, and a 0.25 mL·min^{-1} feed of 50 mM sodium citrate buffer (pH 4.8) was established. The buffer had been derived by 20-fold dilution with DI water from a 1 M sodium citrate buffer (pH 4.5), produced by dissolution of the appropriate amounts of citric acid monohydrate and sodium hydroxide in DI water. The temperature inside the flow modules was controlled at 22.00 ± 0.02 ℃. When the

scaled rate of change of the 3rd overtone frequency, ($\Delta f_3/3$), became less than 2 Hz·h^{-1}, the substrates were considered saturated and equilibrated, and the buffer feed was replaced with a feed of enzyme solution with the same flow rate. The enzyme solution had been prepared by dilution of 0.5 g Celluclast 1.5L, a commercial cellulase solution derived from *Trichoderma reesei*, with 50 mM sodium citrate buffer to a volume of 100 mL. The changes in the quartz crystal's oscillation frequency, Δf, and dissipation factor, ΔD were recorded in real time at the fundamental frequency (5 MHz) and 6 overtone frequencies (15, 25, 35, 45, 55, and 65 MHz) with QSoft 401 acquisition software (Q-Sense). Experiments were terminated when Δf reached a plateau.

6.3.8. Surface morphology and RMS surface roughness determination

The surface morphology and RMS surface roughness of the LC substrates before and after hydrolysis were analyzed by atomic force microscopy (AFM). Hydrolyzed substrates were taken out of the flow modules, thoroughly rinsed with DI water, dried in a stream of nitrogen, and placed in a vacuum oven at 65 ℃ for several hours. Substrates were imaged with an Asylum Research MFP-3D-BIO atomic force microscope. Substrates were scanned in air at ambient relative humidity and temperature in intermittent-contact mode with OMCL-AC160TS standard silicon probes (Olympus Corp.) with a scan frequency of 1 Hz, and 512 scans with 512 points/scan. RMS surface roughness values were determined from 2 μm × 2 μm areas in AFM height images.

6.4. Results and discussion

6.4.1. Surface properties of the LC substrates

The CLC substrates, consisting of an intimate blend of lignin and CNCs, were characterized in terms of surface morphology, RMS surface roughness, surface density, and atomic composition. The CLC substrates were prepared as a model for the plant cell wall, in which cellulose microfibrils are embedded in a lignin matrix. The LLC substrates, consisting of a

lignin layer on top of a CNC layer, were characterized in terms of surface morphology, RMS surface roughness, and surface density of the lignin layer. The LLC substrates were prepared as a model for cellulose onto which lignin has redeposited, commonly found in pretreated LC biomass. Figure 6.2 shows AFM height images of CLC substrates with a 30% nominal lignin content. An AFM height image of a cellulose substrate prepared from CNCs is also shown for comparison. Images of CLC substrates with nominal lignin contents of 10 and 20% are shown in Figure D.1 in Appendix D. As seen in Figure 6.2, the rod-like CNCs, clearly visible in the cellulose substrate, were still discernible in the CLC substrates even at a nominal lignin content of 30%. The fact that the CNCs were discernible in the CLC substrates indicated that some of them were at the surface of the substrate or only thinly coated with lignin.

The cellulose substrate had a comparatively high RMS surface roughness (3.6 nm) due to the uneven stacking of the rigid, rod-like CNCs. The surface roughnesses of the CLC substrates (Table 6.1), ranging from 2.4 to 3.3 nm, were lower than that of the cellulose substrate and were on average highest for the MWL containing substrate and lowest for the KL containing substrate. The lower surface roughnesses of the CLC substrates, compared to the cellulose substrate, were probably due to the ability of the lignin particles to fill up the voids between the CNCs and thus even out the surfaces of the CLC substrates.

The surface densities of the CLC substrates (Table 6.1), ranging from 31.7 to 37.6 $mg \cdot m^{-2}$, were also lower than the surface density of the CNC substrate (42.3 $mg \cdot m^{-2}$) and were on average slightly lower for the KL substrates than for the OL and MWL substrates. The surface density of a film obtained by spin coating is a complex function of several parameters, including the concentration and viscosity of the spin coating solution or suspension and the spinning velocity of the substrate.[42] The concentration of the spin coating suspension and the spinning velocity of the substrate were the same in the preparation of the CNC and CLC substrates. Therefore, differences in the viscosities of the spin coating suspensions must have been the reason for the different surface densities. The viscosity of a CNC suspension is governed by the attractive interactions between the CNCs, due in large part to hydrogen bonding. In the mixed lignin/CNC suspensions, used for the preparation of the CLC substrates, a fraction of the CNCs had been replaced with lignin particles. The surface interactions of the spherical lignin particles were likely less extensive than those of the CNCs. Consequently, the mixed lignin/CNC suspensions likely

had slightly lower viscosities than the CNC suspension, causing more suspension to be spun off of the substrate during spin coating and therefore lower substrate surface densities.

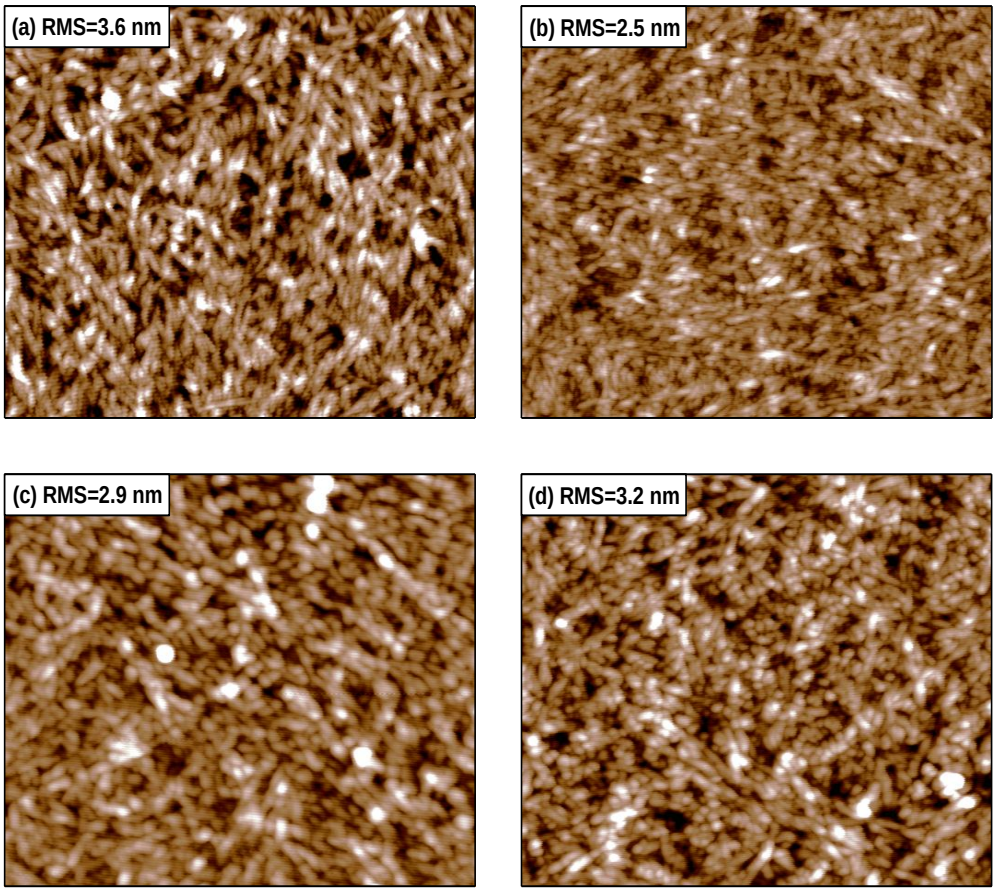

Figure 6.2. AFM height images of (a) a cellulose substrate and CLC substrates with a 30% nominal content of (b) KL, (c) OL, and (d) MWL. The scan size and z-scale are 2 μm × 2 μm and 15 nm, respectively, for all images.

To determine the surface composition and sulfur content of the CLC substrates, we measured their carbon, oxygen, and sulfur concentrations by XPS. The obtained values are listed in Table 6.1. Sulfur was not detected on the MWL substrates. The sulfur concentrations of the KL and OL substrates ranged from 0.07 to 0.12%. The surface composition of the CLC substrates in terms of lignin content was calculated from their C/O ratios. The C/O ratio of the

CNCs was 1.38, which was higher than the theoretical value for cellulose of 1.20, based on the chemical formula $(C_6H_{10}O_5)_n$. This discrepancy was already reported in Chapter 3 and was attributed to carbonaceous surface contamination. The C/O ratios of the three lignins, determined from lignin substrates, prepared by spin coating silicon wafer pieces with aqueous lignin suspensions, were 3.31, 2.47, and 2.24 for KL, OL, and MWL, respectively. The calculated lignin contents were much lower than the nominal ones, especially for the OL and MWL substrates. The discrepancy indicated either that the composition of the CLC substrates was not uniform along their thickness, *i.e.* that the substrates' surfaces were deficient in lignin, or that the spin coating process was selective for CNCs leading to the preferential deposition of CNCs over lignin particles.

Table 6.1. RMS surface roughnesses, surface densities, atomic concentrations of C, O, and S, and C/O ratios for the cellulose and CLC substrates[a]

Nominal lignin content	RMS Surface roughness (nm)	ρ_S (mg·m^{-2})	Atomic concentrations (%)			C/O ratio	Calculated lignin content (%)
			C	O	S		
0% lignin	3.6	42.3 ± 1.5	57.96	42.04	NA	1.38	–
10% KL	2.8	33.3 ± 1.4	60.36	39.55	0.09	1.53	8
20% KL	2.4	33.5 ± 2.2	62.23	37.68	0.08	1.65	14
30% KL	2.5	31.7 ± 0.8	64.22	35.51	0.07	1.81	22
10% OL	2.6	37.6 ± 0.3	57.96	41.45	0.12	1.40	2
20% OL	2.8	33.7 ± 0.2	59.6	39.76	0.09	1.50	11
30% OL	2.9	31.8 ± 0.2	61.38	38.22	0.09	1.61	21
10% MWL	3.3	34.7 ± 0.2	58.02	41.97	NA	1.38	0
20% MWL	3.3	36.3 ± 0.6	59.24	40.59	NA	1.46	9
30% MWL	3.2	33.1 ± 1.5	60.75	39.07	NA	1.55	20

[a] Data are means ± one standard deviation of three measurements.

Figure 6.3 shows AFM height images of LLC substrates prepared from 0.5 and 1 wt % aqueous lignin suspensions.

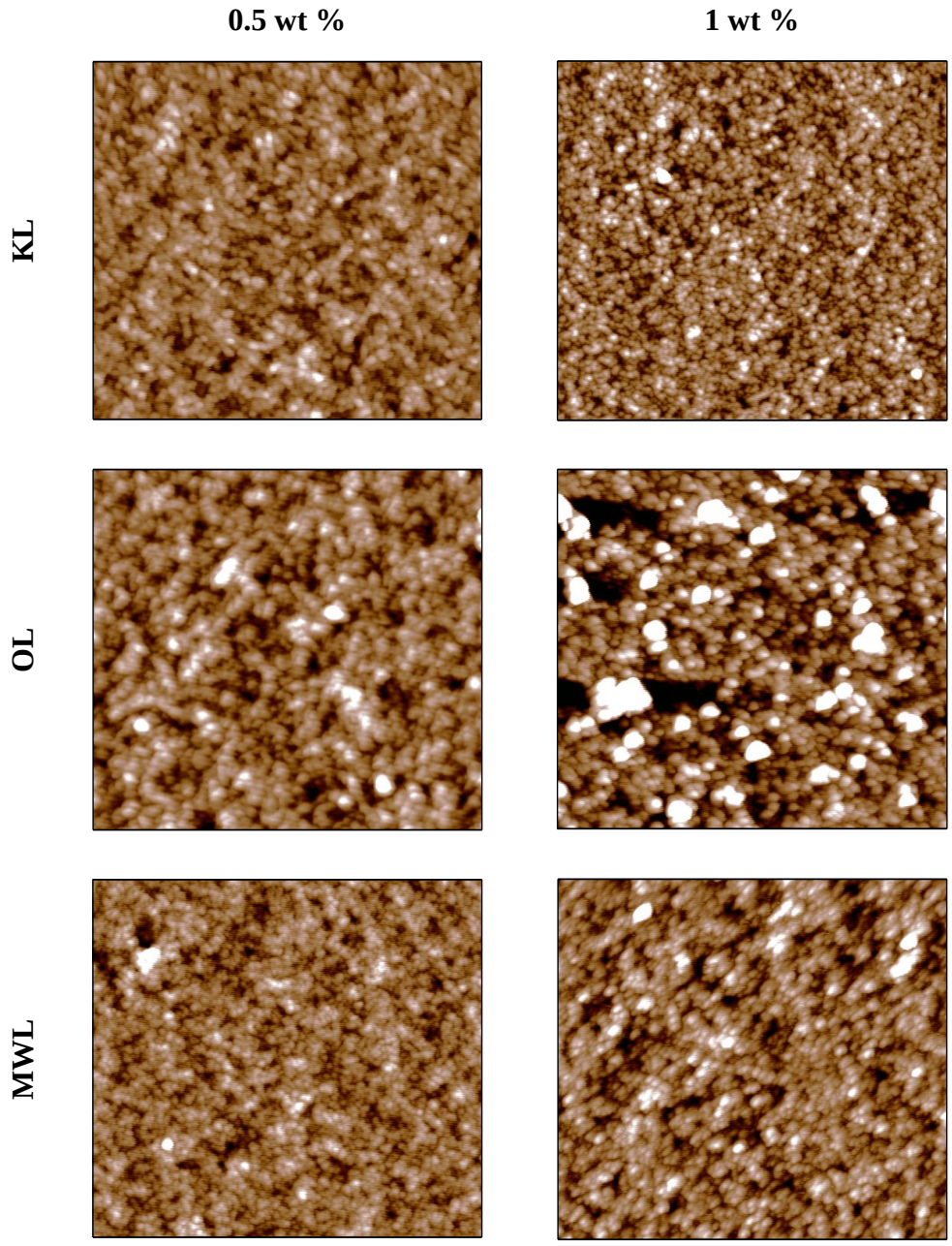

Figure 6.3. AFM height images of LLC substrates prepared from 0.5 and 1 wt % aqueous lignin suspensions. The scan size and z-scale are 2 μm × 2 μm and 15 nm, respectively, for all images.

The morphology of the LLC substrates differed strongly from that of the CLC substrates (Figure 6.2). CNCs were not discernible on the surface of the LLC substrates. The surface of the

LLC substrates seemed to consist of spherical particles of lignin, and the spherical lignin particles appeared to be smallest on the KL substrates and largest on the OL substrates. The size of lignin particles in aqueous suspensions is governed by the hydrophobicity of the lignin. As shown in Chapter 5, OL was the most hydrophobic of the three lignins. The greater hydrophobicity of OL could be the reason for the larger size of the OL particles on the OL substrate. The larger size of the MWL particles, compared to that of the KL particles, could not be due to a higher hydrophobicity of MWL because MWL was more hydrophilic than KL (Chapter 5) and therefore could not be so easily explained.

As could be expected from their lignin particle sizes, the RMS surface roughnesses of the LLC substrates (Table 6.2), ranging from 2.3 to 5.6 nm, were highest for the OL substrates and lowest for the KL substrates. Most of the LLC substrates had a lower surface roughness than the underlying cellulose substrate, confirming again that the lignin particles smoothened the rough topography caused by the CNCs. Also not surprisingly, the surface roughnesses of the substrates prepared from 1 wt % lignin suspensions were higher than those prepared from 0.5 wt % suspensions. The surface densities of the lignin layers were on average 6.9 $mg \cdot m^{-2}$ for the LLC substrates prepared from 0.5 wt % lignin suspensions and 17.6 $mg \cdot m^{-2}$ for substrates prepared from 1 wt % suspensions. The higher surface densities of the LLC substrates prepared from 1 wt % lignin suspensions, compared to those obtained with 0.5 wt % suspensions, showed that a higher lignin concentration in the spin coating solution resulted in the deposition of more lignin.

Table 6.2. RMS surface roughnesses and surface densities of the lignin layer of the LLC substrates

Lignin	Lignin concentration[a] (wt %)	RMS surface roughness (nm)	Surface density ($mg \cdot m^{-2}$)[b]
KL	0.5	2.3	6.8 ± 0.9
	1.0	2.8	16.5 ± 1.9
OL	0.5	2.9	6.5 ± 0.8
	1.0	5.6	16.8 ± 2.6
MWL	0.5	2.5	7.4 ± 1.2
	1.0	3.1	19.4 ± 2.4

[a] of the suspension used for spin coating
[b] Data are means ± one standard deviation of three measurements.

6.4.2. Enzymatic hydrolysis of the LC substrates

The enzymatic hydrolysis of the LC substrates was analyzed in real time by QCM-D. Figure 6.4 shows ($\Delta f_n/n$) and ΔD curves for CLC substrates prepared from KL. The ($\Delta f_n/n$) and ΔD curves for a cellulose substrate are also shown for comparison. The ($\Delta f_n/n$) and ΔD curves for the CLC substrates prepared from OL and MWL are shown in Figure D.2 in Appendix D.

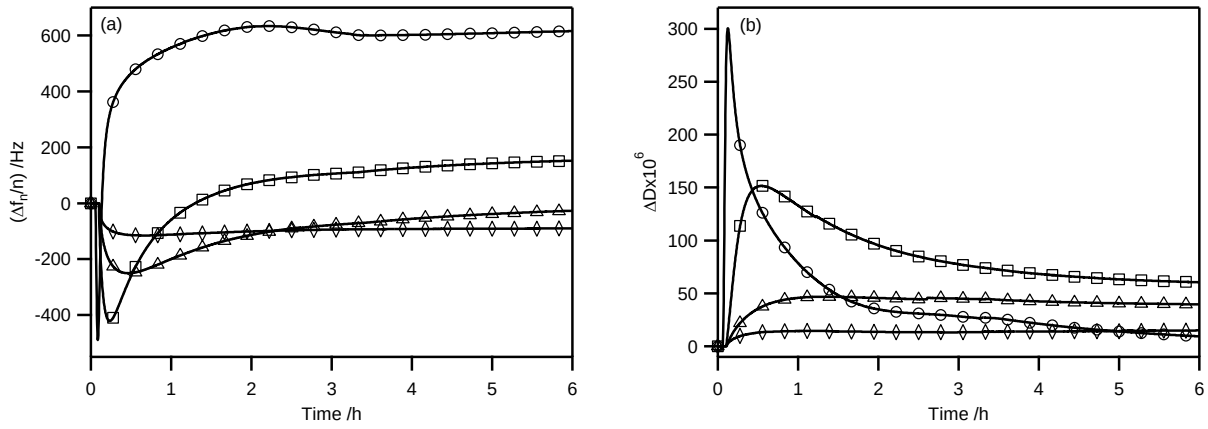

Figure 6.4. (a) ($\Delta f_n/n$) and (b) ΔD curves (3rd overtone) for the enzymatic hydrolysis of the cellulose substrate (○) and CLC substrates with a nominal KL content of 10% (□), 20% (△), and 30% (◇).

The shape of ($\Delta f_n/n$) and ΔD curves from QCM-D cellulose hydrolysis experiments has been explained previously.[15] The initial ($\Delta f_n/n$) decrease, signifying an increase in mass on the quartz crystal, and the associated ΔD increase, signifying the formation of a soft, energy dissipative layer, is due to the adsorption of enzymes onto the substrate. As enzyme adsorption slows and the hydrolysis rate increases, ($\Delta f_n/n$) eventually reaches a minimum and ΔD a maximum. The time at which the ($\Delta f_n/n$) minimum occurs contains information about both the rate of enzyme adsorption and the rate of substrate hydrolysis. The ($\Delta f_n/n$) increase after the minimum, signifying a decrease in mass on the quartz crystal, and the associated ΔD decrease, signifying the removal of soft, energy dissipative material from the quartz crystal, is due to the hydrolytic erosion of the substrate. Eventually, both ($\Delta f_n/n$) and ΔD level off as the hydrolysis of the substrate slows down or ceases.

As seen in Figure 6.4, hydrolysis of the cellulose substrates is rapid and completed within about 2 h. The total increase in $(\Delta f_n/n)$ for the cellulose substrate, due to the degradation and removal of cellulose from the quartz crystal, was about 600 Hz, assuming most of the cellulase desorbed from the substrate after hydrolysis. The fact that the $(\Delta f_n/n)$ curves for the CLC substrates ended at much lower values indicated that hydrolysis of these substrates was incomplete. For the substrate with a nominal KL content of 30%, $(\Delta f_n/n)$ stayed nearly constant after the initial decrease. The absence of an increase in $(\Delta f_n/n)$ after the initial decrease indicated that the extent of hydrolysis of this substrate was low. The conclusion that hydrolysis of the CLC substrates was incomplete was further supported by the high ΔD values at the end of the substrates' ΔD curves, indicating the presence of a soft, energy dissipative layer. This layer could either be a layer of non-productively adsorbed enzyme or a highly swollen, partially hydrolyzed surface layer of the substrate.

The magnitude of the $(\Delta f_n/n)$ minimum, $(\Delta f_n/n)_{min}$, was taken as a measure of the maximum amount of enzyme adsorbed on the substrate. The maximum rate of $(\Delta f_n/n)$ increase after the minimum, marked by the second inflection point in the $(\Delta f_n/n)$ curve and determined from the maximum in its first derivative, $(d(\Delta f_n/n)/dt)_{max}$, was taken as a measure of the hydrolysis rate. Figure 6.5 shows values of $(\Delta f_n/n)_{min}$ and $(d(\Delta f_n/n)/dt)_{max}$, for the CLC substrates, as a percentage of that for a cellulose substrate, $(d(\Delta f_n/n)/dt)_{max,CNC}$.

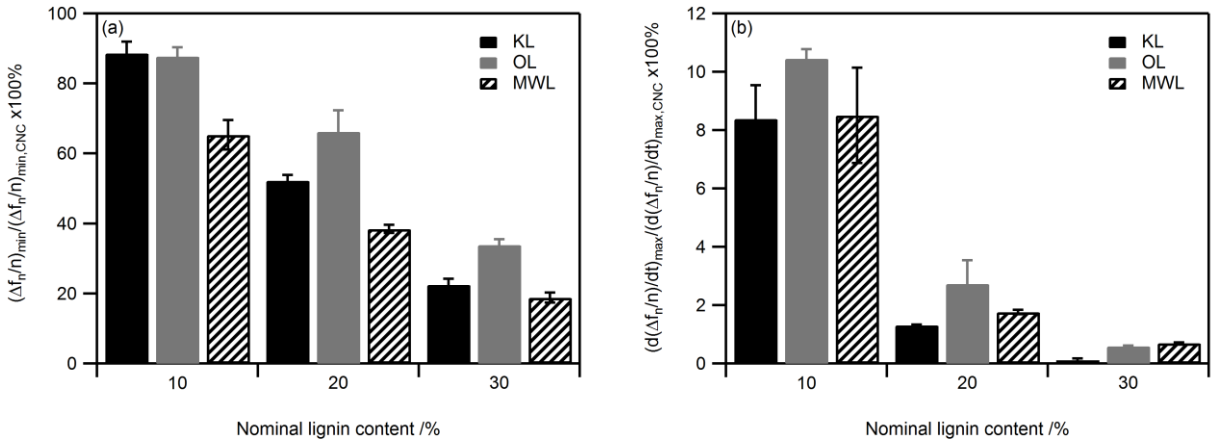

Figure 6.5. Values of (a) $(\Delta f_n/n)_{min}$ and (b) $(d(\Delta f_n/n)/dt)_{max}$, from 3rd overtone $(\Delta f_n/n)$ curves, for the CLC substrates, as percentages of those for the cellulose substrate, $(\Delta f_n/n)_{min,CNC}$ (–489 Hz) and $(d(\Delta f_n/n)/dt)_{max,CNC}$ (2.64 s^{-2}).

As seen in Figure 6.5a, the maximum amount of adsorbed enzyme decreased with increasing lignin content. This trend was confirmed in Figure 6.4b by a decrease in the ΔD maximum with increasing lignin content, indicating that the soft enzyme layer was less thick on substrates with higher lignin content. The decrease in the maximum amount of adsorbed enzyme with increasing lignin content could have two reasons. First, because the lignin particles had filled up the voids between the CNCs and evened out the surface of the CLC substrates, the surface area accessible to the enzyme and available for adsorption might have decrease with increasing lignin content. Second, cellulase might adsorb more readily onto cellulose than onto lignin. Adsorption of cellulase from *T. reesei* onto cellulose is mediated by cellulose binding domains (CBDs), containing three precisely spaced tyrosine residues. Binding of the CBDs to cellulose is postulated to occur through van der Waals interactions and aromatic ring polarization interactions with the pyranose rings exposed on the 110 crystal face of cellulose.[43] The affinity of CBDs for lignin is probably lower than for cellulose because the spacing and orientation of the aromatic rings in amorphous lignin differs from the spacing and orientation of the pyranose ring on the 110 crystal face of cellulose. As shown in Chapter 5, adsorption of cellulase onto lignin substrates caused a maximum frequency decrease of 53, 66, and 94 Hz for KL, OL, and MWL, respectively. In contrast, the magnitude $(\Delta f_n/n)_{min}$ for the cellulose substrate (Figure 6.4a) was

489 Hz. The greater magnitude of $(\Delta f_n/n)_{min}$ for the cellulose substrate, compared to those for the three lignin substrates, could be due to a higher affinity of cellulase for crystalline cellulose than for lignin or to a higher surface accessibility of the cellulose substrates, compared to the lignin substrates. For comparison, the maximum frequency decrease caused by cellulase adsorption onto the CLC substrates with a nominal lignin content of 30% was 114, 160, and 81 Hz for KL, OL, and MWL, respectively. On average, cellulase adsorption was highest on the OL substrate and lowest on the MWL substrate.

Figure 6.5b illustrates that, besides the maximum amount of adsorbed enzyme, the apparent hydrolysis rate also greatly decreased with increasing lignin content. A nominal lignin content of only 10% reduced the apparent hydrolysis rate of the CLC substrates to about 9% that of a cellulose substrate. On average, the apparent hydrolysis rates were highest for the OL substrates, consistent with their higher amounts of adsorbed enzyme, and lowest for the KL substrates, despite them having more adsorbed enzyme than the MWL substrates. The decrease in the apparent hydrolysis rates with increasing lignin content indicated that lignin had an inhibitory effect on the enzymatic hydrolysis of the CLC substrates.

Figure 6.6 shows $(\Delta f_n/n)$ and ΔD curves for the LLC substrates prepared from KL. The $(\Delta f_n/n)$ and ΔD curves for a cellulose substrate are also shown for comparison. The $(\Delta f_n/n)$ and ΔD curves for the LLC substrates prepared from OL and MWL are shown in Figure D.3 in Appendix D.

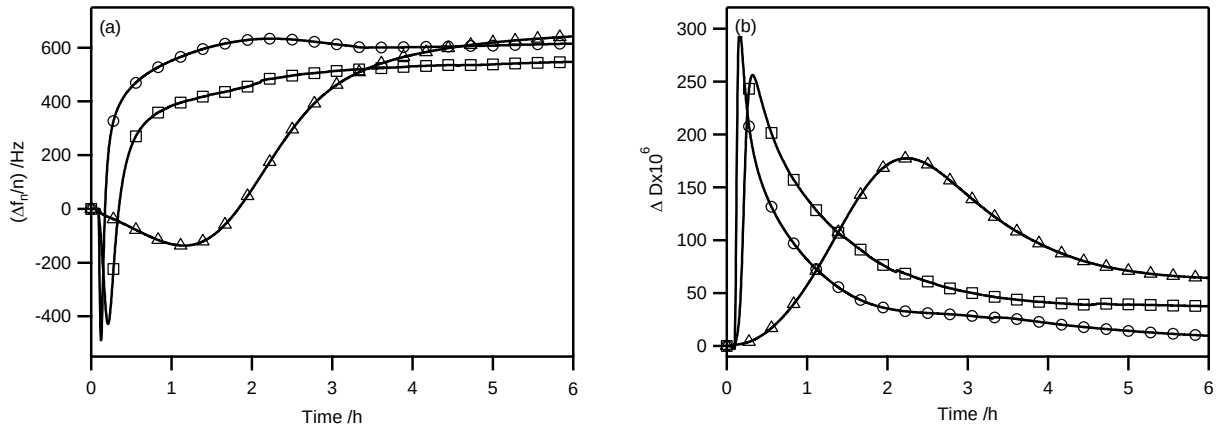

Figure 6.6. (a) ($\Delta f_n/n$) and (b) ΔD curves (3rd overtone) for the enzymatic hydrolysis of the cellulose substrate (○) and LLC substrates prepared from 0.5 wt % (□) and 1 wt % (△) KL suspensions.

As opposed to the ($\Delta f_n/n$) curves for the CLC substrates (Figure 6.2), most of which ended below 200 Hz, those for the LLC substrate reached fairly high ($\Delta f_n/n$) values at the end of the hydrolysis experiment, many exceeding 400 Hz. The ($\Delta f_n/n$) value for the completely hydrolyzed cellulose substrate was 600 Hz. However, because of the additional lignin layer, the initial mass of the LLC substrates was larger than that of the cellulose substrate, and consequently complete removal of the substrate from the quartz crystal should yield higher ($\Delta f_n/n$) values than obtained for the cellulose substrate. Therefore, final ($\Delta f_n/n$) values equal to or lower than that obtained for the cellulose substrate indicated incomplete degradation and removal of the substrates. The fact that the final ($\Delta f_n/n$) values obtained for the LLC substrates approached but did generally not exceed the final ($\Delta f_n/n$) value for the cellulose substrate could indicate that the mass loss was due to the complete removal of the cellulose layer possibly leaving the lignin on the quartz crystal. The high ΔD values at the end of the ΔD curves of some of the LLC substrates (Figure 6.6b and A4.3) indicated the presence of a soft, energy dissipative layer. As was the case for the CLC substrates, this layer could either be a layer of non-productively adsorbed enzymes or a highly swollen, partially hydrolyzed surface layer of the substrate.

Figure 6.7 shows the values of $(\Delta f_n/n)_{min}$ and $(d(\Delta f_n/n)/dt)_{max}$ for the LLC substrates, as percentages of those for the cellulose substrate, $(\Delta f_n/n)_{min,CNC}$ and $(d(\Delta f_n/n)/dt)_{max,CNC}$,

respectively. As mentioned above, the former was taken as a measure of the maximum amount of enzyme adsorbed on the substrate and the latter as a measure of the hydrolysis rate.

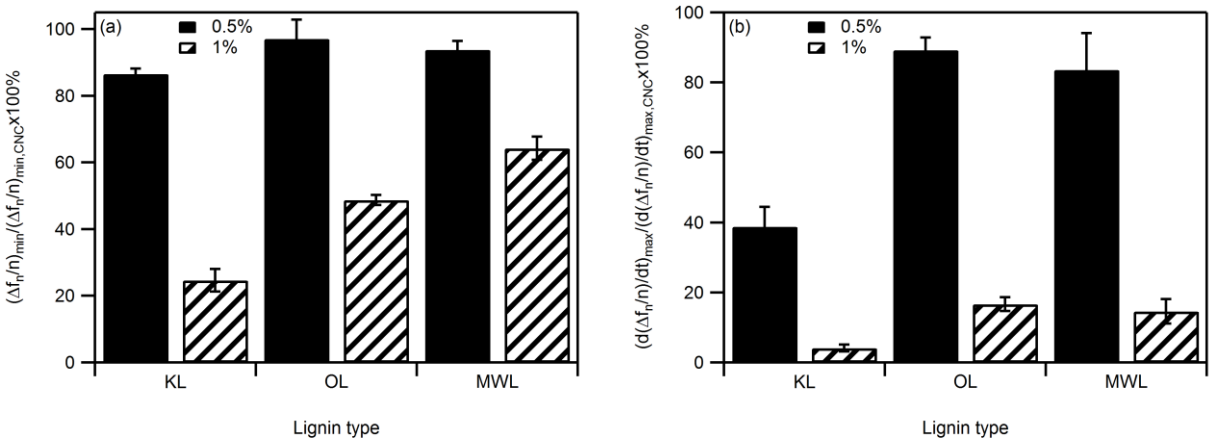

Figure 6.7. Values of (a) $(\Delta f_n/n)_{\min}$ and (b) $(d(\Delta f_n/n)/dt)_{\max}$, from 3rd overtone $(\Delta f_n/n)$ curves, for the LLC substrates, as percentages of those for the cellulose substrate, $(\Delta f_n/n)_{\min,CNC}$ (–489 Hz) and $(d(\Delta f_n/n)/dt)_{\max,CNC}$ (2.64 s^{-2}), respectively.

As seen in Figure 6.7a, the maximum amount of enzyme adsorbed on the LLC substrates prepared from 0.5 wt % lignin suspensions was above 80% that adsorbed on the cellulose substrate. However, the amount was greatly reduced for the LLC substrates prepared from 1 wt % lignin suspensions. Thus, a thicker lignin layer resulted in a lower amount of adsorbed enzyme. This conclusion was further supported in Figure 6.6b by a decrease in the ΔD maximum with increasing thickness of the lignin layer, indicating that the soft enzyme layer was less thick on substrates with a thicker lignin layer. Also, the amount of adsorbed enzyme decreased from the LLC substrate prepared from MWL to the LLC substrate prepared from KL. This decrease indicated that KL had the strongest reducing effect on cellulase adsorption. As discussed above, the decrease in the maximum amount of adsorbed enzyme with increasing thickness of the lignin layer could be due to a decrease in the total surface area available for adsorption or the lower affinity of cellulase for lignin than for cellulose. However, as seen in Table 6.2, the LLC substrates prepared from 1 wt % lignin suspensions had higher RMS surface roughnesses than the LLC substrates prepared from 0.5 wt % suspensions. Therefore, the total surface areas for adsorption of the former should be larger than those of the latter and result in larger amounts of

adsorbed enzyme. The fact that enzyme adsorption was greater on the LLC substrates with smaller surface roughnesses could suggest that the lower cellulase affinity for lignin than for cellulose was the primary reason for the decrease in the maximum amount of adsorbed enzyme with increasing lignin layer thickness.

Figure 6.7b shows that the apparent hydrolysis rates of the LLC substrates were also greatly reduced with respect to that of the cellulose substrate and that the decrease was more pronounced for the substrates with thicker lignin layers (prepared from a 1 wt % lignin suspension) than those with thinner lignin layers (prepared from a 0.5 wt % lignin suspension). The substrates prepared from KL showed the strongest reduction in apparent hydrolysis rate. The thinner KL layer reduced the apparent hydrolysis rate of the substrate to 39% that of a cellulose substrate and the thicker lignin layer to 4%. As in the case of the CLC substrates, lignin had an inhibitory effect on the enzymatic hydrolysis of the LLC substrates.

A comparison of the relative apparent hydrolysis rates of the CLC and LLC substrates revealed that the lignin layer of the LLC substrates was less effective in reducing the substrate's apparent hydrolysis rate than the lignin blended in with the CNCs in the CLC substrates. The reason was probably the larger cellulose–lignin interface in the CLC substrates, compared to that in the LLC substrates, blocking access for the enzyme to the cellulose fraction.

In addition to the rate of substrate hydrolysis, the rate of cellulase adsorption might have been affected by the lignin layer of the LLC substrates. The location (time) of the minimum, t_{min}, in the ($\Delta f_n/n$) curves depends on both the rate of cellulase adsorption and the rate of substrate hydrolysis because the minimum will be located where the frequency decrease due to cellulase adsorption is equal to the frequency increase due to substrate hydrolysis. The values for t_{min} for the LLC substrates are listed in Table 6.3 together with that for the cellulose substrate. As seen in Table 6.3, the t_{min} value for the cellulose substrate was much smaller than the values for the LLC substrates. The reason for the larger t_{min} values of the LLC substrates was most likely the reduced accessibility of the CNCs, which would also explain why the substrates with thinner lignin layers had lower t_{min} values than the substrates with thicker lignin layers. The t_{min} values for the LLC substrates prepared from KL were much larger than the values for the LLC substrates prepared from OL and MWL. The finding that KL caused the greatest delay in substrate hydrolysis was consistent with the findings reported above that KL caused the greatest reductions in cellulase

adsorption and apparent substrate hydrolysis rate relative to those of a cellulose substrate and compared to OL and MWL. The smaller size of the KL particles, observed in Figure 6.3, might allow them to cover the cellulose substrate more completely and thus more effectively limit the access for the cellulase molecules.

Table 6.3. Times of the ($\Delta f_n/n$) minima, t_{min}, for the cellulose and LLC substrates[a]

Lignin	Lignin concentration[b] (wt %)	t_{min} (s)
None[c]	–	110 ± 11
KL	0.5	454 ± 7
	1.0	4069 ± 269
OL	0.5	223 ± 18
	1.0	380 ± 11
MWL	0.5	240 ± 10
	1.0	1010 ± 28

[a] Data are means ± one standard deviation of three measurements.
[b] of the suspension used for spin coating
[c] cellulose substrate

6.4.3. Morphology change during enzymatic hydrolysis

Figure 6.8 shows AFM height images of CLC substrates with a 30% nominal lignin content after enzymatic hydrolysis. An AFM height image of a cellulose substrate after enzymatic hydrolysis is also shown for comparison. Images of CLC substrates with nominal lignin contents of 10 and 20% are shown in Figure D.4 in Appendix D. After hydrolysis, CNCs were no longer discernible on the cellulose and CLC substrates. Instead, one could see globular features, which could either be spherical lignin particles, in the case of the CLC substrates, or adsorbed enzyme. The RMS surface roughnesses of the substrates after hydrolysis, ranging from 4.1 to 5.7 nm, were higher than before hydrolysis (2.4–3.6 nm, Table 6.1). The increase in surface roughness could be due to the erosion of the substrates during hydrolysis or the presence of adsorbed enzyme on the substrates after hydrolysis.

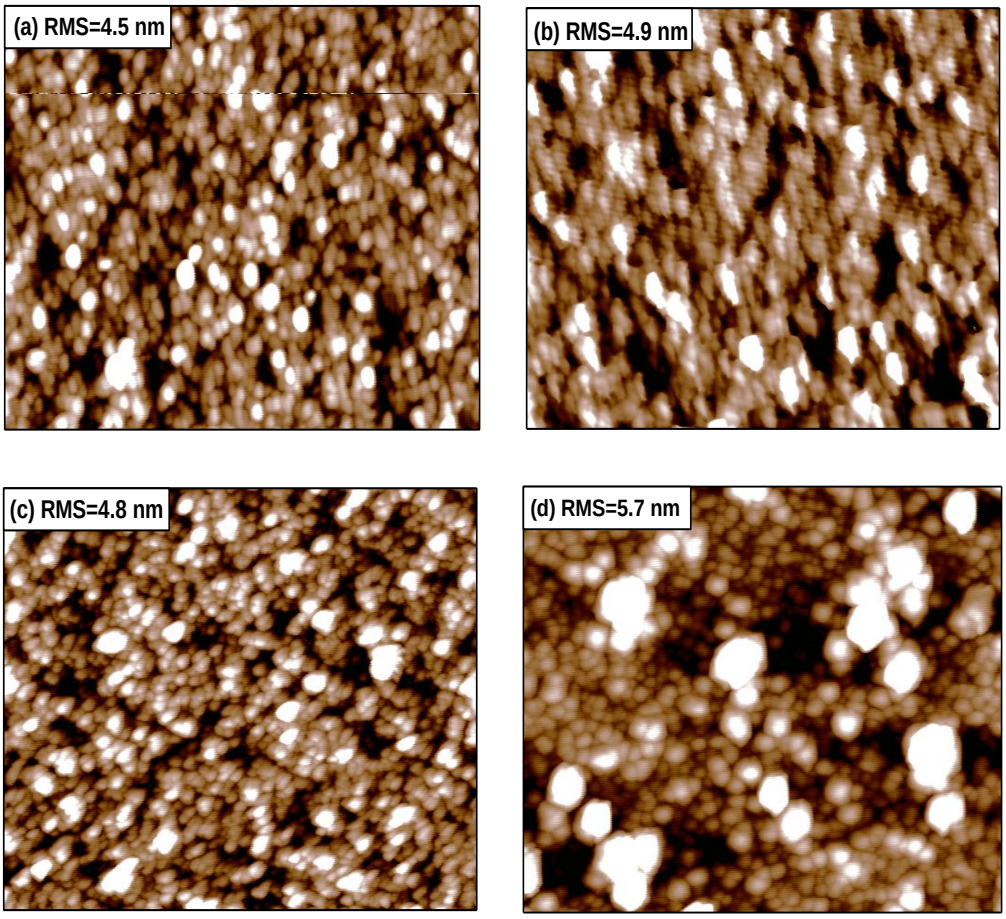

Figure 6.8. AFM height images of CLC substrates with a 30% nominal content of (a) KL, (b) OL, and (c) MWL and (d) a cellulose substrate after enzymatic hydrolysis. The scan size and z-scale are 2 μm × 2 μm and 15 nm, respectively, for all images.

Figure 6.9 shows AFM height images of LLC substrates prepared from 1 wt % lignin suspensions after enzymatic hydrolysis. An AFM height image of a bare silica quartz crystal is also shown for comparison. The LLC substrates after hydrolysis had globular features similar as before (Figure 6.3) but the features were of different size than the spherical lignin particles observed on the LLC substrates before hydrolysis. As opposed to the CLC substrates, the LLC substrates were smoother after hydrolysis than before. Their RMS surface roughnesses after hydrolysis ranged from 1.4 to 2.2 nm, as compared to 2.3–5.6 nm before (Table 6.2). The fact that their surface roughnesses were higher than that of a bare quartz crystal (0.8 nm) indicated

that there was still some material from the substrate present on the surface of the quartz crystal after hydrolysis. This conclusion was further supported by the high ΔD values at the end of the QCM-D hydrolysis experiments (Figures 6.6 and A4.3), indicating the presence of a soft layer on the surface of the quartz crystals. The absence of the large spherical particles, observed on the CLC substrates after hydrolysis and believed to be adsorbed enzyme, suggested that there was little adsorbed enzyme on the LLC substrates after hydrolysis. The small globular features could potentially be the lignin left behind on the quartz crystal after the cellulose had been hydrolyzed.

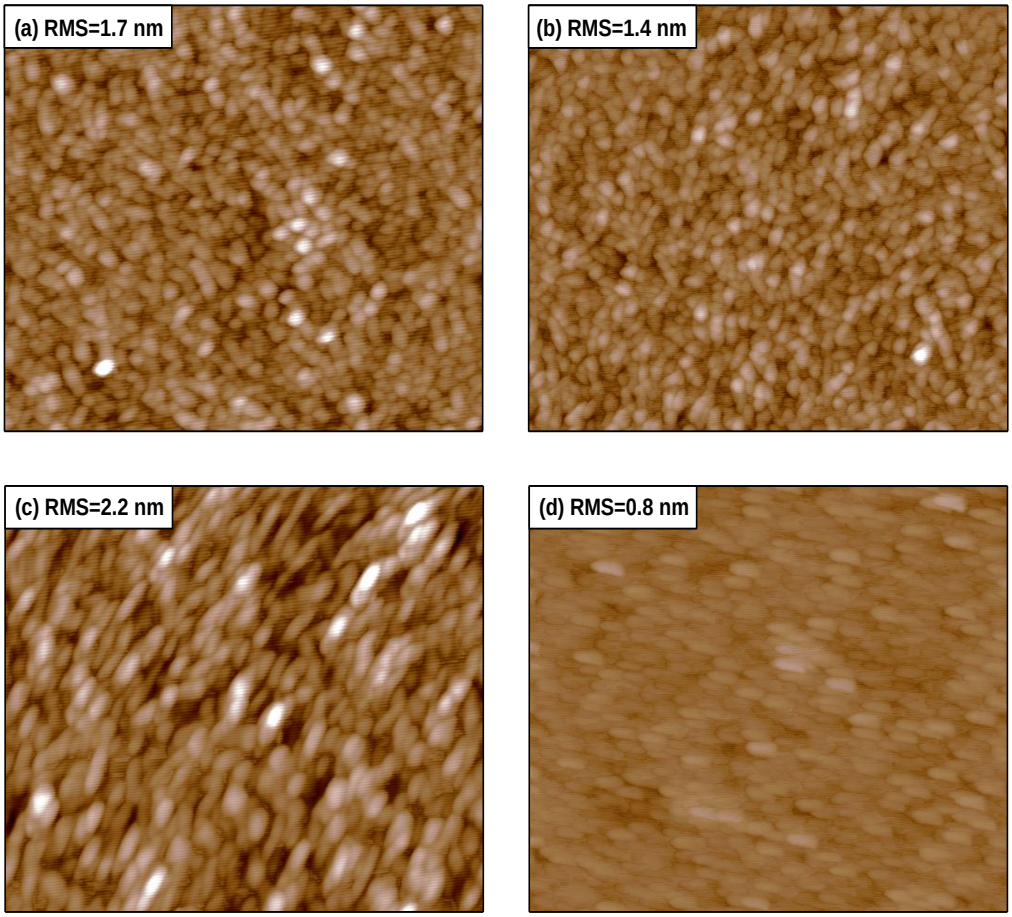

Figure 6.9. AFM height images of LLC substrates prepared from 1 wt % aqueous suspensions of (a) KL, (b) OL, and (c) MWL after enzymatic hydrolysis. d) is an image of a bare silica quartz crystal, shown for comparison. The scan size and z-scale are 2 μm × 2 μm and 15 nm, respectively, for all images.

6.5. Conclusions

The objective of this study was to elucidate the effects of lignin on the enzymatic hydrolysis of cellulose by means of QCM-D. The study has shown that LC substrates modeling the plant cell wall can be prepared by spin coating of mixed aqueous lignin/CNC suspensions and LC substrates modeling the cellulose fraction of pretreated biomass, containing redeposited lignin, can be prepared by spin coating of aqueous lignin suspensions onto cellulose substrates. Enzymatic hydrolysis of the LC substrates, monitored by QCM-D, has revealed that lignin hinders both the adsorption of *T. reesei* cellulases onto the substrates and the enzymatic hydrolysis of the substrates. The inhibitory effect of lignin increases with its content or layer thickness in the LC substrate. A lignin surface layer has less of an inhibitory effect on cellulose hydrolysis than an embedding lignin matrix.

6.6. Acknowledgments

This project was supported by the National Research Initiative of the USDA Cooperative State Research, Education and Extension Service under Grant 2005-35504-16088, the National Science Foundation under Grant CHE-0724126 and DMR-0907567, the U.S. Department of Transportation through the Southeastern Sun Grant Center, and the Institute for Critical Technology and Applied Science. Parts of this work were carried out with instruments of the Nanoscale Characterization and Fabrication Laboratory, a Virginia Tech facility operated by the Institute for Critical Technology and Applied Science. The authors thank Dr. Jerry Hunter for assistance with the XPS experiments and Dr. Wolfgang G. Glasser for providing the lignin samples.

6.7. References

1. Lynd, L. R.; Weimer, P. J.; van Zyl, W. H.; Pretorius, I. S. Microbial Cellulose Utilization: Fundamentals and Biotechnology. *Microbiology and Molecular Biology Reviews* **2002,** *66,* 506-577.

2. Sun, Y.; Cheng, J. Y. Hydrolysis of Lignocellulosic Materials for Ethanol Production: A Review. *Bioresource Technology* **2002,** *83,* 1-11.

3. Beguin, P.; Aubert, J. P. The Biological Degradation of Cellulose. *Fems Microbiology Reviews* **1994,** *13,* 25-58.

4. Cowling EB; W., B. Structural Features of Cellulosic Materials in Relation to Enzymic Hydrolysis. *About the advances in chemistry series* **1969,** *95*.

5. Zhang, Y. H. P.; Lynd, L. R. Toward an Aggregated Understanding of Enzymatic Hydrolysis of Cellulose: Noncomplexed Cellulase Systems. *Biotechnology and Bioengineering* **2004,** *88,* 797-824.

6. Chang, V. S.; Holtzapple, M. T. Fundamental Factors Affecting Biomass Enzymatic Reactivity. *Applied Biochemistry and Biotechnology* **2000,** *84-6,* 5-37.

7. Guo, G. L.; Hsu, D. C.; Chen, W. H.; Hwang, W. S. Characterization of Enzymatic Saccharification for Acid-Pretreated Lignocellulosic Materials with Different Lignin Composition. *Enzyme and Microbial Technology* **2009,** *45,* 80-87.

8. Draude, K. M.; Kurniawan, C. B.; Duff, S. J. B. Effect of Oxygen Delignification on the Rate and Extent of Enzymatic Hydrolysis of Lignocellulosic Material. *Bioresource Technology* **2001,** *79,* 113-120.

9. Sewalt, V. J. H.; Glasser, W. G.; Beauchemin, K. A. Lignin Impact on Fiber Degradation .3. Reversal of Inhibition of Enzymatic Hydrolysis by Chemical Modification of Lignin and by Additives. *Journal of Agricultural and Food Chemistry* **1997,** *45,* 1823-1828.

10. Mooney, C. A.; Mansfield, S. D.; Touhy, M. G.; Saddler, J. N. The Effect of Initial Pore Volume and Lignin Content on the Enzymatic Hydrolysis of Softwoods. *Bioresource Technology* **1998,** *64*, 113-119.

11. Pan, X. J.; Arato, C.; Gilkes, N.; Gregg, D.; Mabee, W.; Pye, K.; Xiao, Z. Z.; Zhang, X.; Saddler, J. Biorefining of Softwoods Using Ethanol Organosolv Pulping: Preliminary Evaluation of Process Streams for Manufacture of Fuel-Grade Ethanol and Co-Products. *Biotechnology and Bioengineering* **2005,** *90*, 473-481.

12. Meunier-Goddik, L.; Penner, M. H. Enzyme-Catalyzed Saccharification of Model Celluloses in the Presence of Lignacious Residues. *Journal of Agricultural and Food Chemistry* **1999,** *47*, 346-351.

13. Mosier, N.; Wyman, C.; Dale, B.; Elander, R.; Lee, Y. Y.; Holtzapple, M.; Ladisch, M. Features of Promising Technologies for Pretreatment of Lignocellulosic Biomass. *Bioresource Technology* **2005,** *96*, 673-686.

14. Wyman, C. E.; Dale, B. E.; Elander, R. T.; Holtzapple, M.; Ladisch, M. R.; Lee, Y. Y. Coordinated Development of Leading Biomass Pretreatment Technologies. *Bioresource Technology* **2005,** *96*, 1959-1966.

15. Turon, X.; Rojas, O. J.; Deinhammer, R. S. Enzymatic Kinetics of Cellulose Hydrolysis: A QCM-D Study. *Langmuir* **2008,** *24*, 3880-3887.

16. Ahola, S.; Turon, X.; Österberg, M.; Laine, J.; Rojas, O. J. Enzymatic Hydrolysis of Native Cellulose Nanofibrils and Other Cellulose Model Films: Effect of Surface Structure. *Langmuir* **2008,** *24*, 11592–11599.

17. Hu, G.; Heitmann, J. A.; Rojas, O. J. In Situ Monitoring of Cellulase Activity by Microgravimetry with a Quartz Crystal Microbalance. *Journal of Physical Chemistry B* **2009,** *113*, 14761-14768.

18. Hu, G.; Heitmann, J. A.; Rojas, O. J. Quantification of Cellulase Activity Using the Quartz Crystal Microbalance Technique. *Analytical Chemistry* **2009,** *81*, 1872-1880.

19. Habibi, Y.; Foulon, L.; Aguie-Beghin, V.; Molinari, M.; Douillard, R. Langmuir-Blodgett Films of Cellulose Nanocrystals: Preparation and Characterization. *Journal of Colloid and Interface Science* **2007,** *316*, 388-397.

20. Tammelin, T.; Saarinen, T.; Osterberg, M.; Laine, J. Preparation of Langmuir/Blodgett-Cellulose Surfaces by Using Horizontal Dipping Procedure. Application for Polyelectrolyte Adsorption Studies Performed with QCM-D. *Cellulose* **2006,** *13*, 519-535.

21. Constantino, C. J. L.; Juliani, L. P.; Botaro, V. R.; Balogh, D. T.; Pereira, M. R.; Ticianelli, E. A.; Curvelo, A. A. S.; Oliveira, O. N. Langmuir-Blodgett Films from Lignins. *Thin Solid Films* **1996,** *284*, 191-194.

22. Constantino, C. J. L.; Dhanabalan, A.; Curvelo, A.; Oliveira, O. N. Preparation and Characterization of Composite Lb Films of Lignin and Cadmium Stearate. *Thin Solid Films* **1998,** *327*, 47-51.

23. Constantino, C. J. L.; Dhanabalan, A.; Cotta, M. A.; Pereira-da-Silva, M. A.; Curvelo, A. A. S.; Oliveira, O. N. Atomic Force Microscopy (AFM) Investigation of Langmuir-Blodgett (LB) Films of Sugar Cane Bagasse Lignin. *Holzforschung* **2000,** *54*, 55-60.

24. Kontturi, E.; Thune, P. C.; Niemantsverdriet, J. W. Cellulose Model Surfaces-Simplified Preparation by Spin Coating and Characterization by X-Ray Photoelectron Spectroscopy, Infrared Spectroscopy, and Atomic Force Microscopy. *Langmuir* **2003,** *19*, 5735-5741.

25. Kontturi, E.; Thune, P. C.; Niemantsverdriet, J. W. Novel Method for Preparing Cellulose Model Surfaces by Spin Coating. *Polymer* **2003,** *44*, 3621-3625.

26. Kontturi, E.; Tammelin, T.; Osterberg, M. Cellulose - Model Films and the Fundamental Approach. *Chemical Society Reviews* **2006,** *35*, 1287-1304.

27. Kontturi, E.; Johansson, L. S.; Kontturi, K. S.; Ahonen, P.; Thune, P. C.; Laine, J. Cellulose Nanocrystal Submonolayers by Spin Coating. *Langmuir* **2007,** *23*, 9674-9680.

28. Edgar, C. D.; Gray, D. G. Smooth Model Cellulose I Surfaces from Nanocrystal Suspensions. *Cellulose* **2003,** *10*, 299-306.

29. Norgren, M.; Notley, S. M.; Majtnerova, A.; Gellerstedt, G. Smooth Model Surfaces from Lignin Derivatives. I. Preparation and Characterization. *Langmuir* **2006,** *22*, 1209-1214.

30. Norgren, M.; Gardlund, L.; Notley, S. M.; Htun, M.; Wagberg, L. Smooth Model Surfaces from Lignin Derivatives. II. Adsorption of Polyelectrolytes and Pecs Monitored by QCM-D. *Langmuir* **2007,** *23*, 3737-3743.

31. Notley, S. M.; Norgren, M. Measurement of Interaction Forces between Lignin and Cellulose as a Function of Aqueous Electrolyte Solution Conditions. *Langmuir* **2006,** *22*, 11199-11204.

32. Notley, S. M.; Norgren, M. Adsorption of a Strong Polyelectrolyte to Model Lignin Surfaces. *Biomacromolecules* **2008,** *9*, 2081-2086.

33. Notley, S. M.; Norgren, M. Surface Energy and Wettability of Spin-Coated Thin Films of Lignin Isolated from Wood. *Langmuir* **2010,** *26*, 5484-5490.

34. Kaya, A.; Du, X. S.; Liu, Z. L.; Lu, J. W.; Morris, J. R.; Glasser, W. G.; Heinze, T.; Esker, A. R. Surface Plasmon Resonance Studies of Pullulan and Pullulan Cinnamate Adsorption onto Cellulose. *Biomacromolecules* **2009,** *10*, 2451-2459.

35. Ahola, S.; Salmi, J.; Johansson, L. S.; Laine, J.; Osterberg, M. Model Films from Native Cellulose Nanofibrils. Preparation, Swelling, and Surface Interactions. *Biomacromolecules* **2008,** *9*, 1273-1282.

36. Fort, D. A.; Remsing, R. C.; Swatloski, R. P.; Moyna, P.; Moyna, G.; Rogers, R. D. Can Ionic Liquids Dissolve Wood? Processing and Analysis of Lignocellulosic Materials with 1-N-Butyl-3-Methylimidazolium Chloride. *Green Chemistry* **2007,** *9*, 63-69.

37. Lindstrom, T. The Colloidal Behaviour of Kraft Lignin Part I.: Association and Gelation of Kraft Lignin in Aqueous Solutions. *Colloid and polymer science* **1979,** *257*, 277-285.

38. Glasser, W. G.; Barnett, C. A.; Sano, Y. Classification of Lignins with Different Genetic and Industrial Origins. *Journal of Applied Polymer Science: Applied Polymer Symposium* **1983,** *37*, 441-460.

39. Sauerbrey, G. Verwendung Von Schwingquarzen Zur Wägung Dünner Schichten Und Zur Mikrowägung. *Z. Phys.* **1959,** *155*, 206-222.

40. Chapter 10, Q. In: Physical Properties and Data of Optical Materials; Optical Science and Engineering; CRC Press: 2007; pp 355-378.

41. Kanazawa, K. K.; Gordon, J. G. Frequency of a Quartz Microbalance in Contact with Liquid. *Analytical Chemistry* **1985,** *57*, 1770-1771.

42. Schubert, D. W.; Dunkel, T. Spin Coating from a Molecular Point of View: Its Concentration Regimes, Influence of Molar Mass and Distribution. *Materials Research Innovations* **2003,** *7*, 314–321.

43. Lehtio, J.; Sugiyama, J.; Gustavsson, M.; Fransson, L.; Linder, M.; Teeri, T. T. The Binding Specificity and Affinity Determinants of Family 1 and Family 3 Cellulose Binding Modules. *Proceedings of the National Academy of Sciences of the United States of America* **2003,** *100*, 484-489.

CHAPTER 7

Effects of the non-ionic surfactant Tween 80 on the enzymatic hydrolysis of model cellulose and lignocellulosic substrates

7.1. Abstract

Non-ionic surfactants, such as Tween 80, are known to benefit the enzymatic conversion of lignocellulosic (LC) biomass. Their mechanisms of actions, however, are incompletely understood. This study was conducted to elucidate the effects of the non-ionic surfactant Tween 80 on the enzymatic hydrolysis of cellulose and LC substrates by means of quartz crystal microbalance with dissipation monitoring (QCM-D). The interactions of Tween 80 and cellulases were analyzed by surface tension measurement and fluorescence spectroscopy. The adsorption of Tween 80 onto model cellulose substrates and their enzymatic hydrolysis were studied by QCM-D and Surface Plasmon Resonance Spectroscopy (SPR). The adsorption of Tween 80 onto model LC substrates and their enzymatic hydrolysis were studied by QCM-D and AFM. It was found that Tween 80 forms surfactant–protein complexes with cellulases in solution but that the complexation does not compromise cellulase activity. Tween 80, either adsorbed on the substrate or in solution, had no effect on the hydrolysis of cellulose substrates by cellulase. Substrate-adsorbed Tween 80 increased the apparent cellulase hydrolysis rates of LC substrates but the ability of Tween 80 to increase the apparent hydrolysis rate depended strongly on the structural

properties of the LC substrate (composite *versus* layered) and the chemical properties of the lignin.

7.2. Introduction

Finding alternatives to fossil fuels has been given high priority because of concerns about declining petroleum reserves, energy security, and climate change. Extensive attention has been given to bioethanol produced from lignocellulosic (LC) biomass because of the vast availability of LC biomass on earth and the carbon-neutral impact on combustion of cellulosic bioethanol in transportation. Enzymatic saccharification followed by microbial fermentation has been proven to be a promising process for the production of cellulosic bioethanol.[1-3] However, the costs associated with the required high cellulase loadings and feedstock pretreatment processes represent obstacles for the large-scale production of cellulosic bioethanol.[4,5] High cellulase loadings are necessary because of the detrimental effect of lignin on the hydrolysis by unproductive binding of cellulase to the lignin.[6-10]

Addition of non-ionic surfactants during biomass pretreatment and saccharification has been studied and shown to have beneficial effects on the enzymatic hydrolysis of LC biomass.[11-17] According to previous studies, non-ionic surfactants, biosurfactants, or other non-hydrolytic proteins, such as Tween 20,[11,14,17] Tween 80,[11,15] or bovine serum albumin (BSA),[8,15] can improve the conversion of cellulose to glucose, while decreasing non-productive adsorption of cellulase onto the substrate, and thus can potentially reduce the processing costs for LC biomass conversion. Castanon and Wilke[12] have reported that the addition of Tween 80 enhances the enzymatic hydrolysis rate of newspaper cellulose by 33% while doubling the amount of recoverable enzyme. Kaya *et al.*[13] studied the effects of surfactants on the saccharification of carboxymethyl cellulose and xylan and found that addition of Tween 80 increased their conversion by 50% and 9%, respectively. Kaar *et al.*[14] studied the effects of both Tween 20 and Tween 80 on the enzymatic hydrolysis of corn stover and found Tween 20 to be slightly more effective than Tween 80, causing a maximum increase of cellulose, xylan, and total conversion by 42, 40, and 42%, respectively.

Several efforts to elucidate the mechanisms by which non-ionic surfactants enhance the enzymatic hydrolysis of LC biomass have been made. However, no consistent explanations have emerged from these studies. Eriksson *et al.*[11] concluded that the major effect of non-ionic surfactants during hydrolysis is to reduce unproductive binding of cellulase to lignin. In Chapter 5, we showed that adsorption of Tween 80 onto model lignin substrates increased their hydrophilicity, caused removal of lignin from their surfaces, appeared to reduce cellulase adsorption *via* hydrophobic interactions, and reduced the rate of cellulase adsorption onto the substrates. Qing *et al.*[16] studied the removal of lignin from biomass by non-ionic surfactants during pretreatment and found that lignin removal could lead to an increase in the hydrolysis yield.

In recent years, quartz crystal microbalance with dissipation monitoring (QCM-D) has evolved as a valuable new tool for studying the enzymatic hydrolysis of cellulose.[18,19] The use of QCM-D in combination with well-defined model cellulose substrates to monitor the enzymatic hydrolysis process has the following benefits. First, QCM-D is very sensitive to mass changes on the cellulose substrates and able to detect mass increases, *e.g.* due to enzyme adsorption, or mass decreases, *e.g.* due to substrate erosion, as small as 1 $ng \cdot cm^{-2}$.[20,21] Second, QCM-D is able to detect changes in the dissipation factor of the cellulose substrate during enzymatic hydrolysis, which provides information about changes in the substrates structural and mechanical properties and level of hydration.[19]

This study was conducted to elucidate the effects of the non-ionic surfactant Tween 80 on the enzymatic hydrolysis of cellulose and LC substrates by means of QCM-D. First, the interactions between Tween 80 and cellulases from the fungus *Trichoderma reesei* in solution were analyzed by surface tension measurement and fluorescence spectroscopy. Then, the adsorption of Tween 80 onto model cellulase substrate its effect on their hydrolysis were studied by QCM-D and surface plasmon resonance (SPR). Finally, the adsorption of Tween 80 onto two types of LC substrates prepared from three different types of lignin, namely kraft lignin (KL), organosolv lignin (OL), and milled wood lignin (MWL) were studied by QCM-D. The preparation of the model LC substrates and their characteristics have been described in Chapter 6.

7.3. Experimental section

7.3.1. Materials

Dissolving-grade softwood sulfite pulp (Temalfa 93A-A) was kindly provided by Tembec, Inc. KL (M_n = 5·10^3 g·mol^{-1}, M_w = 28·10^3 g·mol^{-1}), Tween 80 (SigmaUltra), pyrene (>99.0%, Fluka) and Celluclast 1.5L (Novozyme) were purchased from Sigma-Aldrich. Sulfuric acid (95.9 wt %, Certified ACS Plus), pyridine (99.5%, Chemservice), citric acid monohydrate (Fisher Scientific, Certified ACS), sodium hydroxide (Acros Organics, 98.5%), hydrogen peroxide (34–37%, Technical Grade), ammonium hydroxide (28.9%, Certified ACS Plus), sodium dodecyl sulfate (99%, Acros Organics), ethanol (200 proof, Decon labs, Inc), dimethyl sulfoxide (DMSO, Certified ACS), and methanol (99.8%, Acros Organics) were purchased from Fisher Scientific. MWL from hemlock (*Tsuga* sp., M_n = 2.6·10^3 g·mol^{-1}, M_w = 15.2·10^3 g·mol^{-1})[22] and OL from cottonwood (*Populus trichocharpa*, M_n < 10^3 g·mol^{-1}, M_w < 3·10^3 g·mol^{-1})[22] were kindly provided by Prof. Em. Wolfgang Glasser. All water used was deionized (DI) water with a resistivity of 18.2 MΩ·cm, obtained from a Millipore Direct-Q 5 Ultrapure Water Systems.

7.3.2. Cellulose nanocrystal (CNC) preparation

CNCs were prepared from wood pulp by sulfuric acid hydrolysis followed by solvolytic desulfation, as described in detail in Chapter 3. In brief, milled (60-mesh) softwood sulfite pulp was hydrolyzed with 64 wt % sulfuric acid (10 mL·g^{-1} cellulose) at 45 ℃ for 1 h. The acid was removed from the CNC suspension by centrifugation and dialysis against DI water. The final suspension was sonicated and filtered through a 0.45 μm poly(vinylidene fluoride) (PVDF) syringe filter (Whatman, Ltd.). For desulfation of the CNCs, the suspension was neutralized with pyridine and lyophilized (Freezone 4.5L freeze-dry system, Labconco Corp.). The freeze-dried CNCs (pyridinium salt) were heated for 2 h at 80 ℃ at a concentration of ~1% (w/v) in a 9:1 (v/v) mixture of DMSO and methanol. After cooling and dilution of the reaction mixture with DI water, the suspension was dialyzed against DI water for several weeks and then sonicated and filtered through a 0.45 μm (PVDF) syringe filter.

7.3.3. Lignin purification and fractionation

The lignins were purified and fractionated as described in detail in Chapter 5. In brief, KL and MWL were dissolved in 0.75 M and OL in 1.5 M aqueous ammonia at a concentration of 1 wt %. The lignin solutions were dialyzed against DI water using Spectra/Por 4 dialysis tubing (MWCO: 12–14 kDa, Spectrum Lab, Inc.) for two weeks for removal of the low molecular weight fraction and water-soluble impurities and then centrifuged at 25 ℃ and 4900 rpm for 15 min for removal of any sedimenting larger particles. Finally, the lignin suspensions were concentrated to 1.5 wt % with a rotary evaporator under vacuum at 45 ℃ and stored in the refrigerator until use. Prior to use, the suspensions were diluted to 1 wt % with DI water.

7.3.4. Cellulose and LC substrate preparation

Cellulose and LC substrates for QCM-D experiments were prepared on silicon dioxide-coated AT-cut quartz crystals (Q-Sense). The quartz crystals were cleaned by immersion and shaking for 1 min in fresh piranha solution (7:3 (v/v) mixture of sulfuric acid and hydrogen peroxide), then rinsed with DI water, dried in a stream of nitrogen, and irradiated for 15 min with an ozone-producing mercury lamp (UV/Ozone cleaner, Bioforce Nanosciences). Cellulose substrates for SPR experiments were prepared on SPR sensor slides (12.0 mm × 12.0 mm × 0.9 mm). The SPR sensors were cleaned by immersion for 1 h in a boiling mixture of aqueous ammonia, hydrogen peroxide, and DI water at a volume ratio of 1:1:5 and then for 1 h at ambient temperature in fresh piranha solution, rinsed with DI water, dried in a stream of nitrogen. To minimize surface contamination, we cleaned the quartz crystals and SPR sensor slides immediately prior to use.

Cellulose substrates were prepared by spin coating (WS-400B-6NPPLite, Laurell Technologies Corp.) the cleaned quartz crystals and SPR sensor slides for 1 min at 4000 rpm with 140 µl of a 1 wt % CNC suspension. Two types of LC substrates were prepared, referred to as composite substrates and layered substrates. Composite LC (CLC) substrates were prepared *via* direct spin coating of lignin- and CNC-containing aqueous suspensions. Suspensions with a lignin-to-CNC ratio of 1:9, 2:8, and 3:7 (w/w) and a solids concentration of 1 wt % were prepared by mixing the appropriate volumes of a 1 wt % lignin suspension and a 1 wt % CNC

suspension. The composite substrates were prepared by spin coating the cleaned quartz crystals for 1 min at 4000 rpm with 140 µl of the lignin/CNC suspension. Layered LC (LLC) substrates were prepared by spin coating of cellulose substrates with aqueous lignin suspensions. A cleaned quartz crystal was first spin-coated for 1 min at 4000 rpm with 140 µl of a 1 wt % CNC suspension. The obtained cellulose substrate was then spin-coated for 1 min at 4000 rpm with 140 µl of a 0.5 or 1 wt % lignin suspension. Different lignin concentrations were used for different thicknesses of the lignin layer. All substrates were dried in a vacuum oven at 65 °C for several hours for improved stability in aqueous media.

7.3.5. Surface tension measurements

The surface tension of 50 mM sodium citrate buffer (pH 4.8) and cellulase solutions with different Tween 80 concentrations, ranging from 10^{-5} to 1 mM, were determined with a Wilhemy plate tensiometer using a roughened platinum plate. The buffer was prepared by 20-fold dilution with DI water from a 1 M sodium citrate buffer (pH 4.5), produced by dissolution of the appropriate amounts of citric acid monohydrate and sodium hydroxide in DI water. The cellulase solution was prepared by dilution of 0.5 g Celluclast 1.5L, a commercial cellulase solution derived from *Trichoderma reesei* with a protein content of 143 $mg \cdot mL^{-1}$, with 50 mM sodium citrate buffer to a volume of 100 mL. The temperature during the measurements was maintained at 25 °C with a thermostat-controlled circulating water bath. The platinum plate was cleaned after each measurement with 2% sodium dodecyl sulfate solution and rinsed thoroughly with DI water for removal of adsorbed cellulase.

7.3.6. Steady-state fluorescence spectroscopy

The fluorescence of pyrene, acting as a probe, in 50 mM sodium citrate buffer and cellulase solutions with different Tween 80 concentrations, ranging from 10^{-5} to 1 mM, was analyzed by steady-state fluorescence spectroscopy (Perkin-Elmer LS 50 fluorescence spectrometer). The Tween 80-containing buffer and cellulase solutions were prepared as described above. Pyrene was dissolved at a concentration of 10^{-3} M in ethanol. Aliquots of the pyrene solution were

measured into glass vials and dried. After evaporation of the ethanol, aliquots of the Tween 80 solutions were measured into the vials so that the Pyrene concentration was 10^{-6} M. The solutions were shaken on an Orbit Shaker for 24 h. Emission spectra were recorded at an excitation wavelength of 334 nm over the wavelength range 360–500 nm. The slit settings for excitation and emission were 5 and 2.5 nm, respectively.

7.3.7. Tween 80 adsorption onto cellulase substrates

The adsorption of Tween 80 onto cellulase substrates was measured by QCM-D (Q-sense E4) and SPR (Reichert SR 7000). Tween 80 solutions in 50 mM sodium citrate buffer were prepared with Tween 80 concentrations ranging from 1 to 100 mM.

For QCM-D measurements, cellulose substrates were placed in the QCM-D flow modules, and a 0.25 mL·min^{-1} sodium citrate buffer feed (50 mM) was established with a peristaltic pump. The temperature inside the flow modules was controlled at 25.00 ± 0.02 ℃. When the normalized rate of change of the 3rd overtone frequency, ($\Delta f_3/3$), became less than 2 Hz·h^{-1}, the substrates were considered saturated and equilibrated, and the buffer feed was replaced with a Tween 80 solution feed with the same flow rate. After 30 min, the buffer feed was restored and maintained for 10 min to rinse off any reversibly adsorbed Tween 80 molecules. After the buffer rinse, the two-step process was repeated for the next higher Tween 80 concentration, progressing from the lowest to the highest Tween 80 concentration. Changes in the oscillation frequency, Δf, and dissipation factor, ΔD, of the quartz crystals were recorded in real time at the fundamental frequency (5 MHz) and 6 overtone frequencies (15, 25, 35, 45, 55, and 65 MHz) with QSoft 401 acquisition software (Q-Sense).

The surface excess concentration of adsorbed Tween 80 was determined by modeling Δf and ΔD for the 3rd and 5th overtones with a one-layer Voigt element-based viscoelastic film model[23,24] with the QTools modeling center (Q-Sense). The model treats the CNC layer on the quartz crystal's surface as an extension of the quartz crystal. The input parameters for the model are the density and viscosity of the bulk liquid above the viscoelastic layer and the density of the viscoelastic layer. The parameters to fit are the viscosity, shear modulus, and thickness, h_t, of the viscoelastic layer. For the density and viscosity of the bulk liquid, we used the density and

viscosity of water at 25 ℃, which are 997 kg·m^{-3} and 0.89·10^{-3} kg·m^{-1}s^{-1}.[25] The density of the viscoelastic Tween 80 film, ρ_t, was fixed at 1100 kg·m^{-3}. The fitting ranges for the viscosity, shear modulus, and thickness of the viscoelastic layer were 5·10^{-4}–10^{-2} kg·m^{-1}s^{-1}, 10^5–10^6 Pa, and 10^{-9}–10^{-7} m, respectively. The hydrodynamic surface excess concentration, Γ_{QCM}, was calculated from h_t and ρ_t as

$$\Gamma_{QCM} = h_t \rho_t \qquad [7.1]$$

Using a different value for ρ_t, *e.g.* 1500 kg·m^{-3}, resulted in a different h_t values but did not affect the calculated surface excess concentration.

For SPR measurements, cellulose substrates were nearly refractive index-matched with immersion oil (n_D = 1.5150) to the prism of the SPR refractometer. The system used a laser diode with an emission wavelength of 780 nm. The flow cell body was equipped with a Viton gasket (Dupont Dow Elastomers LLC) and was mounted on top of the sensor slide. Before the experiment, a 0.25 mL·min^{-1} sodium citrate buffer feed (50 mM) to the flow cell was established *via* Teflon tubing with a cartridge pump (Masterflex). The temperature inside the flow cell was controlled at 25 ± 0.02 ℃. Both the buffer and Tween 80 solutions had been degassed prior to the start of the SPR experiments. When the baseline was stable, the buffer feed was replaced with a Tween 80 solution feed with the same flow rate. After 30 min, the buffer feed was restored and maintained for 10 min to rinse off any reversibly adsorbed Tween 80 molecules. After the buffer rinse, the two-step process was repeated for the next higher Tween 80 concentration, progressing from the lowest to the highest Tween 80 concentration.

The surface excess concentration of the adsorbed Tween 80, Γ_{SPR}, was calculated with the equation of de Feijter *et al.*[26]

$$\Gamma_{SPR} = \frac{\Delta\theta_a (n_f - n)}{(d\theta/dL)(dn/dc)} \qquad [7.2]$$

where n_f is the refractive index of the film (assumed to be 1.45)[27], and n (≈ 1.32813) is the refractive index of the solvent (water).[28] ($d\theta/dL$), which is the change of the resonance angle upon change in the thickness of the adsorbed layer, was deduced from Fresnel calculations

performed with a Matlab-based computer simulation program using a six-layer model. The ($d\theta/dL$) value for polymer surfaces is $(4.2 \pm 0.2)\cdot 10^{-3}$ deg·A^{-1}. (dn/dc), which is the refractive index increment of the Tween 80 solution, was determined with a Wyatt Optilab rEX differential refractometer. (dn/dc) measurements were carried out at λ = 690 nm and 25 ℃ over the concentration range 0–100 mg·L^{-1}. The (dn/dc) value for Tween 80 is 0.132 mL·g^{-1}. $\Delta\theta_a$, which is the change in the resonance angle associated with adsorption, was obtained by subtraction of the contribution of the bulk refractive index changes from the total resonance angle change, $\Delta\theta_{tot}$:

$$\Delta\theta_a = \Delta\theta_{tot} - c\left(\frac{d\theta_{sp}}{dc}\right) \quad [7.3]$$

$$\left(\frac{d\theta_{sp}}{dc}\right) = \left(\frac{d\theta_{sp}}{dn}\right)\left(\frac{dn}{dc}\right) \quad [7.4]$$

where c is the bulk Tween 80 concentration and ($d\theta_{sp}/dn$) is an instrument-specific parameter with the value 61.5 °.

The difference between Γ_{QCM}, which includes both the mass of the adsorbate and coupled buffer solution, and Γ_{SPR}, which includes only the mass of the adsorbate, was used to calculate the coupled buffer content in the hydrated Tween 80 layer[29] according to the equation

$$\%\ \text{buffer content} = \left(\frac{\Gamma_{QCM} - \Gamma_{SPR}}{\Gamma_{QCM}}\right) \times 100\% \quad [7.5]$$

7.3.8. QCM-D hydrolysis experiments

The binding onto and subsequent hydrolysis of cellulose and LC substrates by cellulases was monitored by QCM-D (Q-sense E4). At the beginning of the experiments, all substrates were equilibrated in 50 mM sodium citrate buffer as described above. The temperature inside the flow modules was controlled at 22.00 ± 0.02 ℃. With the cellulose substrates, two sets of

experiments were performed. In “pre-adsorption experiments”, after equilibration of the substrates, the buffer feed was replaced with a feed of Tween 80 solution in buffer with the same flow rate. After 1 h, the buffer feed was restored so that any reversibly adsorbed Tween 80 molecules would be rinsed off. After 10 min of buffer rinse, the buffer feed was replaced with a feed of cellulase solution, prepared as described above. In “mixed-solution experiments”, after equilibration of the substrates, the buffer feed was replaced with a feed of Tween 80-containing cellulase solution. Both, the pre-adsorption and the mixed-solution experiments were carried out at different Tween 80 concentrations, ranging from 0.01 to 5 mM. Experiments without Tween 80 were carried out for reference. In hydrolysis experiments with LC substrates, after equilibration of the substrates, the buffer feed was replaced with a cellulase solution feed at the same flow rate. In hydrolysis experiments of Tween 80-treated LC substrates, after equilibration of the substrates, the buffer feed was first replaced with a feed of 1 mM Tween 80 solution in buffer for 2 h and then, after 20 min of buffer rinse, with a cellulase solution feed at the same flow rate. Δf and ΔD were recorded in real time at the fundamental frequency (5 MHz) and 6 overtone frequencies (15, 25, 35, 45, 55, and 65 MHz) with QSoft 401 acquisition software (Q-Sense). Experiments were terminated when Δf reached a plateau.

7.3.9. Surface morphology and RMS surface roughness determination

The surface morphology and RMS surface roughness of untreated and Tween 80-treated LLC substrates were analyzed by atomic force microscopy (AFM). Tween 80-treated substrates were taken out of the flow modules, thoroughly rinsed with DI water, dried in a stream of nitrogen, and placed in a vacuum oven at 65 ℃ for several hours. Substrates were imaged with an Asylum Research MFP-3D-BIO atomic force microscope. Substrates were scanned in air at ambient relative humidity and temperature in intermittent-contact mode with OMCL-AC160TS standard silicon probes (Olympus Corp.) with a scan frequency of 1 Hz, and 512 scans with 512 points/scan. RMS surface roughness values were determined from 2 μm × 2 μm areas in AFM height images.

7.3.10. Statistical analysis

Statistical analysis of the data was performed by the Student's t-test ($p < 0.05$) with SAS software (v9.2, SAS Institute Inc.).

7.4. Results and discussion

7.4.1. Interactions between Tween 80 and cellulase

The interactions between Tween 80 and cellulase molecules in solution were analyzed by surface tension measurements. Figure 7.1 shows the surface tension of 50 mM sodium citrate buffer and cellulase solution (in buffer) as a function of the Tween 80 concentration. At the lowest Tween 80 concentration (10^{-5} mM), the surface tension of the buffer (72.2 $mN \cdot m^{-1}$) was close to that of water (72.0 $mN \cdot m^{-1}$ at 25 °C)[25] whereas that of the cellulase solution (51.6 $mN \cdot m^{-1}$) was much lower. The ability to lower the surface tension of liquids has been reported for many proteins, including BSA,[30,31] HSA,[31,32] and β-lactoglobulin,[31,33] and has been attributed to their amphiphilic nature caused by hydrophilic and hydrophobic functional groups in their amino acids and resulting in their partitioning to the air/liquid interface. The lower surface tension of the cellulase solution, compared to that of the buffer, was therefore probably a result of cellulase partitioning to the air/buffer interface. As seen in Figure 7.1, above certain concentrations, Tween 80 caused a decrease in the surface tensions of both the buffer and the cellulase solution. For the buffer, this concentration was 10^{-4} mM whereas it was $4 \cdot 10^{-3}$ mM for the cellulase solution. The surface tension-lowering effect of surfactants is due to their partitioning to the air/liquid interface. Thus, the decrease in surface tension with increasing Tween 80 concentration observed for both the buffer and cellulase solution was probably due to the partitioning of Tween 80 molecules to the air/buffer interface. The fact that the cellulase solution required a higher Tween 80 concentration for this decrease to occur suggested that some Tween 80 molecules engaged in surfactant–protein complexes with the cellulase molecules instead of partitioning to the air/buffer interface. Complex formation between Tween 80 and proteins has also been reported for BSA.[30,34]

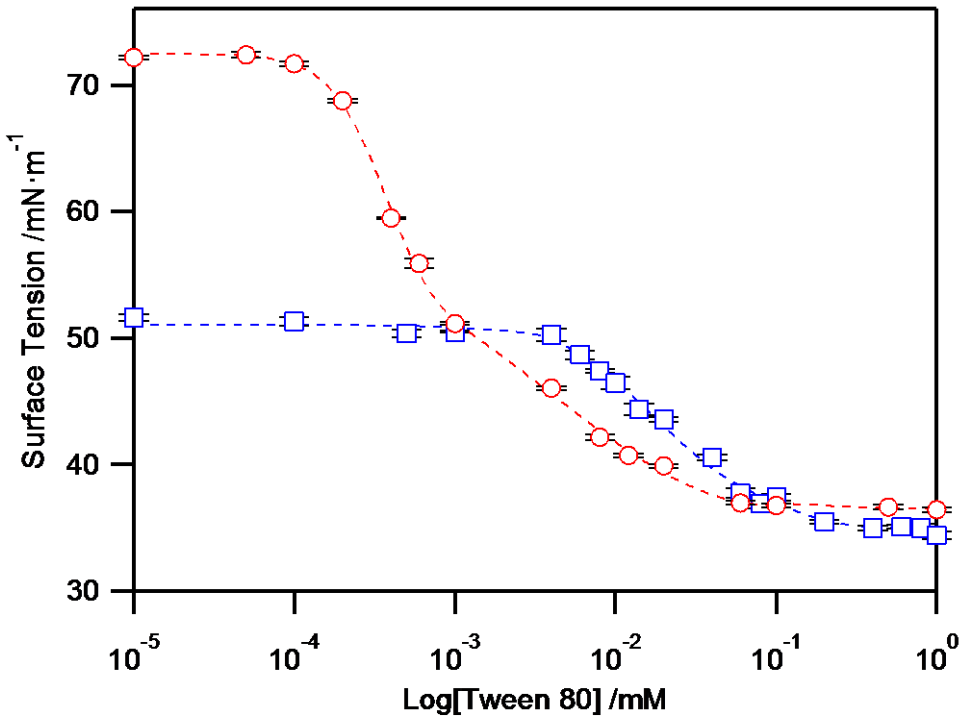

Figure 7.1. Surface tension of 50 mM sodium citrate buffer (○) and cellulase solution (in buffer) (□) as a function of the Tween 80 concentration. (The dashed lines are guides to the eye.)

When the surfactant concentration in surfactant solutions exceeds the critical micelle concentration (CMC), the surfactant molecules form aggregates, known as micelles. Above the CMC, the surface tension of the surfactant solution remains constant upon further increase of the surfactant concentration. The surface tension of the buffer remained constant at a value of about 36.5 $mN \cdot m^{-1}$ above a Tween 80 concentration of 0.06 mM, which was higher than previously reported CMC values for Tween 80 in water ranging from 0.007 to 0.018 mM.[30,34-36] The surface tension of the cellulase solution remained constant at about 35 $mN \cdot m^{-1}$ above a Tween 80 concentration of 0.2 mM. An increase in the CMC of Tween 80 has also been reported for the Tween 80–BSA system.[30,34] The observed increase in CMC was likely due to a decreased number of free Tween 80 molecules available for partitioning to the air/liquid interface as a result of Tween 80–cellulase complexation. The fact that the surface tensions of the buffer and cellulase solution at high Tween 80 concentrations (≥ 0.2 mM) were nearly the same indicated

that the Tween 80 molecules had largely displaced the cellulase molecules at the air/buffer interface. By enclosing their hydrophobic parts in the interior, surfactant–protein complexes can be more hydrophilic than the protein alone.[34] Consequently, complexation of the cellulase with Tween 80 molecules might have increased their solubility in the buffer.

The complexation of cellulase with Tween 80 molecules was further analyzed by fluorescence spectroscopy. Figure 7.2a shows the intensity ratio of the 1st and 3rd vibrational peaks (I_1/I_3) of pyrene emission spectra in buffer and cellulase solution as functions of the Tween 80 concentration.

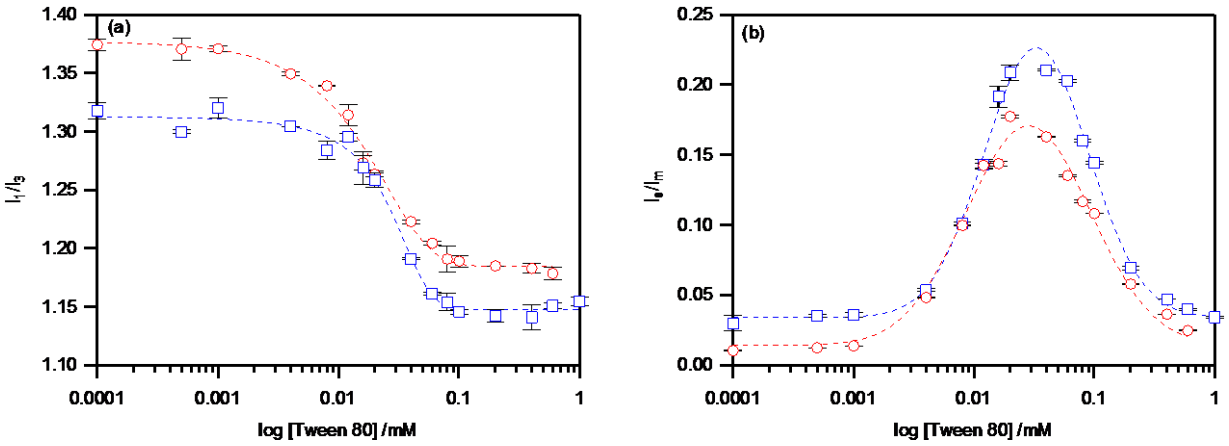

Figure 7.2. (a) Intensity ratio of the 1st and 3rd vibrational peaks (I_1/I_3) of the pyrene emission spectrum and (b) ratio of the pyrene excimer-to-monomer fluorescence emission (I_e/I_m) in 50 mM sodium citrate buffer (○) and cellulase solution (in buffer) (□) as functions of the Tween 80 concentration. (The dashed lines are guides for the eye.)

I_1/I_3 is a measure for the polarity of the microenvironment that the pyrene molecules are experiencing.[37,38] At the lowest Tween 80 concentration (10^{-5} mM), I_1/I_3 in the cellulase solution (1.32) was lower than in the buffer (1.39). The lower I_1/I_3 value in the cellulase solution indicated a more hydrophobic microenvironment, possibly due to partitioning of the pyrene molecules to hydrophobic pockets and patches of the cellulase molecules, as has been reported for BSA.[37,39] Above certain Tween 80 concentrations, I_1/I_3 in the buffer and cellulase solution decreased with increasing Tween 80 concentrations. The decrease in I_1/I_3 indicated an increase in the hydrophobicity of the microenvironment of the pyrene molecules, likely caused by the formation

of surfactant micelles or Tween 80–cellulase complexes and partitioning of the pyrene molecules to their hydrophobic cores. In buffer, the I_1/I_3 decrease started at a lower Tween 80 concentration (0.004 mM) than in the cellulase solution (0.008 mM). The later onset of the I_1/I_3 decrease in cellulase solution indicated that more Tween 80 molecules were required for the creation of hydrophobic microenvironments that would trigger pyrene partitioning. The I_1/I_3 values at high Tween 80 concentration (≥ 0.1 mM) were 1.18 in buffer and 1.14 in cellulase solution. The lower I_1/I_3 value in cellulase solution, compared to that in buffer, indicated that Tween 80–cellulase complexes provided a more hydrophobic microenvironment for the pyrene molecules than Tween 80 micelles.

In hydrophobic environments, pyrene molecules do not only exist as monomers but also as excimers, which are dimers of an excited and a ground-state pyrene molecule. Figure 7.2b shows the ratio of the excimer-to-monomer fluorescence emission (I_e/I_m) in buffer and cellulase solution as a function of the Tween 80 concentration. At very low Tween 80 concentration, I_e/I_m was low because the number of hydrophobic microenvironments in the solution and therefore pyrene excimers was low. Above certain Tween 80 concentrations, I_e/I_m increased and reached a maximum. The I_e/I_m increase, which coincided with the I_1/I_3 decrease, indicated an increase in the number of pyrene excimers and thus confirmed the accumulation of pyrene molecules in the hydrophobic cores of newly formed surfactant micelles or Tween 80–cellulase complexes. The maximum values for I_e/I_m were 0.17 in buffer and 0.21 in cellulase solution. The higher I_e/I_m value in the cellulase solution indicated that the hydrophobic cores of the Tween 80–cellulase complexes were larger than those of the Tween 80 micelles and accommodated more pyrene molecules. After the maximum, I_e/I_m decreased upon further increase of the Tween 80 concentration. The decrease could be explained by the distribution of the pyrene molecules over a larger number of hydrophobic cores resulting in a decrease of the number of pyrene excimers.

7.4.2. Adsorption of Tween 80 onto cellulose substrates

The adsorption of Tween 80 onto cellulose substrates was measured by QCM-D and SPR. Figure 7.3 shows the Tween 80 adsorption isotherms from the QCM-D and SPR data. The Langmuir adsorption model provided good fits to the experimental data, with R^2 values of 0.9871

for the QCM-D and 0.9869 for the SPR data. The coupled buffer content, in percent of the total mass of the adsorbed Tween 80 layer, was determined according to eq 7.5 from the difference in the maximum QCM-D and SPR Tween 80 surface excess concentrations. The Langmuir isotherms gave maximum surface excess concentrations of 8.35 $mg \cdot m^{-2}$ for the QCM-D data and 0.76 $mg \cdot m^{-2}$ for the SPR data. The resulting coupled buffer content of 91% indicated that the adsorbed Tween 80 layer on the cellulose substrate was highly hydrated.

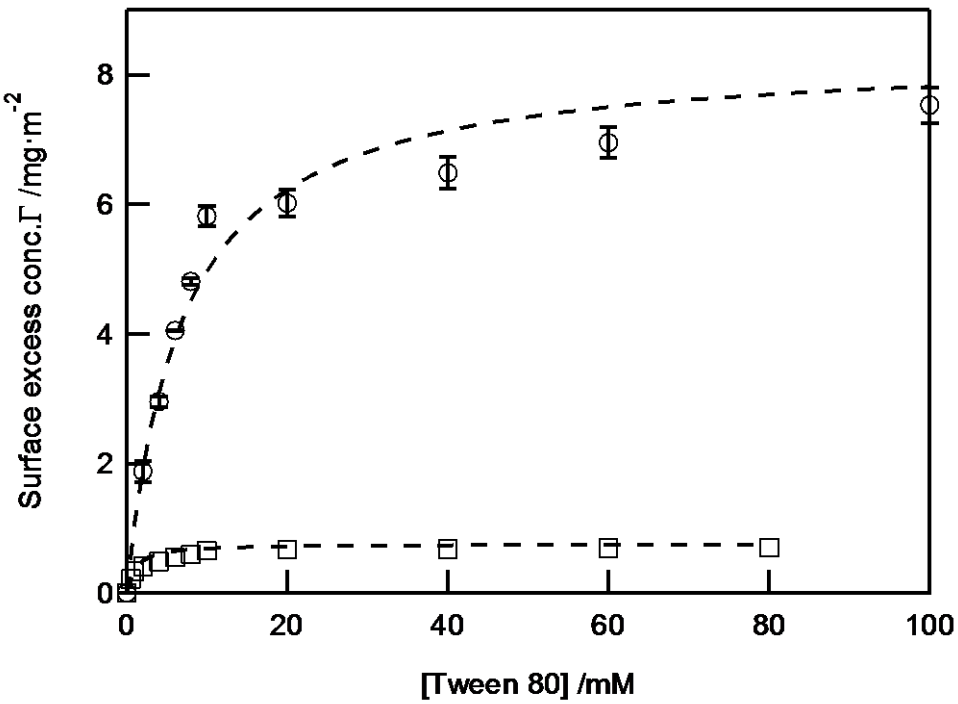

Figure 7.3. Langmuir adsorption isotherm for Tween 80 adsorption onto a model cellulose substrate measured by QCM-D (○) and SPR (□). The dash line is the fitting curve.

7.4.3. Effects of Tween 80 on the enzymatic hydrolysis of cellulose substrates

The effects of Tween 80 on the enzymatic hydrolysis of cellulose substrates were studied with two sets of experiments. In the first set, termed pre-adsorption experiments, Tween 80 molecules were adsorbed onto the cellulose substrate prior to substrate hydrolysis. In the second

set, termed mixed-solution experiments, Tween 80 was added at different concentrations to the cellulase solution prior to substrate hydrolysis. The pre-adsorption experiments were expected to provide information about the potential effects of substrate-adsorbed Tween 80 molecules on cellulase adsorption onto and hydrolysis of the substrates, whereas the mixed-solution experiments were expected to provide information about the potential effects of Tween 80–cellulase interactions in solution.

The shape of the temporal curves of the normalized frequency change, $(\Delta f_n/n)$, from cellulase adsorption and substrate hydrolysis QCM-D experiments has been discussed in Chapters 4 and 6. A typical $(\Delta f_n/n)$ curves shows an initial decrease due to cellulase adsorption, followed by an increase due to substrate hydrolysis. The magnitude of the $(\Delta f_n/n)$ minimum, $(\Delta f_n/n)_{min}$, between the initial decrease and subsequent increase is a measure of the maximum amount of cellulase adsorbed on the substrate. The maximum rate of $(\Delta f_n/n)$ increase after the minimum, marked by the second inflection point in the $(\Delta f_n/n)$ curve and measurable from the maximum in its first derivative, $(d(\Delta f_n/n)/dt)_{max}$, is a measure of the hydrolysis rate. Figure 7.4 shows the values of $(\Delta f_n/n)_{min}$ and $(d(\Delta f_n/n)/dt)_{max}$ for the pre-adsorption experiments. As seen in Figure 7.4, substrate-adsorbed Tween 80 molecules had no effect on the maximum amount of cellulase adsorbed on the cellulose substrates and the apparent hydrolysis rate of the substrates. The absence of an effect of substrate-adsorbed Tween 80 molecules indicated that cellulase molecules were able to displace Tween 80 molecules on the substrate without compromising enzyme activity.

Figure 7.5 shows the values of $(\Delta f_n/n)_{min}$ and $(d(\Delta f_n/n)/dt)_{max}$ for the mixed-solution experiments. Although Tween 80 formed surfactant–protein complexes with cellulase in solution, as demonstrated above (Figures 7.1 and 7.2), at most concentrations the presence of Tween 80 in the cellulase solution had no effect on the maximum amount of cellulase adsorbed on the cellulose substrates and the apparent hydrolysis rate of the substrates.

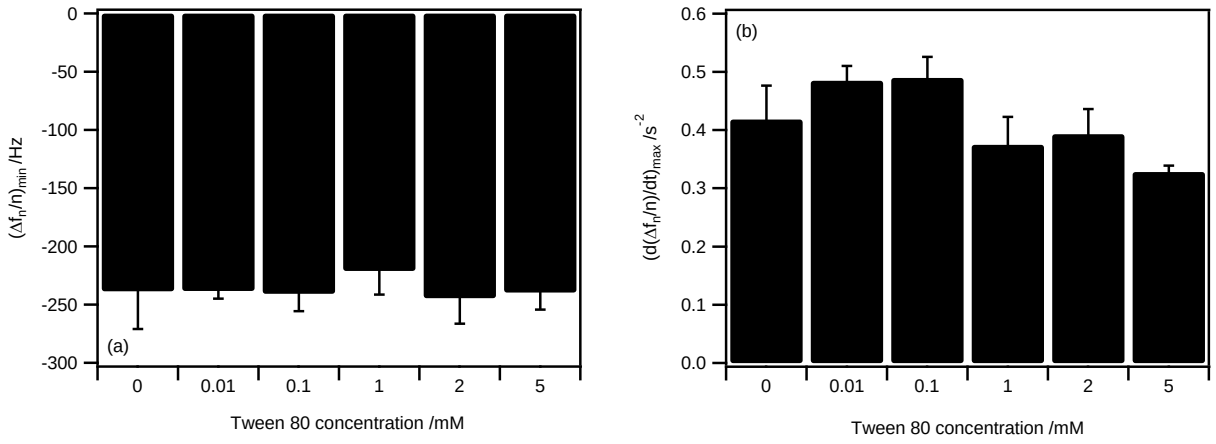

Figure 7.4. Values of (a) $(\Delta f_n/n)_{min}$ and (b) $(d(\Delta f_n/n)/dt)_{max}$ from 3rd overtone $(\Delta f_n/n)$ curves for the pre-adsorption experiments. The values are means of at least three measurements. An asterisk indicates a significant difference (Student's t-test, $p < 0.05$) from the 0-mM mean.

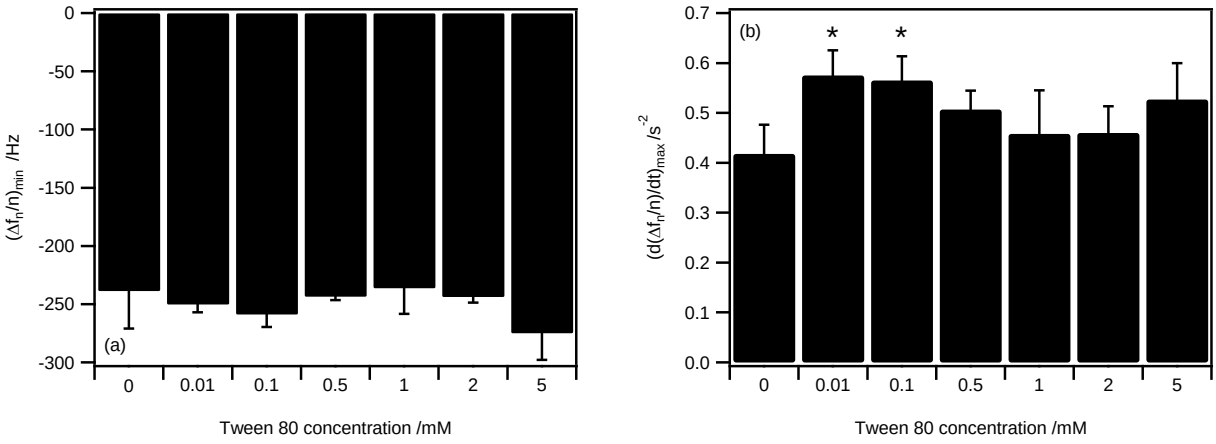

Figure 7.5. Values of (a) $(\Delta f_n/n)_{min}$ and (b) $(d(\Delta f_n/n)/dt)_{max}$ from 3rd overtone $(\Delta f_n/n)$ curves for the mixed-solution experiments. The values are means of at least three measurements. An asterisk indicates a significant difference (Student's t-test, $p < 0.05$) from the 0-mM mean.

Substrate hydrolysis at Tween 80 concentrations of 0.01 and 0.1 mM was statistically significantly faster than in the absence of Tween 80 but hydrolysis at higher Tween 80 concentrations was not. The absence of an effect of Tween 80 molecules in the cellulase solution indicated that cellulase molecules were able to compete with Tween 80 molecules for adsorption sites on the cellulose substrate and cellulase–Tween 80 complexation did not compromise enzyme activity. The reason for the increased apparent hydrolysis rates at Tween 80 concentrations of 0.01 and 0.1 mM is not obvious. At low concentrations, Tween 80 molecules might facilitate cellulase desorption whereas at high concentrations cellulase–Tween 80 complexation and the competition for adsorption sites might negate that effect.

7.4.4. Adsorption of Tween 80 onto LC substrates

The properties of CLC and LLC substrates have been discussed in Chapter 6. Figure 7.6 shows ($\Delta f_n/n$) and ΔD curves for the adsorption of Tween 80 onto CLC substrates with a nominal lignin content of 30%. The ($\Delta f_n/n$) and ΔD curves for a cellulose substrate are also shown for comparison. As indicated by the decrease in ($\Delta f_n/n$) and increase in ΔD, Tween 80 adsorbed onto both the cellulose and CLC substrates. The final value of ($\Delta f_n/n$) upon Tween 80 adsorption on the cellulose substrate was –54 Hz. However, on the CLC substrates the final values of ($\Delta f_n/n$) were –130 Hz, –62 Hz, and –61 Hz for substrates prepared from KL, OL, and MWL, respectively. The higher final values of ($\Delta f_n/n$) on the CLC substrates, compared to that on the cellulose substrate, indicated that more Tween 80 adsorbed onto the CLC substrates than onto the cellulose substrate. The final values of ΔD were $8.4 \cdot 10^{-6}$ for the cellulose substrate and $34 \cdot 10^{-6}$, $10.4 \cdot 10^{-6}$, and $6 \cdot 10^{-6}$ for the CLC substrates prepared from KL, OL, and MWL, respectively. The fact that the final values of ΔD were higher than 10^{-6} indicated that the adsorbed Tween 80 layers were viscoelastic, as opposed to rigid, suggesting that they were highly hydrated. Figure 7.6 also shows that more Tween 80 adsorbed onto CLC substrates prepared from KL than onto those prepared from OL and that hydrophobic interactions might have accounted for most of the Tween 80 adsorption on the former whereas adsorption on the latter was probably largely driven by polar interactions (refer to Chapter 5). Removal of lignin by Tween 80, observed on lignin substrates in Chapter 5, was not observed on any of the CLC substrates.

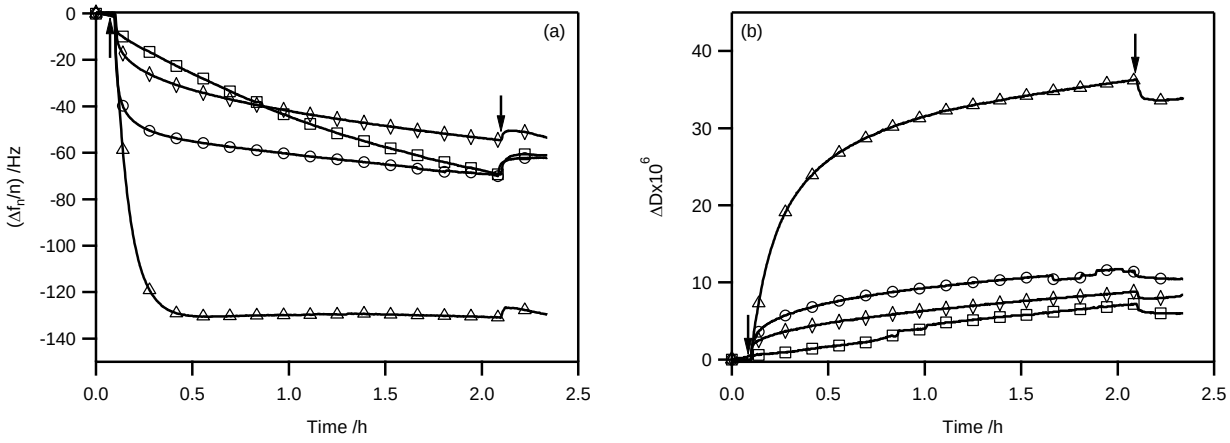

Figure 7.6. Representative (a) ($\Delta f_n/n$) and (b) ΔD curves (3rd overtone) for Tween 80 adsorption onto a cellulose substrate (◊) and CLC substrates with a 30% nominal content of KL (△), OL (○), and MWL (□). The arrows indicate the switch of the liquid feed to Tween 80 solution (1st) and buffer (2nd).

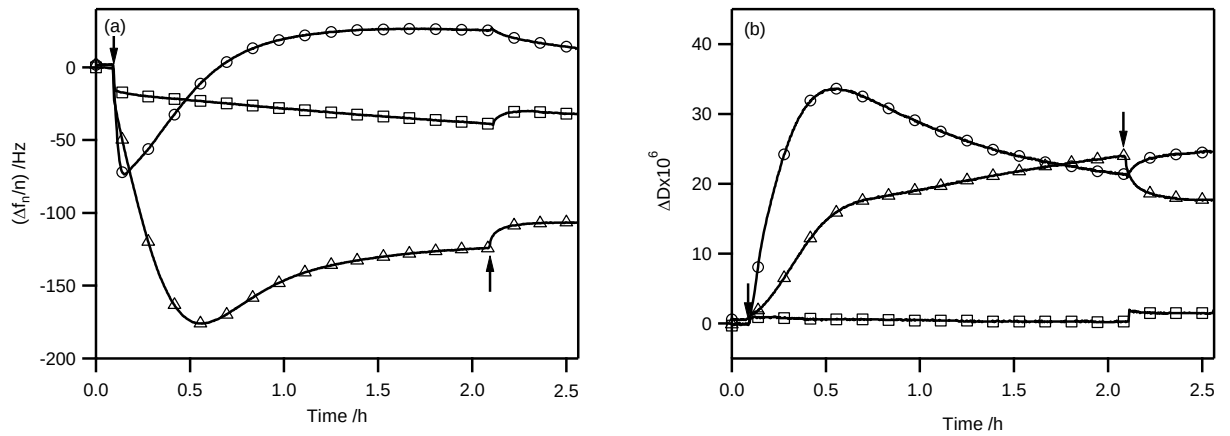

Figure 7.7. Representative (a) ($\Delta f_n/n$) and (b) ΔD curves (3rd overtone) for Tween 80 adsorption onto LLC substrates prepared from 1 wt % aqueous suspensions of KL (△), OL (○), and MWL (□). The arrows indicate the switch of the liquid feed to Tween 80 solution (1st) and buffer (2nd).

Figure 7.7 shows ($\Delta f_n/n$) and ΔD curves for the adsorption of Tween 80 onto LLC substrates prepared from 1 wt % lignin suspensions. The initial decrease in ($\Delta f_n/n$) and increase in ΔD indicated Tween 80 adsorption onto the LLC substrates. Similar to that on CLC substrates, Tween 80 adsorption was highest on the LLC substrates prepared from KL and lowest on those prepared from MWL. The sudden increase in ($\Delta f_n/n$) after the initial decrease, observed for the LLC substrates prepared from KL and OL, signifying a decrease in mass on the oscillating quartz crystal, indicated removal of lignin by Tween 80 similar to that observed on the KL and OL substrates in Chapter 5. The amphiphilic Tween 80 molecules might have interacted with the lignin molecules through hydrophobic interactions between the hydrocarbon chains of the Tween 80 molecules and hydrophobic regions of the lignin molecules. Simultaneous interaction of the hydrophilic headgroups of the Tween 80 molecules with the aqueous buffer might have enabled removal of the lignin molecules from the LLC substrates. As was the case for the MWL substrate in Chapter 5, lignin removal was not observed on the LLC substrate prepared from MWL. The absence of lignin removal on the MWL substrate in Chapter 5 had been attributed to the higher hydrophilicity of MWL, compared to KL and OL.

The ΔD curves for the LLC substrates differed strongly from one another. The curve for the LLC substrate prepared from OL showed an initial increase, due to the formation of a hydrated Tween 80 adsorption layer, followed by a decrease, presumably due to the removal of lignin from the substrate's surface. The final buffer rinse caused a slight increase in ΔD, which was associated with a decrease in ($\Delta f_n/n$), and therefore most likely indicated redeposition of lignin onto the substrate upon removal of the Tween 80 molecules from the system. The ΔD curve for the LLC substrate prepared from KL showed an initial steep increase, attributable to Tween 80 adsorption, followed by a more gradual increase. Interestingly, the more gradual ΔD increase was associated with a ($\Delta f_n/n$) increase, signifying a decrease in mass on the oscillating quartz crystal. The ΔD increase could possibly be explained by the occurrence of two simultaneous processes. The loosening of the lignin molecules on the substrate's surface by the Tween 80 molecules would cause an increase in dissipation whereas the removal of the lignin molecules from the substrate would cause a decrease. On the LLC substrate prepared from KL, the ΔD increase from the former process might outweigh the ΔD decrease from the latter. The final buffer rinse caused a slight decrease in ΔD, which was associated with an increase in ($\Delta f_n/n$), and therefore most

likely indicated the removal of partially solubilized lignin or desorption of Tween 80 molecules from the substrate upon switching to the buffer feed. The ΔD curve for the LLC substrate prepared from MWL showed a very small increase upon initial Tween 80 adsorption but showed no significant change upon the subsequent more gradual Tween 80 adsorption, indicated by a gradual ($\Delta f_n/n$) decrease. The low ΔD values observed for this substrate suggested that the adsorbed Tween 80 layer was highly compact and rigid. The final buffer rinse caused a slight increase in ΔD, which was associated with an increase in ($\Delta f_n/n$), and could possibly indicate an increase in the extent of hydration of the substrate upon removal of hydrophilically adsorbed Tween 80 molecules and exposure of the substrate's hydrophilic adsorption sites.

The ($\Delta f_n/n$) and ΔD curves for LLC substrates differed strongly from the curves reported in Chapter 5 for the adsorption of Tween 80 onto lignin substrates (Figure 5.4). The differences were most likely due to the different substrate preparation methods. The lignin substrates studied in Chapter 5 were prepared from lignin solutions in aqueous ammonia whereas the LLC substrates were prepared from aqueous lignin suspensions.

The surface morphology of the LLC substrates after Tween 80 treatment were analyzed by AFM. Figure 7.8 shows AFM height images of untreated and Tween 80-treated LLC substrates prepared from 1 wt % lignin suspensions. As discussed in Chapter 6, the surface of untreated LLC substrates consisted of spherical lignin particles, which were smallest for KL and largest for OL. The lignin particles on the LLC substrate prepared from OL were much larger than those observed on the OL substrate studied in Chapter 5. The difference in particle size was most likely the result of the different substrate preparation methods, *i.e.* preparation of the substrate from a lignin suspension (LLC substrates) *versus* a lignin solution (lignin substrates in Chapter 5).

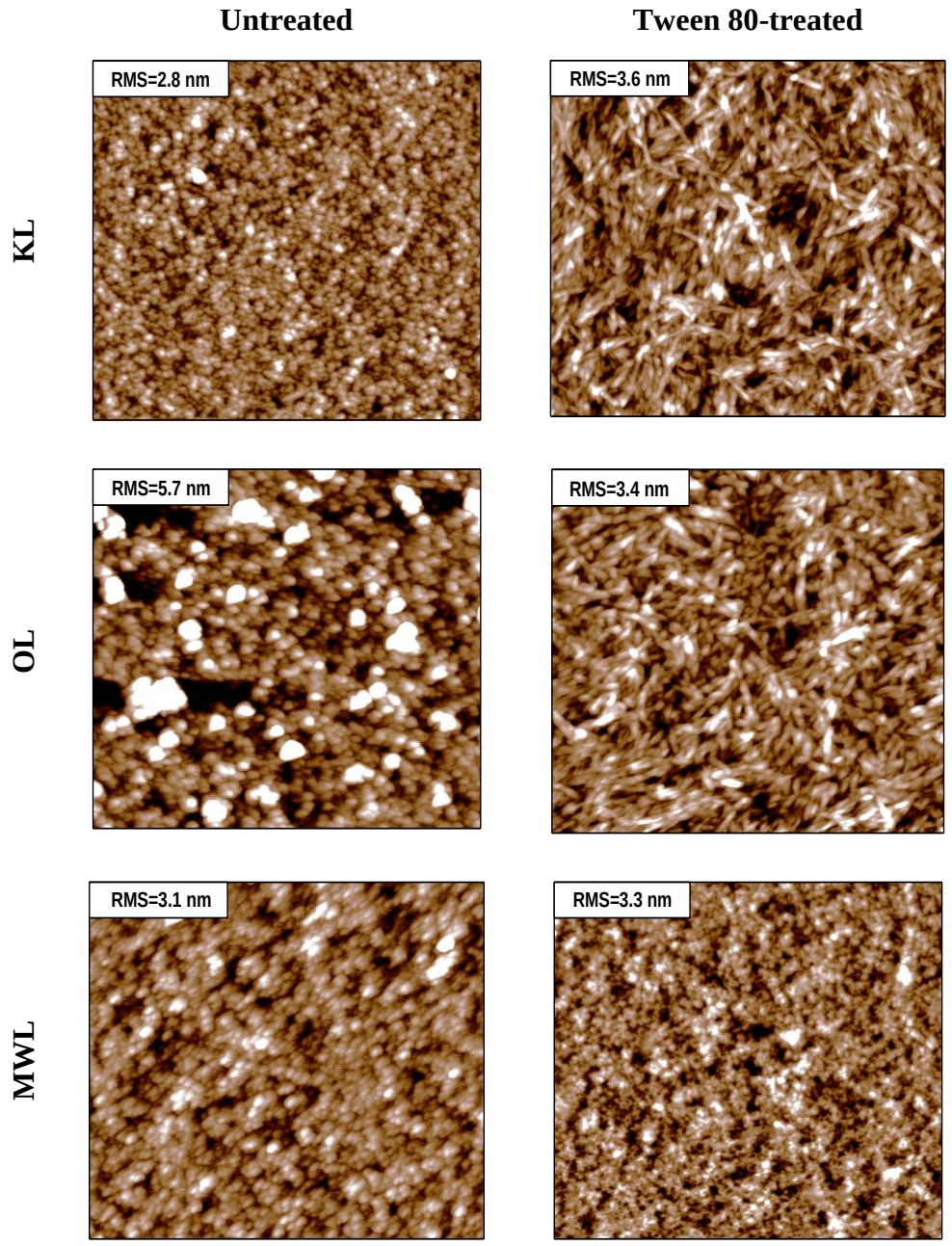

Figure 7.8. AFM height images of untreated and Tween 80-treated LLC substrates prepared from 1 wt % aqueous lignin suspensions. The scan size and z-scale are 2 μm × 2 μm and 15 nm, respectively, for all images.

After Tween 80 treatment (right column in Figure 7.8), CNCs were visible on both the LLC substrates prepared from KL and from OL. The fact that CNCs were visible on these substrates confirmed the removal of lignin molecules from these substrates by Tween 80, observed in the QCM-D adsorption experiments (Figure 7.7). The RMS surface roughnesses of the Tween 80-treated LLC substrates prepared from KL and OL were 3.6 and 3.4 nm, respectively, and were therefore similar to the surface roughness of a cellulose substrate (3.6 nm, reported in Chapter 6). CNCs were not visible on Tween 80-treated LLC substrates prepared from MWL. Both the surface morphology and the surface roughness of these substrates did not change much upon Tween 80 treatment. The fact that CNCs were not visible on the these substrates after Tween 80-treatment was in agreement with the QCM-D adsorption experiments, which showed that lignin removal did not occur on these substrates. As mentioned above, the absence of lignin removal on the LLC substrates prepared from MWL could be due to the higher hydrophilicity of MWL, compared to KL and OL.

Redeposition of lignin onto cellulose is a common problem of lignocellulosic biomass pretreatment processes. The observed removal of lignin from LLC substrates prepared from KL and OL suggests that non-ionic surfactants may be able to remove redeposited lignin from pretreated biomass.

7.4.5. Effects of Tween 80 on the enzymatic hydrolysis of LC substrates

Figure 7.9 shows ($\Delta f_n/n$) and ΔD curves for the enzymatic hydrolysis of untreated and Tween 80-treated CLC substrates with a nominal lignin content of 30%. ($\Delta f_n/n$) and ΔD curves for CLC substrates with nominal lignin contents of 10 and 20% are shown in Figures A5.1 and E.2, respectively, in Appendix E. All ($\Delta f_n/n$) curves showed the typical initial ($\Delta f_n/n$) decrease, associated with a ΔD increase and attributable to cellulase adsorption onto the substrate, followed by a more or less pronounced ($\Delta f_n/n$) increase, associated with a ΔD decrease and attributable to substrate hydrolysis. The untreated CLC substrates generally showed high ΔD values at the end of the experiment, which indicated that substrate hydrolysis was incomplete and that a soft, hydrated layer remained on the substrate.

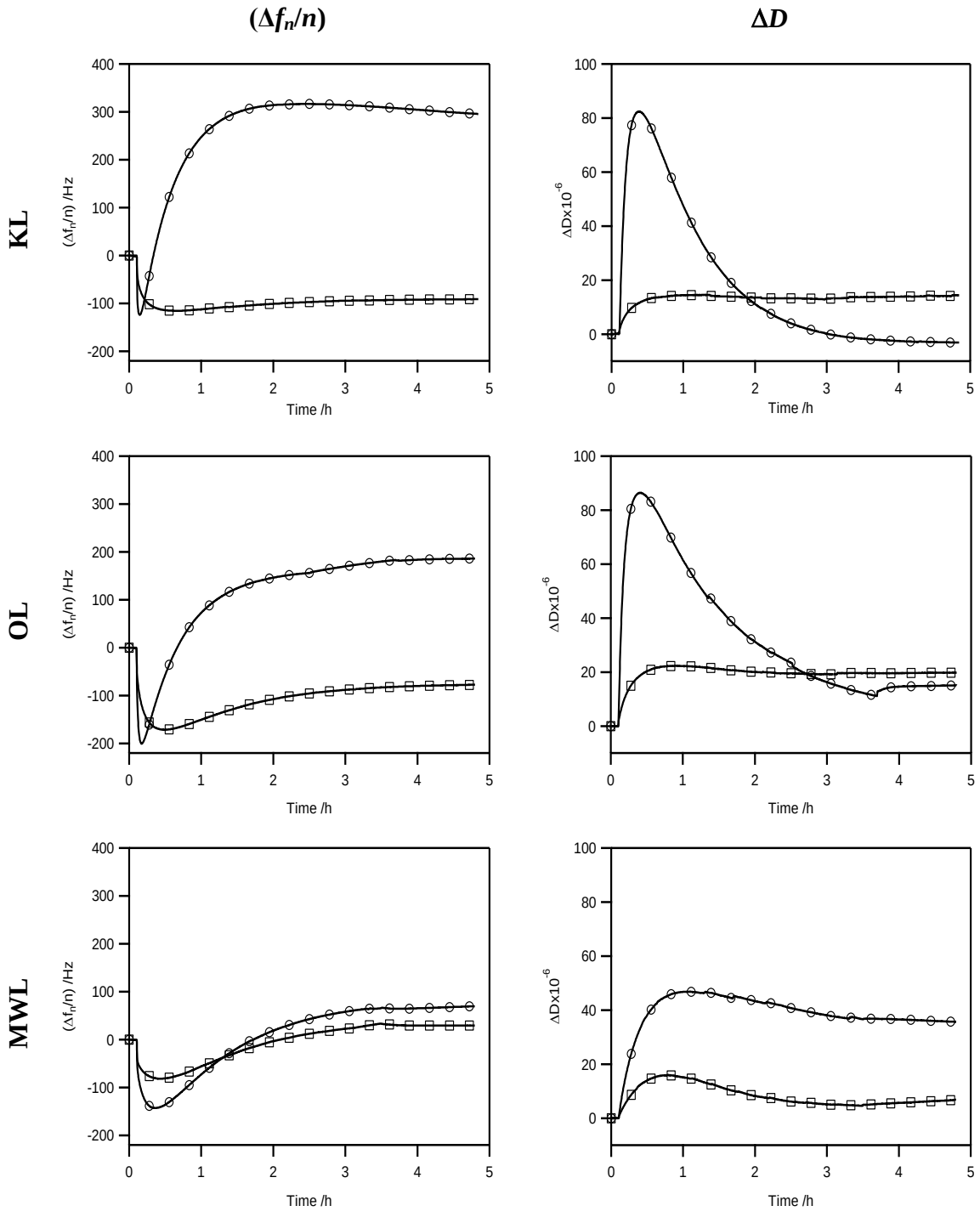

Figure 7.9. ($\Delta f_n/n$) and ΔD curves (3rd overtone) for the enzymatic hydrolysis of untreated (□) and Tween 80-treated (○) CLC substrates with a nominal lignin content of 30%.

The Tween 80-treated CLC substrates exhibited more pronounced ($\Delta f_n/n$) increases after the minimum and higher final ($\Delta f_n/n$) values, than the untreated CLC substrates, indicating that Tween 80 treatment effected higher hydrolysis rates and greater substrate mass losses.

Figure 7.10 shows the values of $(d(\Delta f_n/n)/dt)_{max}$ for the untreated and Tween 80-treated CLC substrates, as a percentage of that for a cellulose substrate, $(d(\Delta f_n/n)/dt)_{max,CNC}$. The exact values are listed in Table E.1 in Appendix E.

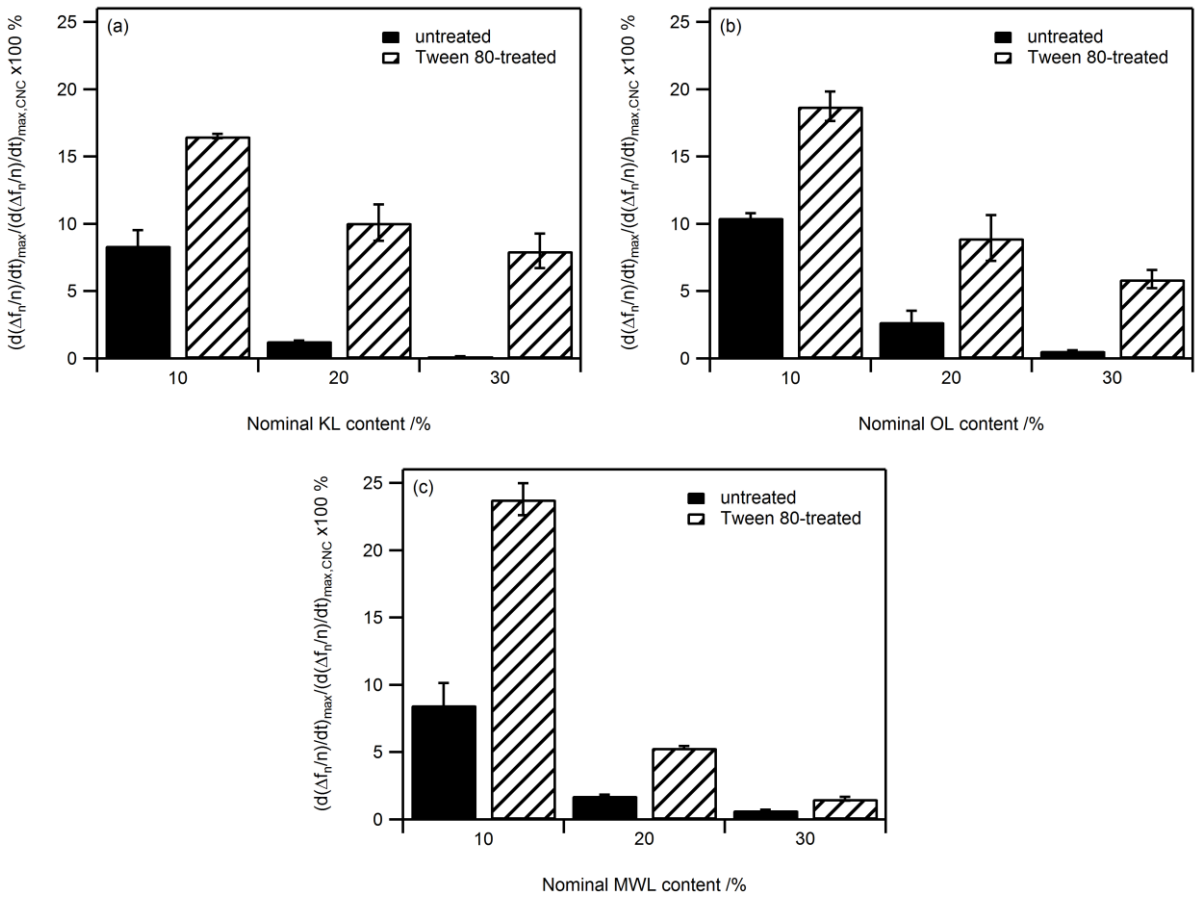

Figure 7.10. $(d(\Delta f_n/n)/dt)_{max}$, from 3rd overtone ($\Delta f_n/n$) curves, for untreated and Tween 80-treated CLC substrates, prepared from a) KL, b) OL, and c) MWL, as a percentage of that for a cellulose substrate, $(d(\Delta f_n/n)/dt)_{max,CNC}$ (2.64 s^{-2}).

As mentioned above, $(d(\Delta f_n/n)/dt)_{max}$ is a measure for the hydrolysis rate. Because of the inhibitory effect of lignin, discussed in Chapter 6, the apparent hydrolysis rates of untreated CLC substrates were significantly reduced, relative to that of a cellulose substrate, and the reduction

was greater at higher lignin contents. For untreated CLC substrates with nominal lignin contents of 10, 20, and 30%, the average $(d(\Delta f_n/n)/dt)_{max}$ were 9, 2, and 0.5% that of a cellulose substrate, respectively. Treatment of the CLC substrates with Tween 80 prior to hydrolysis resulted in a significant increase in their apparent hydrolysis rates. For Tween 80-treated CLC substrates with nominal lignin contents of 10, 20, and 30%, the average $(d(\Delta f_n/n)/dt)_{max}$ were 20, 8, and 5% that of a cellulose substrate, respectively. The largest increase in apparent hydrolysis rate (70 times) upon Tween 80 treatment was observed for CLC substrates with a nominal KL content of 30%, followed by CLC substrates with a nominal OL content of 30% (10 times). CLC substrates with a nominal lignin content of 10% showed increases in apparent hydrolysis rate of 1.8–2.8 times with the MWL-containing substrate exhibiting the largest. The mechanism by which substrate-adsorbed Tween 80 increased the apparent hydrolysis rates of the CLC substrates was not obvious from the experiments.

However, even after Tween 80 treatment, the apparent hydrolysis rates of the CLC substrates were still on average less than 20% that of a cellulose substrate. The CLC substrates, consisting of an intimate blend of lignin and CNCs, could be regarded as a model for the plant cell wall, in which cellulose microfibrils are embedded in a lignin matrix. The fact that the apparent hydrolysis rates of the CLC substrates were still low after Tween 80 treatment suggested that Tween 80 treatment alone would not be sufficient to raise enzymatic hydrolysis rates of lignocellulosic biomass to economic levels and that pretreatment for the breakdown and partial removal of lignin would still be necessary.

Figure 7.11 shows $(\Delta f_n/n)$ and ΔD curves for the enzymatic hydrolysis of untreated and Tween 80-treated LLC substrates prepared from 1 wt % aqueous lignin suspensions. $(\Delta f_n/n)$ and ΔD curves for LLC substrates prepared from 0.5 wt % aqueous lignin suspensions are shown in Figure E.3 in Appendix E. The $(\Delta f_n/n)$ and ΔD curves for the untreated LLC substrates showed smaller differences from the curves for the Tween 80-treated LLC substrates than was the case for the CLC substrates.

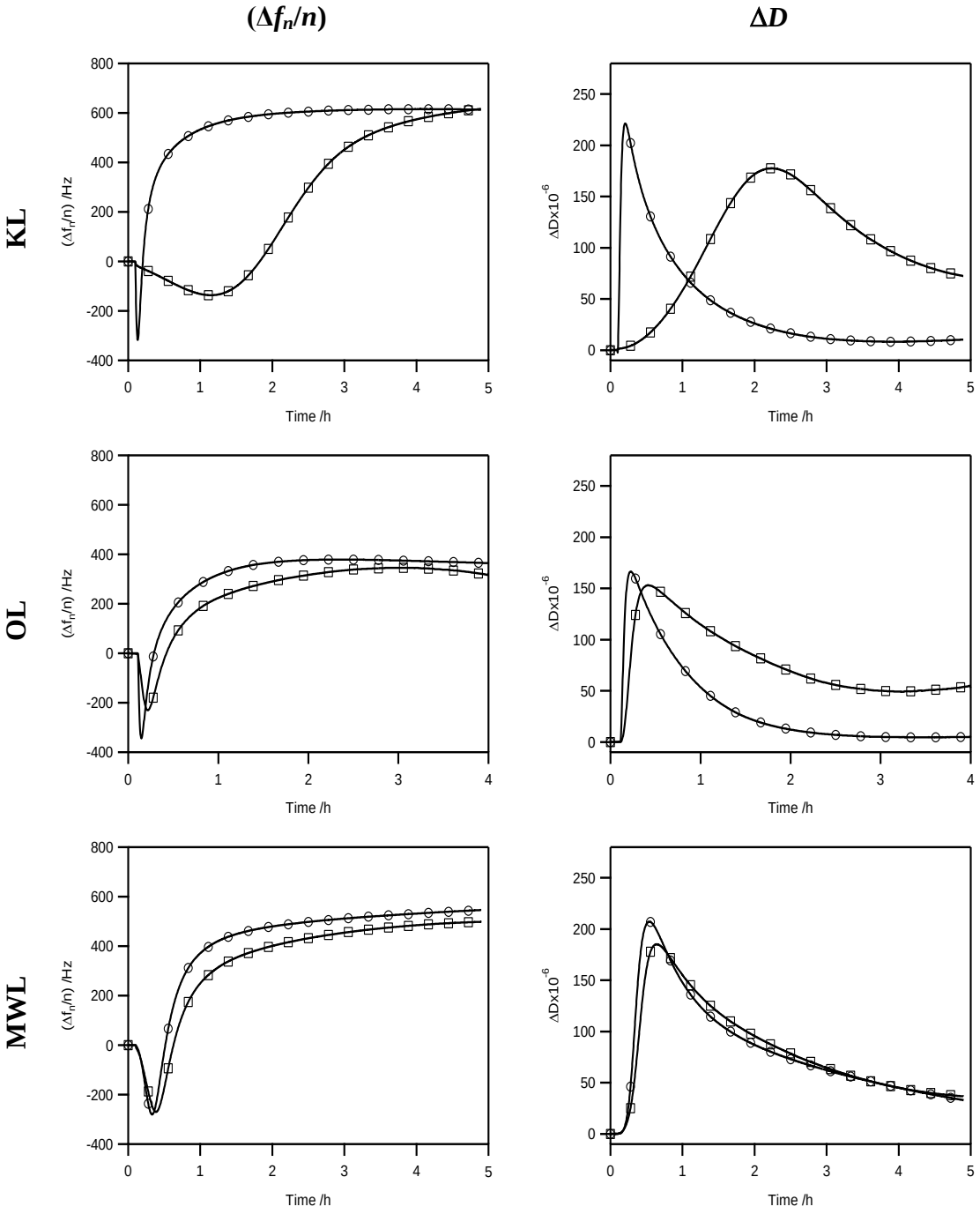

Figure 7.11. ($\Delta f_n/n$) and ΔD curves (3rd overtone) for the enzymatic hydrolysis of untreated (□) and Tween 80-treated (○) LLC substrates prepared from 1 wt % aqueous lignin suspensions.

A large difference between the curves was observed for LLC substrates prepared from 1 wt % KL suspensions (top row in Figure 7.11). For these substrates, the ($\Delta f_n/n$) minimum and ΔD maximum occurred much later than for the LLC substrates prepared from OL or MWL suspensions. The late occurrence of the ($\Delta f_n/n$) minimum and ΔD maximum indicated that both cellulase adsorption and substrate hydrolysis were slow. In addition, the ΔD values for the untreated LLC substrates prepared from 1 wt % lignin suspensions and from 0.5 wt % KL suspensions were high at the end of the experiment. The high ΔD values indicated that hydrolysis of these substrates was incomplete. All Tween 80-treated LLC substrates, except those prepared from 1 wt % MWL suspensions, exhibited ΔD values close to zero at the end of the experiment, indicating that the substrates were as rigid after as before the hydrolysis and that no soft, hydrated layer remained.

Figure 7.12 shows the values of $(d(\Delta f_n/n)/dt)_{max}$ for the untreated and Tween 80-treated LLC substrates, as a percentage of that for a cellulose substrate, $(d(\Delta f_n/n)/dt)_{max,CNC}$. The exact values are listed in Table E.2 in Appendix E.

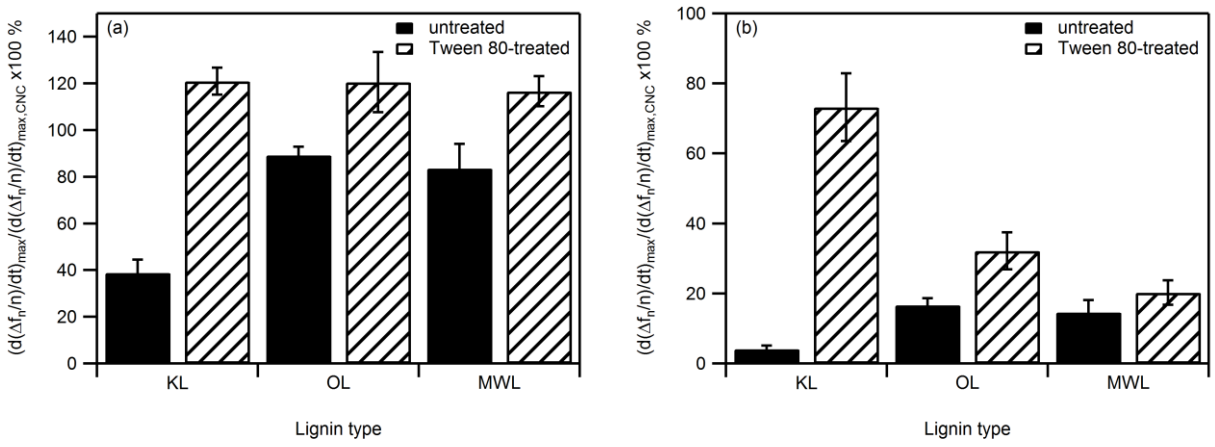

Figure 7.12. $(d(\Delta f_n/n)/dt)_{max}$, from 3rd overtone ($\Delta f_n/n$) curves, for untreated and Tween 80-treated LLC substrates, prepared from a) 0.5 wt % and b) 1 wt % lignin suspensions, as a percentage of that for a cellulose substrate, $(d(\Delta f_n/n)/dt)_{max,CNC}$ ($2.64\ s^{-2}$)

As discussed in Chapter 6, the lignin layer on top of the cellulose substrate impeded its enzymatic hydrolysis of the substrate and led to reduced apparent hydrolysis rates, relative to that

of a cellulose substrate without a lignin layer. The inhibitory effect of lignin was particularly evident on the LLC substrates with thicker lignin layers, *i.e.* prepared from 1 wt % lignin suspensions. For untreated LLC substrates prepared from 0.5 wt % OL and MWL suspensions, the average $(d(\Delta f_n/n)/dt)_{max}$ was 86% that of a cellulose substrate whereas it was only 16% for LLC substrates prepared from 1 wt % OL and MWL suspensions. Untreated LLC substrates prepared from KL suspensions had much lower average $(d(\Delta f_n/n)/dt)_{max}$, specifically 39% that of a cellulose substrate for substrates prepared from 0.5 wt % and 4% for substrates prepared from 1 wt % KL suspensions. The fact that hydrolysis of untreated LLC substrates was observed suggested that cellulase access to the cellulose substrate was not completely blocked by the lignin layer.

As was the case for the CLC substrates, treatment of the LLC substrates with Tween 80 prior to hydrolysis resulted in an increase in their apparent hydrolysis rates. Tween 80-treated LLC substrates prepared from 0.5 wt % lignin suspensions had an average $(d(\Delta f_n/n)/dt)_{max}$ of 119% that of a cellulose substrate. The fact that the rate exceeded 100% signified that hydrolysis of these substrates was faster than that of an untreated cellulose substrate. Alternatively, it could indicate simultaneous desorption of lignin. For Tween 80-treated LLC substrates prepared from 1 wt % KL, OL, and MWL suspensions, the average $(d(\Delta f_n/n)/dt)_{max}$ were 73, 32, and 20% that of a cellulose substrate, respectively. The largest increase in apparent hydrolysis rate (18 times) upon Tween 80 treatment was observed for LLC substrates prepared from 1 wt % KL suspensions, followed by LLC substrates prepared from 0.5 wt % KL suspensions (3 times). All other rates for LLC substrates increased 1.4–1.9 times. The reason for the increased apparent hydrolysis rates after Tween 80 treatment of the LLC substrates was most likely the removal of some lignin from the substrate, seen in Figures 7.7 and 7.8, exposing the cellulose substrate to the enzymes. Lignin removal by Tween 80 was most pronounced on the LLC substrates prepared from KL and least pronounced on the LLC substrates prepared from MWL, in accordance with the observed increases in apparent hydrolysis rates.

In Chapter 6, it has been shown that the lignin layer also causes an increase in the time of the minimum in the $(\Delta f_n/n)$ curves, t_{min}. t_{min} is determined by both the rate of cellulase adsorption and the rate of substrate hydrolysis because the minimum will occur when the frequency decrease due to cellulase adsorption is equal to the frequency increase due to substrate hydrolysis. The

values for t_{min} for untreated and Tween 80-treated LLC substrates are listed in Table 7.1 together with that for the cellulose substrate.

Table 7.1. Times of the ($\Delta f_n/n$) minima, t_{min}, for untreated and Tween 80-treated cellulose and LLC substrates[a]

		t_{min} (s)	
Lignin	Lignin concentration[b] (wt %)	untreated	Tween 80-treated
None[c]	–	110 ± 11	108 ± 4
KL	0.5	454 ± 7	109 ± 13
	1.0	4069 ± 269	139 ± 23
OL	0.5	223 ± 18	125 ± 14
	1.0	380 ± 11	153 ± 14
MWL	0.5	240 ± 10	159 ± 3
	1.0	1010 ± 28	834 ± 37

[a] Data are means ± one standard deviation of three measurements.
[b] of the suspension used for spin coating
[c] cellulose substrate

As seen in Table 7.1, the t_{min} values for the Tween 80-treated substrates were smaller than the values for the untreated LLC substrates. The largest decrease was observed for the LLC substrates prepared from KL (4 and 29 times for substrates prepared from 0.5 and 1 wt % KL suspensions, respectively) and the smallest for the LLC substrates prepared from MWL (1.4 times on average). As discussed in Chapter 6, the increase in t_{min} caused by the lignin layer was most likely due to the obstruction of cellulase access to the cellulose layer beneath. As shown above, Tween 80 treatment caused removal of the lignin layer, which restored cellulase access to the cellulose layer. Therefore, the decrease in t_{min} values for the LLC substrates upon Tween 80 treatment was most likely due to the removal of the obstructing lignin layer. It is interesting to note, that the lignin that had the greatest diminishing effects on maximum cellulase adsorption and apparent substrate hydrolysis rate (KL) also showed the greatest increase in apparent substrate hydrolysis rate and decrease in t_{min} upon Tween 80 treatment. The fact that the LLC substrate prepared from MWL did not exhibit lignin removal from the substrate by Tween 80 in

Figure 7.7 explains why this substrate showed the smallest increase in apparent substrate hydrolysis rate and decrease in t_{min} upon Tween 80 treatment.

7.5. Conclusions

The objective of this study was to elucidate the effects of the non-ionic surfactant Tween 80 on the enzymatic hydrolysis of cellulose and LC substrates by means of QCM-D. The study has shown that Tween 80 forms surfactant–protein complexes with cellulases in solution but that the complexation does not compromise cellulase activity. Tween 80 adsorbs onto cellulose substrates and forms highly hydrated adsorption layers. Tween 80 adsorption onto cellulose is well described by the Langmuir adsorption model. Tween 80, either adsorbed on the substrate or in solution, does not have any effect on the hydrolysis of cellulose substrates by cellulase. Substrate-adsorbed Tween 80 increases the apparent cellulase hydrolysis rates of LC substrates. For layered LC substrates, consisting of a lignin layer on top of a cellulose layer, the increase in apparent hydrolysis rate is due to the removal of lignin from the substrate by Tween 80. The ability of Tween 80 to increase the apparent hydrolysis rate depends strongly on the structural properties of the LC substrate (composite *versus* layered) and the chemical properties of the lignin.

7.6. Acknowledgments

This project was supported by the National Research Initiative of the USDA Cooperative State Research, Education and Extension Service under Grant 2005-35504-16088, the National Science Foundation under Grant CHE-0724126 and DMR-0907567, the U.S. Department of Transportation through the Southeastern Sun Grant Center, and the Institute for Critical Technology and Applied Science. The authors thank Mr. Lei Pan of the Department of Mining and Minerals Engineering for the help with the surface tension measurement, Dr. Gary L. Long of the Department of Chemistry for the access to the fluorescence spectrometer, and Prof. Em. Wolfgang Glasser for providing the OL and MWL samples.

7.7. References

1. Lynd, L. R.; Weimer, P. J.; van Zyl, W. H.; Pretorius, I. S. Microbial Cellulose Utilization: Fundamentals and Biotechnology. *Microbiology and Molecular Biology Reviews* **2002,** *66*, 506-577.

2. Sun, Y.; Cheng, J. Y. Hydrolysis of Lignocellulosic Materials for Ethanol Production: A Review. *Bioresource Technology* **2002,** *83*, 1-11.

3. Beguin, P.; Aubert, J. P. The Biological Degradation of Cellulose. *Fems Microbiology Reviews* **1994,** *13*, 25-58.

4. Gregg, D. J.; Boussaid, A.; Saddler, J. N. Techno-Economic Evaluations of a Generic Wood-to-Ethanol Process: Effect of Increased Cellulose Yields and Enzyme Recycle. *Bioresource Technology* **1998,** *63*, 7-12.

5. Wingren, A.; Galbe, M.; Zacchi, G. Techno-Economic Evaluation of Producing Ethanol from Softwood: Comparison of SSf and SHF and Identification of Bottlenecks. *Biotechnology Progress* **2003,** *19*, 1109-1117.

6. Mooney, C. A.; Mansfield, S. D.; Touhy, M. G.; Saddler, J. N. The Effect of Initial Pore Volume and Lignin Content on the Enzymatic Hydrolysis of Softwoods. *Bioresource Technology* **1998,** *64*, 113-119.

7. Sewalt, V. J. H.; Ni, W. T.; Jung, H. G.; Dixon, R. A. Lignin Impact on Fiber Degradation: Increased Enzymatic Digestibility of Genetically Engineered Tobacco (Nicotiana Tabacum) Stems Reduced in Lignin Content. *Journal of Agricultural and Food Chemistry* **1997,** *45*, 1977-1983.

8. Yang, B.; Wyman, C. E. Bsa Treatment to Enhance Enzymatic Hydrolysis of Cellulose in Lignin Containing Substrates. *Biotechnology and Bioengineering* **2006,** *94*, 611-617.

9. Converse, A. O.; Ooshima, H.; Burns, D. S. Kinetics of Enzymatic-Hydrolysis of Lignocellulosic Materials Based on Surface-Area of Cellulose Accessible to Enzyme and Enzyme Adsorption on Lignin and Cellulose. *Applied Biochemistry and Biotechnology* **1990,** *24-5*, 67-73.

10. Sutcliffe, R.; Saddler, J. N. The Role of Lignin in the Adsorption of Cellulases During Enzymatic Treatment of Lignocellulosic Material. *Biotechnology & Bioengineering Symposium* **1986,** *17*.

11. Eriksson, T.; Borjesson, J.; Tjerneld, F. Mechanism of Surfactant Effect in Enzymatic Hydrolysis of Lignocellulose. *Enzyme and Microbial Technology* **2002,** *31*, 353-364.

12. Castanon, M.; Wilke, C. R. Effects of the Surfactant Tween-80 on Enzymatic-Hydrolysis of Newspaper. *Biotechnology and Bioengineering* **1981,** *23*, 1365-1372.

13. Kaya, F.; Heitmann, J. A.; Joyce, T. W. Influence of Surfactants on the Enzymatic-Hydrolysis of Xylan and Cellulose. *Tappi Journal* **1995,** *78*, 150-157.

14. Kaar, W. E.; Holtzapple, M. T. Benefits from Tween During Enzymic Hydrolysis of Corn Stover. *Biotechnology and Bioengineering* **1998,** *59*, 419-427.

15. Kristensen, J. B.; Borjesson, J.; Bruun, M. H.; Tjerneld, F.; Jorgensen, H. Use of Surface Active Additives in Enzymatic Hydrolysis of Wheat Straw Lignocellulose. *Enzyme and Microbial Technology* **2007,** *40*, 888-895.

16. Qing, Q.; Yang, B.; Wyman, C. E. Impact of Surfactants on Pretreatment of Corn Stover. *Bioresource Technology* **2010,** *101*, 5941-5951.

17. Alkasrawi, M.; Eriksson, T.; Borjesson, J.; Wingren, A.; Galbe, M.; Tjerneld, F.; Zacchi, G. The Effect of Tween-20 on Simultaneous Saccharification and Fermentation of Softwood to Ethanol. *Enzyme and Microbial Technology* **2003,** *33*, 71-78.

18. Ahola, S.; Turon, X.; Österberg, M.; Laine, J.; Rojas, O. J. Enzymatic Hydrolysis of Native Cellulose Nanofibrils and Other Cellulose Model Films: Effect of Surface Structure. *Langmuir* **2008,** *24*, 11592–11599.

19. Turon, X.; Rojas, O. J.; Deinhammer, R. S. Enzymatic Kinetics of Cellulose Hydrolysis: A QCM-D Study. *Langmuir* **2008,** 24, 3880-3887.

20. Hook, F.; Rodahl, M.; Brzezinski, P.; Kasemo, B. Energy Dissipation Kinetics for Protein and Antibody-Antigen Adsorption under Shear Oscillation on a Quartz Crystal Microbalance. *Langmuir* **1998,** *14*, 729-734.

21. Rodahl, M.; Hook, F.; Krozer, A.; Brzezinski, P.; Kasemo, B. Quartz-Crystal Microbalance Setup for Frequency and Q-Factor Measurements in Gaseous and Liquid Environments. *Review of Scientific Instruments* **1995,** *66*, 3924-3930.

22. Glasser, W. G.; Barnett, C. A.; Sano, Y. Classification of Lignins with Different Genetic and Industrial Origins. *Journal of Applied Polymer Science: Applied Polymer Symposium* **1983,** *37*, 441-460.

23. Voinova, M. V.; Rodahl, M.; Jonson, M.; Kasemo, B. Viscoelastic Acoustic Response of Layered Polymer Films at Fluid-Solid Interfaces: Continuum Mechanics Approach. *Physica Scripta* **1999,** *59*, 391-396.

24. Hook, F.; Kasemo, B.; Nylander, T.; Fant, C.; Sott, K.; Elwing, H. Variations in Coupled Water, Viscoelastic Properties, and Film Thickness of a Mefp-1 Protein Film During Adsorption and Cross-Linking: A Quartz Crystal Microbalance with Dissipation Monitoring, Ellipsometry, and Surface Plasmon Resonance Study. *Analytical Chemistry* **2001,** *73*, 5796-5804.

25. Lide, D. R., *Crc Handbook of Chemistry and Physics (Internet Version)*. 91st ed.; CRC Press: Boca Raton, FL, 2011.

26. Defeijter, J. A.; Benjamins, J.; Veer, F. A. Ellipsometry as a Tool to Study Adsorption Behavior of Synthetic and Biopolymers at Air-Water-Interface. *Biopolymers* **1978,** *17*, 1759-1772.

27. Kaya, A.; Du, X. S.; Liu, Z. L.; Lu, J. W.; Morris, J. R.; Glasser, W. G.; Heinze, T.; Esker, A. R. Surface Plasmon Resonance Studies of Pullulan and Pullulan Cinnamate Adsorption onto Cellulose. *Biomacromolecules* **2009,** *10*, 2451-2459.

28. Harvey, A. H.; Gallagher, J. S.; Sengers, J. Revised Formulation for the Refractive Index of Water and Steam as a Function of Wavelength, Temperature and Density. *Journal of Physical and Chemical Reference Data* **1998,** *27*, 761-774.

29. Malmstrom, J.; Agheli, H.; Kingshott, P.; Sutherland, D. S. Viscoelastic Modeling of Highly Hydrated Laminin Layers at Homogeneous and Nanostructured Surfaces: Quantification of Protein Layer Properties Using QCM-D and SPR. *Langmuir* **2007,** *23*, 9760-9768.

30. Zadymova, N. M.; Yampol'skaya, G. P.; Filatova, L. Y. Interaction of Bovine Serum Albumin with Nonionic Surfactant Tween 80 in Aqueous Solutions: Complexation and Association. *Colloid Journal* **2006,** *68*, 162-172.

31. Miller, R.; Fainerman, V. B.; Makievski, A. V.; Kragel, J.; Grigoriev, D. O.; Kazakov, V. N.; Sinyachenko, O. V. Dynamics of Protein and Mixed Protein/Surfactant Adsorption Layers at the Water/Fluid Interface. *Advances in Colloid and Interface Science* **2000,** *86*, 39-82.

32. Fainerman, V. B.; Zholob, S. A.; Leser, M.; Michel, M.; Miller, R. Competitive Adsorption from Mixed Nonionic Surfactant/Protein Solutions. *Journal of Colloid and Interface Science* **2004,** *274*, 496-501.

33. Kragel, J.; O'Neill, M.; Makievski, A. V.; Michel, M.; Leser, M. E.; Miller, R. Dynamics of Mixed Protein-Surfactant Layers Adsorbed at the Water/Air and Water/Oil Interface. *Colloids and Surfaces B-Biointerfaces* **2003,** *31*, 107-114.

34. Ruiz-Pena, M.; Oropesa-Nunez, R.; Pons, T.; Louro, S. R. W.; Perez-Gramatges, A. Physico-Chemical Studies of Molecular Interactions between Non-Ionic Surfactants and Bovine Serum Albumin. *Colloids and Surfaces B-Biointerfaces* **2010,** *75*, 282-289.

35. le Maire, M.; Champeil, P.; Moller, J. V. Interaction of Membrane Proteins and Lipids with Solubilizing Detergents. *Biochimica Et Biophysica Acta-Biomembranes* **2000,** *1508*, 86-111.

36. Patist, A.; Bhagwat, S. S.; Penfield, K. W.; Aikens, P.; Shah, D. O. On the Measurement of Critical Micelle Concentrations of Pure and Technical-Grade Nonionic Surfactants. *Journal of Surfactants and Detergents* **2000,** *3*, 53-58.

37. Turro, N. J.; Lei, X. G.; Ananthapadmanabhan, K. P.; Aronson, M. Spectroscopic Probe Analysis of Protein-Surfactant Interactions - the BSA/SDS System. *Langmuir* **1995,** *11*, 2525-2533.

38. Kalyanasundaram, K.; Thomas, J. K. Environmental Effects on Vibronic Band Intensities in Pyrene Monomer Fluorescence and Their Application in Studies of Micellar Systems. *Journal of the American Chemical Society* **1977,** *99*, 2039-2044.

39. Vasilescu, M.; Angelescu, D.; Almgren, M.; Valstar, A. Interactions of Globular Proteins with Surfactants Studied with Fluorescence Probe Methods. *Langmuir* **1999,** *15*, 2635-2643.

CHAPTER 8

Conclusions and future work

8.1. Conclusions

With respect to the goals and objectives of the research, stated in Chapter 1, the following conclusions can be drawn:

- Model cellulose substrates that have chemical properties similar to those of native cellulose can be prepared from cellulose nanocrystals (CNCs) that were obtained by sulfuric acid hydrolysis of wood pulp.

- Removal of the sulfate groups, present on CNCs prepared by sulfuric acid hydrolysis, is critical to their use as model cellulose substrates.

- Partial removal of the sulfate groups can be achieved by HCl-catalyzed desulfation whereas complete removal can be achieved by solvolytic desulfation in DMSO of the CNC pyridinium salt.

- Sulfate groups on cellulose substrates hinder cellulase adsorption through the cellulose binding domains but promote cellulase adsorption through electrostatic interactions and slow down or inhibit enzymatic hydrolysis of the substrates.

- Tween 80 adsorbs onto lignin substrates and, depending on the chemical properties of the lignin, may remove lignin molecules from surface.

- The adsorption behavior of cellulases on lignin substrates depends on the chemical properties of the lignin.

- Adsorbed Tween 80 molecules on lignin substrates affect cellulase adsorption behavior and reduce the adsorption rate.

- Model lignocellulosic (LC) substrates consisting of lignin/cellulose blends can be prepared by spin coating of mixed aqueous lignin/CNC suspensions whereas model LC substrates consisting of a lignin layer on top of a cellulose layer can be obtained by spin coating of aqueous lignin suspensions onto a layer of CNCs.

- Lignin hinders both the adsorption of cellulases onto the LC substrates and the enzymatic hydrolysis of the substrates.

- A lignin surface layer has less of an inhibitory effect on cellulose hydrolysis than an embedding lignin matrix.

- Tween 80 forms surfactant–protein complexes with cellulases in solution without compromising cellulase activity.

- Tween 80 adsorbs onto cellulose substrates and forms highly hydrated adsorption layers.

- Tween 80, either adsorbed on the substrate or in solution, does not have any effect on the hydrolysis of cellulose substrates by cellulase.

- Substrate-adsorbed Tween 80 increases the apparent cellulase hydrolysis rates of LC substrates. For layered LC substrates, the increase in hydrolysis rate is due to the removal of lignin from the substrate by Tween 80.

- The ability of Tween 80 to increase the hydrolysis rate depends strongly on the structural properties of the LC substrate (composite *versus* layered) and the chemical properties of the lignin.

8.2. Future work

8.2.1. Preparation of model wood substrates

The presented studies were conducted with model cellulose and lignocellulosic substrates. An important limitation of these substrates is their lack of hemicellulose and pectin, both present in lignocellulosic biomass. Consequently, the preparation of model wood substrates, suitable for quartz crystal microbalance studies, by spin coating or other thin film techniques would be of great value to future studies in this area. To this end, we have dissolved wood flour in an ionic liquid but have found the resulting solution to be too viscose for spin coating. Addition of dimethyl sulfoxide reduced the viscosity of the wood solution but lead to precipitation of the wood components. For future work, I suggest continuing the search for a solvent system, possibly based on ionic liquids and a suitable co-solvent, for the preparation of wood solutions from which model wood substrates can be prepared.

8.2.2. Study of other non-ionic surfactants

In the current research, we only studied the effect of Tween 80 on the enzymatic hydrolysis of lignocellulosic substrates. The observed ability of Tween 80 to remove lignin molecules from the substrates made it difficult to quantify cellulase adsorption onto the substrates. For future work, I suggest studying other non-ionic surfactants, preferably with different hydrophilic–lipophilic balance (HLB), to understand at which HLB value the surfactant adsorbs onto lignin or is most effective in removing lignin molecules from the substrate. These results would also be a valuable reference for future surfactant selection and design for use in biomass hydrolysis.

Appendix

Appendix A

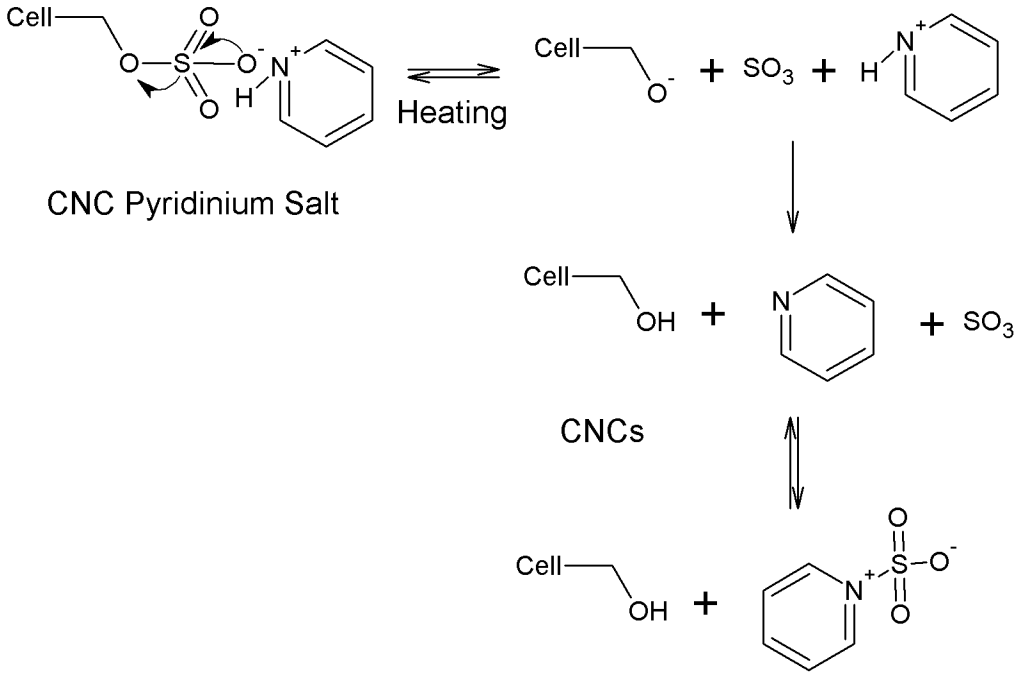

Figure A.1. Mechanism for the solvolytic desulfation of CNC pyridinium salt

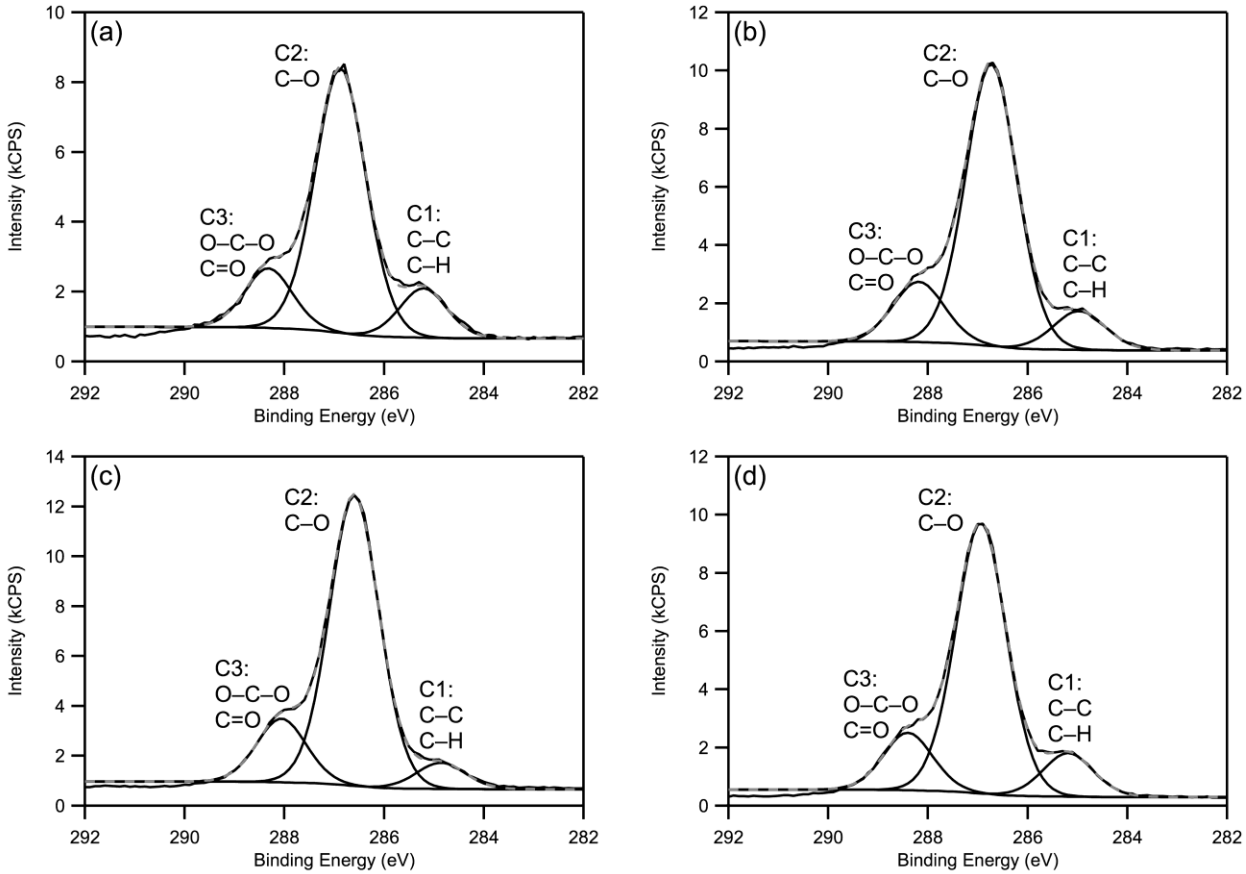

Figure A.2. High-resolution C 1s photoelectron spectra of the CNC samples (a) SH, (b) HH, (c) HD7, and (d) SD.

Table A.1. Relative amounts of C1, C2, and C3 carbon species and C2/C3 ratios for different CNC samples

	Percentage of C 1s peak area			
Sample	C1	C2	C3	C2/C3
SH	12.52	72.24	15.24	4.74
HH	10.27	73.95	15.78	4.69
HD7	6.74	76.64	16.62	4.61
SD	11.71	73.20	15.09	4.85
Cellulose	0.00	83.00[a]	17.00[a]	4.88

[a] from ref 1

References

1. Ahmed, A.; Adnot, A.; Grandmaison, J. L.; Kaliaguine, S.; Doucet, J. *Cellulose Chem. Technol.* 1987, *21*, 483–492.

Appendix B

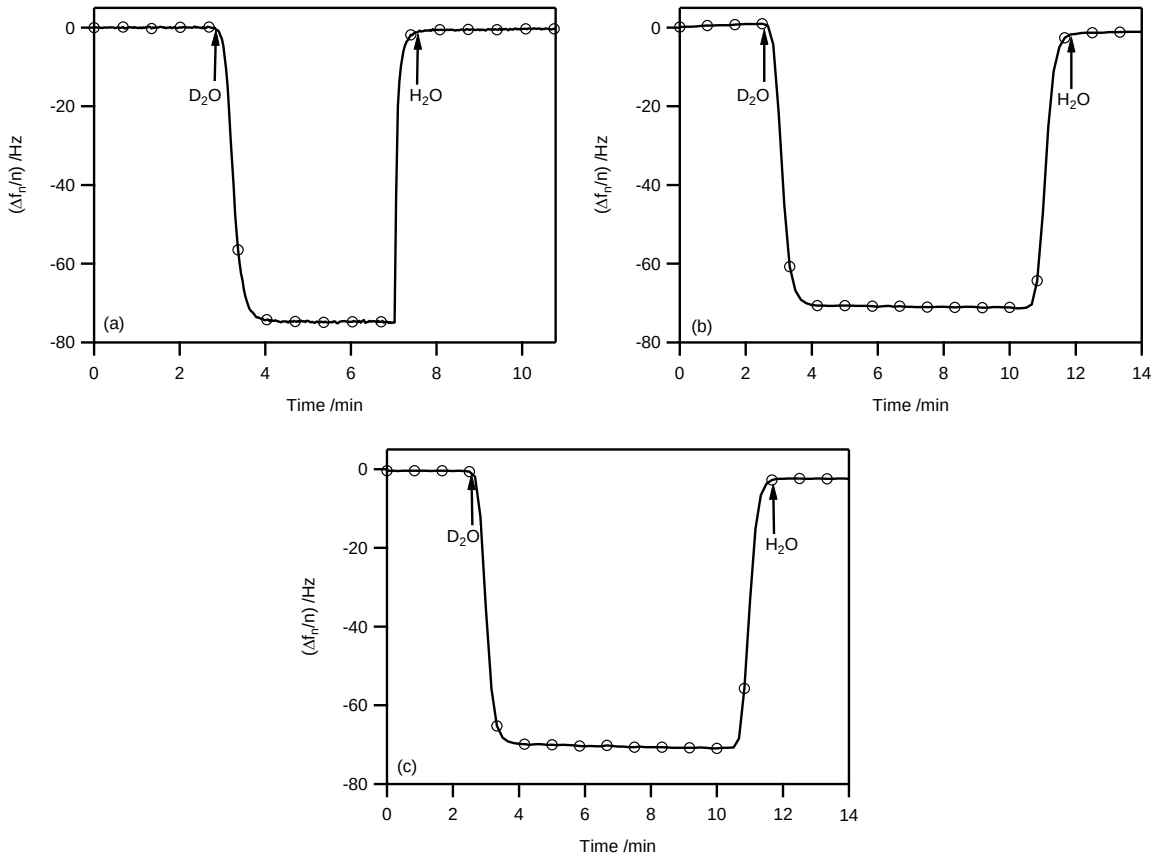

Figure B.1. Representative ($\Delta f_n/n$) curves (5^{th} overtone) from H_2O/D_2O solvent exchange QCM-D experiments for (a) the SH-55 substrate, (b) the SH-151 substrate, and (c) the SH-293 substrate.

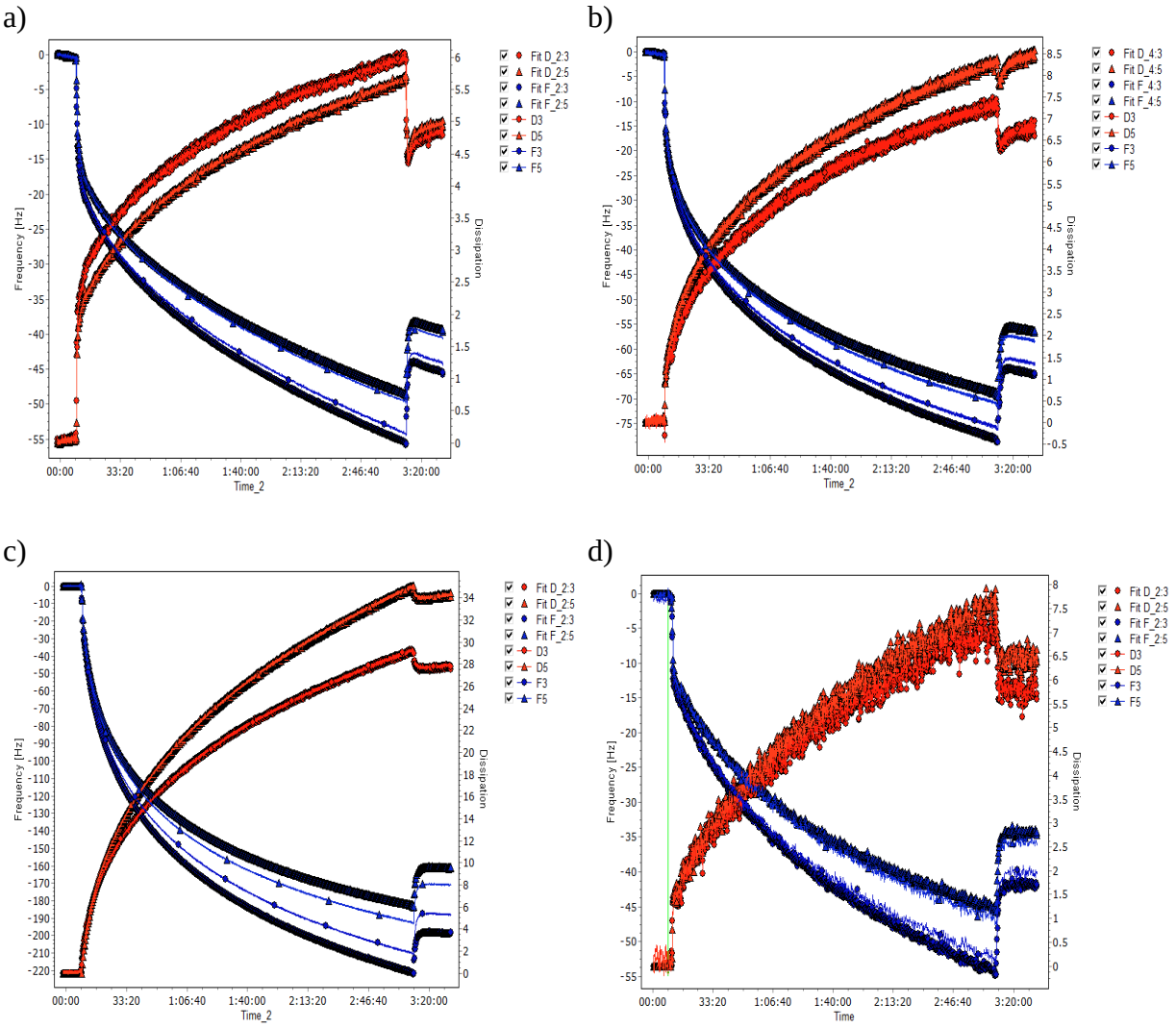

Figure B.2. Representative fitting curves for the adsorption of CBDs (100 μg·mL^{-1}) onto the CNC substrates SH-292 (a), SH-55 (b), SH-0 (c), and HH-0 (d). Fitting was conducted with QTools 3 software using the 3rd and 5th overtones. The density and viscosity of water at 25 ℃ are 997 kg·m^{-3} and 0.89·10^{-3} kg·m^{-1}s^{-1}, and the density of the viscoelastic film was fixed at 1152 kg·m^{-3}.

Appendix C

Table C.1. Average contact angles of the three test liquids on untreated and Tween 80-treated lignin substrates[a]

	OL		KL		MWL	
Test liquids	untreated	treated	untreated	treated	untreated	treated
water	65.0º ± 1.0º	60.3º ± 0.2º	62.0º ± 1.2º	57.7º ± 0.3º	54.1º ± 0.6º	51.6º ± 1.0º
diiodomethane	24.2º ± 0.8º	32.1º ± 0.3º	21.6º ± 0.5º	32.7º ± 1.0º	17.5º ± 0.5º	28.2º ± 1.0º
formamide	27.2º ± 0.5º	26.9º ± 0.2º	25.4º ± 0.3º	24.6º ± 0.8º	25.7º ± 0.6º	18.9º ± 0.9º

[a] Data are means ± one standard deviation of three measurements.

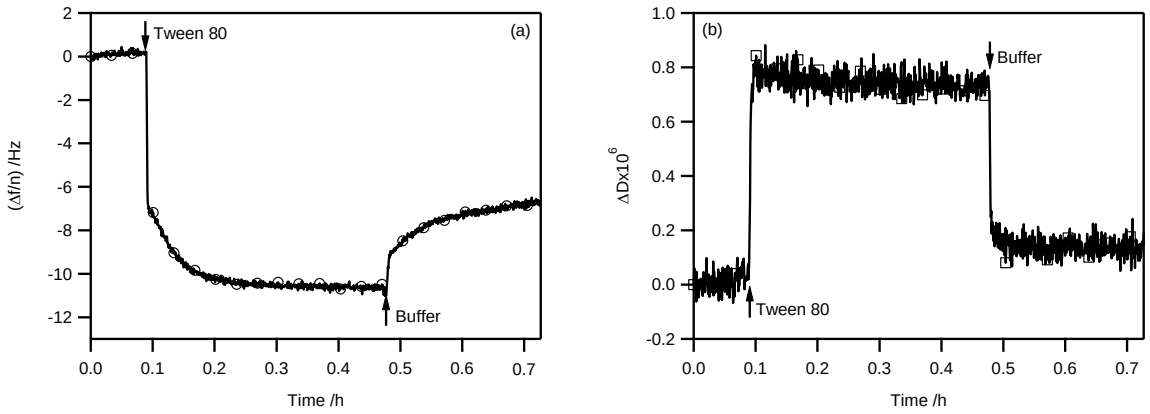

Figure C.1. (a) ($\Delta f_n/n$) and (b) ΔD curves (5^{th} overtone) from Tween 80 adsorption experiments on gold substrates. The arrows indicate a switch in liquid feed to the QCM-D flow modules.

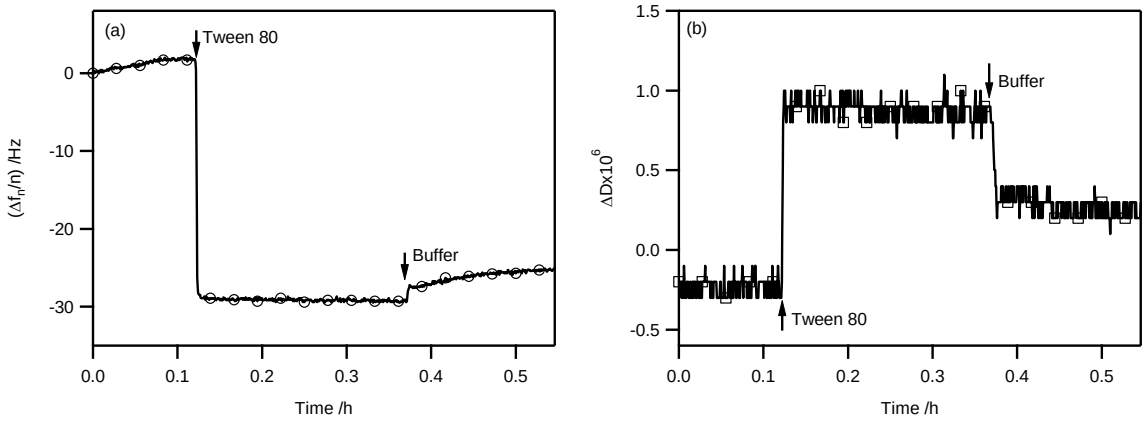

Figure C.2. (a) ($\Delta f_n/n$) and (b) ΔD curves (5^{th} overtone) from Tween 80 adsorption experiments on silica substrates. The arrows indicate a switch in liquid feed to the QCM-D flow modules.

Appendix D

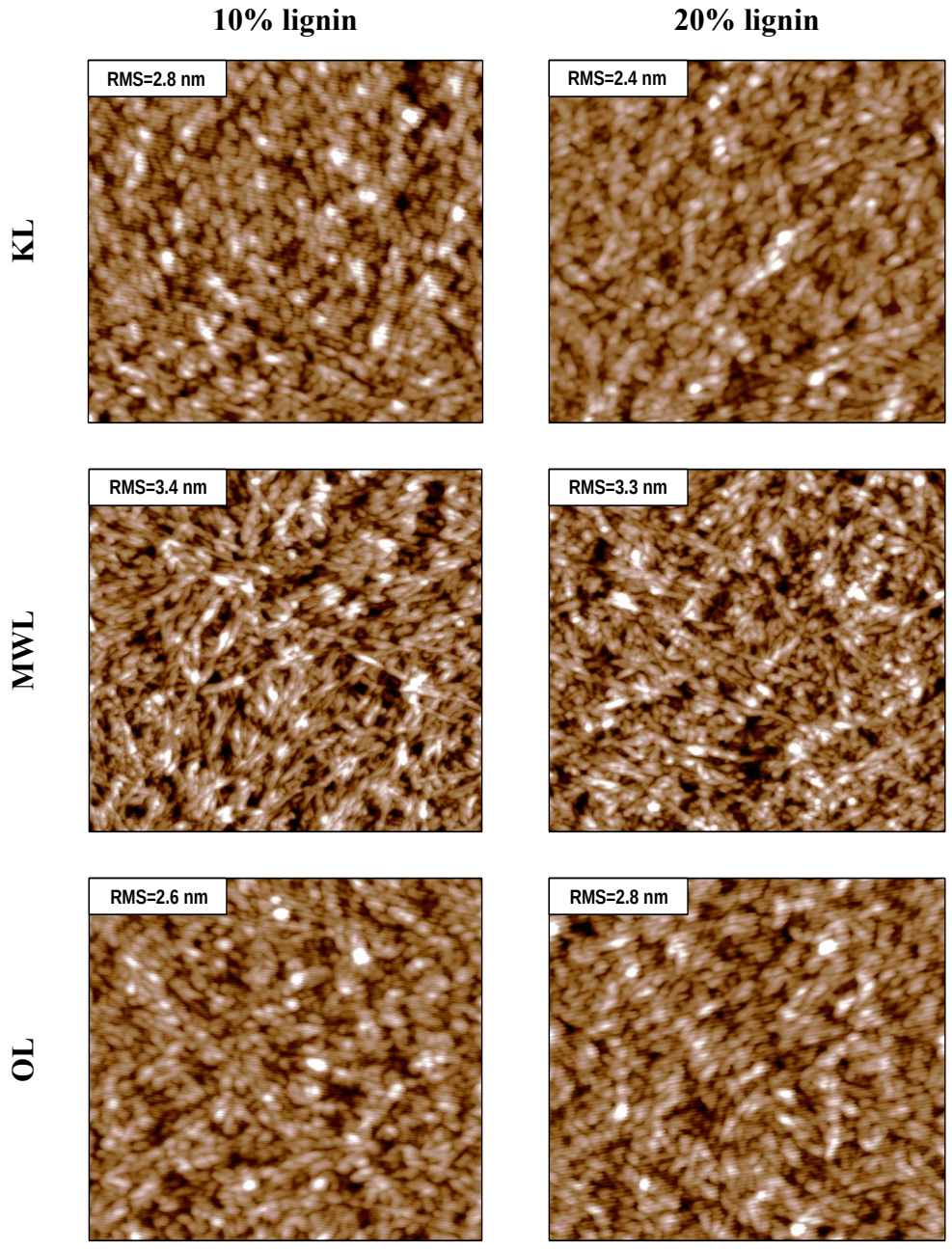

Figure D.1. AFM height images of CLC substrates with a 10 or 20% nominal lignin content. The scan size and z-scale are 2 μm × 2 μm and 15 nm, respectively, for all images.

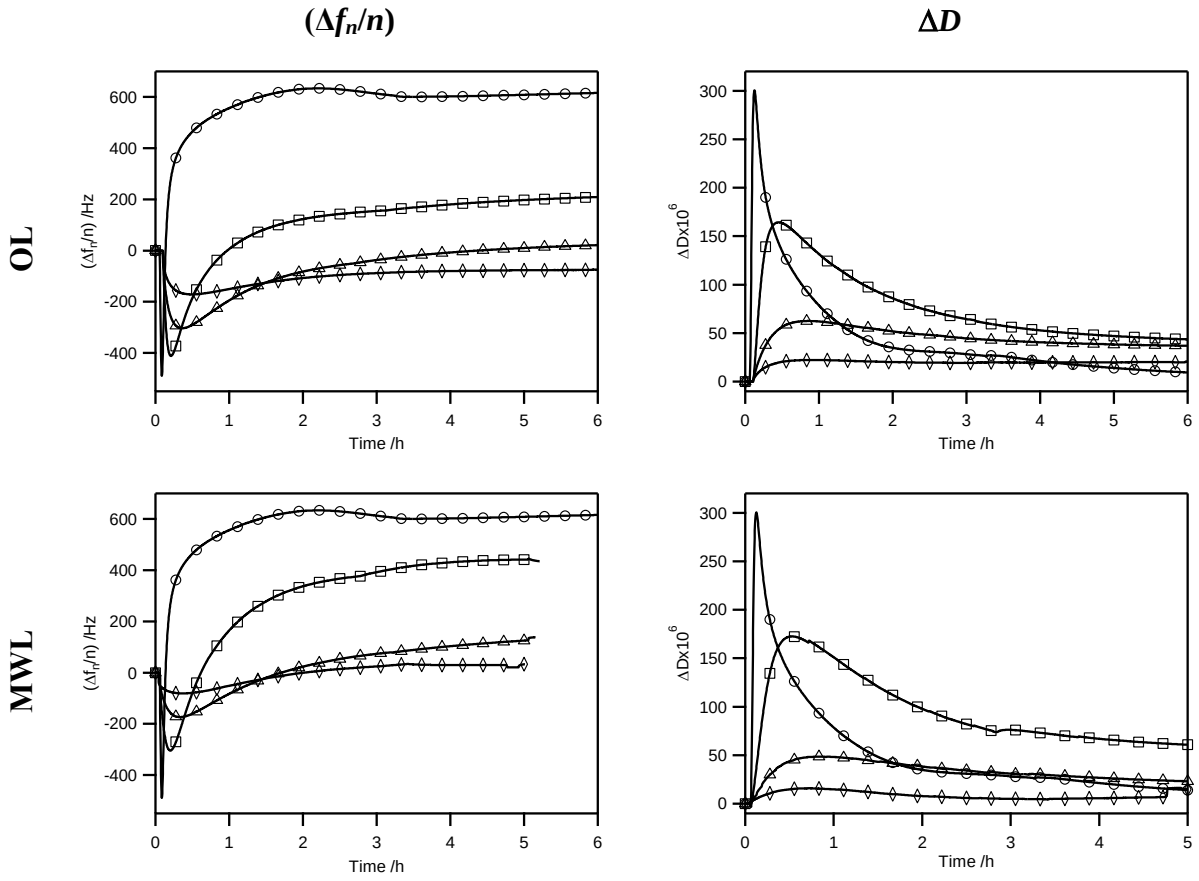

Figure D.2. ($\Delta f_n/n$) and ΔD curves (3rd overtone) for the enzymatic hydrolysis of the cellulose substrate (○) and CLC substrates with a nominal OL or MWL content of 10% (□), 20% (△), and 30% (◊).

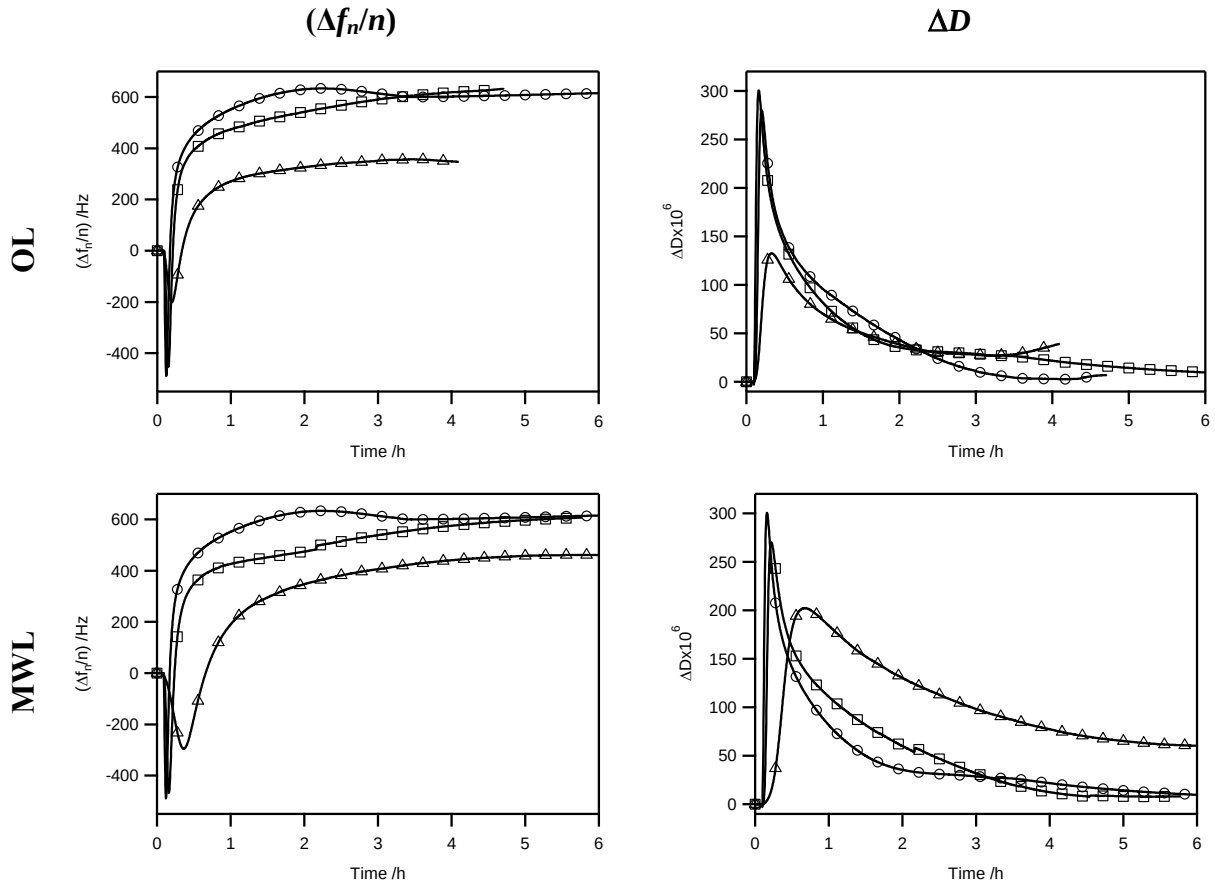

Figure D.3. ($\Delta f_n/n$) and ΔD curves (3rd overtone) for the enzymatic hydrolysis of the cellulose substrate (○) and LLC substrates prepared from 0.5 wt % (□) and 1 wt % (△) OL or MWL suspensions.

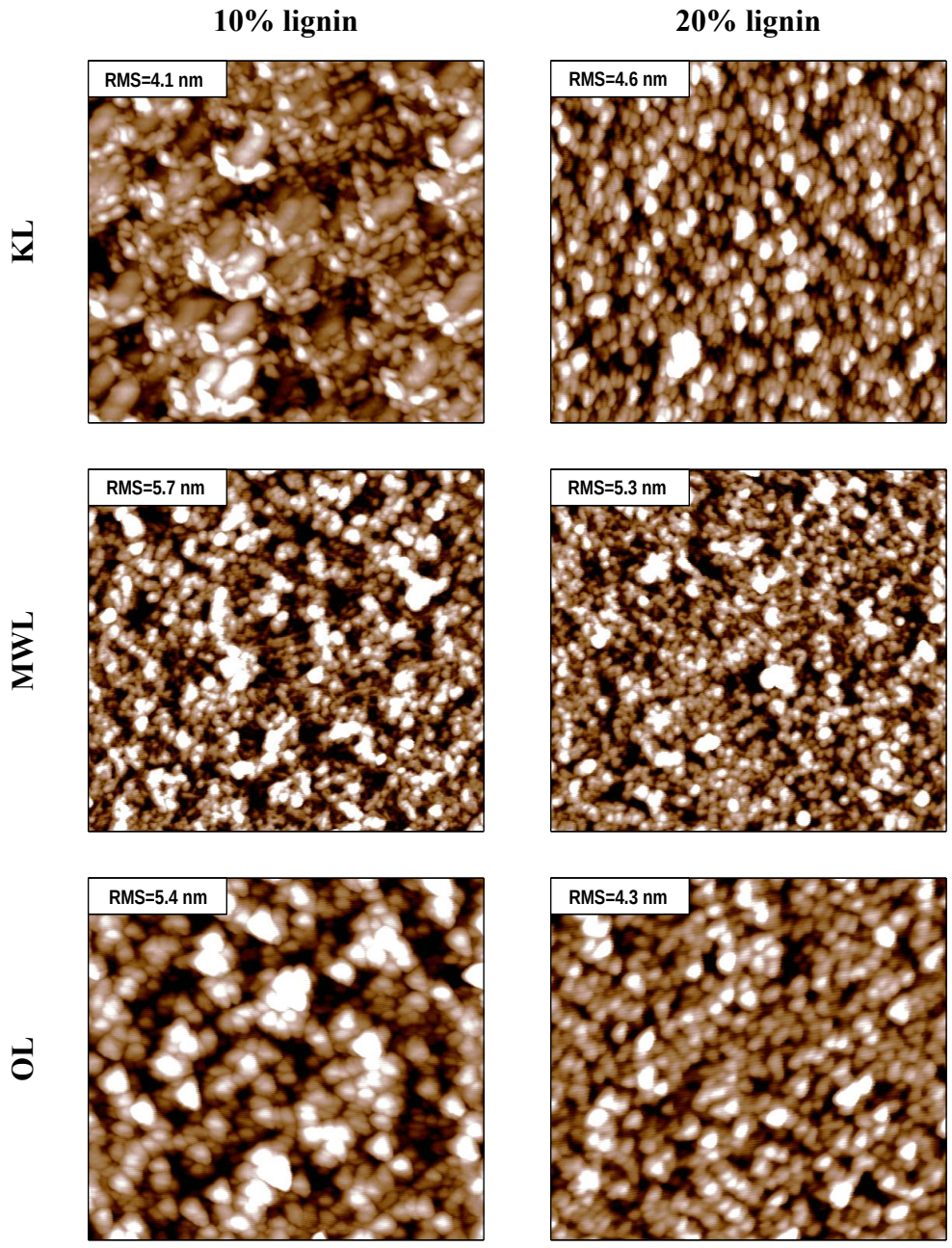

Figure D.4. AFM height images of CLC substrates with a 10 or 20% nominal lignin content after enzymatic hydrolysis. The scan size and z-scale are 2 μm × 2 μm and 15 nm, respectively, for all images.

Appendix E

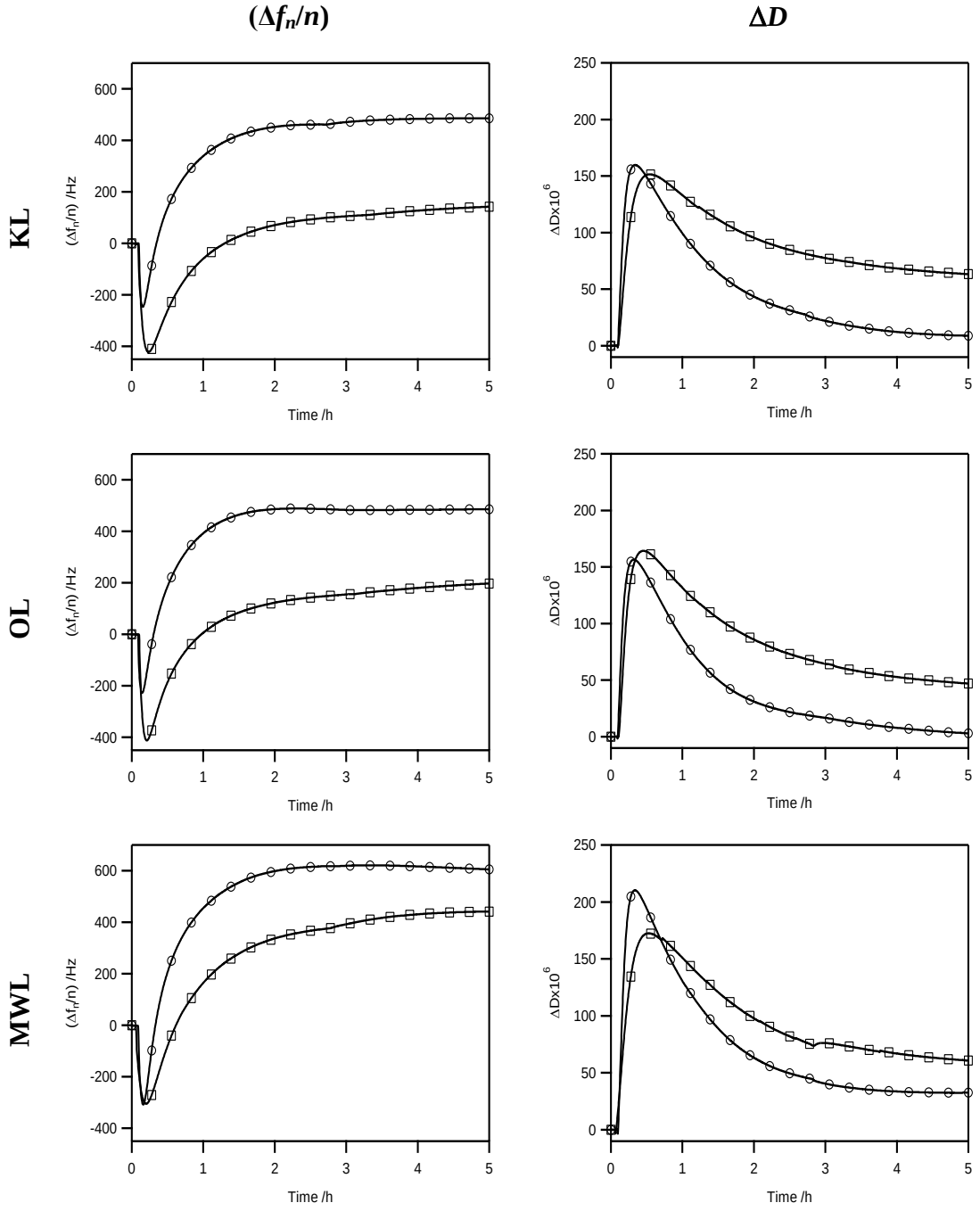

Figure E.1. ($\Delta f_n/n$) and ΔD curves (3rd overtone) for the enzymatic hydrolysis of untreated (□) and Tween 80-treated (○) CLC substrates with a nominal lignin content of 10%.

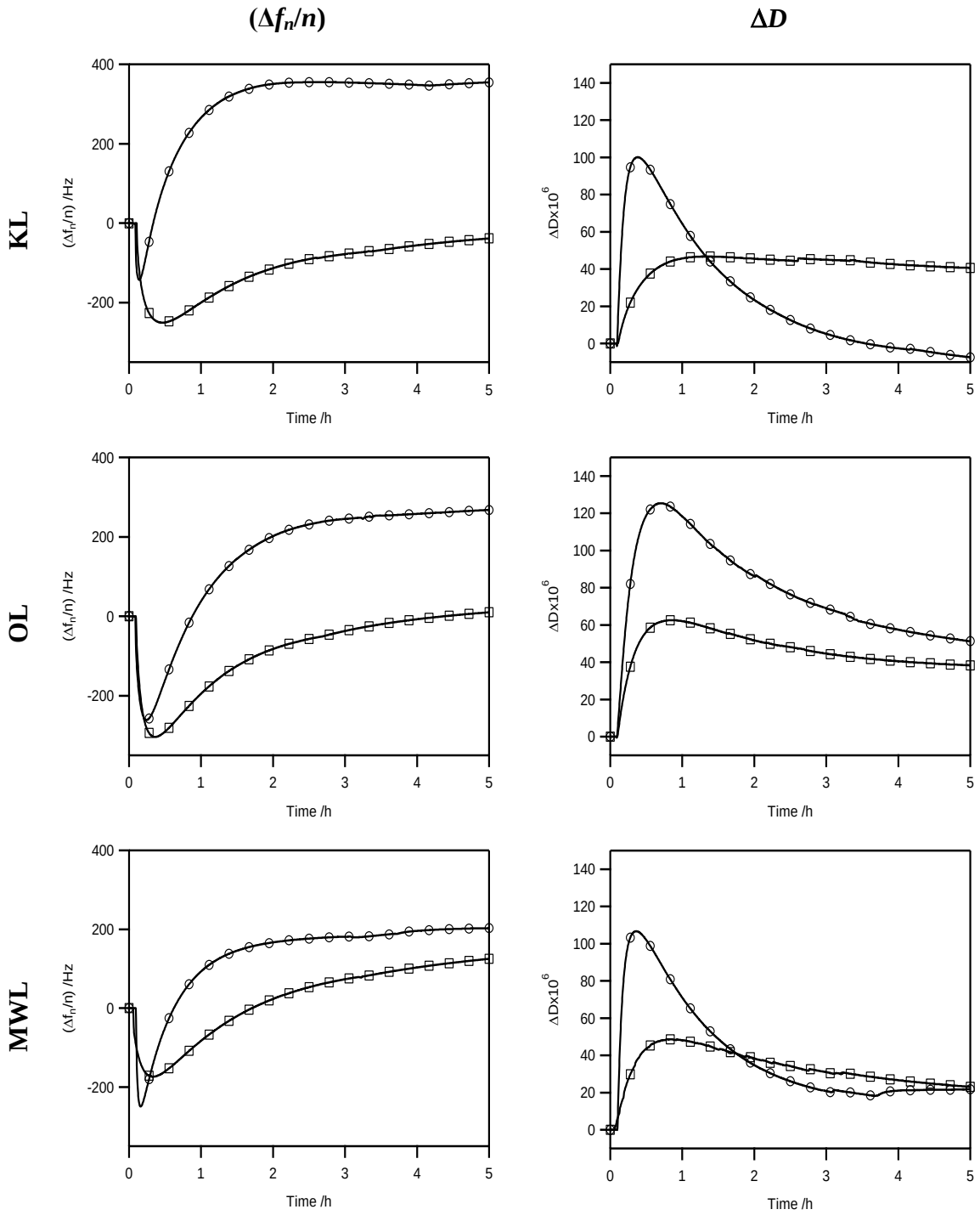

Figure E.2. ($\Delta f_n/n$) and ΔD curves (3rd overtone) for the enzymatic hydrolysis of untreated (□) and Tween 80-treated (○) CLC substrates with a nominal lignin content of 20%.

Table E.1. $(d(\Delta f_n/n)/dt)_{max}/(d(\Delta f_n/n)/dt)_{max,CNC} \times 100\%$, from 3rd overtone ($\Delta f_n/n$) curves, for untreated and Tween 80-treated CLC substrates[a]

Nominal lignin content	KL		OL		MWL	
	untreated	treated	untreated	treated	untreated	treated
10%	8.4 ± 1.2	16.5 ± 0.2	10.5 ± 0.3	18.7 ± 1.1	8.5 ± 1.6	23.8 ± 1.2
20%	1.3 ± 0.03	10.1 ± 1.3	2.7 ± 0.8	8.9 ± 1.7	1.8 ± 0.1	5.3 ± 0.1
30%	0.1 ± 0.05	8.0 ± 1.3	0.6 ± 0.03	5.9 ± 0.7	0.7 ± 0.03	1.5 ± 0.1

[a] Data are means ± one standard deviation of three measurements.

Table E.2. $(d(\Delta f_n/n)/dt)_{max}/(d(\Delta f_n/n)/dt)_{max,CNC} \times 100\%$, from 3rd overtone ($\Delta f_n/n$) curves, for untreated and Tween 80-treated LLC substrates[a]

Lignin concentration[b]	KL		OL		MWL	
	Untreated	treated	untreated	treated	untreated	treated
0.5%	38.8 ± 5.6	120.9 ± 5.8	89.3 ± 3.6	120.6 ± 12.9	83.6 ± 10.5	116.7 ± 6.4
1%	4.1 ± 1.0	73.2 ± 9.6	16.6 ± 2.0	32.2 ± 5.3	14.6 ± 3.5	20.3 ± 3.5

[a] Data are means ± one standard deviation of three measurements.
[b] of the lignin suspension used for spin coating

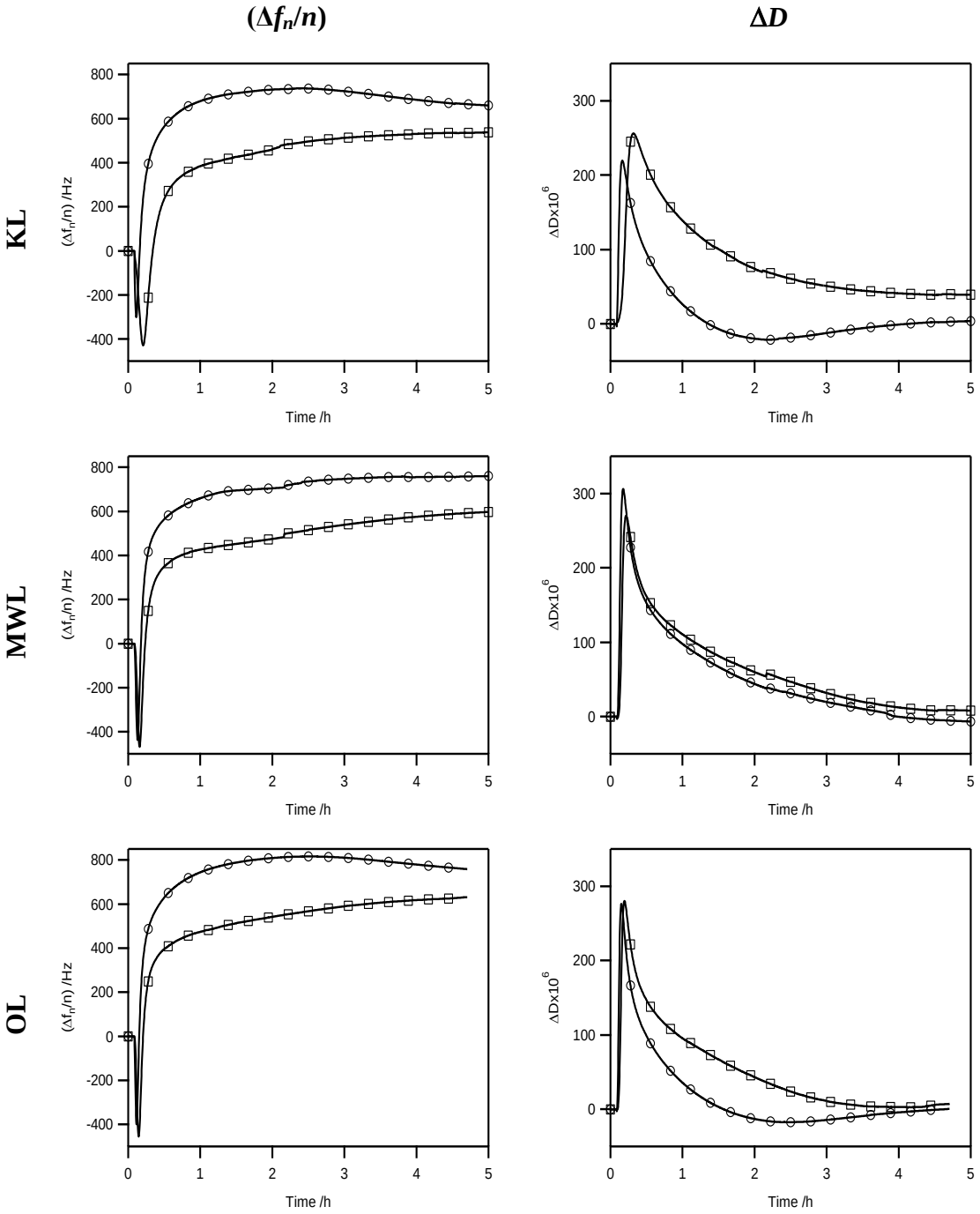

Figure E.3. ($\Delta f_n/n$) and ΔD curves (3rd overtone) for the enzymatic hydrolysis of untreated (□) and Tween 80-treated (○) LLC substrates prepared from 0.5 wt % aqueous lignin suspensions.

Appendix F: Additional experiments

F.1. Enzymatic hydrolysis of non-sulfated and sulfated cellulose substrates studied by surface plasmon resonance (SPR)

F.1.1. Experimental section

Cellulose substrates for SPR hydrolysis experiments were prepared on SPR sensor slides (12.0 mm × 12.0 mm × 0.9 mm). The SPR sensors were cleaned by immersion for 1 h in a boiling mixture of aqueous ammonia, hydrogen peroxide, and DI water at a volume ratio of 1:1:5 and then for 1 h at ambient temperature in fresh piranha solution (7:3 (v/v) mixture of sulfuric acid and hydrogen peroxide), rinsed with DI water, dried in a stream of nitrogen. Cellulose substrates were prepared by spin coating (WS-400B-6NPPLite, Laurell Technologies Corp.) the cleaned SPR sensor slides for 1 min at 4000 rpm with 140 µl of a 1 wt % CNC suspension, prepared as described in Chapter 4. After retrieval from the spin coater, the substrates were dried in a vacuum oven at 65 ℃ for several hours for improved stability in aqueous media. The cellulose substrates were refractive index-matched with immersion oil (n_D = 1.5150) to the prism of the SPR refractometer (SR 7000, Reichert, Inc.). The system used a laser diode with an emission wavelength of 780 nm. The flow cell body was equipped with a Viton gasket (Dupont Dow Elastomers LLC) and was mounted on top of the sensor slide. Before the experiment, a 0.25 $mL \cdot min^{-1}$ feed of 50 mM sodium citrate buffer feed, prepared as described in Chapter 4, to the flow cell was established *via* Teflon tubing with a cartridge pump (Masterflex). The temperature inside the flow cell was controlled at 25 ± 0.02 ℃. When the baseline was stable, the buffer feed was replaced with a feed of cellulase solution, prepared as described in Chapter 4, with the same flow rate. Both the buffer and cellulase solutions had been degassed prior to the start of the SPR experiments. The shift in SPR resonance angle, $\Delta\theta_{SP}$, was recorded during the experiment. When $\Delta\theta_{SP}$ reached a plateau, the buffer feed was restored and maintained for 30 min.

F.1.2. Results and discussion

Figure F.1 shows $\Delta\theta_{SP}$ curves for the enzymatic hydrolysis of the substrates SH-0 and HH-0. A comparison of the $\Delta\theta_{SP}$ curves with the ($\Delta f_n/n$) curves in Figure 4.4 in Chapter 4 shows that the hydrolysis curves measured by SPR were very similar to those measured by QCM-D.

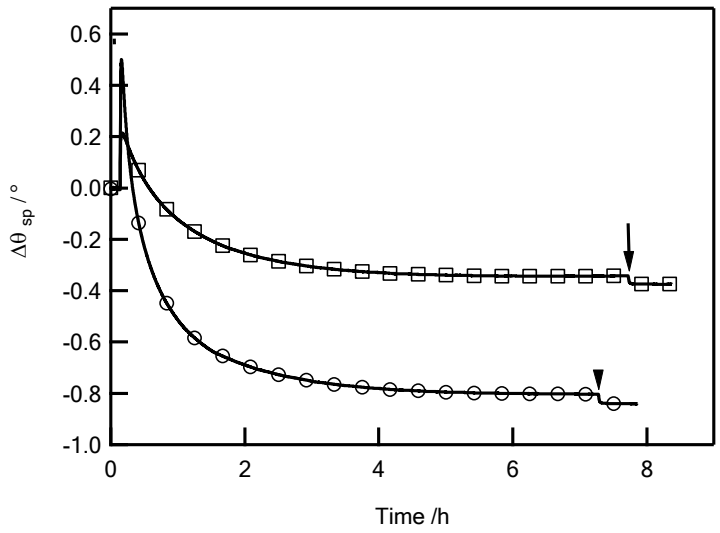

Figure F.1. $\Delta\theta_{SP}$ curves for the enzymatic hydrolysis of the substrates SH-0 (○) and HH-0 (□). The arrows indicate a switch of the liquid feed from enzyme solution to buffer.

The initial rapid increase in $\Delta\theta_{SP}$ indicated cellulase adsorption onto the cellulose substrates. The $\Delta\theta_{SP}$ maximum for the SH-0 substrate was much larger than that for HH-0 substrate. The larger maximum indicated greater enzyme adsorption onto the SH-0 substrate than onto the HH-0 substrate. At the end of the hydrolysis, the $\Delta\theta_{SP}$ values for both substrates were below zero. The negative $\Delta\theta_{SP}$ values indicated a decrease in optical density near the sensor surface, possibly due to the removal of the substrates from the sensor during hydrolysis. The plateau value of $\Delta\theta_{SP}$ for the SH-0 substrate was much lower than that for HH-0 substrate. The lower plateau value was due to the greater CNC surface density of the SH-0 substrate, compared to the HH-0 substrate, as discussed in Chapter 4. These finding were in agreement with the QCM-D results.

Figure F.2 shows $\Delta\theta_{SP}$ curves for the enzymatic hydrolysis of the substrates SH-55, SH-152, and SH-293. In accordance with the QCM-D results in Chapter 4, the magnitude of the $\Delta\theta_{SP}$ maximum increased with increasing sulfate group density of the substrate. The increase signified an increase in the maximum amount of cellulase adsorbed on the substrate. For all substrates, $\Delta\theta_{SP}$ at the end of the hydrolysis was greater than 0. The positive $\Delta\theta_{SP}$ values indicated that these substrates underwent less hydrolysis than SH-0 in Figure F.1, *i.e.* that part of the substrate remained on the sensor, and that the sulfate groups hindered the enzymatic hydrolysis of the substrates. The increase in the $\Delta\theta_{SP}$ plateau values with increasing sulfate group density indicated that the inhibitory effect of the sulfate groups depended on their density on the substrate.

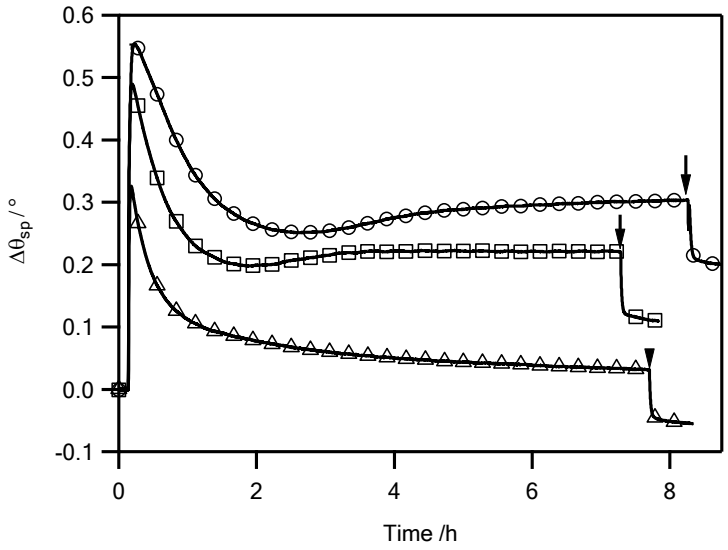

Figure F.2. $\Delta\theta_{SP}$ curves for the enzymatic hydrolysis of the substrates SH-55 (△), SH-152 (□), and SH-293 (○). The arrows indicate a switch of the liquid feed from enzyme solution to buffer.

F.2. Effects of Tween 80 on the enzymatic hydrolysis of cellulose substrates covered with a dehydrogenase polymer (DHP) lignin layer

F.2.1. Experimental section

Hydrogen peroxide (30%, Certified ACS) was purchased from Fisher Scientific. Sodium phosphate monobasic (SigmaUltra, min. 99.0%), sodium phosphate dibasic (SigmaUltra, min. 99.0%), coniferyl alcohol (98%), horseradish peroxidase (type I, 50-150 units/mg solid) were purchased from Sigma-Aldrich and used without further purification. Phosphate buffer (50 mM, pH = 6.5) was prepared in the lab. Solutions of hydrogen peroxide (10 mM), coniferyl alcohol (5 mM), and horseradish peroxide (0.2 g/L) in phosphate buffer were used as stock solutions.

Cellulose substrates on cleaned silicon dioxide-coated AT-cut quartz crystals (Q-Sense) were prepared as described in Chapter 7. After spin-coating, the cellulose substrates were placed into polystyrene Petri dishes. Five milliliters of each of the three stock solutions were simultaneously transferred into the Petri dish so that the coniferyl alcohol concentration (CAC) in the reaction medium was 1.67 mM. The reaction was carried out at room temperature for 48 h. After the reaction, the substrates were rinsed thoroughly with DI water, dried in a stream of nitrogen, and heated in a vacuum oven at 65 ℃ for several hours. A second set of substrates was prepared with a CAC of 0.167 mM in the reaction medium. The reaction medium for this reaction was prepared by simultaneous transfer of 0.5 mL of each of the three stock solutions into the Petri dish, followed by dilution with phosphate buffer to a final volume of 15 mL. The substrates will be referred to as high-CAC and low-CAC substrates.

The surface morphology and RMS surface roughness of the high CAC substrates were analyzed by atomic force microscopy (AFM). Substrates were imaged with an Asylum Research MFP-3D-BIO atomic force microscope. Substrates were scanned in air at ambient relative humidity and temperature in intermittent-contact mode with OMCL-AC160TS standard silicon probes (Olympus Corp.) with a scan frequency of 1 Hz, and 512 scans with 512 points/scan. RMS surface roughness values were determined from the whole scan areas in AFM height images.

For QCM-D hydrolysis experiments, the high-CAC and low-CAC substrates were placed in QCM-D flow modules, and a 0.25 $mL \cdot min^{-1}$ feed of 50 mM sodium citrate buffer (pH 4.8), prepared as described in Chapter 6, was established. The temperature inside the flow modules was controlled at 25 ± 0.02 ℃. When the normalized rate of change of the 3rd overtone frequency, ($\Delta f_3/3$), became less than 2 $Hz \cdot h^{-1}$, the substrates were considered saturated and equilibrated, and the buffer feed was replaced with a feed of enzyme solution with the same flow rate. The enzyme solution had been prepared as described in Chapter 6. In hydrolysis experiments with Tween 80-treated substrates, after equilibration of the substrates in buffer, the buffer feed was replaced with a feed of 1 mM Tween 80 solution in buffer at the same flow rate. After some time, which depended on the experiment, the buffer feed was restored for a few minutes and then replaced with a cellulase solution feed. Δf and ΔD were recorded in real time at the fundamental frequency (5 MHz) and 6 overtone frequencies (15, 25, 35, 45, 55, and 65 MHz) with QSoft 401 acquisition software (Q-Sense). Experiments were terminated when Δf reached a plateau.

F.2.2. Results and discussion

Figure F.3 shows AFM height images of high-CAC substrates at different magnifications. The tall globular particles observed in Figure F.3a might be adsorbed horseradish peroxidase molecules or aggregates. CNCs from the subjacent cellulose substrate were not visible in either of the images. The small globular particles on the surface of the substrates were most likely DHP lignin aggregates. A globular morphology of DHP lignin particles on cellulose substrates has also been reported by others.[1] The RMS surface roughness of cellulose substrates from CNCs, measured over a 2 μm × 2 μm area, was reported in Chapter 6 as 3.6 nm. The lower surface roughness of the high-CAC substrate (1.4 nm) was probably a result of DHP lignin particles filling the voids between the CNCs and thus smoothening the surface of the substrate.

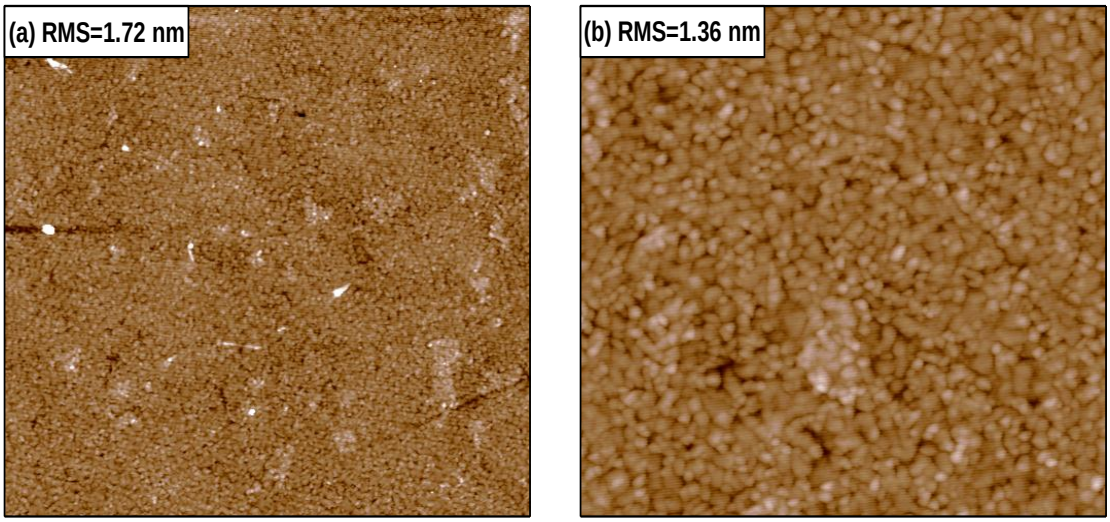

Figure F.3. AFM height images of DHP lignin covered cellulose substrates (high-CAC). The scan sizes are (a) 5 μm × 5 μm and (b) 2 μm × 2 μm. The z-scale is 15 nm. The RMS surface roughness was determined from the entire area of the image.

Adsorption of Tween 80 onto the high-CAC and low-CAC substrates was studied by QCM-D. Figure F.4 shows the obtained ($\Delta f_n/n$) and ΔD curves. On the high-CAC substrate, the value of ($\Delta f_n/n$) at the end of Tween 80 adsorption was –20 Hz whereas it was –6.6 Hz on the low-CAC substrate. The higher value of ($\Delta f_n/n$) on the high-CAC substrate at the end of Tween 80 adsorption signified that more Tween 80 was adsorbed on this substrate than on the low-CAC substrate. A possible reason could be that the high-CAC substrate contained more DHP lignin, leading to stronger hydrophobic interactions between DHP lignin molecules and the hydrophobic tails of Tween 80.

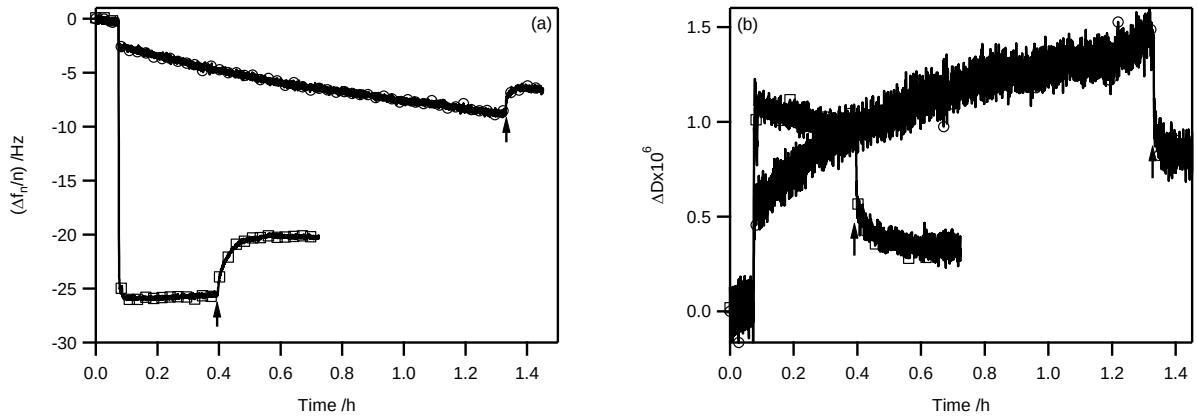

Figure F.4. (a) ($\Delta f_n/n$) and (b) ΔD curves (3rd overtone) for the adsorption of Tween 80 onto the high-CAC substrates (□) and low-CAC substrates (○). The arrows indicate the switch of the liquid feed from Tween 80 to buffer.

Figure F.5 shows ($\Delta f_n/n$) and ΔD curves for the enzymatic hydrolysis of untreated and Tween 80-treated high-CAC substrates. As seen in Figure F.5a, switch of the liquid feed to the QCM-D flow modules to cellulase solution caused a sharp decrease in ($\Delta f_n/n$), indicating the adsorption of cellulase onto the substrates. However, the usual increase in ($\Delta f_n/n$) after the decrease, signifying a mass loss on the quartz crystal due to hydrolytic substrate erosion, was missing. The absence of a ($\Delta f_n/n$) increase after the decrease indicated that the enzymatic hydrolysis of the subjacent cellulose substrate was suppressed by the DHP lignin layer. The Tween 80-treated substrate only showed a slight decrease in ($\Delta f_n/n$). The fact that the ($\Delta f_n/n$) decrease on the Tween 80-treated substrate was smaller than on the untreated substrate indicated that less enzyme adsorbed onto the Tween 80-treated substrate than onto the untreated substrate. In Chapter 5, Tween 80 has been shown to reduce cellulase adsorption onto hydrophobic gold substrates and to inhibit cellulase adsorption onto hydrophilic silica substrates. The lower cellulase adsorption onto the Tween 80-treated high-CAC substrate might have had the same reason as the reduced cellulase adsorption onto the Tween 80-treated gold substrate. As was the case for the untreated high-CAC substrate, enzymatic hydrolysis was not observed for the Tween 80-treated substrate.

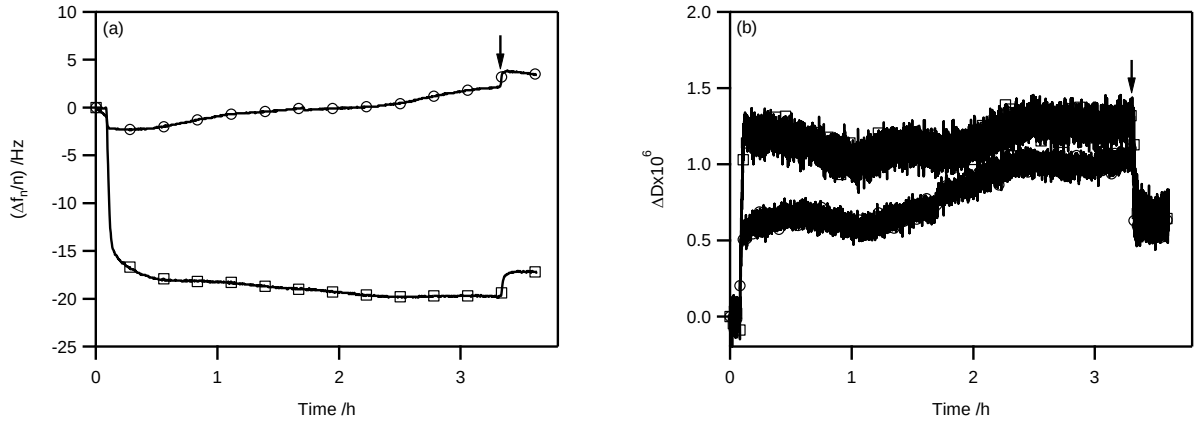

Figure F.5. (a) ($\Delta f_n/n$) and (b) ΔD curves (3rd overtone) for the enzymatic hydrolysis of untreated (□) and Tween 80-treated (○) high-CAC substrates. The arrows indicate a switch of the liquid feed from enzyme solution to buffer.

Figure F.6 shows ($\Delta f_n/n$) and ΔD curves for the enzymatic hydrolysis of untreated and Tween 80-treated low-CAC substrates. In contrast to Figure F.5a, Figure F.6a showed ($\Delta f_n/n$) curves typical for the enzymatic substrate hydrolysis. However, compared to that of cellulose substrates, the hydrolysis of the low-CAC substrates was very slow and did not come to completion, as indicated by the high ΔD values at the end of the experiment signifying that a soft layer remained on the quartz crystal. The Tween 80-treated substrate showed similar ($\Delta f_n/n$) and ΔD curves as the untreated substrate.

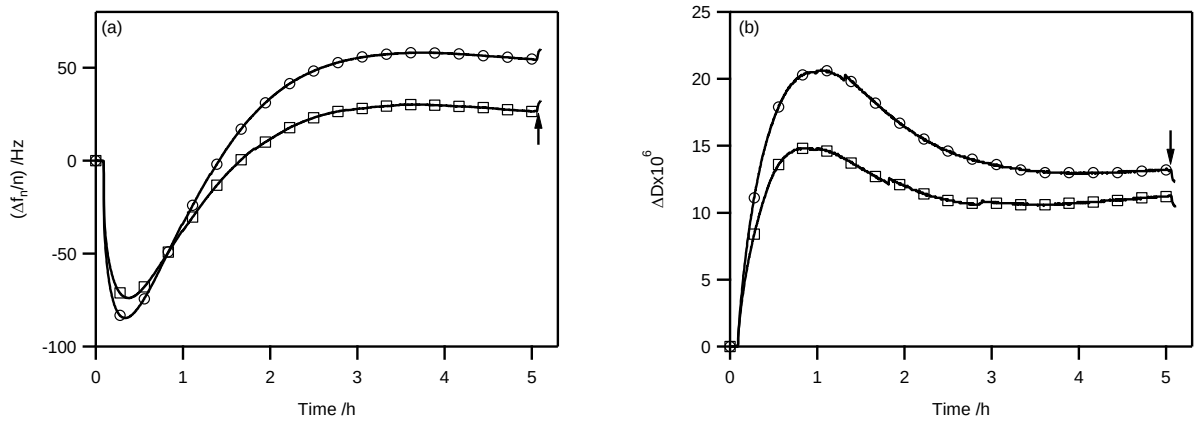

Figure F.6. (a) ($\Delta f_n/n$) and (b) ΔD curves (3^{rd} overtone) for the enzymatic hydrolysis of untreated (□) and Tween 80-treated (○) low-CAC substrates. The arrows indicate a switch of the liquid feed from enzyme solution to buffer.

On the basis of these results, the following conclusions can be drawn: *In situ* synthesis of DHP lignin produces a DHP lignin layer on top of the cellulose substrate. Depending on the coniferyl alcohol concentration of the reaction medium, presumably affecting its thickness, the DHP lignin layer hinders or suppresses the enzymatic hydrolysis of the subjacent cellulose substrate. As opposed to that of layered lignocellulosic (LLC) substrates (Chapters 6 and 7), the enzymatic hydrolysis of DHP lignin-covered cellulose substrates is only weakly affected by Tween 80. The observed differences could either be due to a more effective blocking of enzyme access to the cellulose substrate by the DHP lignin or to covalent bonds between the cellulose substrate and the superjacent DHP lignin layer making it impossible for Tween 80 to remove the lignin layer.

References

1. Micic, M.; Radotic, K. A.; Jeremic, M.; Djikanovic, D.; Kammer, S. B. Study of the Lignin Model Compound Supramolecular Structure by Combination of near-Field Scanning Optical Microscopy and Atomic Force Microscopy. *Colloids and Surfaces B-Biointerfaces* **2004,** *34*, 33-40.